

Application of Satellite Gradiometry and Terrestrial Gravimetry to Identify Regional Stress Anomalies in the North Chilean Subduction System

Dissertation

zur Erlangung des Doktorgrades

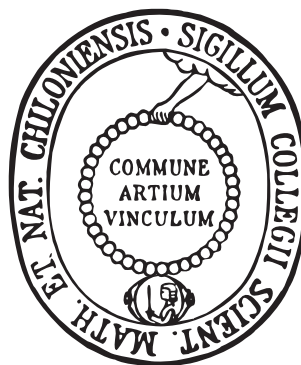
der Mathematisch-Naturwissenschaftlichen Fakultät

der Christian-Albrechts-Universität zu Kiel

vorgelegt von

Benjamin D. Gutknecht

Kiel, 2015



Erster Gutachter: Prof. Dr. Hans-Jürgen Götze

Zweiter Gutachter: Prof. Dr. Jörg Ebbing

Tag der Disputation: 14. Oktober 2015

Zum Druck genehmigt: 14. Oktober 2015

gez. Prof. Dr. Wolfgang J. Duschl, Dekan

Rise above the crowds
And wade through toxic clouds
Breach the outer sphere
The edge of all our fears
Rest with you
We are counting on you
It's up to you
M.J. Bellamy

Contents

1	Introduction	11
2	Methods, Data and Models	15
2.1	Methods	15
2.1.1	Gravity and 3D density forward modelling	15
2.1.2	Analysis of the full gravity gradient tensor	17
2.1.3	Lithostatically induced stresses	23
2.1.4	Dynamic stresses	24
2.1.5	Methods of geodetic gravity field modelling	24
2.2	Data	24
2.3	Models	26
3	Applicability of gravity/–gradient data and models	29
3.1	Lithospheric modelling by using optimized GOCE gravity gradient data	31
3.1.1	Motivation	31
3.1.2	Methods and results	32
3.1.3	Discussion and summary	39
3.2	The seismically active Andean and Central American margins: can satellite gravity map lithospheric structures?	42
3.2.1	Introduction	43
3.2.2	Tectonic setting	45
3.2.3	Gravity database and geophysical constraints	47
3.2.4	Results and discussion	48
3.2.5	Conclusions	61
3.3	Applicability Summary	62
4	Application of GOCE data	63
4.1	Combined regional gravity model of the Andean convergent subduction zone and its application to crustal density modelling in active plate margins	64
4.1.1	Introduction	65
4.1.2	Data	66

4.1.3	Methodological background	69
4.1.4	Validation and preprocessing of the terrestrial data	74
4.1.5	Combined regional gravity modelling	77
4.1.6	Application: density modelling	83
4.1.7	Conclusions	88
4.2	Structure and state of stress of the Chilean subduction zone from terrestrial and satellite-derived gravity and gravity gradient data	90
4.2.1	Introduction and motivation	91
4.2.2	Tectonic setting	92
4.2.3	Database and constraints	94
4.2.4	Density models	95
4.2.5	Methodology	96
4.2.6	Results and discussion	104
4.2.7	Conclusions	116
4.3	Application summary and supplement	118
5	Further implications from GNSS modelling	129
6	Concluding remarks and outlook	139
	References	145
	Appendix	162
	List of figures	173
	List of tables	173
	Acronyms	173
	Acknowledgements	177
	Copyright acknowledgement	179
	Declaration	181
	Curriculum Vitae	183

Abstract

The effect of the lithospheric density distribution on physical coupling of the subduction system in the area of the Central Andes (18° – 35° S) has been investigated. Amongst the composition of the subducting oceanic plate and properties of the subduction interface itself, there has also been evidence that increased coupling of the system may be linked to excess masses above the descending plate. High plate coupling is associated with an increased risk for megathrust earthquakes which occur at respective locations when the accumulated stresses are released and dispersed as seismic energy.

Methodological considerations, forward-modelling as well as GPE- and stress calculations – that base on the utilisation and interpretation of the gravity field and its gradient tensor – have been applied in order to examine and analyse the density- and stress distribution in the target area. Particular attention has also been paid to the evaluation of gravity data from the GOCE satellite mission, which, for the first time, provides near-globally measured full-tensor gradiometric data. Methodological analysis concerning the resolving capacity of gravity and gradiometry reveal that measured gravity gradients of the GOCE mission are just sensitive enough to receive information at the order of the expected coastal batholiths' gravity anomaly in North Chile. Those are believed to significantly affect coupling of the subduction system through their relative excess mass.

Synthetic 3D density forward modelling of a standard subduction setting has been applied to further test the analysis. It confirms that density contrasts beyond resolvability for gravity data at the orbit height (~ 250 km) are just resolved in the gradient tensor and its invariants though.

The spatial resolution of most recent potential field models that represent measurements from satellite missions is not better than spherical-harmonic degree and order (d/o) 300 (≈ 67 km half-wavelength). This is still not sufficient for very detailed lithospheric or even crustal studies. It is mainly attributed to the signal-to-noise ratio conditions and to overlapping signals in the measurement systems at large distance to the source-masses. However, satellite-based data are virtually globally available and they are acquired and processed in homogeneous manner. They may therefore be consistently handled, analysed and interpreted. Terrestrial data, on the other hand, are strongly heterogeneously distributed, sometimes inadequately processed and meta-data is often not available. Their advantage is a good spatial resolution because of the short distance to the source-masses which allows the distinction of signals.

When satellite-derived data are co-located with ground-based data, the respective advantages of both sets — homogeneous coverage and processing of satellite data and high resolution of terrestrial data — may be jointly utilized in one combined potential field model. Here, the combined regional gravity field model IMOSAGA01C has been employed which incorporates terrestrial gravity data of the Central Andes from more than 20 years and satellite-based data from the GOCO03S gravity field model. It has been used on a 6×6 -minute (≈ 11 km) grid at 8 km altitude to optimize a pre-existing 3D-density model of North Chile between 18 – 31.5° S and 66 – 73° W. By applying geometry adjustments and density inversion,

the standard deviation of the residual anomaly could be reduced by 62.3% to $6.3 \times 10^{-5} \text{ m s}^{-2}$ for the model area. When also parts of the model area are considered that are not covered by terrestrial gravity data, this correspond to an overall error decrease by 68.7%.

The adjusted geometry and density information of the density model served as an input to the computation of static stress anomalies on top of the subducting Nazca Plate. The interface–normal rotated component of the lithostatically–induced stress anomaly exhibits a clear segmentation of the forearc. It is characterized by a sequence of positive stress anomalies of up to 80 MPa along the coastal Jurassic batholith belt. It correlates well with the major seismicity of the active margin in North Chile and is attributed to mass excess in the continental crust and lithosphere above the subduction interface.

A joint analysis with coupling coefficients from GPS–modelling revealed that positive stress anomalies in the order of 0–100 MPa act as an approximate threshold for the minimum plate coupling (in per cent) within the scope of the seismogenic zone between 18.75°S and 21.75°S. Thus, there must exist patches along the margin where the plate coupling is generally higher than in areas with less relative load (except co-seismic state). Furthermore, a systematic analysis in the area of the April 2014 megathrust earthquake offshore Pisagua/Iquique revealed that coupling and stress anomalies in the area of the fracture plane form virtual loops in their common parameter–space. This could be understood as a strong indicator for the validity of the stress–induced coupling hypothesis. In the future, this finding could help to better understand the seismo–periodic state of a subduction system.

This work comes to the conclusion that potential field data from the GOCE mission, despite its high sensitivity, must be understood to reside at the very edge of an appropriate resolution for detailed lithospheric studies. The IMOSAGA01C combined gravity field model however, which collocates the satellite– and surface–based gravity data, clearly outperforms the existing combined models in this regard. Hereby the quality of density models can be improved, which in turn leads to better constrained derivatives such as dynamic models or stress anomalies. From the latter it could finally be concluded that the hypothesis for the North Chile case is acceptable, that relative mass excess above the subducting Nazca Plate co–generates asperities with increased potential for megathrust earthquakes.

Zusammenfassung

Mit der vorliegenden Arbeit wurde der Einfluss der Dichteverteilung kontinentaler Lithosphäre auf die physikalische Kopplung des Subduktionssystems im Bereich der Zentralanden (18° – 35° S) untersucht. Neben der Beschaffenheit der subduzierenden ozeanischen Platte und den Eigenschaften der Grenzfläche der Subduktion selbst, gibt es Hinweise darauf, dass ein relativer Massenüberschuss oberhalb der abtauchenden Platte in Zusammenhang mit erhöhter Kopplung des Systems steht. Gleichzeitig erhöht sich die Gefahr durch Starkbeben, die an entsprechenden Lokationen auftreten, wenn die aufgebauten Spannungen an den Blockaden gelöst werden und in Form seismischer Energie freigesetzt werden.

Methodische Überlegungen, Fortwärtsmodellierungen, sowie GPE- und Stressberechnungen, die auf der Interpretation des Schwerfeldes und seines Gradiententensors beruhen, wurden angewendet, um die Dichte- und Stressverteilung im Untersuchungsgebiet näher zu bestimmen und zu analysieren. Ein besonderes Augenmerk lag auch auf der Evaluierung der Schweredaten der Satellitenmission GOCE, welche erstmals gemessene gradiometrische Daten des gesamten Schwere-Tensors nahezu global zur Verfügung stellte. Methodische Analysen zum Auflösungsvermögen der Schwere- und Gradiometrie-Daten ergaben, dass die gemessenen Gradienten der GOCE Mission hinreichend sensitiv sind, um Informationen in der Größenordnung der erwarteten Schwereanomalie der Küstenbatholithe in Nordchile zu registrieren. Es wird angenommen, dass diese durch ihren Massenüberschuss die Kopplung des Subduktionssystems signifikant beeinflussen.

Die synthetische 3D-Dichtemodellierung eines standardisierten Subduktions-Settings wurde verwendet, um diese Überlegung zu überprüfen. Sie bestätigt das Ergebnis, dass Dichtekontraste, die sich für Schweredaten in Orbithöhe (~ 250 km) jenseits der Auflösbarkeit befinden, durch den Schweregradienten-Tensor und seine Invarianten hingegen gerade noch aufgelöst werden können.

Die räumliche Auflösung aktueller Potenzialfeld-Modelle, welche Messungen von Satellitenmissionen wiedergeben, ist nicht besser als Grad/Ordnung 300 (≈ 67 km Halbwellenlänge). Das ist für sehr detaillierte Studien der Lithosphäre oder Kruste noch unzureichend. Ursachen hierfür sind in erster Linie die Kondition des Signal-Rausch-Verhältnisses und sich überlagernde Signale im Messsystem bei großer Distanz zu den verursachenden Massen. Dafür sind Satelliten-basierte Daten quasi-global verfügbar und homogen aufgenommen. Sie können konsistent prozessiert, analysiert und interpretiert werden. Terrestrische Daten hingegen sind zumeist extrem heterogen verteilt, sehr unterschiedlich prozessiert und Metadaten stehen oft nicht zur Verfügung. Der Vorteil bei ihrer Verwendung liegt darin, dass sie aufgrund des geringen Abstandes zu den Quellen ein hohes räumliches Auflösungsvermögen haben und eine entsprechend klare Signaltrennung möglich ist.

Die jeweiligen Vorteile beider Datenarten — homogene Aufnahme, Abdeckung und Prozessierung der Satellitendaten sowie hohe Auflösung der terrestrischen Daten — können in einer kombinierten Bearbeitung vereinigt werden, wenn beide Datensätze über Kollokation zusammengeführt werden. In der vorliegenden Arbeit wurde das kombinierte regionale Schwerfeldmodell IMOSAGA01C verwendet, welches terrestrische Schweredaten aus mehr

als 20 Jahren Bodenmessungen in den Zentralanden, sowie Satelliten-basierte Daten aus dem GOCO03S Schwerefeldmodell zusammenführt. Hier wurde ein 6×6 -Minuten (≈ 11 km) Grid in 8 km Höhe verwendet, um ein vorhandenes 3D Dichtemodell von Nordchile im Bereich $18\text{--}31.5^\circ\text{S}$ und $66\text{--}73^\circ\text{W}$ zu optimieren. Durch Anpassungen der Modellgeometrie und durch Dichte-Inversion konnte die Standardabweichung der Residualanomalie im Bereich der Modellierung um 62,3% auf $6.3 \times 10^{-5} \text{ m s}^{-2}$ gesenkt werden. Unter zusätzlicher Berücksichtigung der Modellgebiete, die nicht mit terrestrischen Schweremessungen abgedeckt sind, entspricht dies einer Verbesserung um 68,7%.

Die angepassten Geometrie- und Dichteinformationen des Dichtemodells dienen als Eingangsgrößen zur Berechnung statischer Stressanomalien auf der subduzierten Nazca-Platte. Die normal zur Subduktion rotierte Komponente der lithostatisch induzierten Stressanomalie weist eine deutliche Segmentierung des Forearcs auf. Diese zeichnet sich durch ein Band mit positiven Stressanomalien von bis zu 80 MPa im Bereich der Jurassischen Küstenbatholithe aus. Es korreliert mit der vorherrschenden Seismizität des aktiven Kontinentalrandes in Nordchile und ist auf Massenüberschüsse innerhalb der kontinentalen Kruste und Lithosphäre oberhalb der Subduktions-Grenzfläche zurückzuführen.

Im Gebiet der seismogenen Zone zwischen 18.75°S und 21.75°S zeigte eine gemeinsame Analyse mit Kopplungs-Koeffizienten aus GPS-Modellen, dass positive Stressanomalien im Bereich 0–100 MPa jeweils als näherungsweise Schwellenwerte für die minimale Kopplung (in Prozent) eingesetzt werden können. Demnach muss es Regionen geben, in denen die Kopplung der Platten, bis auf den co-seismischen Zustand, ständig höher ist als in Regionen mit geringerer relativer Auflast. Darüber hinaus zeigte eine systematische Analyse im Bereich des Starkbebens von Pisagua/Iquique vom April 2014, dass Plattenkopplung und Stressanomalien innerhalb ihres gemeinsamen Parameterraumes für den Bereich der Bruchfläche über virtuelle Schleifen verknüpft sind. Dies kann als Kennzeichen für die Gültigkeit der These zur Stress-induzierten Kopplung gewertet werden. Dieses Erkenntnis könnte zukünftig dabei helfen, den seismozyklischen Zustand eines Subduktionssystems besser zu verstehen.

Die vorliegende Arbeit kommt zu dem Schluss, dass sich die Potenzialfeld-Daten der GOCE Mission trotz der hohen Sensitivität im Grenzbereich der notwendigen Auflösung für detaillierte Lithosphärenstudien liegen. Das kombinierte Schwerefeldmodell IMOSA-GA01C hingegen, welches die Satelliten- und Boden-gestützten Schweredaten zusammenführt, übertrifft existierende kombinierte Modelle in dieser Hinsicht deutlich. Hierdurch lässt sich die Qualität der Dichtemodelle erhöhen, was zu einer besser validierten Zusatzinterpretation führt, wie zum Beispiel dynamische Modelle oder Stressanomalien zeigen. Aus letzteren konnte abgeleitet werden, dass die Hypothese, derzufolge relative Massenüberschüsse oberhalb der subduzierenden Nazca-Platte Asperities mit erhöhtem Gefährdungspotenzial für Starkbeben mitverursachen, für das Untersuchungsgebiet in Nordchile gültig ist.

1 Introduction

The occurrence of several devastating megathrust earthquakes in the beginning of the 21st century was a painful reminder that the underlying mechanisms of plate tectonics are still only understood at rather broad scales. An exact prediction of space and, most notably, time of the nucleation of an earthquake is today still difficult or — in the majority of cases — simply not possible.

Since many years, it is generally well understood that the most intense earthquakes of magnitude $M_w \geq 8$ occur in a shallow- to intermediate-depth level in the subduction environment (e.g. *Byrne et al.*, 1988; *Tichelaar and Ruff*, 1991) where dense oceanic lithosphere subducts beneath less dense continental lithosphere. *Lay and Kanamori* (1981) already proposed a model to describe the characteristics of subduction zones in terms of distribution and interaction of asperities. These are patches along a subducting plate that have strong coupling with the overriding plate and prevent the system from stable sliding. The basic understanding is that asperities can be of different size, shape and distribution and that they may fail while releasing stored strain energy individually. The main seismogenic event may last from seconds to minutes and the failure of an entire segment, including aftershocks that succeed the main event, may last for weeks. A failed asperity will load adjacent patches depending on its size and distribution. Failing of segments along a subduction zone tends to be periodic with repeat times in the order of roughly 100 years. The frequency, however, may be considerably variable and tends to be linked with the total width of failure along the margin.

The periodicity can be described as the *seismic cycle*. The concept of the seismic cycle comes with a nomenclature that is also used throughout the present work: The terms *pre-* and *post-seismic* specify the time before and after a seismogenic failure, respectively. The *co-seismic phase* is the time frame of the event itself; the time span in between two major failures is called *inter-seismic*.

In the past years, this 'classic' model about earthquakes in subduction systems was shown to be complemented by *slow-slip events* (*Hirose et al.*, 1999; *Dragert et al.*, 2001; *Schwartz and Rokosky*, 2007), in which large patches of the system show the ability to release accumulated energy through an *aseismical* mode. Other than that, continuous and stable sliding of the plates is to be seen as a fundamental mode of subduction.

A number of different properties and mechanisms have been discussed in the past to be

responsible for the build-up of asperities in subduction zones:

- Bathymetric features and properties (e.g. age, temperature and buoyancy of the incoming oceanic plate, subducted ridges or seamounts).
- Composition and characteristics of the subduction *interface*, fluids, frictional properties.
- Physical properties and influence of the overriding crust (rigidity, lithostatic loading etc.).

It is assumed that each of the three categories plays its roll in asperity generation during the seismic cycle. However, it is still matter of debate how much the respective mechanism varies in space and time and how significant its effect actually is.

Wells et al. (2003) found that free-air gravity lows over deep-sea terraces in the forearc of circum-Pacific subduction systems spatially correlate with the seismic moment release and asperities of megathrust earthquakes. They concluded that “deep-sea terraces and basins may evolve not just by growth of the outer arc high but also by interseismic subsidence not recovered during earthquakes”. Similarly, *Song and Simons* (2003) stated that largest co-seismic moment release of subduction earthquakes occurred predominantly in regions where the free-air gravity anomaly is low compared to the average trench-normal gravity anomaly and attributed this to “spatial variations in frictional properties on the plate interface”. However, both studies did not consider the Central Andean forearc, as *Tassara* (2010) summarized.

Following seemingly contrary suggestions made by *Sobiesiak et al.* (2007) about the positive forcing effect of the continental density distribution on the rupture of the $M_w = 8.0$ 1995 Antofagasta earthquake, the present work concentrates on the role of mass distributions of the overriding plate along the continental margin of North Chile from a gravity perspective.

Several studies have already indicated that temporal and spatial changes in the overburden might generally be linked to seismic events: *Wdowinski et al.* (2010) stated that unloading through hurricanes and erosion could eventually lead to the release of pre-stressed faults as in the Haiti $M_w = 7.0$ earthquake from 2010, when normally stabilising stresses decrease below the threshold of the respective stress-system. *Ader et al.* (2012) found for the main fault of the southern Himalayas that high topography, which forces principal Coulomb stresses into the vertical, is linked to drops in the ambient microseismicity. For the continental margin of Chile, *Tassara* (2010) pointed out that the forearc density structure exercises control on megathrust shear strength along the subducting Nazca Plate.

When a magnitude 8.2 earthquake hit Chile’s North on 1st April 2014 offshore Pisagua and Iquique, it was, for that matter, anything but unexpected. Surprisingly, no major hazardous seismicity (megathrust-earthquakes) had occurred on a 500 km wide seismic gap

between 19°S and 24°S since the 19th century. Therefore, considering the seismic cycle of the subducting Nazca plate below the South American continent, one or more major shocks at this part of the active margin had to be expected (e.g. *Schurr et al.*, 2012; *Metois et al.*, 2013, and many others).

Several inter-/national projects and collaborations had been promoted and set up in order to investigate the state of the continental margin with all sorts of geo-scientific techniques. A recent project is the "Integrated Plate boundary Observatory Chile" (IPOC), which is a European–South American network of institutions and scientists organizing and operating a distributed system of instruments and projects dedicated to the study of earthquakes and deformation at the continental margin of Chile (www.ipoc-network.org). It applies methods and instrumentation from seismology, Global Positioning System (GPS), magnetotellurics, creep meters, accelerometers, Interferometric Synthetic Aperture Radar (InSAR) and others. A dedicated gravity campaign (DFG GO380/29-1) complemented a data base of terrestrial gravity data at the western South-American margin, which has a record of gravity measurements of more than 20 years (*Schmidt and Götze*, 2006; *Oncken et al.*, 2006). The new data have recently been processed in a master's thesis by *Schaller* (2013).

The published work of chapters 3.1 and 3.2 in the present thesis was compiled during the "*NOvel Geophysical And Petrological applications of new-generation Satellite-derived GRAVity data with a focus on hazardous and frontier regions*" (NOGAPSGRAV) project, which was part of the German Research Foundation (DFG)'s priority programme 1257 "Mass Transport and Mass Distribution" (*Kusche et al.*, 2012, 2014). NOGAPSGRAV was established to bring together experts from solid earth geophysics (Kiel University) and dynamic-modelling geophysics (Frierich-Schiller-Universität Jena), complemented by petrology (University of Potsdam). Petrology would help to improve the parametrisation of density models and the dynamic-modelling section would utilise the static density forward models in order to further compute these models geo-dynamically. With regard to the present dissertation, the key questions addressed in the project were:

- What is the applicability of available gravity data to lithospheric studies in Central and South America (*Köther et al.*, 2012, chapter 3.2)?
- Could gravity and gravity gradient models and data of the Gravity Field and Steady-State Ocean Circulation Explorer (GOCE) mission (*Drinkwater et al.*, 2003) be expected to add significant value to the conception of plate tectonics (*Gutknecht*, 2011; *Gutknecht et al.*, 2014, see chapters 3.1 & 4.2)?

The NOGAPSGRAV project was followed by the "*Integrated MOdelling of Satellite- and Airborne Gravity data of Active plate margins*" (IMOSAGA) project (DFG GO380-/29-2), in which a partner group from the geodesy branch (Technical University of Munich) substituted the petrophysical component in order to establish a direct link between geodetic and

geophysical modelling. It addressed the combination of existing gravity data from the surface with new satellite data of the GOCE mission in order to derive the precise IMOSAGA01C combined gravity model for the study area of the active margin in North Chile. The model processing and also the evaluation, which is part of this dissertation, was published by *Hosse et al.* (2014) and is presented in chapter 4.1.

Gutknecht et al. (2014) contains the application of the combined gravity field to optimise the well constrained 3D density model of *Prezzi et al.* (2009) by forward-modelling and parameter inversion. Chapter 4.2 is a central part of the present work as it also describes the utilisation of the improved density model in order to subsequently derive maps of Gravitational Potential Energy (GPE) of the Central Andes and in order to calculate the mass-induced anomalous stress distribution on top of the subducting Nazca plate. In this way, the new satellite data should help to paint a more accurate picture of the state of stress along the subduction zone. Depending on the achievable resolution, it would also be possible to identify segmentation in the fore-arc and compare the results to the known seismicity.

Other measuring systems, e.g. InSAR and GPS, which were also implemented in the IPOC project, had previously already been applied by others to estimate strain accumulation and plate movements (e.g. *Chlieh et al.*, 2004). In chapter 5 of this thesis it is described how plate-coupling data as inferred from GPS observations (*Metois et al.*, 2013) were utilised for the purpose of the present thesis: the combined analysis and interpretation of coupling and stress anomalies from chapter 4.2 leads to a deeper understanding of asperity generation within the seismic cycle of the North Chilean subduction zone.

Author's contribution and copyright information: Each of the chapters 3.1, 3.2, 4.1 and 4.2, which have been published in international peer-reviewed journals and collections, contains an introducing declaration of the author's contribution to the article. Detailed copyright and citation info can be found in a corresponding section at the end of this work. All other sections are additional 'own' work to complement this dissertation which shall be classified as *mixed form*.

2 Methods, Data and Models

One aim of this dissertation is a critical examination of the applicability of available gravity- and gravity gradient data and -models with respect to the study of asperity generation at the Chilean active continental margin. The variety of methods, data and models that were directly or indirectly applied throughout the thesis is introduced in the following sections 2.1–2.3, accordingly.

2.1 Methods

A wealth of geophysical methods have been applied throughout this work in order to perform the required tasks at the specific stages of the work, respectively. This section gives an overview of the applied methods. Central method has been the concept of gravity in general and gravity forward modelling of the solid Earth in particular. Motivated by the success of the GOCE satellite mission, the concept of full tensor gravity gradiometry was added to the analysis and is introduced in section 2.1.2. The additional use of satellite gravity and gravity gradients in modelling should potentially lead to more plausible density models of the subsurface. In the course of this work, such improved or refined models have been a central topic in view of the fact that they were used to derive static stress anomalies on the subducting Nazca Plate that were exclusively dependent on the model's density distribution and geometry. The stress anomalies were subsequently evaluated along seismological information and plate coupling parameters from Global Navigation Satellite Systems (GNSS) observations. Project partners used on the one hand also static density models as input to geodynamic finite element modelling (*Zeumann, 2013; Zeumann et al., 2014*, cf. sections 3.2.4.5 and 4.2.5.3) and were on the other hand responsible for geodetic gravity modelling and developing the IMOSAGA01C combined regional gravity model (*Hosse et al., 2014*, chapter 4.1).

2.1.1 Gravity and 3D density forward modelling

3D modelling of the subsurface density structure was the principle method used throughout the present work. Terrestrial gravity data, i.e. the first spatial derivative of the Earth's gravity potential measured at the surface, has already been used for centuries in order to determine

mass- or density–anomalies in the subsurface. In Cartesian coordinates, the gravity potential U of a mass element

$$dm = \rho \cdot dV \quad (2.1)$$

can be described as

$$U = -G \cdot \int_x \int_y \int_z \rho \frac{dV}{r} \quad (2.2)$$

with:

- ρ : bulk density of
- volume element dV ,
- gravity constant $G = 6.673 \times 10^{-11} \frac{m^3}{kg \cdot s^2}$,
- $\int_x \int_y \int_z dV$: volume integral,
- r : distance to mass element.

It may be recognised as the potential ability of a source mass to accelerate (attract) an infinitesimal test mass. The *geoid* is defined as an equipotential surface at which a calm sea would stay still at 0 m of sea–level. The first centri–directional derivative

$$U_r = \frac{\partial U}{\partial r} \quad (2.3)$$

is the expression of what is widely denoted as *gravity* or gravitational acceleration.

Gravity is thus a function of density distribution and distance to the source masses. Applying gravimetry in the geo–sciences generally means to analyse spatial or temporal anomalies in the measured gravity field. These variations are often several orders of magnitude smaller than absolute gravity. In order to avoid masking effects of differing positions, gravity data are commonly corrected for several overlaying effects:

- height above reference level, latitude–dependent gravity of reference ellipsoid, instrument drift and tides for the *Free-Air anomaly*
- and furthermore: removal of the attraction of a Bouguer slab at the observation point and of surrounding topographic masses, respectively, for the *Bouguer anomaly*.

Then, the resulting field represents the gravity effect of anomalous masses or density. This residual distribution in the underground is of major interest with regard to the present work: A deficit in the Bouguer anomaly may be interpreted as a region of lower–density rocks than in a reference density model (e.g. crustal roots below high topography). A positive Bouguer anomaly is an indicator for excess masses (e.g. intrusions, ore bodies etc.) and is expected at

locations where dense bodies are suspected of exerting additional lithostatic stresses on the subduction interface.

Using the 3D forward modelling software packages IGMAS (*Götze and Lahmeyer, 1988*) and IGMAS+ (*Götze et al., 2010; Alvers et al., 2015*), several virtual density models of the Central Andes were developed and refined over the past years (e.g. *Tassara et al., 2006; Alasonati-Tašárová, 2007; Prezzi et al., 2009*, and others). It is an interactive application in which the user basically sets up a parametrised subsurface geometry by defining polygons of constant density (or susceptibility for magnetics) on a set of parallel vertical cross-sections. The software triangulates between the sections and generates virtual three-dimensional bodies of constant density (or susceptibility), respectively. Constraining data, as for example hypocentres and geo-referenced seismic images, can be visualised along with the geometry. By transforming the volume integral for gravitational attraction into a line integral, the software quickly adapts to interactive changes of geometry and density and displays the forward calculated gravity anomaly of the model along with the measured gravity data. The computation of the full symmetric gravity gradient tensor and rotational invariants is possible, as well. The user tries to model an optimal fit of observed and calculated fields by applying iterative changes to the model according to the bounds of constraining data. The differences between observed and calculated field should be minimised until the residuals have a lower amplitude than the estimated error of the observed anomaly and show a tight concentration around zero with low standard deviation. The recent rebuild IGMAS+ is furthermore capable of performing inversions for density and geometry (*Haase, 2008, 2014; Schmidt et al., 2011; Alvers et al., 2015*) and provides multi-processor support.

For the present thesis, IGMAS+ was used in order to set up the synthetic simple 'shoe-box' model for idealised coastal batholiths and in order to compute its gravity and gravity gradient tensor with rotational invariants as shown in chapters 3.1 and 3.2. IGMAS+ was furthermore intensively used during optimisation of existing models and for the derivation of stress anomalies shown in chapter 4.2. Eventually, for the comparing analysis and evaluation of the IMOSAGA01C combined regional gravity model (chapter 4.1, *Hosse et al., 2014*), IGMAS+ served as a tool in order to visualise and compute competing gravity models.

2.1.2 Analysis of the full gravity gradient tensor

When the direction of distance r in the gravity equation 2.3 points into the vertical from the reference niveau, equation 2.3 is often expressed as

$$U_z = \frac{\partial U}{\partial z} \quad (2.4)$$

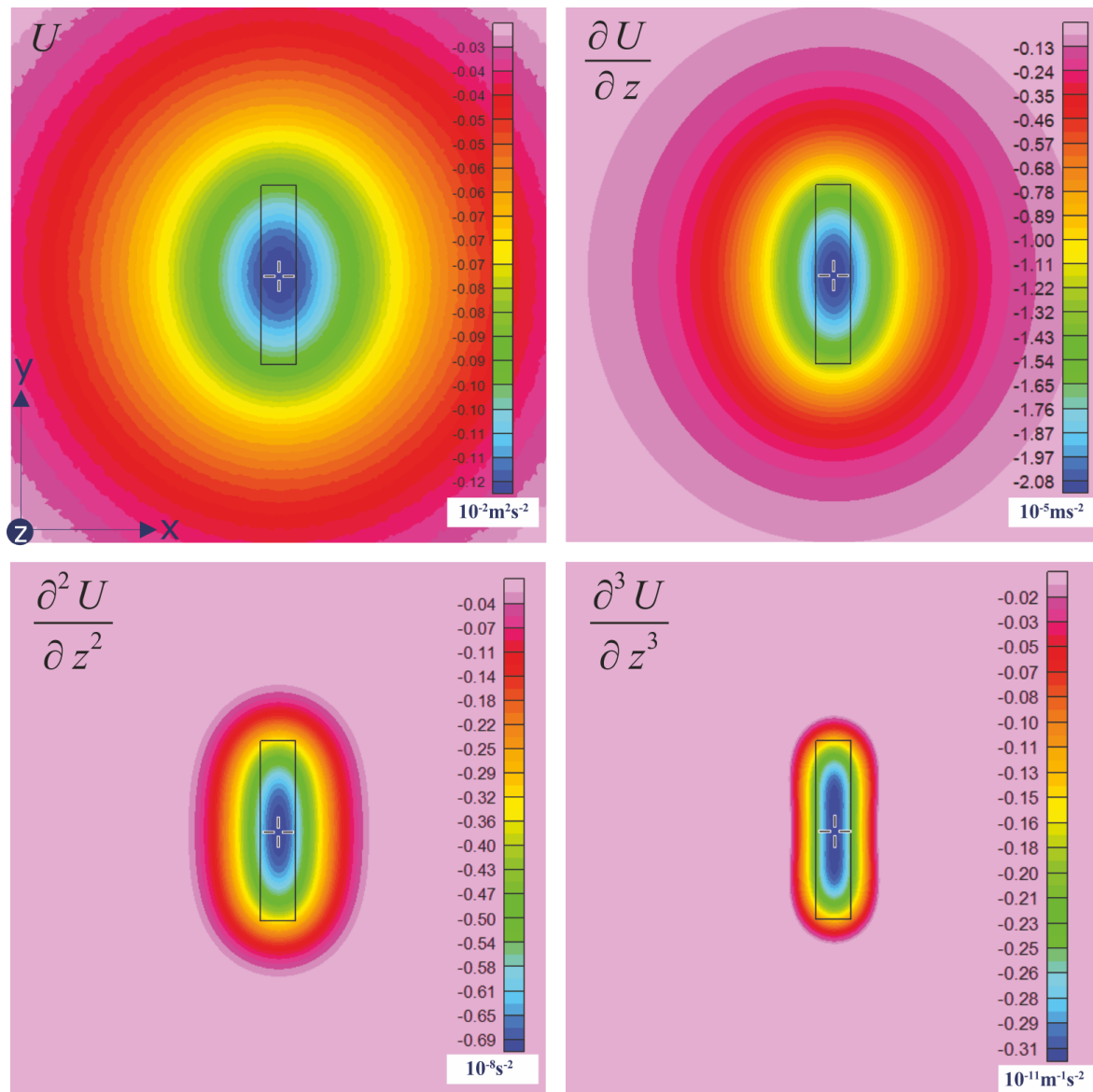


Figure 2.1: Anomaly of gravity potential U and its first three vertical derivatives for a buried cuboid (light black lines). After Gutknecht (2008).

and describes the vertical gravity component (please note that the sign changes here since z points away from the source mass). It represents the change in gravity potential with z : U_z is negative when the density of the source mass is lower than in the surrounding volume and vice versa. Figure 2.1 (upper left) shows at sea-level the calculated anomaly of the gravity potential of a buried cuboid with low density compared to the surrounding volume. All synthetic examples in this section were calculated at stations on the ground and without applying additional random noise. The upper right of figure 2.1 shows the first spatial derivative (vertical gravity component), which is most often used and interpreted in gravimetry. Figure 2.1 (lower left) is the second vertical derivative of the potential: the

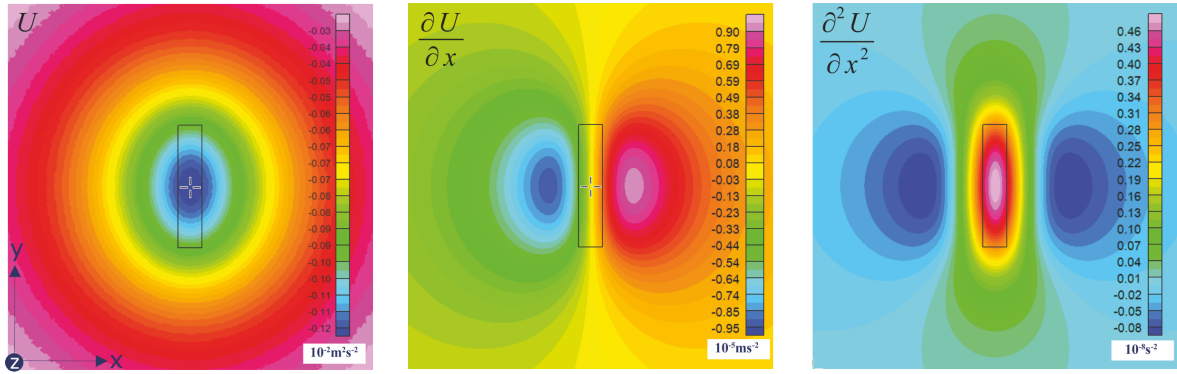


Figure 2.2: Anomaly of the gravity potential of a buried cuboid (light black lines) and its first and second horizontal derivative. After *Gutknecht* (2008).

vertical gravity gradient

$$U_{zz} = \frac{\partial^2 U}{\partial z^2}. \quad (2.5)$$

The term *gravity gradient* applies to all components of the Cartesian coordinate system, which means U double-differentiated with respect to both horizontal components ∂x and ∂y and vertical component ∂z . Figure 2.1 (lower right) shows for demonstration purposes also the third vertical derivative

$$U_{zzz} = \frac{\partial^3 U}{\partial z^3}. \quad (2.6)$$

It can easily be seen that with each derivation the contours of the field converge towards the edges of the buried object. This is an advantage of gradients over pure gravity that should be utilised in gradiometry in order to improve findings about subsurface structures and their inherent parametrisation.

Interpreting gravity is rather intuitive in comparison to gradients. The latter may be perceived as a quantity or rate at which gravitational acceleration changes under differential variation of the relative distance. To see this a bit clearer, the potential of the same buried object and its first and second derivative in horizontal x -direction, which were again calculated at the surface, are plotted in figure 2.2. While the left panel shows the same potential as in the previous figure, the centre panel now shows the gravity anomaly in the x -direction and the right panel shows the gradient of the x gravity component in x direction. It indicates how strong gravitational acceleration in the x direction changes with x .

The gravity gradient tensor: There is a total number of three gradients of the potential of first order U_i , with $i \in \{x, y, z\}$; these are the three components of gravitational acceleration. Each of these components may now again be differentiated with respect to one of the three dimensions (Hessian matrix) resulting in a nine-element tensor $U_{i,j}$, with $i, j \in \{x, y, z\}$ for second-order gradients of the potential. It is called the *Eötvös-Tensor*, see table 2.1.

Since U describes a conservative force field, the order of taking partial derivatives can be interchanged. The tensor is symmetric, i.e. tensor elements below the trace are mirrored

	x	y	z
x	$\frac{\partial^2 U}{\partial x^2}$	$\frac{\partial^2 U}{\partial x \partial y}$	$\frac{\partial^2 U}{\partial x \partial z}$
y	$\frac{\partial^2 U}{\partial y \partial x}$	$\frac{\partial^2 U}{\partial y^2}$	$\frac{\partial^2 U}{\partial y \partial z}$
z	$\frac{\partial^2 U}{\partial z \partial x}$	$\frac{\partial^2 U}{\partial z \partial y}$	$\frac{\partial^2 U}{\partial z^2}$

Table 2.1: The Eötvös tensor is the Hessian matrix, i.e. the matrix consists of the second partial derivatives of the gravity potential U . The tensor is symmetric since U describes a conservative force field.

above the trace or vice versa. For the trace itself Laplace's equation applies:

$$\Delta U = \nabla^2 U = \text{div}(\text{grad}U) = U_{xx} + U_{yy} + U_{zz} = 0 \quad (2.7)$$

It actually means that the gradient tensor consists of only five independent elements. In the following, six elements are listed of which only five are independent since one trace element may always be found from the two others.

Figure 2.3 shows the complete symmetric tensor for a synthetic salt pillow with negative density contrast in the subsurface. It can be summarised that the interpretation is highly dependent on knowledge about the orientation of the coordinate system but one exception: The vertical gravity gradient is generally defined identically throughout several applications and it produces easier to understand figures that are similar to those of vertical gravity. This might – besides the strong signal amplitudes and easy artificial calculation of vertical gradient – be one of the main reasons for the observation that most studies about gravity gradients in the recent past concentrated a lot on the vertical gravity gradient but less on the other components.

- Trace–elements:

$$U_{xx} = \frac{\partial^2 U}{\partial x^2} = -U_{yy} - U_{zz}$$

$$U_{yy} = \frac{\partial^2 U}{\partial y^2} = -U_{xx} - U_{zz}$$

$$U_{zz} = \frac{\partial^2 U}{\partial z^2} = -U_{xx} - U_{yy}$$

- Symmetric elements:

$$U_{xy} = U_{yx} = \frac{\partial^2 U}{\partial x \partial y} = \frac{\partial^2 U}{\partial y \partial x}$$

$$U_{xz} = U_{zx} = \frac{\partial^2 U}{\partial x \partial z} = \frac{\partial^2 U}{\partial z \partial x}$$

$$U_{yz} = U_{zy} = \frac{\partial^2 U}{\partial y \partial z} = \frac{\partial^2 U}{\partial z \partial y}$$

Rotational Invariants may be used in order to overcome the problem that knowledge of the orientation of the coordinate system is vital for the interpretation of gravity gradients. In contrast to the single components of the tensor, invariants do not change their appearance in

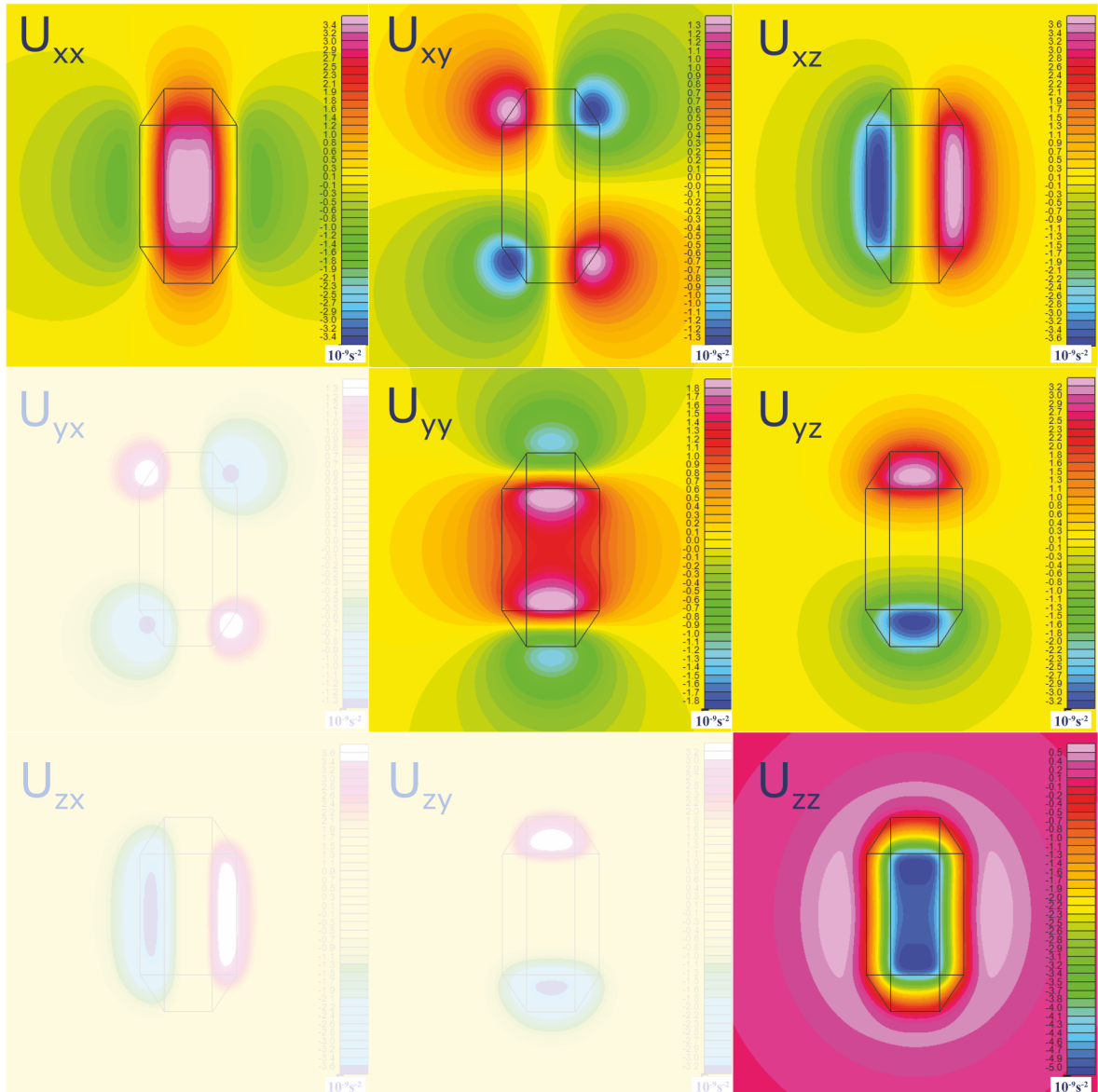


Figure 2.3: Full symmetric gravity gradient tensor of a synthetic salt pillow (light black lines). After Gutknecht (2008).

I_0	$trace(H(U)) = U_{xx} + U_{yy} + U_{zz} = 0$
I_1	$= U_{xx}U_{yy} + U_{yy}U_{zz} + U_{xx}U_{zz} - U_{xy}^2 - U_{yz}^2 - U_{xz}^2$
	$Det(H(U))$
I_2	$= U_{xx}(U_{yy}U_{zz} - U_{yz}^2) + U_{xy}(U_{yz}U_{xz} - U_{xy}U_{zz}) + U_{xz}(U_{xy}U_{yz} - U_{xz}U_{yy})$

Table 2.2: Overview over calculations of different invariants; $H(U)$ is the gravity gradient tensor or rather the Hessian matrix of the gravity potential. After *Pedersen and Rasmussen (1990)*.

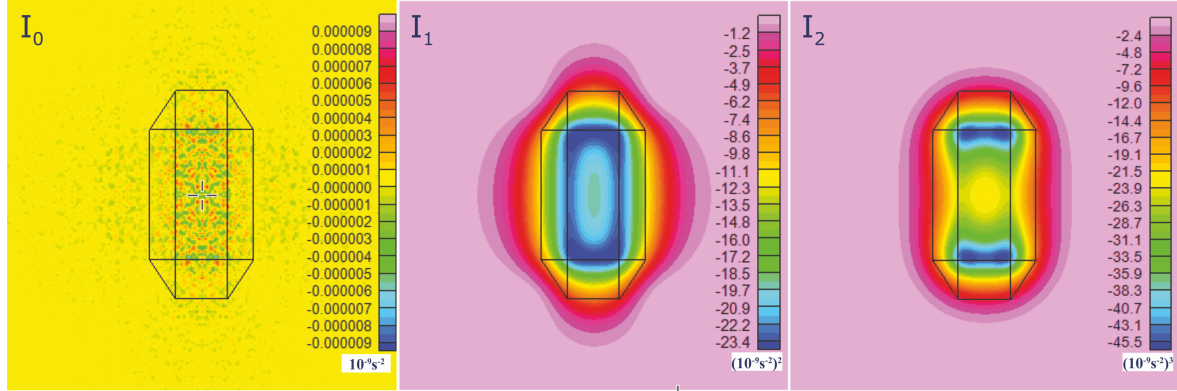


Figure 2.4: Invariants I_0 , I_1 and I_2 over the simple synthetic salt pillow (light black lines) in figure 2.3. After *Gutknecht (2008)*.

a rotated coordinate system. The first invariant I_0 results after Laplace from the trace of the gradient tensor:

$$I_0 = \frac{\partial^2 U}{\partial x^2} + \frac{\partial^2 U}{\partial y^2} + \frac{\partial^2 U}{\partial z^2} = 0 \quad (2.8)$$

Figure 2.4 (left panel) shows I_0 for the example of the density contrast of a simple synthetic salt pillow. Following equation 2.8, all stations should be zero. Given the effect of numeric noise and internal round-off errors, the signal level is 6 orders of magnitude smaller than the gradients. The first invariant is not directly useful for structural modelling and interpretation but rather helpful as a consistency check up for the model. Measured and calculated tensor elements on the trace should generally sum up to zero. If this test obviously fails, then model, data and computation must be counter-checked.

Figure 2.4 (centre panel) shows the second invariant I_1 accordingly:

$$I_1 = \frac{\partial^2 U}{\partial x^2} \frac{\partial^2 U}{\partial y^2} + \frac{\partial^2 U}{\partial y^2} \frac{\partial^2 U}{\partial z^2} + \frac{\partial^2 U}{\partial x^2} \frac{\partial^2 U}{\partial z^2} - \left(\frac{\partial^2 U}{\partial x \partial y}\right)^2 - \left(\frac{\partial^2 U}{\partial y \partial z}\right)^2 - \left(\frac{\partial^2 U}{\partial x \partial z}\right)^2 \quad (2.9)$$

and figure 2.4 (right panel) shows the third invariant I_2 :

$$\begin{aligned}
 I_2 &= \text{Det}(H(U)) \\
 &= \frac{\partial U}{\partial x^2} \left(\frac{\partial U}{\partial y^2} \frac{\partial U}{\partial z^2} - \left(\frac{\partial U}{\partial y \partial z} \right)^2 \right) \\
 &\quad + \frac{\partial U}{\partial x \partial y} \left(\frac{\partial U}{\partial y \partial z} \frac{\partial U}{\partial x \partial z} - \frac{\partial U}{\partial x \partial y} \frac{\partial U}{\partial z^2} \right) \\
 &\quad + \frac{\partial U}{\partial x \partial z} \left(\frac{\partial U}{\partial x \partial y} \frac{\partial U}{\partial y \partial z} - \frac{\partial U}{\partial x \partial z} \frac{\partial U}{\partial y^2} \right)
 \end{aligned} \tag{2.10}$$

While I_1 has a tendency to depict the general shape of the density anomaly, I_2 seems to emphasise parts of the model at which the anomaly changes at short scales in all directions in shallow depths. In general, I_2 should be less sensitive to deeper anomalies than I_1 as an additional multiplication in the derivation of I_2 has a high-pass filter like effect (distance to the exponent 9 dependence for I_2 compared to distance to the exponent 6 dependence for I_1 ; as distance-cubed and -squared for gradients and gravity, respectively).

In view of the present work, a key question in this regard has to be raised: How strong would be the impact of measured gradients from the GOCE mission on lithospheric modelling, and would it appear via forward modelling of the full tensor and its invariants or rather through the implementation of combined gravity models because the resolution would not fit? Chapters 3.1 and 3.2 contain further analyses on this question in more detail.

2.1.3 Lithostatically induced stresses

Well constrained 3D density models of the Central Andes region were exploited for their lithostatic footprint at different depths. Inspired by a similar method published by *Tassara* (2010), the idea described there becomes refined in the present work. In view of the hazardous active margin between the subducting Nazca Plate and the South American continent, it was of high interest to get an exact imprint of the lithostatic load of the continental masses onto the subducting plate. The idea behind this is that abnormally high excess masses could significantly hinder stable sliding in the subduction zone.

During the course of this dissertation, in a joint collaboration a plug-in for the software package IGMAS+ was co-developed that makes use of geometry and parametrisation of the density model in order to derive lithostatically induced stresses at selectable depths or interfaces. Stresses can be optionally computed as absolute stresses or as relative effect with respect to a standard density distribution of a reference and/or voxel background model. In addition, GPE can be derived in the same way as a function of the modelled density distribution.

A more detailed description of the method and subsequent results for the North Chile case may be found in chapters 4.2–5.

2.1.4 Dynamic stresses

NOGAPSGRAV and IMOSAGA project partners from the University of Jena used the static density models as an input for geodynamic modelling on the finite-element method basis. This means, they adopted the static parametrisation and pushed/accelerated the models into the future in order to derive stress, strain and uplift information of the active margin. The dynamic modelling was technically not part of this thesis but is included in the joint chapters 3.2 and 4.2.

2.1.5 Methods of geodetic gravity field modelling

Least Squares Collocation (LSC) after *Krarup* (1969) and *Moritz* (1972, 1978) was used by *Hosse et al.* (2014, see chapter 4.1) to consolidate the terrestrial gravity database (cf. section 2.2) and the GOCO03S model (*Mayer-Gürr et al.*, 2012) of the gravity/full gradient tensor data of the GOCE satellite mission.

They applied a Remove-Compute-Restore (RCR) technique besides LSC in order to remove long- and short-wavelength components from different types of input data, e.g. in order to exclude the lower part of the frequency spectrum that is under-represented in the extensionally limited terrestrial data. In a later step, the components are restored in the target grid, respectively.

Geodetic gravity field modelling was no direct part of this thesis but is included in the joint chapter 4.1.

2.2 Data

A common way to obtain gravity field data is to perform point measurements using relative gravimeters. These provide gravity readings *relative* to reference points at which *absolute* gravity is known. The precision of relative field gravimeters is — in theory — as low as some microgals ($1\mu Gal \equiv 10^{-8}ms^{-2}$). However, during field campaigns, the total error may add up to a few milligals ($1mGal \equiv 10^{-5}ms^{-2}$), when uncertainties in instrument drift, latitudinal positioning and height determination are concerned. In the Central Andes, this is still less than 1% of the regional gravity anomaly (*Schmidt and Götze*, 2006).

If the study area is well accessible, a high level of spatial resolution and repeatability is given and, thus, surface-bound gravity campaigns may deliver data of high quality. But practically, different types of measurement devices and unclear, varying or undocumented data processing can often shed different light on the quality of terrestrial gravity data sets. Moreover, high resolution gravity data in the Central Andes are only available in positions where topography and infrastructure allow for it.

This means, at very rough topography as in the Central Andes, gravity data from the surface is highly inhomogeneously distributed and only abundant near the coast and in valleys. Big data gaps are 'normal' here and lead to significant undesired developments of ill-posed fill-in data in global gravity field models (cf. chapter 3.2).

Hence, in recent years, the interest in using gravity data from satellites has gained growing interest. In this work it was investigated, to what extent satellites with their homogeneous measurement systems and distribution, e.g. from the GRACE and GOCE missions, may contribute to lithospheric or crustal studies at active continental margins. Particular attention is drawn to the applicability of measured gravity gradients, as described in the previous section. The published work of chapters 3.1 and 3.2 contain analyses of the expected applicability for lithospheric or crustal studies.

Countless types of input and constraining data found their way into this modelling in a direct or indirect way. This includes onshore gravity data collections of more than 30 years (e.g. Collaborative Research Centre 267 (*Oncken et al.*, 2006)) and satellite gravity data of the Gravity Recovery and Climate Experiment (GRACE) and GOCE missions. Also data of the CHALLENGING Minisatellite Payload (CHAMP) mission was included in the GOCO02S/03S gravity models (www.goco.eu). Moreover, a multitude of topographic, seismic, seismological and petrological data found their way into the present work. Those are listed and explained in more detail in the respective chapters and sections. One key type of dataset for this thesis eventually came from *Metois et al.* (2013) who provided their pre-seismic plate coupling results for North Chile, which they derived from GPS observations.

Data point density reduction has been applied before forward-modelling and stress computation as described in chapter 4.2 using the CIDRe algorithm (*Menzel, 2015; Götze et al.*, 2014, chapter 2.6 therein). Although most calculations for the present work were performed on a recent workstation computer equipped with a 2.8 GHz Intel Xeon W3530 quad-core processor unit and a dedicated Nvidia Quadro 600 graphics card, long computation time tended to limit fluent interactive modelling when high-resolution grid data were used over large areas of complex geometry. This slackening was due to the increased number of calculations that needed to be performed for the entirety of all polygons and stations of the model and also due to limits of available memory. It was, therefore, relevant to reduce the number of stations in a way that the quality of resulting models would be little affected. Applying the CIDRe algorithm provided the possibility to skip data points that may be redundant in triangulated representations of the data up to a definable statistical degree. Data of the IMOSAGA01C combined gravity model (chapter 4), for example, could be reduced by more than 77% for the purpose of interactive forward-modelling, with a mean resampling error of 0.366% and a maximum resampling error below 1.2% when compared to the complete data set. Computation time of gravity in IGMAS+ scales linearly with the decrease in

the number of data points.

While this data point reduction is applicable for interactive gravity forward modelling and for topographic data in stress computations, the point reduction must *not* be used in inversion-based calculations: Employing a downsized data set in a minimisation process like density- or geometry inversion would effectively leave out measured samples and hence distort the actual weighting and lead to ill-conditioned results. *Measured*, in this sense, can mean actually measured data and also model data like spherical-harmonics based gravity models that represent measured data.

2.3 Models

There exist three main types of model categories that were used during the course of this study:

1. Gravity models: The term *gravity model* is used throughout this work in the geodetic sense, meaning model-based representations of originally measured data. These models are generally expressed in spherical harmonics coefficients of widely differing maximum resolution, e.g. between degree and order 250 for the satellite-only gravity model GOCO03S (Mayer-Gürr *et al.*, 2012) and 2190 for the combined Earth Gravitational Model EGM2008 (Pavlis *et al.*, 2008), which corresponds to half-width wavelengths of approximately 80 and 9 km, respectively. EGM2008 is a reprocessed compilation of global surface gravity data, filled with additional satellite-aided or artificial data in regions with lacking measurements. GOCO03S is a mathematical representation of measurements from the GOCE satellite gradiometry mission. Other gravity models that found its way into this work, directly or indirectly and without completeness, were DTU10 (Andersen, 2010), EIGEN5C (Förste *et al.*, 2008), ITG-GRACE03s (Mayer-Guerr, 2007), several GOCE GCF_2 releases and other. One key element of the present work was the development (Hosse *et al.*, 2014), evaluation and application of the IMOSAGA01C combined gravity model. It is a combined solution of an existing terrestrial gravity database (high-resolution) and synthesized GOCE satellite gradiometric data (high homogeneity) for North Chile. Its derivation and evaluation is described in chapter 4.1. In chapter 4.2, IMOSAGA01C has been used in order to optimize an existing density model and in order to infer gravitational stress anomalies from it. A particular kind of field that is to be listed here is the Rock-Water-ICE (RWI) model by Grombein *et al.* (2014a). It is not a 'classic' gravity model by its means but it was designed to correct satellite gravity gradient data for the effect of topography and isostasy. Its application in this work is described in chapter 4.
2. Density models: Several synthetic expressions of the subsurface distribution of dens-

ity were used in the course of this thesis. All of them were build with the modelling software IGMAS (Götze and Lahmeyer, 1988) and its successor IGMAS+ (e.g. Götze *et al.*, 2010) by gravity forward modelling. The Central Chile 3D density model by (Alasonati-Tašárová, 2007) served as sample to extract a general geometry for the synthetic 'shoe-box' modelling presented in chapters 3.1 and 3.2. The regional 3D density model of (Tassara *et al.*, 2006) along the western South American margin served as initial test model for the derivation of stress anomalies and as a regional model to compute maps of GPE and stress anomalies on the subducting Nazca Plate (see chapter 4.2). The 3D density model of (Prezzi *et al.*, 2009) was chosen to be revised and optimised using the new IMOSAGA01C combined gravity field because its geo- and petrophysical set of constraints was found to be of high quality. This led finally to maps of the normal component of the vertical stress anomaly on the subducting Nazca Plate (see chapter 4.2. In a separate modelling branch, a transformation of the initial model of (Prezzi *et al.*, 2009) into the new IGMAS+ format was performed in this study. The resulting model (not shown in this thesis) served as starting model for further re-modelling by Schaller (2013).

3. Digital Terrain Model (DTM)s: Several DTMs were directly or indirectly used throughout this work. Among them are GLOBE, ETOPO5, ACE (which includes GLOBE, ERS-1, ERS-2 and ENVISAT data) and DNSC08 (bathymetry model included in ACE).

Specific details, where applicable, are given within the respective sections.

3 Applicability of gravity/–gradient data and models

Several geopotential models have been released in the past years that provide a combined spherical representation of available surface gravity data and satellite gravity data at places of low quality- or missing coverage at the surface, e.g. EGM2008 (*Pavlis et al., 2008*) or EIGEN-5C (*Förste et al., 2008*). The EGM2008 provides, in theory, a spatial resolution of less than 10 km which makes it extremely appealing to be used in crustal studies, as also in the present work. However, the apparent high resolution comes with a major drawback in that less informed users may assume the model globally represents proper measured data at any study area – which is substantially wrong. Even when considering this and adding auxiliary information that is available with EGM2008, it is not forthwith obvious whether a selected station in the study area has a strong link to measured surface data or is based on a fill-in of GRACE satellite- and topographic data.

It is clear that many places on this planet can practically not be accessed, e.g. because of rough topography or persistent political challenges. In this regard, satellite data can be seen as an unaffected option to fill data gaps at a global scale. Its challenge, in turn, is that in its orbit it is generally at such great distance from the source masses that the spatial resolution (>100 km) becomes too wide to be used in detailed lithospheric or even crustal studies. The GOCE mission (*Drinkwater et al., 2003*) was placed at a very low orbit at approximately 250 km (and 235 km in its final lifetime) above the geoid, which is in fact so low that it had to be continuously accelerated against atmospheric drag. First releases of its data and the respective geo-potential models had a spatial resolution of degree and order 250 (~80 km).

In the present thesis, before data from the GOCE mission has been applied to studies with lithospheric focus, it was evaluated to what extend the new data could be expected to add significant value to the geophysical interpretation. Chapters 3.1 and 3.2 contain, amongst others, methodological analyses of the expected sensitivity of GOCE gravity and gravity gradients based on the accuracy design of the mission. The analysis is followed by a study of a synthetic 3D forward model of anomalous density structures in a subduction zone environment in order to compute gravity, the full gravity gradient tensor and its rotational invariants at near surface- and satellite orbit heights. Chapter 3.2 contains also a general comparison and quality assessment of available gravity data and models for Central and

South America at the time of submission. While most recent gravity model releases show slightly improved quantitative values, i.e. signal–to–noise ratio and spatial resolution, the quintessence of the presented papers may be understood to remain valid.

3.1 Lithospheric modelling by using optimized GOCE gravity gradient data

- Publisher: ESA
- Journal: Special Publication SP-696 (2011), 5 pp., ISBN: 978-92-9092-260-5
- Author: Benjamin D. Gutknecht
Institute of Geosciences, Kiel University, Otto-Hahn-Platz 1, 24118
Kiel, Germany
- Author's contribution: The entire manuscript is Benjamin D. Gutknecht's work from the initial PhD phase.

Abstract The observed gravity and gravity gradient tensor components from the GOCE mission add new dimension to the interpretation of lithospheric and mantle structure. Here we present two applications of GOCE data to solid Earth modelling: For the $M_W=8.9$ 11 March 2011 earthquake offshore Sendai, Japan, GOCE gravity data has been used as a regional field in order to identify positive residual gravity anomalies close to the earthquake epicentre. Such anomalies are suspected of having significant influence on the stress regime of the subduction-zone interface. Concerning density modelling, it is of much interest to investigate density contrast and spatial distribution of the smallest density anomalies detectable with the GOCE gradiometer system. Allowing for accuracies of a few mE (1 milli-Eötvös = 10^{-12} s^{-2}) and 1–1000 mGal (1 mGal = 10^{-5} m s^{-2}), we derived a relation for the diameter of a density anomaly located below the Geoid as a function of density contrast. However, this method does not consider spatial resolution of the sampled GOCE data but rather takes the sensitivity of the system into account. Thus, our results indicate what minimum size and density contrast of the underlying geophysical structures are required in order to produce a signal of the order of GOCE's gradiometer sensitivity. These findings can have considerable impact on forward modelling and interpretation due to the fact that they suggest lower boundary conditions for the size of geophysical structures to be modelled. Consequent 3D density modelling tests with a synthetic model of the Chilean-Pacific convergent margin show that gravity gradients and invariants upward continued to orbit height clearly outperform the gravity field in terms of information yield on location and shape of anomalous structures.

3.1.1 Motivation

In the literature, large subduction-zone earthquakes have repeatedly been linked to diverse geological scenarios as subducted seamounts (e.g. *Cloos*, 1992) or strong crust in the over-

riding plate (e.g. *Byrne et al.*, 1988; *Sobiesiak et al.*, 2007). Following the idea described in *Sobiesiak et al.* (2007) that positive density anomalies in the overlaying continental crust of subduction zones can have significant impact on the locking of a subduction zone interface, we investigated whether the GOCE satellite has sufficient instrument sensibility in order to provide gravity (and gravity gradient) data that can be used for crustal studies related to major earthquakes.

It is assumed that positive density anomalies in the forearc region of the erosive subduction zone of the central Andes can be related to Jurassic–Early Cretaceous batholithic structures (*Götze et al.*, 1994; *Götze and Krause*, 2002). Since these anomalies can be shown to be located near the epicentres of large earthquakes (*Sobiesiak et al.*, 2007, and section 3.1.2.1), it is of much interest to assess potential use of GOCE–derived gravity data for identification of suchlike structures.

3.1.2 Methods and results

Here we use two different approaches to make use of GOCE gravity field data. In section 3.1.2.1 GOCE gravity data is being used as regional gravity field in order to calculate a residual Bouguer gravity anomaly field for the $M_W=8.9$ earthquake of 11 March 2011 offshore Sendai, Japan. In section 3.1.2.2 it is evaluated what size and density contrast a batholithic structure must have in order to generate an anomaly signal in the order of the satellite’s accuracy.

3.1.2.1 Gravity residuals offshore Sendai

For the $M_W=8.9$ Sendai earthquake the EGM 2008 gravity field (*Pavlis et al.*, 2008) and the GOCE GCF2 direct approach gravity field (release 2 of March 2011 via <http://icgem.gfz-potsdam.de/ICGEM>) were used in order to calculate residual fields for the region between 135–150°E and 30–45°N. The residual field was calculated by subtracting the simple Bouguer anomaly field of the GOCE data from the simple Bouguer anomaly field of the EGM2008 data. The expected result for the residual field is a high–pass filter like effect so that only short wave content remains. The GOCE data thereby acts as a regional gravity field which primarily comprises the gravity effects of longer wavelength structures greater than 80 km, i.e. of subduction slabs, mountain ranges etc.

Figure 3.1 gives an overview of the Japan–Pacific collision zone centred at the epicentre as given by the GEOFON service (<http://geofon.gfz-potsdam.de/geofon/>). Figure 3.2 shows the residual Bouguer anomaly field after the GOCE–derived field has been subtracted from the EGM 2008 field. The epicentre is clearly situated at the edge of a positive residual Bouguer anomaly.

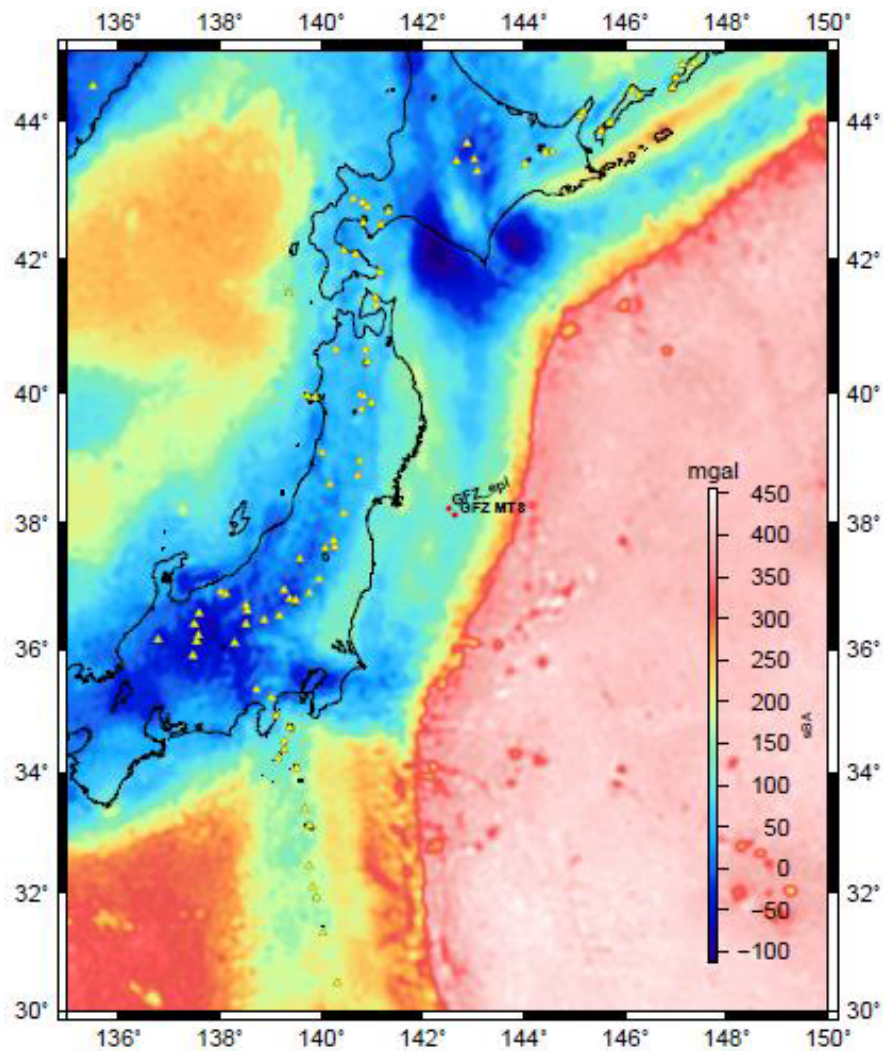


Figure 3.1: Bouguer gravity anomaly map of the Japan–Pacific continental margin (EGM 2008). Yellow triangles denote volcanoes. GFZ locations for epicentre (GFZ_epi) and moment tensor solution (GFZ_MTS) of the 11 March 2011 Sendai earthquake are given as red dots, respectively. 1 mgal = 10^{-5}m s^{-2} .

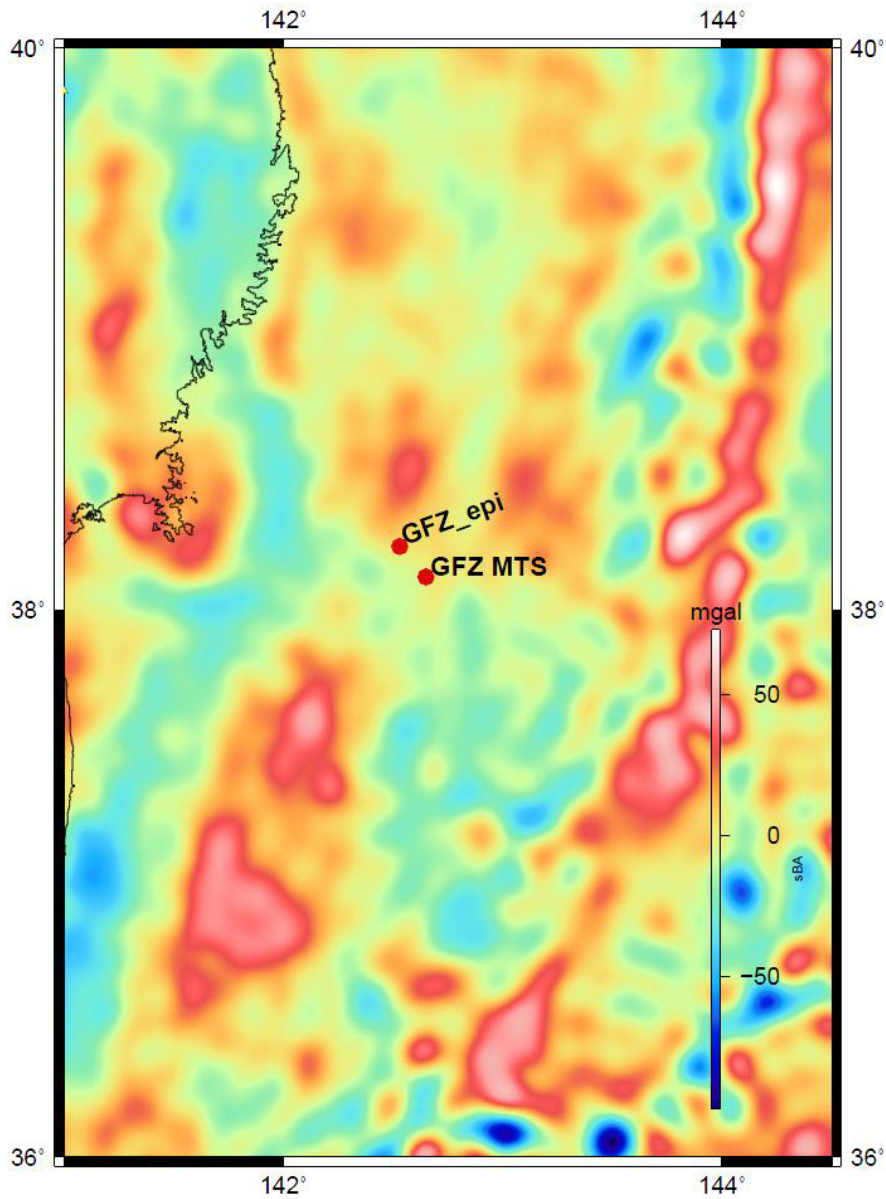


Figure 3.2: Residual Bouguer anomaly map of the Japan–Pacific continental margin after the GOCE gravity field has been subtracted from EGM 2008. GFZ locations for epicentre (GFZ_epi) and moment tensor solution (GFZ_MTS) of the 11 March 2011 Sendai earthquake are given as red dots, respectively.

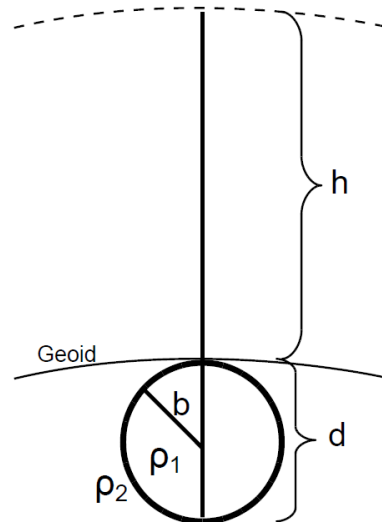


Figure 3.3: Simple spherical model of a batholithic density residual structure with diameter $d=2b$ and density contrast $\Delta\rho = \rho_1 - \rho_2$, located directly below the geoid. The satellite orbit height above the geoid is assumed to be constant with $h=254.9$ km

3.1.2.2 Sensitivity analysis with a simple spherical density residual

In order to derive an equation that gives us the minimum parameter configuration, i.e. density contrast and size of a gravity anomaly so that it generates at least a signal in the order of the sensitivity of the satellite gradiometer (or gravity field), we start with the most simple geometry: a spherical density anomaly located directly below the geoid (Figure 3.3).

$d/\Delta\rho$ -ratio for fixed gravity accuracy

Starting from Newtonian gravity acceleration

$$g_{Newton} = G \cdot m \cdot R^{-2} = G \cdot V \cdot \Delta\rho \cdot R^{-2}, \quad (3.1)$$

with gravitational constant $G = 6.67 \times 10^{-11} \text{ Nm}^2 \text{ kg}^{-2}$, mass m , distance $R = 254.9 \times 10^3 \text{ m}$, volume V and density contrast $\Delta\rho = \rho_1 - \rho_2$, the vertical residual anomaly of a sphere with diameter

$$d = 2b \quad (3.2)$$

in the order of the instrument sensitivity Δg_z is defined as

$$\Delta g_z = G \cdot \frac{4}{3} \pi b^3 \Delta\rho \cdot z^{-2} = \frac{4}{3} \pi G \cdot \Delta\rho \cdot \frac{b^3}{(h+b)^2} \quad (3.3)$$

that eventually becomes Eq. 3.4 and 3.5 which gives us the minimum density contrast with respect to the anomaly radius (Eq. 3.4) and diameter (Eq. 3.5), respectively:

$$\Delta g_z = \text{const} \Leftrightarrow \Delta\rho(b) = \frac{3}{4} \frac{\Delta g_z}{\pi G} \cdot \frac{(h+b)^2}{b^3} \quad (3.4)$$

$$\Delta g_z \stackrel{=const}{\Leftrightarrow} \Delta \rho (d) = \frac{3 \Delta g_z}{4 \pi G} \cdot \frac{(h + \frac{d}{2})^2}{(\frac{d}{2})^3} \quad (3.5)$$

d/Δρ–ratio for fixed vertical gradient accuracy

For the vertical gravity *gradient*, we do basically the same, again starting from Newton

$$\frac{\partial g_{Newton}}{\partial R} = -2 \cdot G \cdot m \cdot R^{-3} \quad (3.6)$$

and at right angle on top of the spherical residual anomaly in Cartesian coordinates

$$\begin{aligned} \Delta g_{zz} &= \frac{\partial}{\partial z} (G \cdot V \cdot \Delta \rho \cdot z^{-2}) \\ &= -2 \cdot G \cdot V \cdot \Delta \rho \cdot z^{-3} \\ &= -2 \cdot G \cdot \frac{\frac{4}{3} \pi b^3 \Delta \rho}{(h + b)^3} \\ &= -\frac{8}{3} \pi \cdot G \cdot \Delta \rho \cdot \frac{b^3}{(h + b)^3} \end{aligned} \quad (3.7)$$

And just as for the gravity case, we assume a fixed sensitivity. On the long run, a value of 12 mE (1 mili–Eötvös=10^{−9}s^{−2}) seems achievable within the measurement bandwidth (R. Pail, TU München, pers. comm.).

Equations 3.8 and 3.9 then respectively give the relation for the minimum density contrast with respect to the anomaly radius and diameter in order to produce a residual signal in the order of Δg_{zz}.

$$\Delta g_{zz} \stackrel{=const}{\Leftrightarrow} |\Delta \rho (b)| = \frac{3 \Delta g_{zz}}{8 \pi G} \cdot \frac{(h + b)^3}{b^3} \quad (3.8)$$

$$\Delta g_{zz} \stackrel{=const}{\Leftrightarrow} |\Delta \rho (d)| = \frac{3 \Delta g_{zz}}{8 \pi G} \cdot \frac{(h + \frac{d}{2})^3}{(\frac{d}{2})^3} \quad (3.9)$$

Equations 3.5 and 3.9 allow an evaluation of the gravity and gravity gradient sensibility, respectively. Figure 3.4 compares different residual values of 1 and 10 mgal (1 mgal = 10^{−5} m s^{−2}), and 12, 24, 36 and 1000 mE, respectively. Assuming target values of 1 mgal for the gravity field and 12 mE for the vertical gravity gradients, it can be found that the gradients clearly outperform the gravity field. For a given density contrast, the gravity field 'needs' a structure about twice the size as for the gradient case. Depending on density contrast in the order of 30–200 kg m^{−3}, the smallest resolvable anomaly in the gradient domain (with respect to accuracy, not space) is then some 30 to 45 × 10³ m. Yet a level of 24 or 36 mE in this study gives better results for the gradients than for 1 mgal gravity.

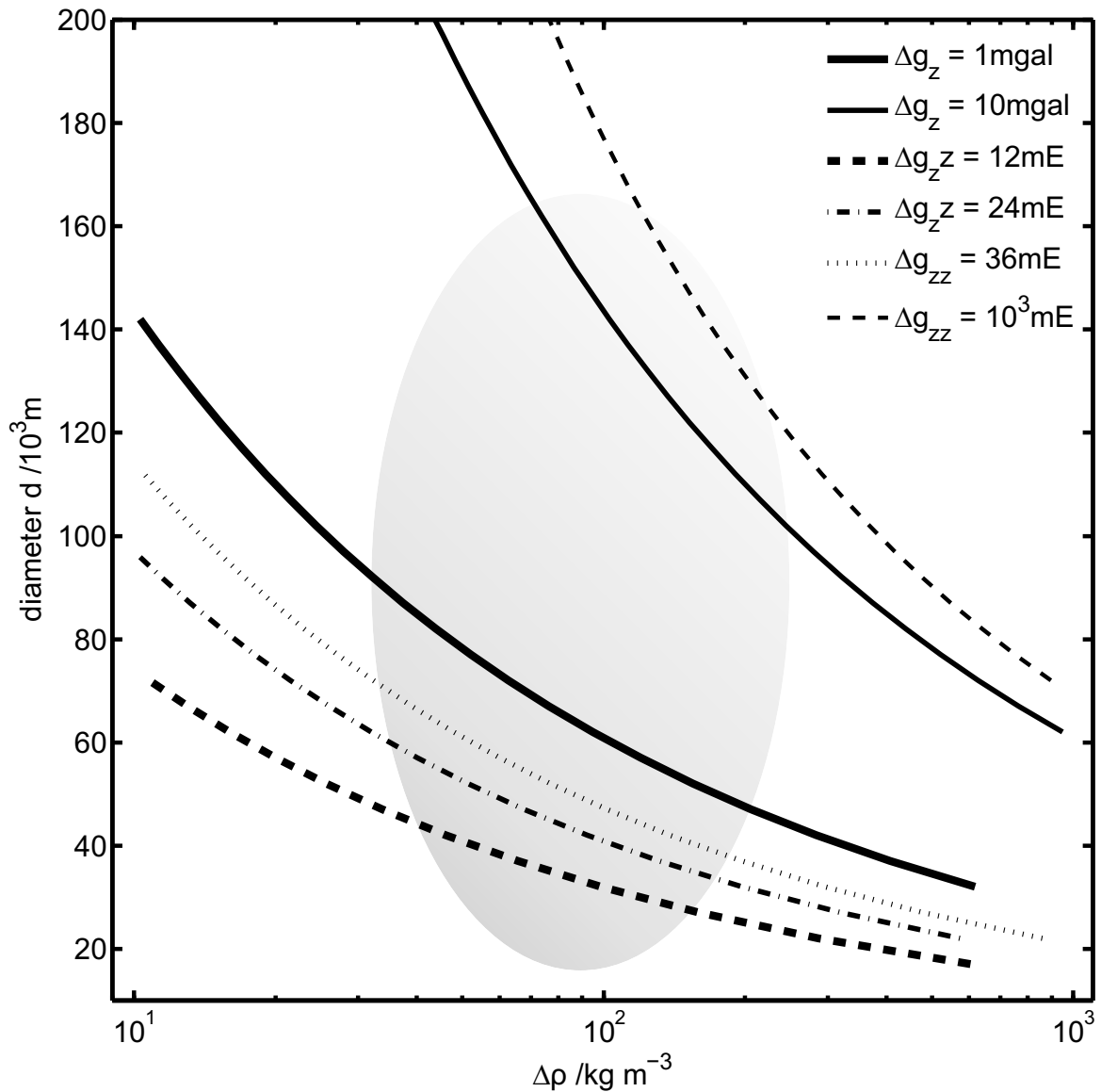


Figure 3.4: Density contrast versus minimum diameter of a density anomaly generating a residual anomaly in the order of a given instrument/field accuracies. Areas below and to the left of the curves cannot be resolved. Gradients of GOCE outperform gravity. The grey shaded area depicts appropriate parameter ranges of possible batholithic structures. In practice, signals 2–3 times the sensitivity amplitude will be required in order to be distinguished from the background level.

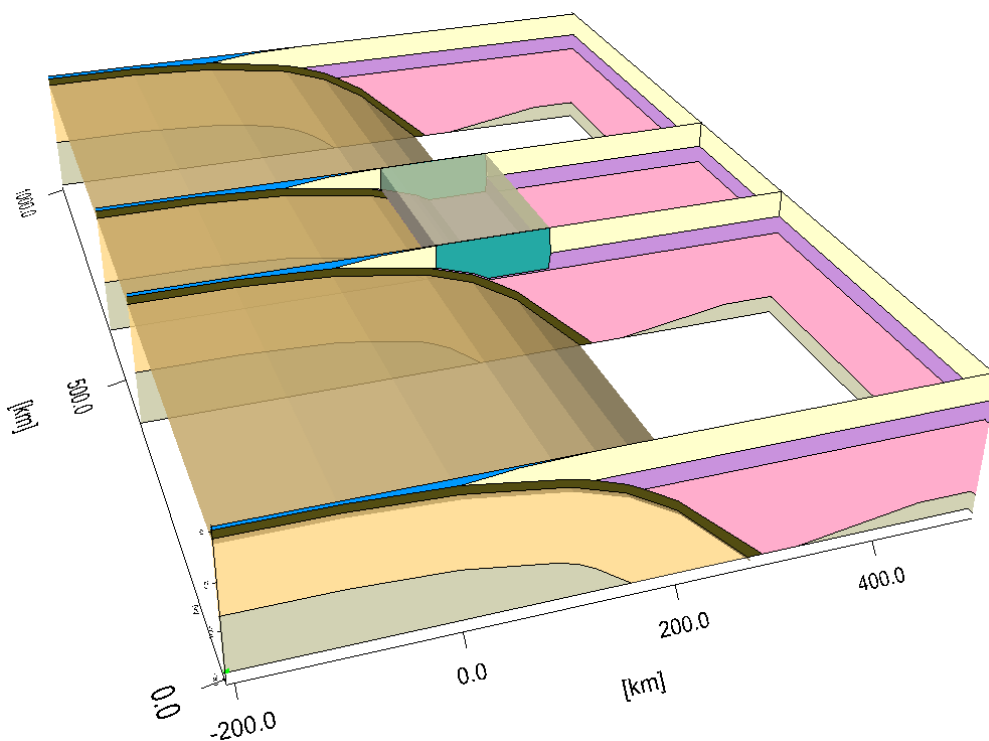


Figure 3.5: Synthetic 3D density model of a Chilean-type subduction zone ('shoe–box model'). There is no varying topology along the strike of the subduction zone. The green coloured 'shoe box' inset in the centre is a simple analogy to a continental crust positive density anomaly simulating a batholithic structure.

Synthetic 3D forward modelling

Subsequently to the rather abstract computations of sections 3.1.2.2 and 3.1.2.2, 3D density forward modelling of gravity and full tensor gravity gradients has been applied in order to estimate the anomaly signal strength at both, near surface and orbit height. The density model (Figure 3.5) is based on existing models of the Chile–Pacific margin by *Alasonati-Tašárová* (2007). Unlike 'real' models, the geometry used for this study does not show any variability along the N–S–axis and rather synthesizes arbitrary constant average–subduction zone geometry along strike. Within this geometry lies a 'shoebox'–like dummy structure to simulate a giant batholithic density anomaly. The dimensions of the structure are considerably oversized ($125 \text{ km} \times 200 \text{ km} \times 30 \text{ km}$, density contrast $\sim 100\text{--}300 \text{ kg m}^{-3}$) and somewhat depicting an upper feasible boundary in a geological sense of size. The inset body's dimension was deliberately chosen large so that negative modelling results would implicitly lead to no further testing when even the largest feasible density anomaly generated no notable signal when measured at orbit height.

Model construction and forward modelling was performed using the modelling software IGMAS+, which represents geological bodies with triangular–faceted polyhedral (*Götze and Lahmeyer, 1988; Schmidt et al., 2011*).

The calculated vertical gravity Bouguer anomaly is shown in Figure 3.6 at near surface

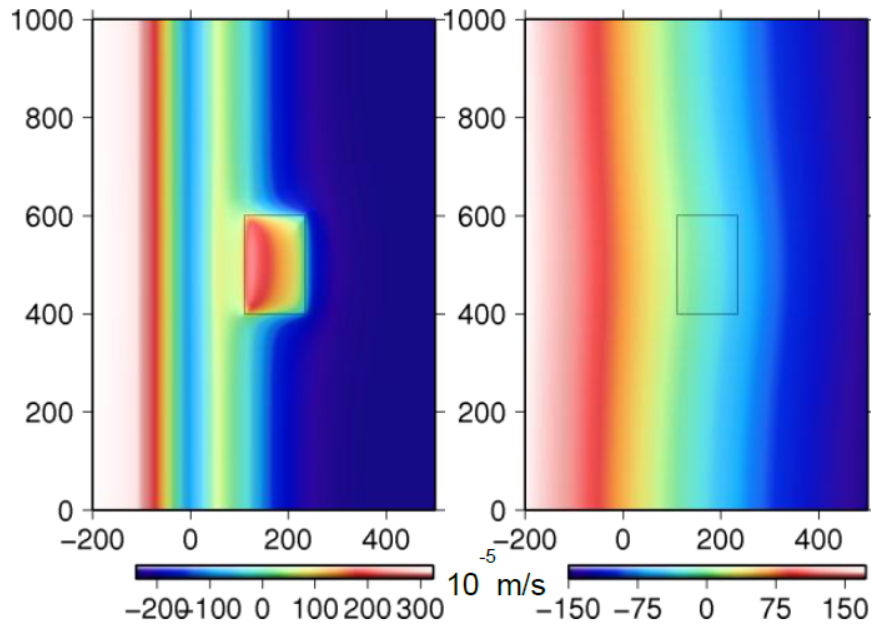


Figure 3.6: Bouguer anomaly of the vertical gravity component (g_z) above the Andean-type density model of Fig. 3.5; left: near surface; right: at GOCE orbit height (254.9 km). Map scale is in km. The amplitude range of the orbit-gravity field is more than 12 times higher than the anomaly maximum of the 'shoe-box'.

(left) and at orbit height $h = 254.9 \times 10^3$ m (right). The gravity signal of the density anomaly is apparently orders of magnitude too weak to be seen from orbit (cf. Figure 3.6, right).

The vertical gravity gradient g_{zz} , however, clearly gives amplitudes from the 'shoebox' in the detectable range (cf. Figure 3.7).

3.1.3 Discussion and summary

Both GOCE gravity and gravity gradient data can be shown to have notable potential for respective, characteristic use. While gravity unsurprisingly fails to be directly usable for the detection of batholithic structures in the overriding crust of subduction zones it has great potential to be applied as regional field during the computation of gravity residual anomaly maps. This application can be recommended if the wavelength of suspected anomalies lies below 80–100 km. Regarding the Sendai earthquake of 11 March 2011, GOCE gravity data helped to identify positive gravity anomaly residuals at the epicentre of the main shock. A possible interpretation of these residuals as high density bodies in the upper plate, affecting the subduction interface, is supported by the existence of large positive anomalies found in aero-magnetic data (Finn, 1994).

However, the gravity gradients show high potential for their use within direct localisation purposes if their proposed noise levels will be matched. For a simple spherical model it was shown that gravity gradients –for given accuracies –are more sensitive to small scales and

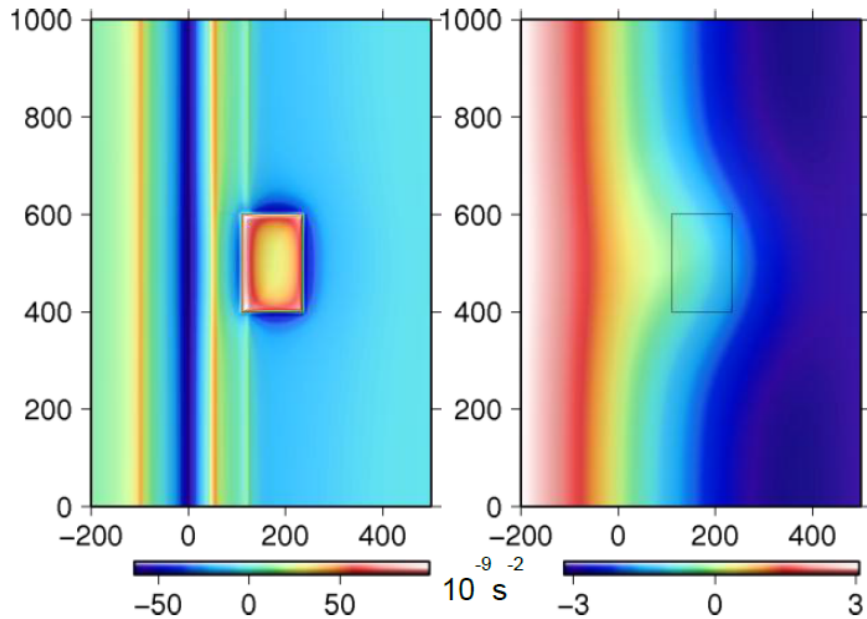


Figure 3.7: The vertical gravity gradient (g_{zz}) of the same model; left: near surface; right: at orbit. Map scale in km. The amplitude range of the orbit–gradient field is only 3.5 times higher than the anomaly signal.

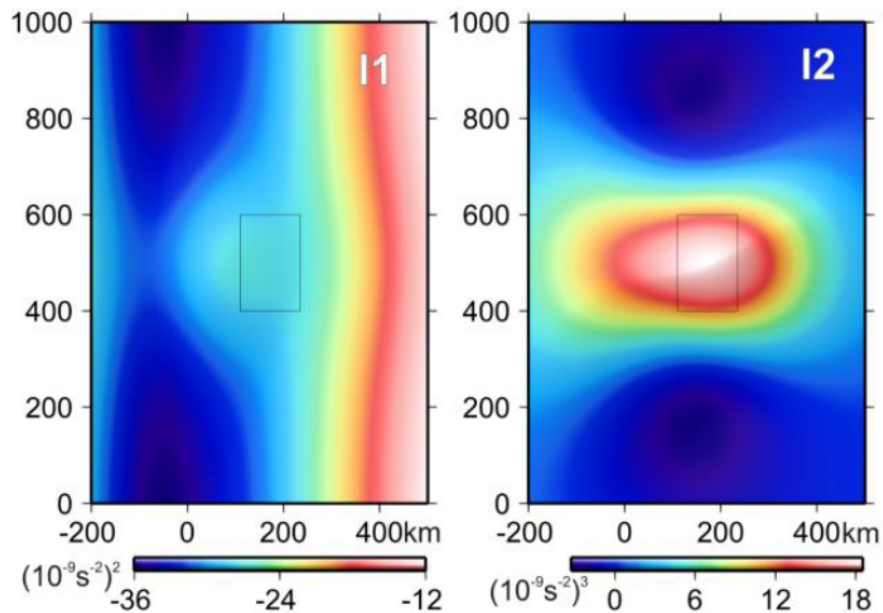


Figure 3.8: Invariants of the full gravity gradient tensor at orbit height. I_2 , i.e. the determinant of the tensor, reveals to be a promising tool for anomaly localisation.

density contrasts than gravity even at GOCE's orbit. Subsequent 3D forward modelling results support these theoretic estimations: The simulated signal of a synthetic density anomaly at a subduction zone disappears in the amplitudes of the surrounding geology. But the signal can clearly be found in the calculated gravity gradients.

Furthermore, invariants of the full gradient tensor are a promising tool for anomaly localisation purposes. A combination of all tensor elements leads to a somewhat easier-to-read picture when compared to gradients, is independent of the coordinate system but lacks direct physical interpretability.

Altogether, the findings of this study encourage to call for an originally unintended release of GOCE gradient grid data by ESA. Nevertheless, for the purposes presented in this paper, GOCE gravity field data is by all means suitable for earthquake studies when it is used as a regional field.

3.2 The seismically active Andean and Central American margins: can satellite gravity map lithospheric structures?

- Publisher: Elsevier Ltd.
- Journal: Journal of Geodynamics, Vol. 59–60 (2012), pp. 207–218,
DOI: 10.1016/j.jog.2011.11.004
- Authors: ^aNils Köther, ^aH.J. Götze, ^aB.D. Gutknecht, ^bT. Jahr, ^bG. Jentzsch, ^aO.H. Lücke, ^aR. Mahatsente, ^bR. Sharma, ^bSt. Zeumann
 - a) Institute of Geosciences, Kiel University, Otto–Hahn–Platz 1, 24118 Kiel, Germany
 - b) Institute of Geosciences Friedrich–Schiller–University of Jena, Burgweg 11, 07749 Jena, Germany
- Author’s contribution: B.D. Gutknecht’s main contribution to the manuscript was about asperity mapping and resolution and accuracy of gravity gradient data, also containing the ‘shoe–box’ modelling of the gradient tensor. He further contributed to all general introducing and concluding sections. N. Köther was corresponding author and responsible for the entire manuscript, especially the direct comparison of methods and models. H.-J. Götze and R. Mahatsente contributed and guided generally in all sections. T. Jahr, G. Jentzsch, R. Sharma and S. Zeumann did the dynamic modelling and contributed generally. O. Lücke’s main contribution is with all aspects that are related to the Central Americas / Costa Rica.

Abstract The spatial resolution and quality of geopotential models (EGM2008, EIGEN-5C, ITG-GRACE03s, and GOCO-01s) have been assessed as applied to lithospheric structure of the Andean and Central American subduction zones. For the validation, we compared the geopotential models with existing terrestrial gravity data and density models as constrained by seismic and geological data. The quality and resolution of the downward continued geopotential models in the Andes and Central America decrease with increasing topography and depend on the availability of terrestrial gravity data. High resolution of downward continued gravity data has been obtained over the Southern Andes where elevations are lower than 3000 m and sufficient terrestrial gravity data are available. The resolution decreases with an increase in elevation over the north Chilean Andes and Central America. The low resolution in Central America is mainly attributed to limited surface gravity data coverage of the region. To determine the minimum spatial dimension of a causative body that could be resolved using gravity gradient data, a synthetic gravity gradient response of a spherical anomalous mass has been computed at GOCE orbit height (254.9 km). It is shown that the minimum

diameter of such a structure with density contrast of 240 kg m^{-3} should be at least $\sim 45 \text{ km}$ to generate signal detectable at orbit height. The batholithic structure in Northern Chile, which is assumed to be associated with plate coupling and asperity generation, is about $60\text{--}120 \text{ km}$ wide and could be traceable in GOCE data. Short wavelength anomalous structures are more pronounced in the components of the gravity gradient tensor and invariants than in the gravity field. As the ultimate objective of this study is to understand the state of stress along plate interface, the geometry of the density model, as constrained by combined gravity models and seismic data, has been used to develop dynamic model of the Andean margin. The results show that the stress regime in the fore-arc (high and low) tends to follow the trend of the earthquake distributions.

Keywords Satellite gravity and gradient data resolution — Density and dynamic modeling — Asperity mapping

3.2.1 Introduction

Novel satellite gravity missions aim at a breakthrough in recovering signals associated with mass transport, mass distribution and the underlying dynamic processes on the Earth's surface, the lithosphere and upper mantle. The missions significantly improved the coverage and availability of gravity data. In the year 2000, CHAMP started to measure the global gravity field with a spatial resolution of about 550 km (e.g. Eigen-2, Reigber *et al.*, 2005). The following GRACE mission measured gravity with an increased spatial resolution of approximately 140 km (ITG-GRACE03s, Mayer-Guerr, 2007). In 2009, the GOCE mission has begun measuring the gradients of the gravity field. Compared to scalar measurements, gradiometry offers better signal to noise ratio, de-emphasises regional trends (Holstein *et al.*, 2007) and provides enhanced sensitivity of geological structures (e.g. Pedersen and Rasmussen, 1990; Fedi *et al.*, 2005). Thus, the direct use of gradients is a new scope for geophysical modelling. However, it has to be determined whether the resolution of downward continued GOCE gradient data is sufficient for direct application to lithospheric studies. One recent high-resolution gravity model of GOCE is GOCO-01s which is a combined model of GRACE solutions for lower degrees and GOCE data for higher degrees (Pail *et al.*, 2010). Higher resolution is provided by combined models of terrestrial and satellite data. The EIGEN-5C (Förste *et al.*, 2008) and the EGM2008 (Pavlis *et al.*, 2008) provide gravity data with spatial resolution of 56 km and 10 km , respectively.

In this paper, we investigate the resolution and quality of various geopotential models as applied to lithospheric structures and mapping of regions of high seismic moment release (asperities) using the active plate boundaries of Central America and Southern Central Chile as case studies. The origin and role of asperities in earthquake recurrence in these regions are much debated (e.g. Wells *et al.*, 2003). Many source time functions of large earthquakes show

distinct onsets of sub-events and episodes of moment release, which signify co-seismic failure of asperities. As causes for these sub-events, varying physical properties such as geometrical and/or material heterogeneities and dynamically generated complexities are suggested (Madariaga and Cochard, 1996; Aochi *et al.*, 2003; Marsan, 2006). Inhomogeneities on the subducting plate (e.g. seamounts, ridges, transform faults) could lead to stronger coupling (Cloos, 1992; Kirby *et al.*, 1996; Barckhausen *et al.*, 1998; DeShon *et al.*, 2003). Deep-sea terraces and sedimentary basins along convergent margins are other proposed indicators of asperities (Song and Simons, 2003; Wells *et al.*, 2003; Fuller *et al.*, 2006).

In regions of high seismic moment release, trench-parallel gravity anomalies positively correlate with topography. Thus, the spatial gravity variations over the fore-arc could serve as proxy for the long-term state of stress on the plate interface (Song and Simons, 2003). Furthermore, Wells *et al.* (2003) showed that epicentres of major earthquakes often tend to concentrate on the pronounced gravity gradients from the fore-arc basins towards gravity highs. Recent studies in the South-Central Chile suggest that pressure exerted by batholithic structure and buoyancy force acting on the Nazca plate could be one of the possible mechanisms of asperity generation (Sobiesiak *et al.*, 2007). An analysis of the 1995 Antofagasta earthquake showed that high b-values correlate with isostatic residual gravity anomalies of the region (Sobiesiak *et al.*, 2007). The isostatic residual anomalies are caused by batholithic bodies of the Jurassic to early Cretaceous magmatic arc system and help to lock the interface of the seismogenic zone. This is also indicated in the local tomography as high P-wave velocity (Husen, 1999). Tassara (2010) expanded this hypothesis for the entire Chilean-Pacific margin and suggested that hazardous earthquakes predominantly occur in regions of positive vertical stress anomalies associated with positive density anomalies of the crust in the fore-arc region.

The scope of this work is to test the resolution of satellite-only and combined models as applied to lithospheric structure, tectonic processes and dynamic evolution of convergent plate boundaries. In order to test the resolution and unravel the 3D structure as well as the dynamic evolution of the two convergent plate margins, three steps have been followed: (1) all terrestrial gravity data from the region of interest have been combined into a single database; (2) satellite-derived gravity data have been used to fill in regions lacking terrestrial gravity coverage; and (3) the combined gravity database has been used to develop 3D lithospheric structures of the two convergent plate margins. Then, the geometry and physical parameters obtained from the well-constrained 3D density models have been used to refine the dynamic models of the Andean margin. The satellite gravity data have been obtained from the ICGEM portal of the GFZ Potsdam (<http://icgem.gfz-potsdam.de/ICGEM/>).

3.2.2 Tectonic setting

The Andes mountain belt is the result of subduction of the Nazca beneath South America plate. The dynamics of subduction are mainly controlled by the convergence rate and age of the subducting plate. Several studies indicate the differences in tectonic style between the Central and Southern Andes (e.g. *Allmendinger et al.*, 1997; *Ramos and Aleman*, 2000). The Central Andes can be divided from west to east into the fore-arc, magmatic arc and backarc (*Reutter and Götze*, 1994). The fore-arc comprises the Coastal Cordillera, the Longitudinal Valley, the Precordillera and the Preandean depression (Fig. 3.9). Since the Jurassic, the magmatic arc front has migrated more than 200 km to the east (e.g. *Scheuber et al.*, 1994), with the Jurassic arc now present along the Coastal Cordillera and on the slope of the fore-arc (about 50–150 km east of the trench). Repeated micro-gravity and GPS measurements reveal the on-going deformation and relaxation processes after the 1960 Valdivia earthquake (*Klotz et al.*, 2001). The main causes for these tectonic differences are changes in slab dip, age and convergence obliquity (e.g. *Gutscher et al.*, 2000). Young and buoyant slabs produce shallow dips and strong seismic coupling. Convergence was always oblique, with obliquity changing with time and latitude. Convergence velocity also fluctuated considerably and has been decreasing throughout the Neogene (*Norabuena et al.*, 1999). However, it was always amongst the faster convergence rates observed on Earth.

In this paper, we will focus on the structures and processes affecting the fore-arc region. For comparison, we will use the gravity field and results of the density modelling from Central America. Therefore, we provide a brief introduction to the geology of the region. For more detail, refer to *Lücke et al.* (2010). The outstanding tectonic feature is the subduction of the oceanic Cocos plate beneath the Caribbean plate along the Middle American Trench. Throughout Central America, the volcanic front is segmented along the isthmus presenting gaps in Quaternary volcanism as well as changes in distance from the Middle American Trench. Such changes have been attributed to both the state of stress in the overriding plate and the disposition of the subduction zone leading to changes in depth to the slab (*Bolge et al.*, 2009). The heterogeneity of the structure of the oceanic Cocos plate due to the influence of the Galapagos hot-spot (*Sallarès et al.*, 2003) leads to inconsistencies upon the arrival of bathymetric features to the subduction zone and may cause seismogenic asperities and uplift (*Barckhausen et al.*, 1998; *Meschede et al.*, 1998). Furthermore, the subduction of seamounts on the oceanic Cocos plate acts as an agent of upper plate erosion (*Ranero and von Huene*, 2000). At the western end of the Middle American Trench, the plate boundary between the Cocos and Nazca plates is marked by the seismically active Panama Fracture Zone. Subduction of the Nazca plate along the southern Panama segment is now considered to be inactive showing instead evidence of left lateral shearing between the Nazca and Caribbean plates (*Lonsdale*, 2005).

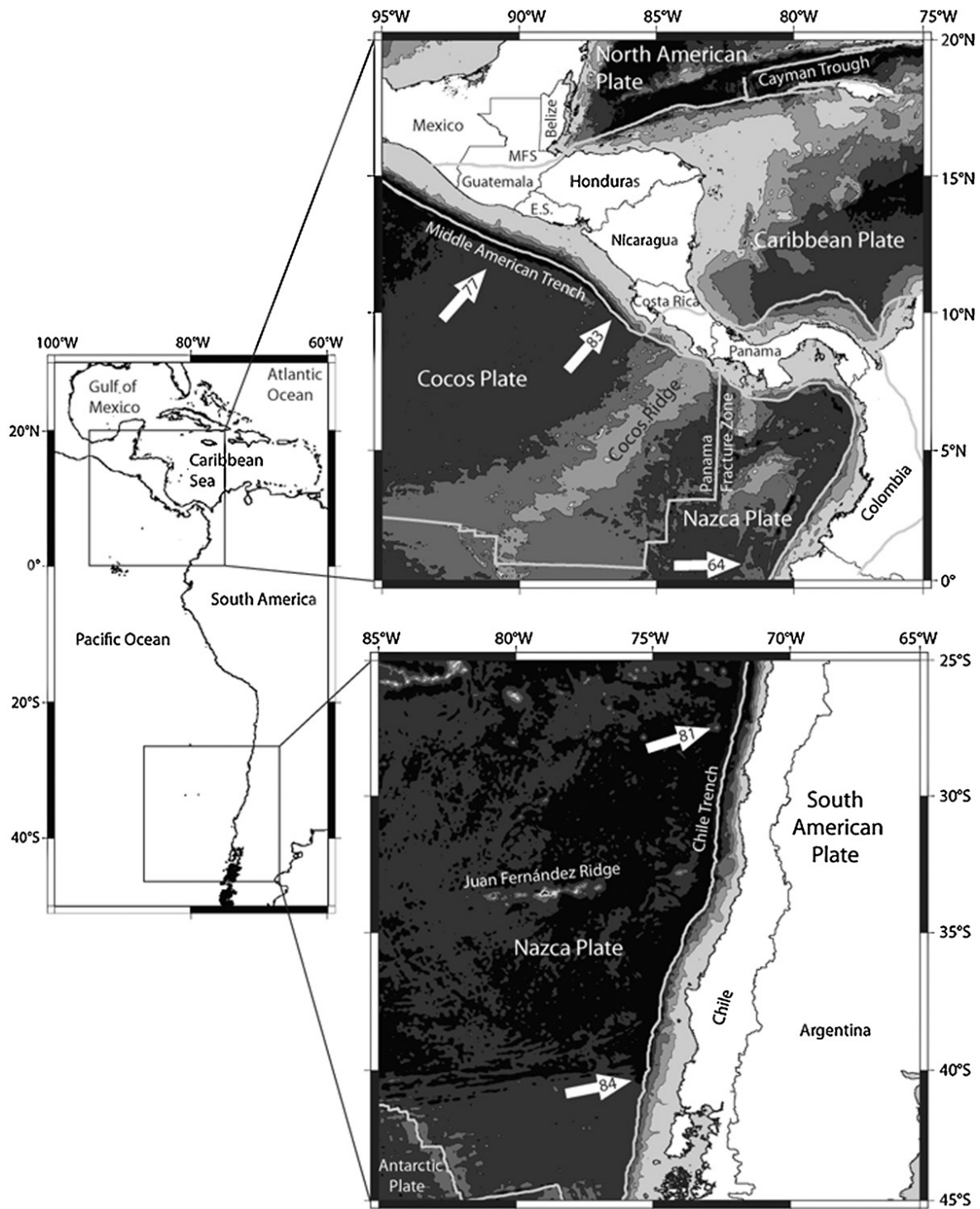


Figure 3.9: Geologic setting of Central (top) and South (bottom) America. The white arrows show the plate movement per year in mm (*DeMets et al., 1994*). Grey lines offshore indicate plate boundaries. Dark colours indicate deep, light colors shallow seafloor.

3.2.3 Gravity database and geophysical constraints

Onshore gravity data collected under the framework of the Collaborative Research Centre 267 (Oncken *et al.*, 2006) have been homogenized to compile Bouguer anomaly map of the Central Andes. The database comprises data acquired over the past 30 years in Argentina, Chile and Bolivia (20°S–29°S and 74°W–64°W). Approximately 2000 gravity stations covering the region in Argentina between the Andes and the Atlantic coast were measured along the southern traverse in 2000 (36°S–42°S and 71°W–62°W) and along the northern traverse between 1982 and 1990 (Götze *et al.*, 1994; Schmidt and Götze, 2006; Hackney *et al.*, 2006; Alasonati-Tašárová, 2007). Additional data have been obtained from industry (ENAP; Chile and Repsol-YPF; Argentina), the Universidad de Chile and the United States National Imagery and Mapping Agency. All measurements are tied to the IGSN71 gravity datum. Bouguer anomalies were computed using the normal gravity formula of 1967 and a spherical Bouguer cap correction (cap radius 167 km, density 2670 kg m⁻³). Terrain corrections on land were computed using triangular facets to approximate topography up to a distance of 167 km from stations. The corrections were applied using the 1 km × 1 km GLOBE (onshore) and ETOPO5 (offshore) digital elevation models. Offshore gravity and seismic data are obtained from shipborne measurements of the SPOC (Subduction Processes Off Chile) project (e.g. Reichert and Schreckenberger, 2002). The former are merged with the KMS-2001 global free-air gravity anomaly database (Andersen and Knudsen, 1998). The Bouguer anomaly in the Central Andes has a resolution of 3–5 × 10⁻⁵ m s⁻².

A series of 3-dimensional density models showing mass distributions at different scales in the western continental margin of South America have previously been developed (Kirchner *et al.*, 1996; Tassara *et al.*, 2006; Alasonati-Tašárová, 2007; Prezzi *et al.*, 2009). Tassara *et al.* (2006) presented a sub-global density model (410 km depth) encompassing the Pacific Ocean (85°W) and the Andean margin between the northern Peru (5°S) and Patagonia (45°S). At a regional scale, 3D density models of the Central (between 36°S and 43°S) and South Central Andes have been developed by Kirchner *et al.* (1996), Alasonati-Tašárová (2007) and Prezzi *et al.* (2009). All models traverse the Andes and provide complete picture of lithospheric density distributions. Modelling was done using the 3D gravity modelling package IGMAS (Götze and Lahmeyer, 1988; Schmidt *et al.*, 2010). Model constraints were taken from active and passive seismic campaigns conducted under the framework of the Collaborative Research Centres 267 (Giese *et al.*, 1999; Oncken *et al.*, 2006; Sick, 2006) and 574 (Ranero *et al.*, 2003; Brasse *et al.*, 2009). Moreover, results of the previous seismic experiments from PISCO (Proyecto de Investigación Sismológica de la Cordillera Occidental; Lessel, 1997; Schmitz *et al.*, 1999), ANCORP (Andean Continental Research Program; ANCORP Working Group, 2003; Buske *et al.*, 2002) and ISSA (Integrated Seismological experiment in the Southern Andes; Bohm *et al.*, 2002; Lüth *et al.*, 2003) have been used to constrain

major structures such as Moho, upper slab surface, lithosphere-asthenosphere boundary and intra-crustal inhomogeneities.

For Central America, a similar database was compiled and homogenized. Offshore databases consisting of ship borne gravity and seismic data acquired within the activities of the Collaborative Research Centre 574 have been used to cover mainly the area along the Middle American trench and the Pacific continental shelf. Seismic reflection, refraction and tomography data sets provided constraints for the modelling (*Sallarès et al.*, 2001, 2003; *Husen et al.*, 2003; *Arroyo et al.*, 2009). The onshore gravity database was also compiled by SFB574 members and consists of data from various government and academic institutions. Bouguer and terrain corrections were carried out following similar processing procedures as for the Andean gravity dataset.

3.2.4 Results and discussion

3.2.4.1 Geophysical and geodetic Bouguer anomaly

The definition of Bouguer anomalies is different in Geophysics and Geodesy. In order to avoid confusion, the differences between "gravity anomalies" and "gravity disturbances" will be explained. Detailed discussions about this issue can be found in the work of *Li and Götze* (2001) and *Hackney and Featherstone* (2003). In general, for geophysical interpretation and modelling, "geophysical Bouguer anomalies" will be used. Here, the measured gravity is corrected for the normal gravity formula at station elevation as well as for the Bouguer slab and the topographic variations. The measured gravity value is still interpreted at its original height (Fig. 3.10). In terms of geodesy, gravity values that are corrected for the normal gravity but still defined at station elevation are called disturbances. The Bouguer anomaly provided by the ICGEM is defined as the gravity calculated at the geoid and corrected for both the normal gravity at the ellipsoid and a plain Bouguer slab (called "classic anomaly" according to ICGEM terms; Fig. 3.10; *Barthelmes*, 2009). In the discussions to follow, we will continue to call this the "geodetic Bouguer anomaly". Downward continuation of the geodetic Bouguer anomaly to the geoid is only valid when it is assumed that all singularities of the gravity field lie below the geoid. This is not the case in regions of high topography. Furthermore, density anomalies located between the geoid and the top of the topography are of interest for geophysical interpretation. Hence, differences between geophysical and geodetic Bouguer anomalies can be high. Moreover, the use of disturbances (geophysical anomalies) is consistent with reduction techniques of existing geophysical terrestrial datasets. Thus, the geophysical Bouguer anomaly should be used in regions of high topography.

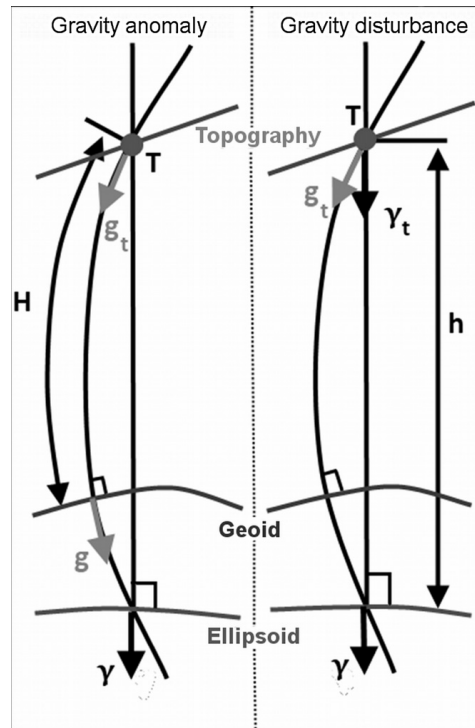


Figure 3.10: Gravity anomaly and gravity disturbance. The gravity anomaly (left) is downward continued from the observation point T to the geoid (g_t to g) and then reduced by the normal gravity from the ellipsoid (γ). Downward continuation is an unstable procedure over mountainous regions. Gravity disturbance (right) can be determined at any level (g_t) and is reduced by the upward continued normal gravity value (γ_t). This procedure is stable.

3.2.4.2 Data quality of the EGM2008

The EGM2008 consists of GRACE satellite data up to a spatial resolution of approximately 140 km. Data from 140 km spatial resolution up to 10 km are derived from other sources such as terrestrial, satellite altimetry and "fill-in" data (Pavlis *et al.*, 2008). Regarding the additional onshore data, several inconsistencies appear because its availability and distribution is not homogeneous. Moreover, in areas void of any terrestrial gravity data, "fill-in" data were used. These datasets were synthesized from GRACE data and augmented with data from the EGM96 and gravity derived from topography by means of residual terrain model (RTM) (Pavlis *et al.*, 2007). At locations, where confidential terrestrial gravity datasets are available, the data were used up to the maximum resolution permitted by the restrictions and then augmented with RTM anomalies. This approximated gravity solution lacks high frequency anomalies ($>$ degree 1650; Pavlis *et al.*, 2007). For the present study, we used terrestrial datasets collected by Schmidt and Götze (2006). It is expected that these data are included in the EGM2008. Thus, the EGM2008 should correlate well with the surface data at its maximum spatial resolution. If the data do not coincide, errors or inconsistencies in the EGM2008 may be assumed.

In the Andes, two onshore areas with different topography were investigated: The North

Chilean part is located between 74°W–67°W/19°S–30°S. Elevation in this region reaches up to 5800 m above sea level. The southern part (between 73°W–60°W and 36°S–43°S) has elevations up to 3000 m. In Central America, the study area is located between 86.5°W–82°W/8°N–11.5°N with elevations up to 3800 m. The number of onshore gravity stations used for the Northern Chile, Southern Chile and Central America are 8373, 14210 and 13387, respectively.

Table 3.1 shows the correlation between the EGM2008 anomalies (geodetic and geophysical) and terrestrial gravity data for the Andes and Central America. In general, the EGM2008 shows high correlation (>95%) in the Andes. However, low correlation has been obtained over the regions with rough topography, where deviations of about 40% are observed (e.g. $128 \times 10^{-5} \text{ m s}^{-2}$). The data correlation in Central America is even lower (about 68% deviations for the geodetic anomaly and ~86% for the geophysical anomaly). This is mainly attributed to sparse terrestrial gravity data coverage.

Table 3.1: Correlation of the EGM2008 with terrestrial data. The maximum deviations of each model are shown. The correlation values in brackets are for the Andes west of 69°W. Thus, only stations located around mountainous areas and the coastal line are considered. In Costa Rica, the brackets show the correlation of stations located above 1000 m of altitude.

	North Andes (19°S–30°S) onshore		South Andes (36°S–43°S) onshore		Central America onshore	
	Geophysical BA	Geodetic BA	Geophysical BA	Geodetic BA	Geophysical BA	Geodetic BA
Correlation between EGM2008 and terrestrial data /%	99.48 (98.29)	98.91 (95.63)	96.51 (93.26)	97.48 (94.32)	85.8 (49.37)	68.2 (40.66)
Min. Deviation / $10^{-5} m s^{-2}$	-50	-128	-66	-77	-55	-203
Max. Deviation / $10^{-5} m s^{-2}$	80	87	58	48	112	169

Fig. 3.11 shows the gravity maps of Central America and the Southern Andes in which the geodetic and geophysical Bouguer anomalies are compared with terrestrial data. The histograms in Fig. 3.12 show the deviation of the geodetic (dotted) and geophysical (hatched) anomaly compared to the terrestrial data in the Andes. The deviation of the geodetic anomaly compared to the geophysical anomaly is larger ($\sim 0.6\%$) in the northern part where topography is higher. In the southern part, the geodetic anomaly is slightly better ($\sim 1\%$) than the geophysical anomaly. However, both datasets show significant deviations from the terrestrial data with values higher than $20 \times 10^{-5} \text{ m s}^{-2}$.

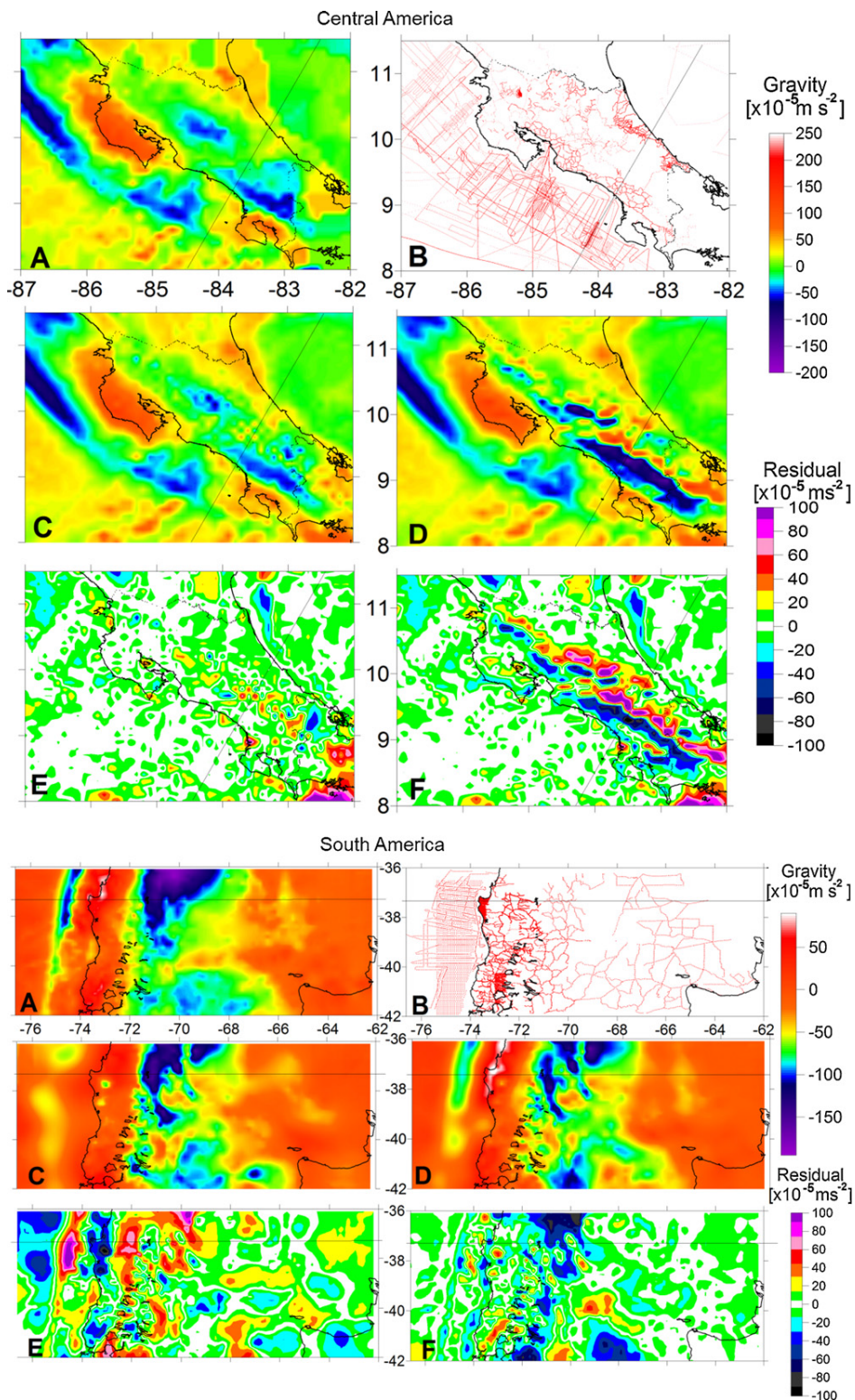
For Central America, a three dimensional density model is being developed within the framework of the SPP1257. The density model is based on gravity data from the EGM2008 geopotential model. The results have shown that the resolution of this model is appropriate for the modelling of regional lithospheric mass distribution and major tectonic structures such as the Middle American subduction zone, the continental and oceanic Moho as well as first order crustal discontinuities represented by the heterogeneities in the crustal basement and the upper crust (see Fig. 3.13).

Fig. 3.13 shows a cross-section of the 3D density model through central Costa Rica in which different datasets are compared and put into the context of the modelled structures. In the offshore areas, a good correlation has been obtained between the EGM2008 satellite gravity model and surface data. The geophysical Bouguer anomaly (offshore) is located on the geoid (on the ocean surface). Thus, it coincides with the geodetic Bouguer anomaly. On-shore, the geophysical Bouguer anomaly shows better correlation to the surface data than the geodetic Bouguer anomaly. In the mountainous areas of Costa Rica, the geodetic Bouguer anomaly (dashed line) differs significantly from the surface data (dotted line) as well as from the geophysical Bouguer anomaly (black).

The analysis of the present study shows that rugged topography downgrades the spatial resolution of the EGM2008 featuring large outliers in the Andes and Central America. Results in Central America show that high and unexpected deviations can be present in areas void of any terrestrial gravity data. Thus, the quoted spatial resolution of 10 km is not valid for all regions. Our case studies in these regions show that in areas of rugged topography, the geophysical anomaly often provides better results (up to 9% in mountainous regions; Table 3.1). Moreover, the use of geophysical anomalies in the calculation is consistent with the existing reduction techniques of terrestrial geophysical datasets.

3.2.4.3 Spatial resolution of different satellite gravity models

The main geophysical objective of using satellite-derived gravity data is the interpretation of lithospheric structures. We have used a well-constrained 3D density model of the South-Central Chile (*Alasonati-Tašárová*, 2007) to assess the spatial resolution of different satel-



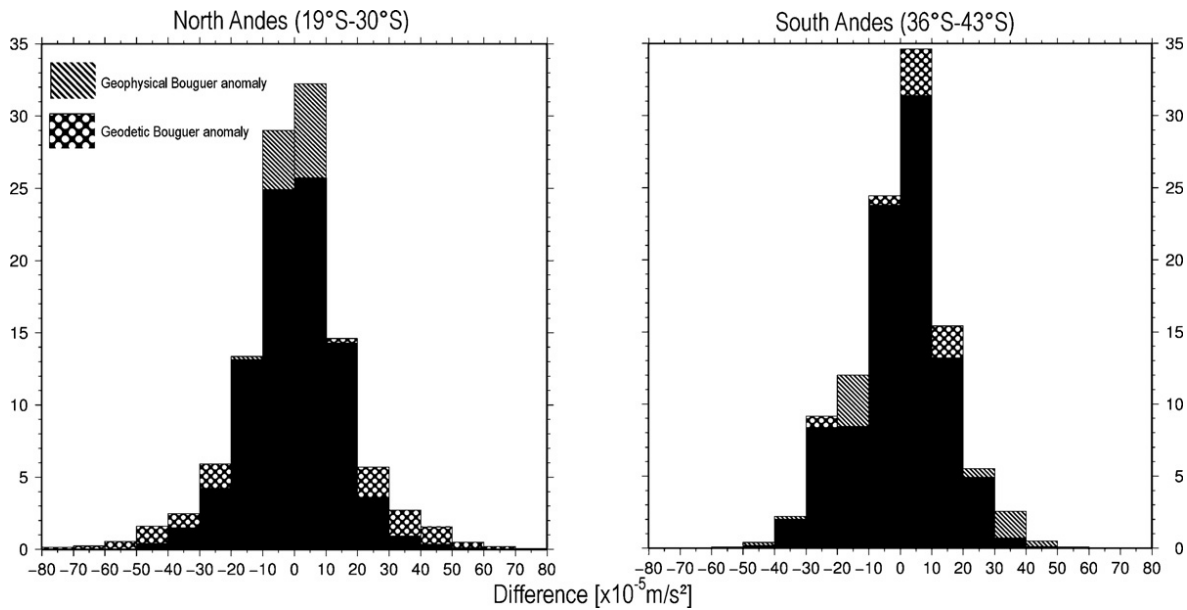


Figure 3.12: The deviation of the geodetic Bouguer anomaly (dotted) and geophysical Bouguer anomaly (hatched) from terrestrial data. The area, marked in black, indicate the overlapping of both datasets. In the northern Andes, the fit of the geophysical Bouguer anomaly is better. Most values are in the range of $\pm 10 \times 10^{-5} \text{ m/s}^2$. In the southern part, the geodetic Bouguer anomaly fits much better to the terrestrial data. Thus, the resolution of the geophysical anomaly is better in areas of large topography. However, large deviations from original datasets make the EGM2008 less reliable in these regions.

lite gravity models. The comparison emphasizes the areas of the models in which problems may occur when using different satellite gravity models (EGM2008, EIGEN-5C, ITG-GRACE03s, and GOCO-01s).

Fig. 3.14 shows a section of the 3D density model from the Central Chile at 37.4°S . Also shown on the top panel are gravity fields derived from different satellite models, measured surface gravity data, and the calculated gravity field from the density model. The dashed black line illustrates the calculated gravity from the density model and the red line shows the measured surface data. The EGM2008 (black) and the EIGEN-5C (yellow) show overall good correlation with the calculated gravity field. In the area of high topography (e.g. at 100 km of the x-axis), the EGM2008 exhibits significant deviations. The EIGEN-5C is smoother and correlates better with the predicted field. However, a deviation of about $15 \times 10^{-5} \text{ m s}^{-2}$ is observed between 350 and 400 km. The same misfit is visible in the GRACE solution (dark blue). The GRACE-GOCE satellite model (light blue) provides a better fit to the calculated gravity. Here again, deviations at 200 and 420 km are observed. However, the gravity low below the Andes at 300 km is better resolved by the GRACE-GOCE model. The gravity low of the deep-sea trench is well fitted by the combined models but the GRACE model does not comprise a distinct gravity low. Compared to other models, the deep-sea trench and the root of the Andes are more visible in the GRACE-GOCE model. The Coastal Cordillera is also shown as gravity high, but not well fitted in amplitude. The new GRACE-GOCE satellite

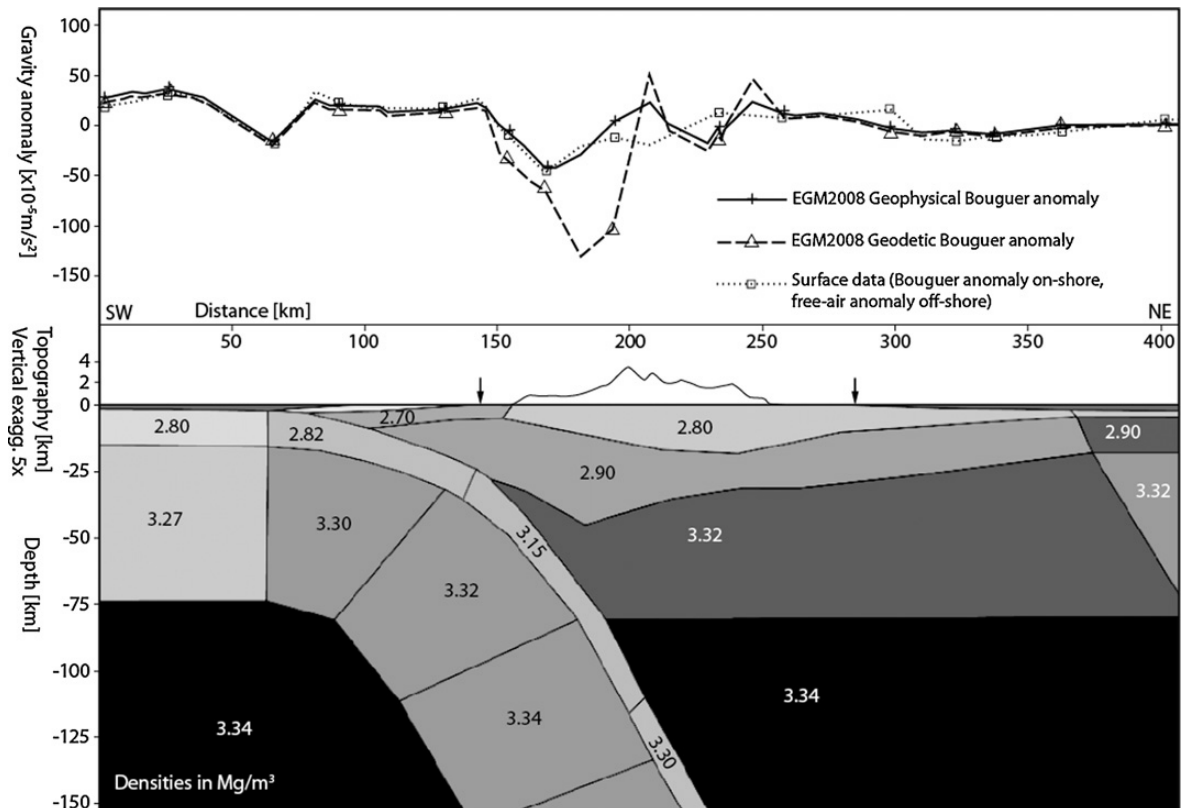


Figure 3.13: Vertical cross-section of a 3D density model from Central America. Different gravity anomalies are shown in the upper panel. The dotted line (with boxes) is derived from surface gravity data and shows the geophysical Bouguer anomaly on-shore and free-air anomaly off-shore (shoreline indicated by arrows). The dashed line (with triangles) shows the geodetic Bouguer anomaly on- and off-shore calculated from the classical gravity anomaly using EGM2008 model (off-shore without Bouguer reduction). The black line (with crosses) shows the geophysical Bouguer anomaly. Offshore, all datasets correlate. Onshore, however, there is still correlation with surface data, but the geodetic Bouguer anomaly shows errors of about $80 \times 10^{-5} \text{ m s}^{-2}$ for this cross section. In this region, elevation reaches up to 3700 m. The errors emphasize the uncertainty of the combined gravity models and instability of the downward continuation method.

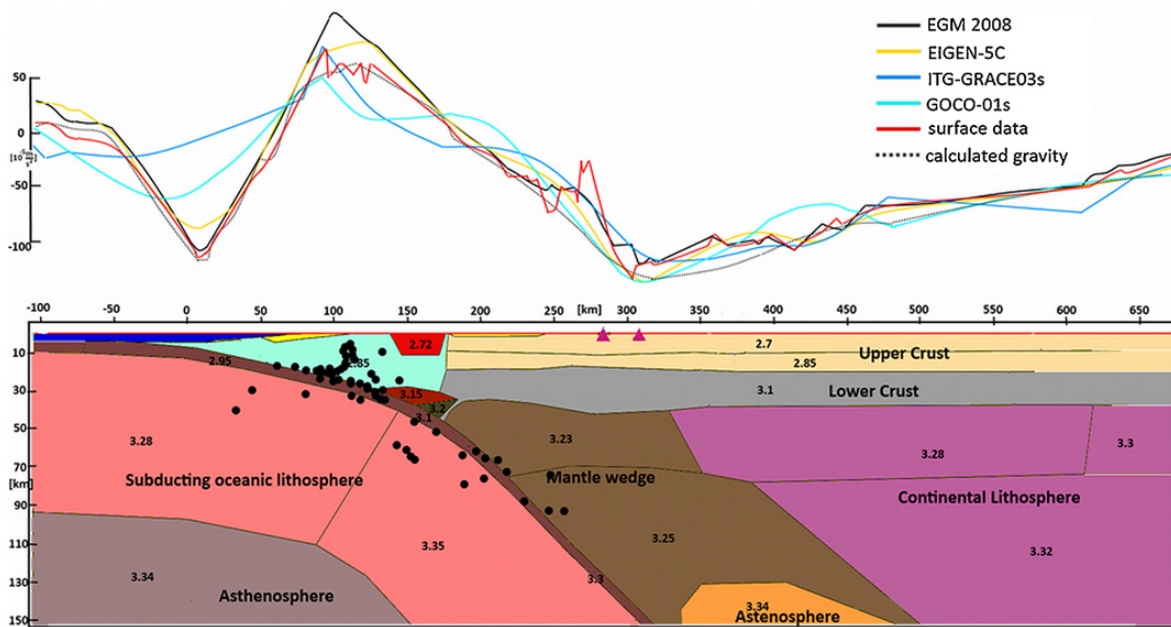


Figure 3.14: Vertical cross-section of a 3D density model from Central Chile at 37.4°S (*Alasonati-Tašárová, 2007*). The model is constrained in part by geological and seismological information (e.g. hypocentres are shown as black circles). The dashed line shows the calculated gravity from the model matched to the surface gravity data (red curve). The combined EIGEN and EGM2008 models fit well to the data. The EIGEN-5C (yellow) correlates well with the predicted gravity values, but it also shows some deviations. The ITG-GRACE03s model does not adequately show the gravity lows of the deep sea trench (at 10 km) and crustal root (at 300 km). The GOCO-01 s (light blue) model shows the best correlation of all satellite only models.

model shows the best fit. The EIGEN-5C provides a good fit over the entire section. The deviation of the EGM2008 in regions of high topography is clearly visible in areas where no surface data is available. The higher degree models such as the EGM2008 and EIGEN-5C cannot provide a high spatial resolution.

Overall, the GRACE-GOCE model shows an increased spatial resolution relative to the GRACE derived field. Since large-scale density models do not resolve local features, the calculated gravity field is smooth and comparable with wavelengths obtained from satellite-only gravity models. Combined models with new GOCE data could be sufficient for compiling density models of regional scale in frontier regions. Although combined gravity models can be used for density modelling of relatively smaller features such as shallower crustal structures, satellite-only models are not appropriate for this purpose due to the low spatial resolution.

3.2.4.4 Asperity mapping and resolution of gravity gradient data

Delineation of potentially hazardous provinces using gradiometry is one of our objectives. In order to examine the applicability of GOCE gradients for asperity detection in a simple way, the minimum dimension of a spherical anomalous mass below the geoid producing gravity and gravity gradient amplitudes of the order of GOCE's accuracy at orbit height (254.9 km)

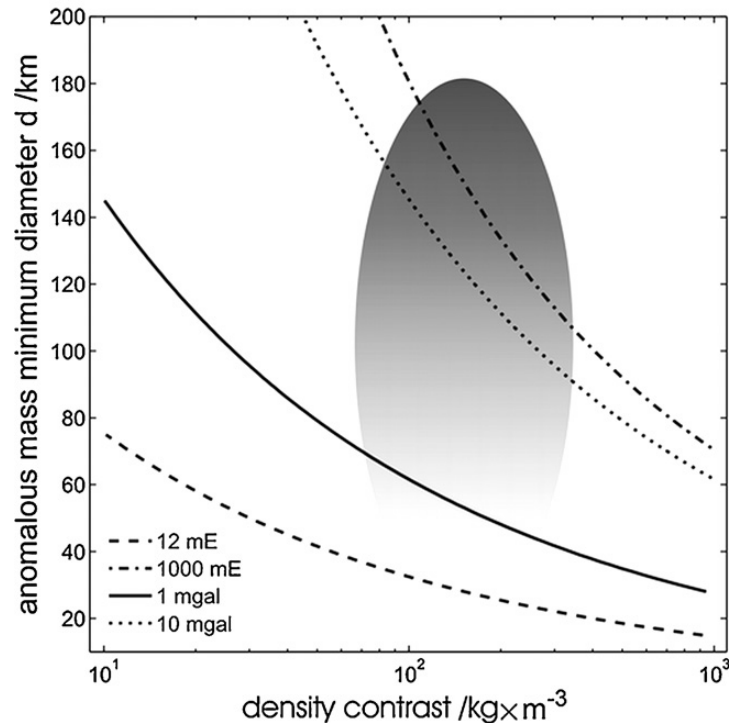


Figure 3.15: Differential gravity and gradient signal caused by a minimum diameter of an anomalous spherical mass of given density contrast below geoid at an orbit height of 254.9 km. The signal is in the range of GOCE's resolution. The thick solid and dotted lines represent differential gravity signals of 1 and $10 \times 10^{-5} \text{ m s}^{-2}$ at an altitude of 254.9 km, respectively. The thin dashed and dash-dotted lines represent gradients of 12 and 1000 mE, respectively. The grey shaded area shows the possible combination of parameters of an asperity generating batholithic structure near subduction zones.

has been calculated. The curves in Fig. 3.15 show the minimum diameter of such a mass of given density contrast required to produce signal differences of $1 \times 10^{-5} \text{ m s}^{-2}$ and $12 \times 10^{-12} \text{ s}^{-2}$ at orbit height. These values are close to the expected accuracies of the gravity and vertical gravity gradient of GOCE global data, respectively (Pail, 2011, pers. comm.). As shown in Fig. 3.15, an anomalous structure with density contrast of 240 kg m^{-3} could be detected in a gravity data at orbit height, if its diameter is at least $\sim 45 \text{ km}$. However, if the diameter of an anomalous structure increases by up to 100%, its density contrast should not be less than 33 kg m^{-3} to be detected. If gradients are considered, even bodies of about half of that size could produce signal in the range of GOCE's gradient data sensitivity. The dimension of Jurassic arc batholiths in Northern Chile is about 60–120 km (Götze *et al.*, 1994; Husen, 1999; Götze and Krause, 2002; Sobiesiak *et al.*, 2007). This supports the idea that batholithic structures, which are assumed to be related to asperity generation, can be detected using GOCE data.

Furthermore, we set up a synthetic model of an arbitrary subduction zone for 3D-density forward modelling. The geometry and density parameters have been adapted from the models developed by Sobiesiak *et al.* (2007) and Alasonati-Tašárová (2007). In order to test the signal response of asperity generating structure at different station heights using forward

modelling, a three dimensional anomalous structure (115 km × 200 km × 45 km) with physical properties resembling the Chilean batholiths has been included in the modelling. A density of $3 \times 10^3 \text{ kg m}^{-3}$ (density contrast of 0 to 300 kg m^{-3}) has been chosen for the batholith body in the model. At the height of 254.9 km, the magnitude of the gravity gradient anomaly ranges from few to some hundred mE ($1 \text{ mE} = 1 \times 10^{-12} \text{ s}^{-2}$). Being the second spatial derivatives of the gravity potential, gradients provide 'sharper' images of anomalies and can be combined into coordinate independent invariants (e.g. *Pedersen and Rasmussen, 1990*). Invariants sharpen density contrasts and help to emphasize structural boundaries. Fig. 3.16 shows how well anomalous underground structures of interest can be detected using gravity gradients at orbit height. Different tensor components give valuable information for geo-scientific interpretation. The above analysis shows that gradient maps from GOCE data may help to delineate major geological structures like fault zones, rims of sedimentary basins and intrusions.

3.2.4.5 Geodynamic model of the Andean margin as constrained by satellite gravity data

The present mass distribution is the result of long and complex geodynamic processes. Therefore, dynamic modelling is necessary to include the effects of time factor to the static density models. The dynamic evolution of the Andean margin has been extensively studied using numerical modelling. This includes studies of the dynamics of the plateau foreland (*Babeyko et al., 2006*), the factors controlling the intensity of tectonic shortening (*Sobolev et al., 2006*) and the influence of curvature of the convergent plate margin on the stress distributions (*Boutelier and Oncken, 2010*). These existing models are constrained by geophysical and geological data, but are based on generalized geometries. One of the objectives of this study is to develop a dynamic model of the Andean margin using realistic geometries from a well-constrained density model. In the present study, the geometries of the 3D dynamic model have been imported from the regional 3D density model of the Andean margin (*Tassara et al., 2006*). The model has 16 tectonic units including the lithosphere and the upper mantle down to a depth of 410 km.

Fig. 9 shows the visco-elastic 3D dynamic model of the Andean margin. The size of the model is 1730 km × 725 km (area between 16°S–22°S and 78°W–63°W). The densities of the units have been adopted from the density model of *Tassara et al. (2006)*. Young's moduli have been calculated using the v_p velocities from the ANCORP profile (*ANCORP Working Group, 2003*) and the P-S wave velocity relation $v_p = 3^{1/2}v_s$. The corresponding Poisson ratio for all units is 0.25. The parameters of the geological units are shown in Fig. 3.17. The asthenosphere has been modelled as a viscous-elastic medium. The lithosphere is pure elastic. In the modelling, it is assumed that the South American plate is fixed and the Nazca

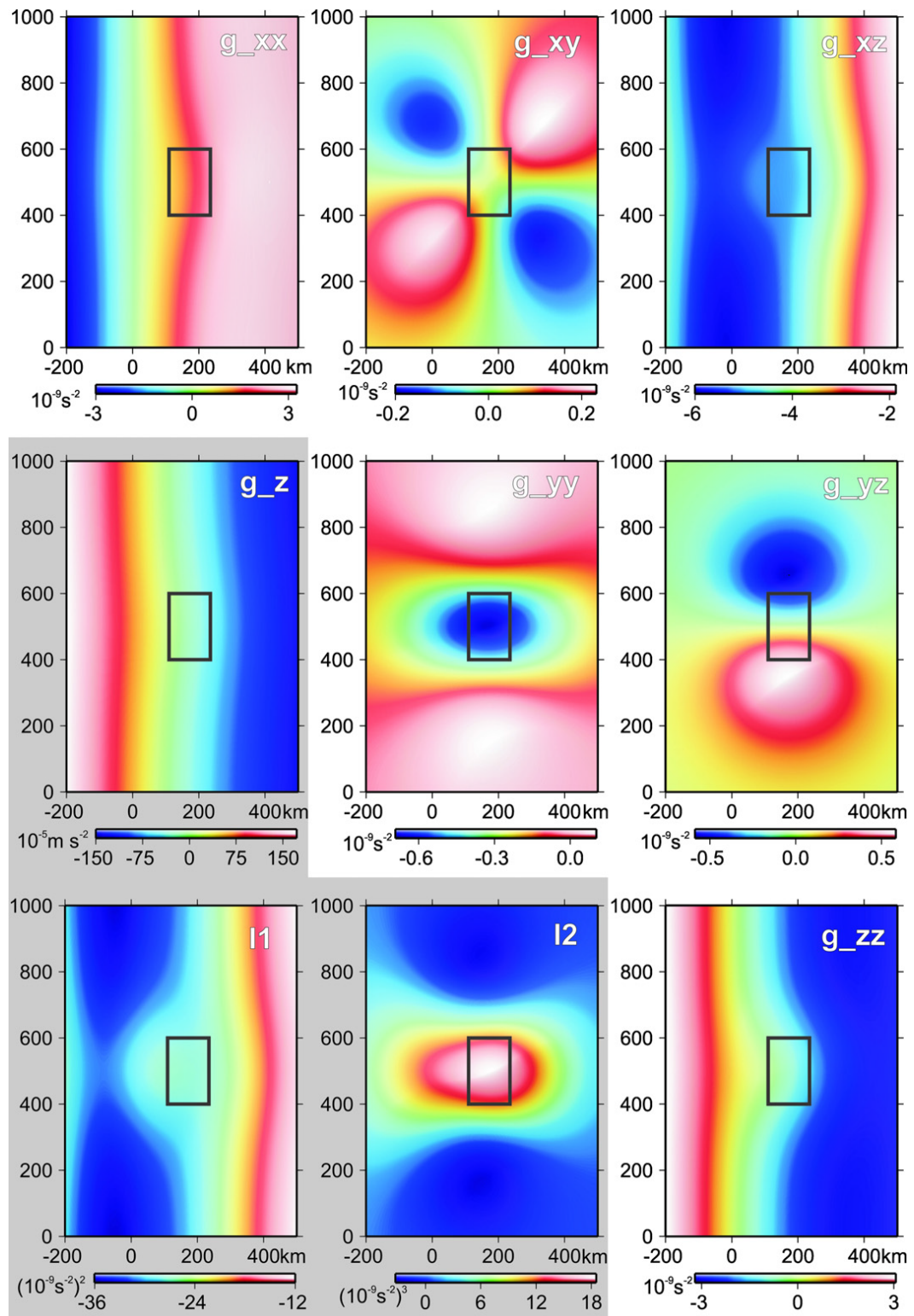


Figure 3.16: 3D-Modelling of synthetic gravity (g_z), gravity gradient tensor and invariants ($I1$ and $I2$) of a subduction zone using vertical gravity field as measured at 250 km height. A batholithic structure (black box) has been included on top of the down-going slab to test the resolution of gravity gradient signal. The gradient maps emphasize the location of the batholithic structure and the general geological strike of the subduction zone.

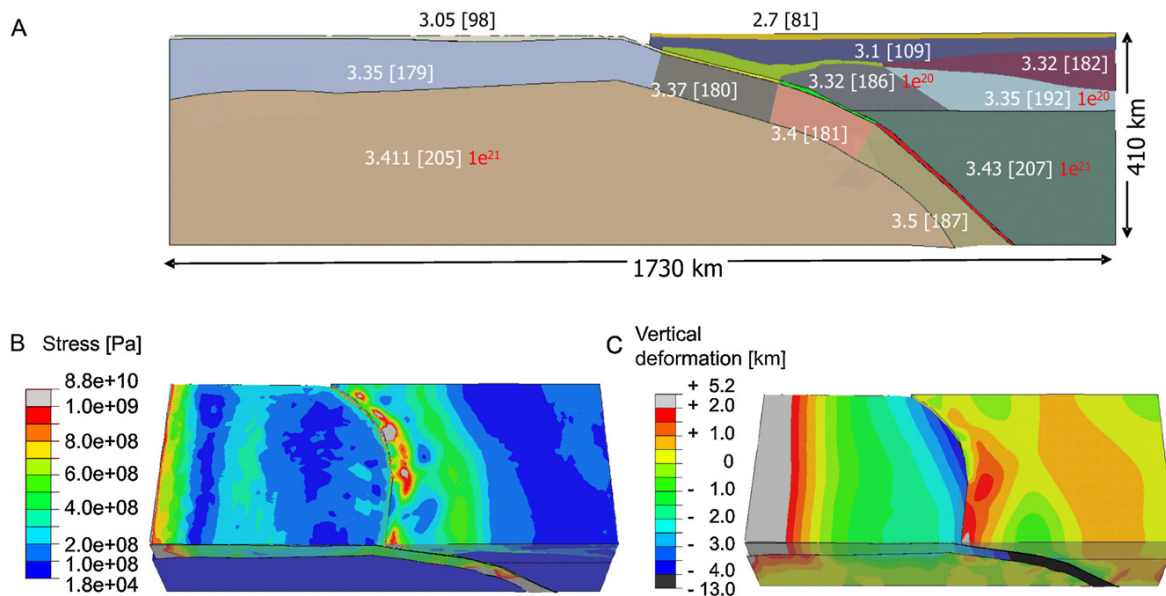


Figure 3.17: Used parameters for the viscous-elastic model (A). Densities (in $\times 10^3 \text{ kg/m}^3$), Young's moduli (in GPa) in brackets, viscosity in red. Oceanic crust: 3.2 [113] yellow, 3.3 [116] green, 3.55 [125] red, mantle wedge 3.23 [160] olive. Vertical deformations (B) and stress distribution (C).

plate moves by 7.8 cm/year for 200,000 years (Somoza, 1998). It is assumed that friction occurs only in the uppermost part of the contact up to approximately 40 km depth with a frictional coefficient of 0.1.

Beside density, however, Young's modulus, width of coupling zone, frictional coefficient and obliquity of the subducting Nazca plate could influence the dynamics of plate interfaces (Heuret and Lallemand, 2005). In order to study the effects of these controlling parameters, rheologies (e.g. plasticity, viscoelasticity and visco-elasto-plasticity) and temperature on the dynamics of the thrust zone area, more generalized and realistic 3D models have been developed.

Fig. 3.17b shows the resulting vertical deformations. The calculated uplift is ~ 1.5 km and this corresponds to 7.5 mm/year. The expected surface uplift is smaller than 2 mm/year (Klotz *et al.*, 2006; Jordan *et al.*, 1997). Though our model neglects erosion, the estimated uplift from the numerical modelling is in the right order of magnitude. Fig. 3.17c shows the stress distributions. The stress (high and low) tends to follow the trend of the earthquake distributions in the region. The green belt indicates where the slab is at depth of 100 km.

The present study shows that well constrained geometries are crucial for dynamic modelling. The availability of satellite-derived gravity data has significantly improved the density models of the Andean region lacking terrestrial data. This in turn refined the geometries and densities of the geodynamic models. In particular, the long wavelength satellite-derived gravity anomaly is suitable to constrain the deep structures of the models. The resulting stress fields and new petrologic models can help to improve the density structure of the static models. Thus, a direct link between the static and dynamic models could be established.

3.2.5 Conclusions

Thorough understanding and interpretation of dynamic processes associated with hazardous regions is one of the major research interests in geosciences. Combined gravity models can provide valuable information for density modelling and geological interpretation where terrestrial gravity data of high resolution are available. In this study, it is shown that gravity prediction and downward continuation in some areas, e.g. the mountain ranges over Costa Rica and Central Andes, could lead to large errors and reduce the reliability of gravity data. Gravity prediction based on topography may not be appropriate for those regions. This calls the need to improve reduction techniques such as Bouguer calculation, topographic correction as well as downward continuation. The satellite only models have low spatial resolution compared to terrestrial data. However, the resolution is sufficient for interpretation of large-scale structures. Especially, in frontier regions such as parts of the Andes or Central America, where terrestrial gravity data coverage is limited, these models are valuable.

3D modelling of synthetic gradients and invariants of subduction zones, using the Andean as case study, proved the applicability of gradient measurements for detection of edges of geological structures. Therefore, gradients from the GOCE mission can resolve structural information and improve the interpretation of asperities.

The long term and complex geodynamic processes of subduction could only be fully understood if model predictions are constrained with surface observables such as satellite gravity data. In the present study, a geodynamic model of the Andean margin has been developed with a realistic geometry based on a density model constrained by gravity data and other relevant prior information. The stress distributions in the fore-arc, as determined from the dynamic modelling, mostly coincide with the locations of the earthquake of the region.

Finally, mapping and interpretation of hazardous regions require good gravity databases (among others) to constrain lithospheric and dynamic processes. Satellite gravity data provide globally best information about frontier regions. Therefore, it is possible to interpret structures globally without limitations and combine regional interpretation of different regions into a one big picture.

3.3 Applicability Summary

Joint analysis of available gravity data and models revealed that quality and applicability of global high-resolution gravity models can easily become overestimated. Especially over rough topography, like in the Central Andes, where surface data is often missing, relevant models as the EGM2008 are not very reliable and would probably benefit from improved topographic correction and from incorporation of well processed high-resolution satellite data as from the quasi-global GOCE mission.

Methodological tests demonstrated that GOCE's gradiometer system would be effectually sensitive in order to detect signals of crustal density inhomogeneities in the gradients of the gravity field. The spatial resolution, however, must be regarded as difficult when the detection of crustal bodies is concerned. By gravity forward calculation of the density distribution of a synthetic subduction setting, it was nevertheless demonstrated that gravity gradients draw sharper contours of lithospheric density anomalies than the integrated gravity, also at orbit height. The gradients might thus be appropriate for lithospheric forward modelling and inversion. Interpretation issues due to the need for consideration of the correct coordinate system can be minimised by using rotational invariants of the gravity gradient tensor, respectively.

Finally, with regard to modelling the density distribution of the forearc in particular, it seems reasonable to co-process existing heterogeneously distributed surface-data with uniformly distributed satellite data in one combined gravity model. The development, evaluation and application of such a regional combined gravity model for subduction studies is documented in the next chapter.

4 Application of GOCE data

Several gravity models containing data of the GOCE mission (*Drinkwater et al., 2003*) have been released, e.g. GOCO01S (*Pail et al., 2010*), EIGEN-6C (*Förste et al., 2012*). In section 4.1 it is described how the GOCO3S model (*Mayer-Gürr et al., 2012*) has been utilized, in conjunction with terrestrial gravity data, in order to compute the IMOSAGA01C combined regional gravity model for North Chile (*Hosse et al., 2014*). A direct comparison study against the EGM2008 (*Pavlis et al., 2008*) is also shown therein.

Section 4.2 deals with the application of IMOSAGA01C to improve existing 3D density models of the North Chile margin and derive static stress anomalies on the subducting oceanic plate. The results are evaluated in terms of the control of the predominant seismicity. One externally written part of this section describes the adoption of the 3D geometry and parametrisation of a density model from gravity forward modelling to perform Finite-Element dynamic modelling in order to derive stress and strain within the same study area. Furthermore, the application of GOCE data to lithospheric interpretation is demonstrated and discussed using the vertical gravity gradient with mass correction at a computed altitude of 8 km.

Sections 4.1 and 4.2 were both published in the journal *Surveys in Geophysics*. The key results with regard to the course of this work are summarised and evaluated in section 4.3 with complementary notes on additional related work that has not been published with the given articles.

4.1 Combined regional gravity model of the Andean convergent subduction zone and its application to crustal density modelling in active plate margins

- Publisher: Springer Netherlands
- Journal: *Surveys in Geophysics*, Vol. 35 (2014), pp. 1393–1415, DOI: 10.1007/s10712-014-9307-x
- Authors: ^aM. Hosse, ^aR. Pail, ^aM. Horwath, ^bN. Holzrichter, ^bB.D. Gutknecht
 - a) Institute of Astronomical and Physical Geodesy, Technische Universität München, Germany
 - b) Institute of Geosciences, Department of Geophysics, Christian–Albrechts–Universität Kiel, Germany
- Author’s contribution: B.D. Gutknechts’s main contribution to this paper was the entire evaluation of the new combined gravity field against EGM2008 by means of the case study with additional contributions to introduction, gravity data and modelling methods, tectonic setting and conclusions. M. Hosse was corresponding author and – together with R. Pail and M. Horwath – responsible for the main part and structure of the manuscript as for the preparation of the IMOSAGA01C combined gravity model. N. Holzrichter contributed the topographic correction section.

Abstract The Central Andean subduction system is one of the most active geological structures on Earth. Although there have been a few previous studies, the structure and dynamics of the system is still not well understood. In the present study we determine a combined regional gravity model of the Andean convergent subduction region for constraining lithospheric models. After a thorough validation and cleaning of the terrestrial gravity and height databases, the method of Least Squares Collocation was applied to consistently combine terrestrial and satellite gravity data, putting much emphasis on the stochastic modelling of the individual data components. In result, we computed the first high–resolution regional gravity model of the study region that includes GOCE satellite gravity information. The inclusion of GOCE is an essential distinction from the independent global gravity model EGM2008. Validation against EGM2008 reveals, that our regional solution is very consistent in regions where terrestrial gravity data is available, but shows systematic differences in areas with terrestrial data gaps. Artefacts in the EGM2008 of up to 150 mGal could be identified. The new combined regional model benefits from the very homogeneous error characteristics and accuracy of GOCE gravity data in the long to medium wavelengths down

to 80–100 km. Reliable density modelling became possible also in the region of Central Andes, which lacks of terrestrial gravity data. Finally, density models were adapted to fit the new regional gravity field solution. The results clearly demonstrate the capabilities of GOCE to better constrain lithospheric models.

Keywords Subduction —GOCE —GOCO —Least Square Collocation —Terrain Correction —Density Modelling —Regional Gravity Model

4.1.1 Introduction

New data from ESA's dedicated gravity field mission GOCE (Gravity Field and Steady-State Ocean Circulation Explorer; *Drinkwater et al.*, 2003) provide high-accuracy and globally uniform information of the Earth's gravity field. The main goal of this study is to investigate the impact of this new gravity field information on lithospheric modelling of active plate margins such as the Andean convergent subduction zone in South America.

The present day structure of the Andean convergent zone is the result of 200 Ma ongoing subduction of the Nazca plate beneath the South American continent (e.g., *Oncken et al.*, 2006), exhibiting changes in subduction angle from north to south, northward thickening of continental crust, varying age of oceanic lithosphere, large-magnitude earthquakes, and volcanism. The flat slab subduction of the Nazca plate in Peru and South Central Chile, whose cause and associated earthquake distribution is still not well understood, makes the Andean convergent zone different from all other active subduction zones on Earth. The rather small number of region specific studies need to be extended to the larger segment of the convergent zones, which requires high density and uniform gravity data coverage. Furthermore, the few existing crustal and upper mantle velocity models in South America are limited to the northern and central parts of the margin (*Alvarado et al.*, 2007; *Feng et al.*, 2007), and the density models are largely unconstrained south of 39°S (*Tassara et al.*, 2006; *Alasonati-Tašárová*, 2007).

Previous studies (e.g. *Köther et al.*, 2012) have shown that lithospheric models of the study region suffer mainly from the fact that up to now high-resolution gravity field information for constraining these models has been irregularly distributed with large data gaps and partly low quality. Also global gravity field models such as EGM2008 (*Pavlis et al.*, 2012) inherit these problems of the underlying terrestrial databases. By including satellite gravity information from GOCE, in the study region gravity information with a spatial wavelength of up to 80 km with homogeneous distribution and accuracy is available, which can be used as a constraint for static and dynamic modelling. A complete understanding of the geodynamical processes requires an entire analysis chain, consisting of the following steps: the determination of a high-resolution combined gravity field based on satellite and terrestrial data; static lithospheric modelling using this gravity field and complementary seismic and geological

information as constraints as well as constrained geodynamic modelling of the interaction between the subducting and overriding plates.

In this paper we concentrate mainly on the derivation of a high-resolution combined gravity field model in the Andean region from 18° to 35° southern latitude and the evaluation of its impact on static lithospheric models of the study region. A second paper (*Gutknecht et al.*, 2014) discusses the use of gravity models based on terrestrial and satellite data in order to gain insight into the state of stress in subduction zones from 3D density models.

4.1.2 Data

For the determination of a regional gravity model covering the full spectral signal content, different gravity data types have to be combined. Satellite data contribute mainly to the long to medium wavelengths, while terrestrial data and satellite altimetry data over the oceans provide mainly the detail structure of the gravity field. Additionally, digital terrain models are used both, to validate the position and height information attributed to the terrestrial gravity data, and as an input to synthesize topographic gravity signals which are then used in the frame of a remove–compute–restore procedure in the frame of the combination.

4.1.2.1 Terrestrial database

The terrestrial database used in this study was collected over the last 30 years, merging the measurements from universities, agencies as well as industrial companies. All measurements were tied to the IGSN71 gravity datum (*Schmidt and Götze*, 2006). Altogether the dataset approximately consists of 175,000 data points and covers large parts of South America between 15°S and 55°S. Beside the position and height, for each point values of absolute gravity, Bouguer anomaly and free–air anomaly are available. Unfortunately the dataset does not include any information about measuring methods, error estimates or correlations among measured points. Therefore it is not possible to give a reliable estimate about the data quality.

4.1.2.2 Digital terrain model (DTM)

The Shuttle Radar Topography Mission (SRTM) was operated during an 11–day mission of the Space Shuttle Endeavour in February 2000. The mission acquired elevation data covering the landmasses between 56°S and 60°N using InSAR.

SRTM consists of several datasets, but only the dataset with a resolution of three arc-seconds (90 m) is available for the study area. The data is divided into 1°×1°–tiles and is downloadable via public web service at <http://dds.cr.usgs.gov/srtm/>.

In the present study the SRTM data is used through the data model Altimeter Corrected Elevations (ACE) in version 2. This model combines different elevation datasets like GLOBE

v1 with satellite altimetry data from ERS-1, ERS-2 and ENVISAT. It is available for registered users at <http://tethys.eaprs.cse.dmu.ac.uk/ACE2/>. Especially in South America the data quality of SRTM was greatly improved by using satellite altimeter data (Berry *et al.*, 2010).

Additionally ACE does not only cover the land masses but is also available for the oceans, where it is complemented with the bathymetry model DNSC08 (Andersen and Knudsen, 2008). This combined dataset is available with a resolution of 30 arcseconds only.

4.1.2.3 Satellite gravity data

Since 2009, the satellite gravity mission GOCE has been measuring the new gravity observation type of satellite gravity gradients. In contrast to other satellite gravity observations such as orbit perturbations or satellite-to-satellite tracking observations as they are measured by the GRACE (Gravity Recovery And Climate Experiment; Tapley *et al.*, 2004) mission, gravity gradients are direct functionals of the Earth's gravitational potential V . They represent second order spatial derivatives of the gravitational potential

$$V_{ij} = \frac{\partial^2 V}{\partial \chi_i \partial \chi_j} \quad (4.1)$$

in a local rotating reference frame, where the axes χ_i , with $i, j = X, Y, Z$ are oriented along the gradiometer axes (Gradiometer Reference Frame; GRF). The GRF deviates from an ideal, radially oriented local orbit reference frame by 3 to 5 degrees. Measuring second order derivatives partly counteracts the attenuation of the gravity field signal with altitude.

During the last years, a series of global gravity field models have been derived in the frame of the ESA project GOCE High-level Processing Facility (Pail *et al.*, 2011), which are parameterized in terms of a harmonic series expansion of the gravitational potential. Additionally, GOCE data have been combined with complementary satellite data, resulting in either satellite-only combined models such as the GOCO series (Gravity Observation Combination; Pail *et al.*, 2010) and combination models also including terrestrial data such as EIGEN-6C2 (Förste *et al.*, 2012).

In the present study, the regional gravity field modelling method of Least Squares Collocation (cf. Chapter 4.1.3.3) is applied to combine in an optimum way satellite gravity data with ground gravity data in the area of interest. In this framework, several strategies to include GOCE data have been investigated. The most direct approach is the use of original gravity gradients, defined in the GRF. The main challenge of this approach is the fact that due to the instrument characteristics of the GOCE gravity gradiometer, the gravity gradient signal is superimposed by coloured noise with 1/frequency characteristics below the gradiometer measurement bandwidth of 5–100 mHz. An alternative approach is to synthesize gravity

field quantities from a global model, where the problem of signal–to–noise separation has been solved globally, and one can make benefit of the high redundancy of observations.

Generally, the main goal of gravity field modelling is the optimum separation of signal and noise, and the parameterization of the signal in the form of a spatial and/or spectral representation. In global gravity field modelling, globally acting filter methods are applied to achieve this goal. However, detailed studies have shown that it is very difficult to achieve reasonable signal and noise separation, e.g., by Wiener Filtering (*Migliaccio et al.*, 2004), in the frame of regional methods. In literature, it is frequently argued, that high–frequency signals which are supposed to be contained in original gradient data are lost in global gravity field modelling due to the truncation of the harmonic series at a maximum degree L (e.g., *Herceg et al.*, 2014). This is, however, not really true, provided that the series is expanded reasonably high, so that the signal–to–noise ratio at the smallest spatial scales is safely below one. Compared to regional gravity field modelling approaches, global gravity field models potentially lose small parts of the high–frequency signal due to the fact, that they are usually regularized by applying a globally optimized regularization, so that in mountainous regions with exceptionally high–amplitude and high–frequency gravity field signal minor parts of it might be damped too strongly.

In summary, the philosophy of this study is based on the fact that the advantages of the direct use of gravity gradients, i.e., exploiting the full signal content in a regional optimization, are largely overruled by the drawbacks, such as the difficult signal–to–noise separation in the case of highly correlated (coloured) noise. This separation can be done much better in a global approach. Therefore, finally it was decided to include the satellite data as pseudo–observations, synthesized from the satellite–only global gravity field model GOCO03S (<http://www.goco.eu>), together with full covariance propagation (cf. Section 4.1.5.2). GOCO03S is an optimum combination of more than 12 months of GOCE data, 7 years of GRACE data, about 10 years of CHAMP data, as well as satellite laser ranging (SLR) data to stabilize the very low harmonic degrees. The synthesized pseudo–observations are gravity values on a grid with a constant geocentric radius of $R + 8\text{km}$ (with $R = 6378137\text{ m}$ being the GRS 80 semi–major axis). The choice of a constant geocentric height, rather than the constant ellipsoidal height of the output grid (see Section 4.1.5.3) is dictated by the error covariance propagation algorithm used.

4.1.2.4 Satellite altimetry data

The DTU10 Gravity Model (*Andersen and Knudsen*, 2009; *Andersen*, 2010) is a global gravity model provided by the Technical University of Denmark. It shows the gravity variations over the oceans with a resolution of one arcminute by one arcminute and a standard deviation of 3.82 mGal without a polar gap. It is mainly based on satellite altimetry from the Danish

National Space Center data set DNSC08. DNSC08 makes use of several satellite missions like ERS-1, ERS-2, TOPEX, JASON, ICESAT and ENVISAT. In our study the model is used to increase the resulting spatial resolution of the input data over the oceans beyond the GOCO03S resolution.

4.1.3 Methodological background

4.1.3.1 Overview

Fig 4.1 shows the architectural design and the product flow through our regional gravity field processing system, which is based on Least Squares Collocation (LSC) in combination with a variant of the classical remove–compute–restore (RCR) technique. The basic idea is to remove the long–wavelength gravity field effect, which cannot be adequately represented by the limited region and terrestrial gravity observations, by applying the global gravity field model GOCO03S up to degree/order 100, and the high–frequency signals, which are mainly related to topography, by a topographic–isostatic reduction (cf. Section 4.1.3.2).

The remove step, which has to be applied consistently for the terrestrial and the satellite data, results in smoother signals of the form

$$\beta_{red} = \beta - \beta_{GOCO100} - \beta_{TI} \quad (4.2)$$

where β are the (free–air) input gravity field observations, $\beta_{GOCO100}$ the long–wavelength component based on GOCO03S, and β_{TI} the topographic–isostatic reduction.

The compute step basically includes the application of LSC (cf. Section 4.1.3.3) to the consistently reduced terrestrial and (synthesized) satellite data, resulting in a target $\beta_{red} = \Delta g_{red}$ grid at 8 km ellipsoidal altitude. Finally, the previously reduced signal components (now evaluated at the target grid positions) are restored to the target output grid.

4.1.3.2 Topographic–isostatic reduction

Terrestrial and satellite gravity data also contain the gravitational effect of the topographic masses, being the dominant part of the high–frequency gravity field signal. In order to smooth the gravity field signals before combination, topographic–isostatic reduction is applied to all input signals consistently.

For this purpose, here we use the integrated gravity effect of rectangular prisms (e.g., Forsberg, 1984). The digital terrain model (DTM) ACE2 (cf. Section 4.1.2.2) is used to define a grid of quadratic prisms with 90m grid spacing and variable height.

The gravitational effect (1st vertical derivative of gravity potential) of each prism reads

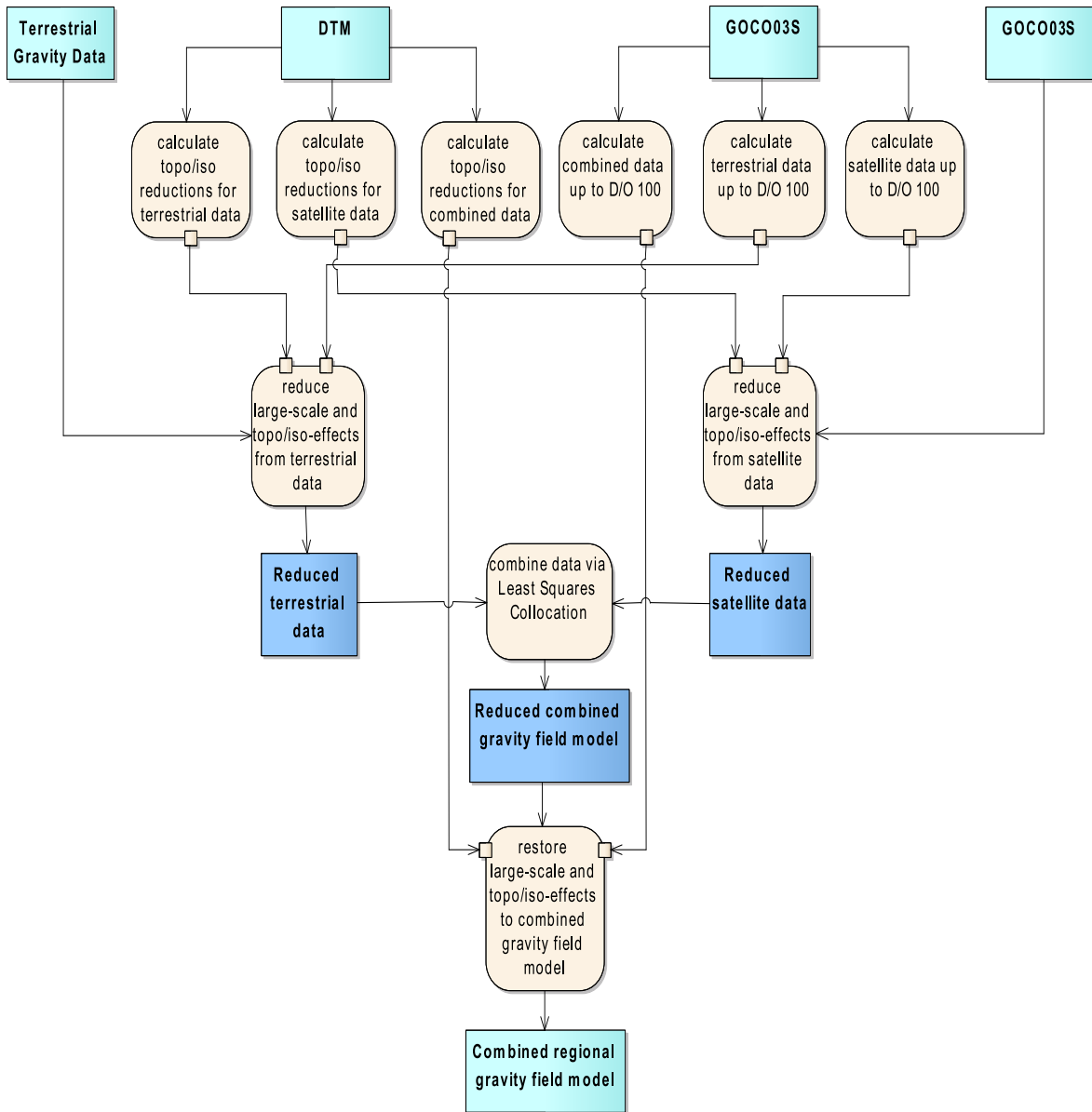


Figure 4.1: Architectural design and the product flow of regional gravity field processing system

(Mader, 1951; Tsoulis, 1999):

$$V_z = G\rho \left[x \ln(y+r) + y \ln(x+r) - z \arctan \frac{xy}{zr} \right]_{x_1, y_1, z_1}^{x_2, y_2, z_2} \quad (4.3)$$

In the same way Tsoulis (1999) also described the 2nd vertical derivative of gravity potential for prisms which is needed to reduce gravity gradients.

$$V_{zz} = G\rho \left[- \arctan \frac{xy}{zr} \right]_{x_1, y_1, z_1}^{x_2, y_2, z_2} \quad (4.4)$$

After applying the topographic correction, the remaining signal is highly anti-correlated with the topography. The topographic masses not only reside on top of a level surface, but they also reach as mountain roots into underlying layers. In order to fully reduce this effect also an isostatic reduction has to be applied. In this study the Airy–Heiskanen isostatic model is used for this purpose (Turcotte and Schubert, 1982).

TC3D_MPI

In this study the software package TC3D_MPI is used for calculating gravitational terrain corrections. It is based on the software package TC written in Fortran 77 (Forsberg, 1984). A complete rework written in Fortran 90 called TC3D was done by Gisinger (2010). For this study TC3D was modified and extended further, by adding missing functionals such as gravity gradients, completely reworking of parallelization algorithm using Message Passing Interface (MPI), implementing a cache for pre-calculated cubes and optimizing the calculation sequence to reduce memory consumption and to raise scalability.

For the topographic correction a constant value of $\rho_0 = 2670 \text{ kg m}^{-3}$ is used for onshore areas and $\rho_0 - \rho_w = 1645 \text{ kg m}^{-3}$ for offshore areas. For the isostatic correction a constant value of $\rho_{MA} - \rho_0 = 600 \text{ kg m}^{-3}$ is used. The main process loops over all stations that need a topo/iso correction. For each station the gravitational effect of the prisms inside a circle with defined radius around the station is computed. We use a radius of 167 km for terrestrial positions, 200 km for gridded data in 8 km height, and 560 km for gravity gradients in satellite orbit height. The Earth's curvature is taken into account by lowering of distant prisms according to the curvature of the reference ellipsoid GRS80.

Validation by TriTop

TriTop is a newly developed software package for topographic correction (Holzrichter, 2013). The software package is able to calculate topographic corrections for gravity and gravity gradients. It calculates the gravity effect of the topographic mass by polyhedral bodies. For validation purposes and to check the implementation updates of TC3D, the results of the topographic part of the topo/iso reduction was compared with the TriTop solution.

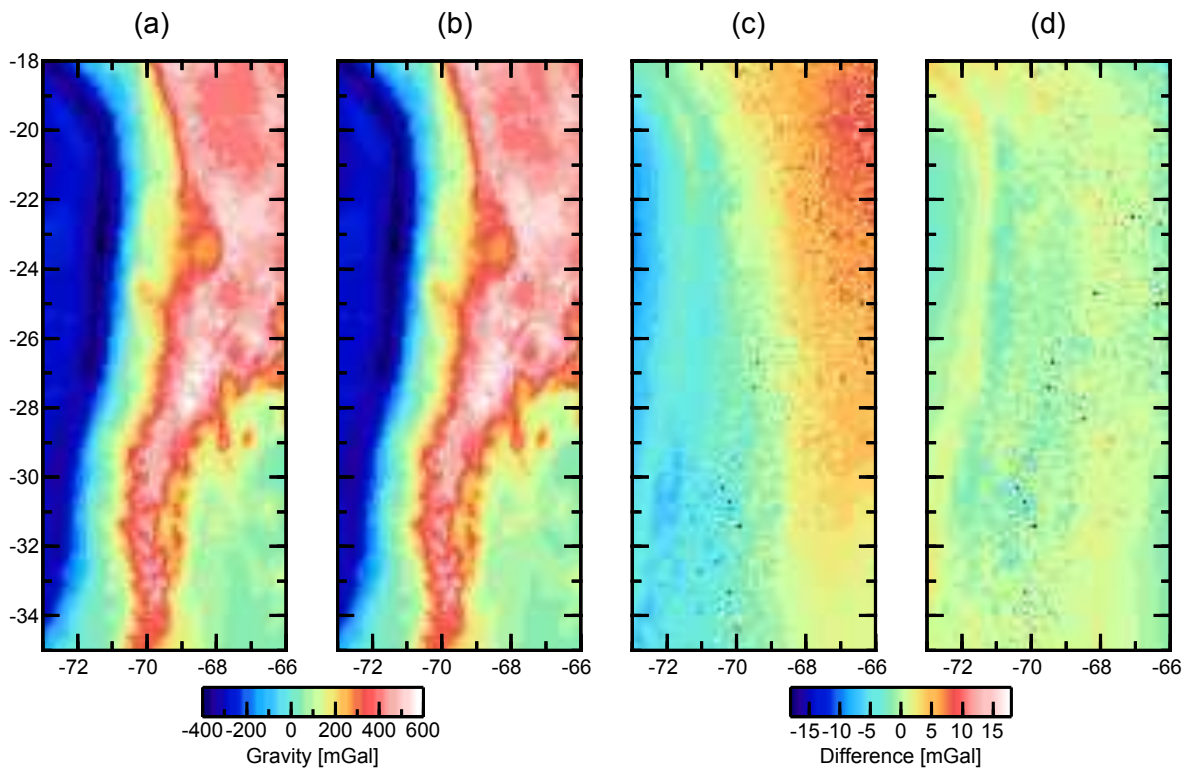


Figure 4.2: Topographic corrections calculated with different algorithms for validation. (a) calculated by TC3D. (b) calculated by TriTop. (c) difference between both corrections which feature a planar trend from West to East. (d) differences after removing a bilinear trend surface.

In this validation the stations are gridded with 0.1° grid spacing from -73°W to -66°W and -35°S to -18°S . The topographic grid for the TriTop calculation is 4° larger than the limits of the station grid. The assumed densities correspond to those used for the TC3D computation. Results of the calculations are shown in Fig 4.2 (a) shows the terrain correction from TC3D, (b) the correction calculated by TriTop and (c) the difference between them. They feature a linear trend running from West to East, which might be due to the different consideration of distant terrain effects. (d) shows the differences after subtraction of a bilinear trend. These final differences have a rms of 1.35 mGal. The minimum and maximum deviations are -19.5 mGal and 15 mGal, respectively.

The few larger differences are observed in high mountainous regions, e.g. at the coastal cordillera, where the different geometric approximations of terrain (cubes versus polyhedrons) cause larger deviations. The number of outliers is small (only 0.5% deviate more than 5 mGal). The standard deviation is far below the assumed accuracy of the terrestrial data of 10 mGal (cf. Section 4.1.5) and the few larger deviations can be nicely explained by the methodical differences of the two approaches. The main effect is related to the approximation of terrain by rectangular prisms versus polyhedral bodies. Correspondingly, we conclude that the TriTop results sufficiently confirm the topographic corrections computed independently by TC3D.

4.1.3.3 Least Squares Collocation

The basic formula of the statistical method of Least Squares Collocation LSC (neglecting the co-estimation of additional deterministic parameters) reads (*Kravarup, 1969; Moritz, 1972, 1978*)

$$\hat{s} = C_{st}(C_{tt} + C_{nn})^{-1}\ell \quad (4.5)$$

where $\ell = t + n$ is the vector of observations with t and n the signal and noise part, respectively, and \hat{s} is the target quantity to be estimated. Both t and \hat{s} have to be functionals of the disturbing potential T (= potential after reduction of the normal potential of a rotating reference ellipsoid): $t = L_1 T$, $\hat{s} = L_2 T$. The covariance matrices C_{tt} and C_{nn} describe the statistical correlations of the signal and noise components of the observations. Correspondingly, C_{nn} represents the stochastic model and acts as relative weighting scheme among the observations. The signal covariance matrix C_{st} represents the signal covariances between the input signals t and the target quantities \hat{s} .

One of the key advantages of LSC is that it provides, together with regional gravity field and geoid models from different gravity data types, also error information in the form of variances or even full variance-covariance matrices:

$$C_{\hat{s}\hat{s}} = C_{ss} - C_{st}(C_{tt} + C_{nn})^{-1}C_{st}^T \quad (4.6)$$

with C_{ss} representing the a-priori (co-)variances.

The LSC software used in this project is based on an algorithm developed for the computation of the Austrian geoid solution (*Pail et al., 2008*). It has been upgraded to include the new observation type of gravity gradients defined in the original GRF, following a numerically efficient strategy proposed by *Tscherning (1993)*.

4.1.3.4 Density modelling

In 3D density forward modelling (e.g., *Götze and Lahmeyer, 1988*), Bouguer gravity can be derived from a synthetic model geometry and density distribution that should generally be constrained by further geophysical parameters (e.g., seismology, petrology). The IG-MAS+ programme used in this study (*Schmidt et al., 2010*), uses triangulated polyhedrons to approximated areas of constant density within the Earth's lithosphere. While the initial geometries are being defined on vertical cross-sections, the triangulation process leads to a 3D calculation of the gravity field at requested altitude above the density model. Through interactive and inversion-based changes to the geometry and density distribution, an optimal fit between observed and calculated gravity is to be achieved within the estimated error bounds of the observed Bouguer anomaly.

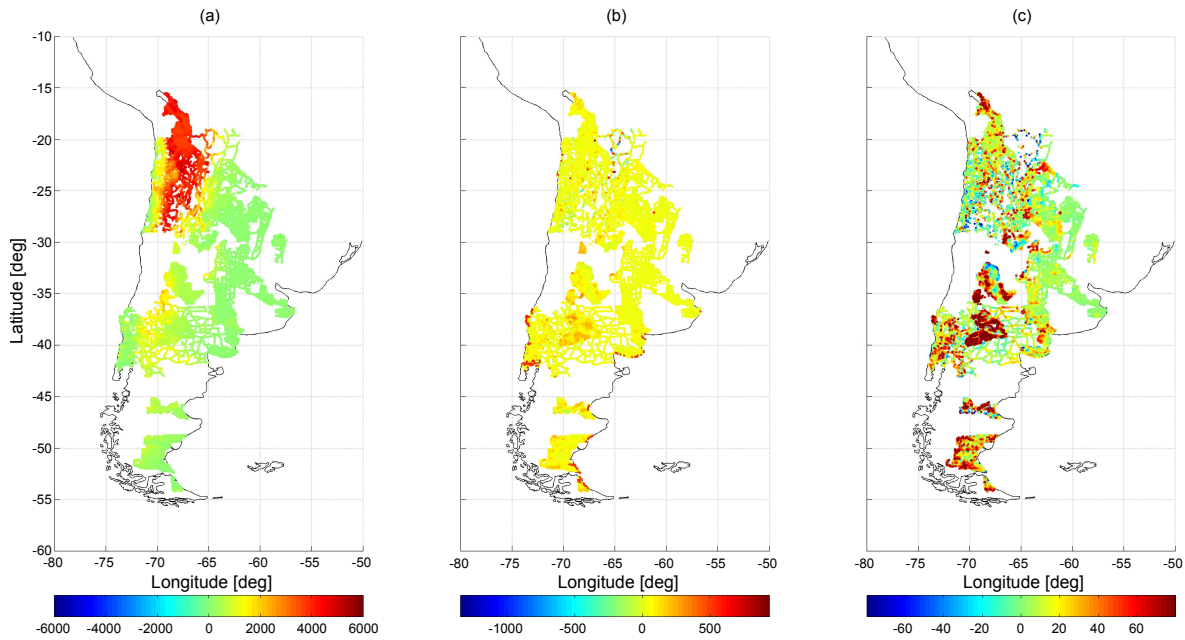


Figure 4.3: Comparison of heights. (a) absolute heights. (b) differences to ACE2. (c) remaining differences after outlier rejection. Units are meter.

4.1.4 Validation and preprocessing of the terrestrial data

4.1.4.1 Validation

As stated in Section 4.1.2.1 the terrestrial data was collected over a long time period with different measurement techniques and does not include any quality metadata. Therefore in the first step, the data have to be validated and outliers have to be identified.

For many stations, even the accuracy of their position is uncertain. In order to get a grip on that, all heights of the points were compared to the DTM ACE2. Fig. 4.3b shows the result of this comparison. The differences are in the range of -1365 m to +915 m with a mean value of 2.8 m and a standard deviation of 53.7 m. All points with height differences of more than 80 m (which corresponds to about 25 mGal in terms of free-air anomaly) were rejected. Applying this empirical outlier criterion, 20,000 out of the 175,000 stations were rejected.

After checking the height information, the gravity values themselves had to be validated. This was done by comparing them to global gravity models in a restricted spectral bandwidth. Therefore the data was compared to the global gravity models GOCO03S and EGM2008 (Fig. 4.4). Expectedly, the differences to GOCO03S are high in the Andes, because the resolution of GOCE does not cover the high-frequency signals of the topography. The small differences to EGM2008 indicate that largely the same data set was used for the computation of EGM2008. Table 4.1 shows some characteristic numbers.

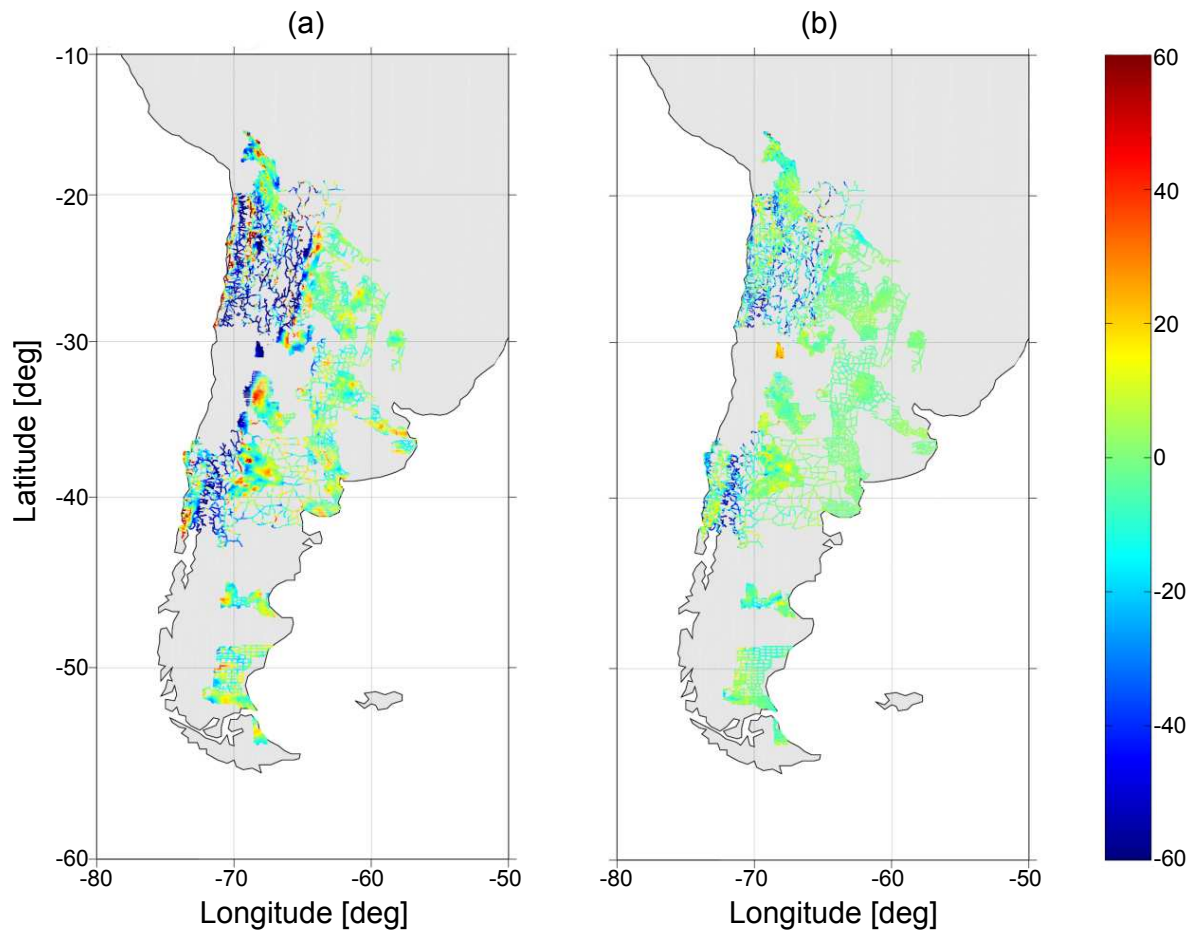


Figure 4.4: Comparison of gravity. (a) differences to GOCO03S resolved up to d/o 250. (b) differences to EGM2008 resolved up to d/o 2190. Units are mGal.

Table 4.1: Statistical parameters for the differences of terrestrial data to global gravity fields.

Difference to	GOCO03S (d/o 250)	EGM2008 (d/o 2190)
	/mGal	/mGal
Min.	-325.72	-303.86
Max.	216.66	102.59
Mean	-6.64	-1.45
RMS	24.08	10.94

Table 4.2: Key statistical parameters of gravity anomalies before and after the reduction process.

Gravity signal /mGal	min /mGal	max /mGal	std.dev. /mGal
Δg	-1668.33	92.59	419.67
$\Delta g - \Delta g_{GOCO100} - \Delta g_{TI}$	-132.23	88.42	26.90

4.1.4.2 Preprocessing

Since in LSC the dimension of the normal equations to be solved is defined by the number of observations, the number of input data has to be restricted. For this purpose, those observations which turn out to have the highest quality and reliability shall be identified and selected as representative values. Additionally, the data distribution is very inhomogeneous (cf. Fig. 4.4). Therefore it was necessary to develop a strategy that, on the one hand, lowers the number of stations in data-dense areas and, on the other hand, preserves the qualitatively best stations. For this purpose a quality criterion q (Eq. 4.7) was introduced, which takes gravitational differences (to GOCO03S) as well as the height differences (to ACE2). It reads

$$q = |g_{red}^{terr} - g_{red}^{goco}| + |h_{measured} - h_{ACE2}| \cdot 0.3086 \text{ mGal/m} \quad (4.7)$$

where g_{red}^{terr} is the measured terrestrial gravity and g_{red}^{goco} the calculated satellite gravity at the station. To make them comparable, both values were consistently reduced for long wavelengths, topography and isostasy (cf. Section 4.1.3.2). It shall be emphasized that such a strong criterion also concerning gravity differences turned out to be necessary, because several terrestrial gravity data do not only show inconsistency in height, but also concerning their horizontal coordinates, resulting in a significant gravity difference in rough terrain. This reduction procedure leads to a significantly smoother signal, cf. Fig 4.5. Table 4.2 provides the statistics of the original gravity anomalies and the reduced gravity anomalies after applying all reduction steps described by Eq. 4.2. The factor 0.3086 mGal/m is the free air gravity gradient which converts the height difference to a comparable free air gravity difference.

The quality parameter q was calculated for each of the about 53,000 stations in the study area covering the region between -73° and -66° longitude and -35° and -18° latitude. For the final combined gravity field modelling, the data were clustered into bins with a 3 km radius. For each bin, those stations with the smallest quality parameter q within a radius of 3 km were selected as representative terrestrial gravity field data. This procedure resulted in a selection of 9,900 stations. It shall be noted that the quality parameter defines a ranking among all observations within a 3 km bin. Even if there occurred a systematic misfit between the terrestrial gravity data and the GOCO model in this bin, a representative value showing this misfit is kept for the final processing. Therefore, this thinning procedure does

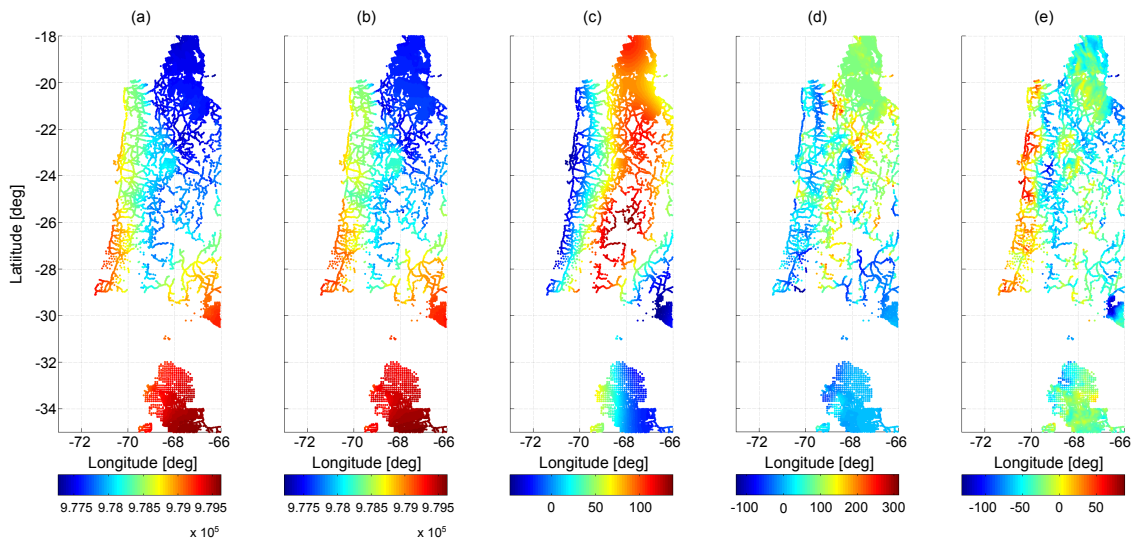


Figure 4.5: Elements of the data preparation (remove step) for the Least Squares Collocation. (a) β_{total} (gravity field observations), (b) β_{GOCO_100} (long-wavelength component of GOCO03S), (c) $\beta_{TI_KA_100}$ (long-wavelength component of a global topo/iso model), (d) β_{TI_TC3D} (topo/iso) and (e) β_{red} (resulting reduced signal). Units are mGal.

not significantly bias the terrestrial gravity data towards the GOCO model.

4.1.5 Combined regional gravity modelling

Based on the input data as derived in chapter 4.1.4, a combined gravity field model, called IMOSAGA01C, was computed. The target functionals were gravity anomalies and gravity gradients at 8 km ellipsoidal height. Here we concentrate on the presentation in terms of gravity anomalies. Here, and throughout this work, the term "gravity anomaly" denotes the difference between gravity and normal gravity evaluated at the same height. This naming follows the custom of geophysicists, while by geodetic terminology the precise name would be "gravity disturbance" (*Heiskanen and Moritz, 1967*).

4.1.5.1 Data preparation

Three types of observations were utilized in the combined gravity field modelling: terrestrial gravimetry, satellite gravimetry, and satellite altimetry over the ocean.

Terrestrial gravimetry was incorporated at the positions and heights of the original observations, after the data evaluation and selection procedure described in Section 4.1.4.

As discussed in Section 4.1.2.3, the GOCE and GRACE satellite contribution was incorporated in the form of pseudo-observations synthesized from the spherical harmonic coefficients of the GOCO03S model. We experimented with using gravity gradients synthesized at satellite height, but finally we resorted to using gravity on a regular grid at $R + 8$ km geocentric radius, extending 1.5° over the target area of the combined model. We thus avoided

complications related to the downward–continuation of a rather smooth functional at satellite height. It should be emphasized, that gravity anomalies at 8 km altitude contain more high–frequency signals than gravity gradients at satellite altitude.

In order to add spatial resolution over the ocean, we introduced additional information based on the DTU10 dataset from satellite altimetry (*Andersen and Knudsen, 2009; Andersen, 2010*). For practical reasons, this information was introduced indirectly from a global combined model (*Fecher et al., 2013*) that uses the altimetry–based gravity anomalies and, in fact, is mainly determined by those observations over the oceanic part of our study area. From this model, gravity values at a regular grid with geocentric radius $R + 8$ km were calculated to represent the oceanic data.

Following the remove–compute–restore approach we attempted to remove the long–wavelength components and the short–wavelength components from all three types of input data. We did so by reducing the low–degree part from degree 0 to 100 of GOCO03S and the topo/iso effects forward–modelled by TC3D as described in Section 4.1.3.2 (cf. Fig. 4.5).

We needed to consider that the long–wavelength topo/iso signal is contained both in the TC3D results and in the long–wavelength part of GOCO03S, and would be removed twice. Therefore we re–added the topo/iso over the spectral range from degree 0 to 100. As with the TC3D calculations we cannot separate a particular spectral range of the topo/iso, we used the RWI_TOIS dataset for this purpose. Insofar as the TC3D results and the RWI model do not perfectly match in their long–wavelength components, this procedure leaves some long–wavelength parts in the pseudo–observations.

As another issue, the topo/iso correction applied to the satellite pseudo–observations needed to be adapted to contain no signal beyond the spatial scale of degree 250, because the satellite pseudo–observations by their very definition contain no topo/iso signal beyond this maximum degree. Therefore, we smoothed the topo/iso before subtracting it from the GOCO03S–based pseudo–observations, using a Gaussian filter with a 80 km two–sigma radius.

Fig. 4.6a and b show the LSC input data thus generated. Table 4.3 summarizes the input datasets and their main characteristics used for the combined regional gravity model.

Table 4.3: Input datasets used for the combined regional gravity model.

Dataset	Type	Number of points	Latitude	Longitude	Height
GOCO03S Δg	Global	7381	-36.5 to -16.5	-74.5 to -64.5	Geocentric radius R+8km
Terrestrial data Δg	Onshore	9910	-35 to -18	ca. -71.4 to -66	Surface
DTU10 Δg	Offshore	2353	-36.5 to -16.5	-74.5 to ca. -70.0	Geocentric radius R+8km

4.1.5.2 Covariance information

A covariance model of the gravity field signal in the study region was defined based on scaled degree variances $c_n = \alpha_n \cdot c_n^{EGM2008}$ of the degree variances $c_n^{EGM2008}$ of the EGM2008 global spherical harmonic model. We defined plausible factors α_n so that the resulting spatial covariance functions are in agreement with empirical covariances of (a) the terrestrial gravimetry data (after the reductions of the remove step) and (b) GOCO03S–based gradients at satellite height (after the remove step). Even though the latter observation type was not used finally in the LSC, we found it important (and challenging) that our signal covariance model represents both the terrestrial data and the functional at satellite height associated to the GOCE observables. We chose

$$\alpha_n = \begin{cases} 0 & n \leq 35 \\ 0.5 & 35 < n \leq 100 \\ 1.5 & n > 100 \end{cases} \quad (4.8)$$

The factor of 1.5 for $n > 100$ reflects the fact that the high–frequency gravity field signal is larger for the study area than on a global average. The inclusion of signal variance below degree 100 reflects the imperfect removal of gravity field components of degrees 0 to 100. The resulting model covariance function has been checked against empirical covariance functions of ground gravity data as well as gravity gradients at satellite altitude.

Concerning the error variance and covariance information, the error variance of the terrestrial data was set to $(10 \text{ mGal})^2$, with no considerations of error covariances between different data points. The error variance of the oceanic gravity information was determined so that it leads to similar formal errors of the LSC over the ocean as over the land areas with terrestrial data coverage. For the GOCO03S–based gravity grids, in contrast, a full error covariance propagation was accomplished to describe the errors of the satellite–based data including their spatial correlation.

The limitation of GOCO03S to degrees up to 250 again requires additional considerations. While the propagated GOCO03S errors quantify the effect of errors in the spherical harmonic coefficients up to degree 250 (the so–called commission error), they do not include the failure of GOCO03S to provide the spectral part above degree 250 (the so–called omission error). Therefore, we supplemented the propagated error covariance matrix by a covariance matrix that characterizes the signal above degree 250. We derived this omission covariance from $1.5 \cdot c_n^{EGM2008}$, starting from degree 251. The factor 1.5 is motivated by the geophysical signal covariance model introduced above. Notably, this omission error (with a standard deviation of about 9.5 mGal) is larger than the commission error (about 3.7 mGal).

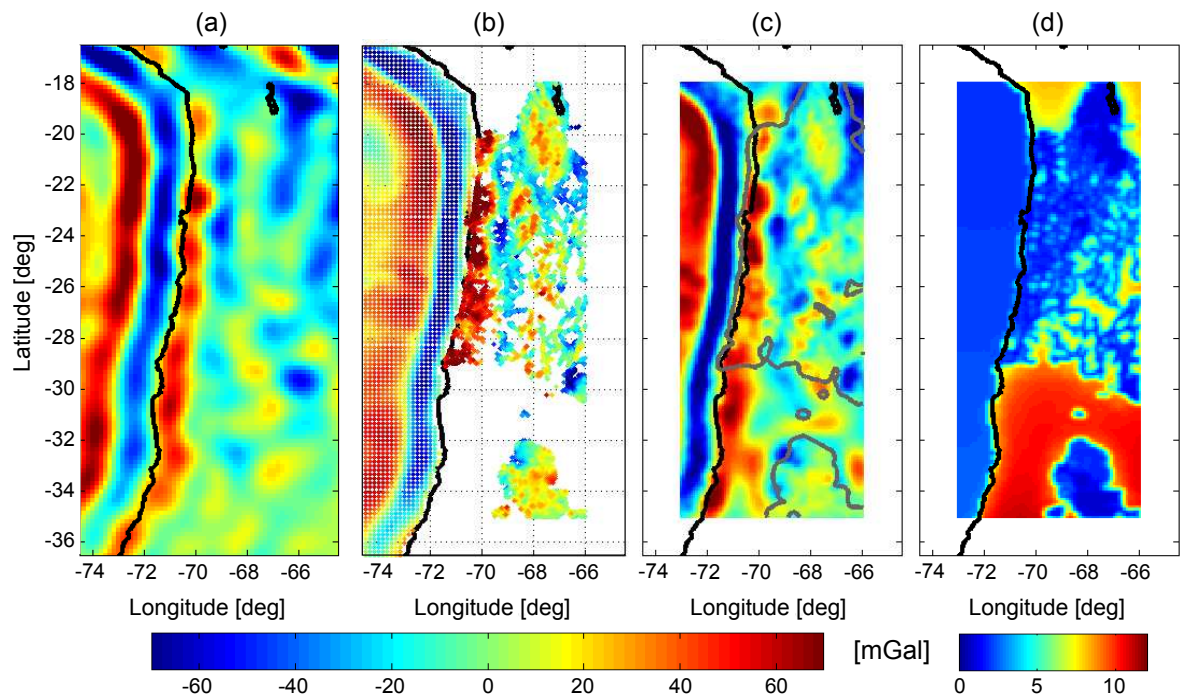


Figure 4.6: Input (a, b) and output (c, d) of the Least Squares Collocation. (a) gravity on a regular grid (at geocentric radius $R + 8$ km), calculated from GOCO03S global satellite-only gravity model. (b) terrestrial gravity data at the positions and heights of observation, and oceanic gravity data determined using ocean altimetry, on a regular grid (at geocentric radius $R + 8$ km). (c) output field (before restoring the removed components) in terms of gravity at 8 km ellipsoidal height. (d) Error standard deviation. Units are mGal. Thick black lines are coastlines. Grey lines in (c) indicate limits of areas with terrestrial data coverage.

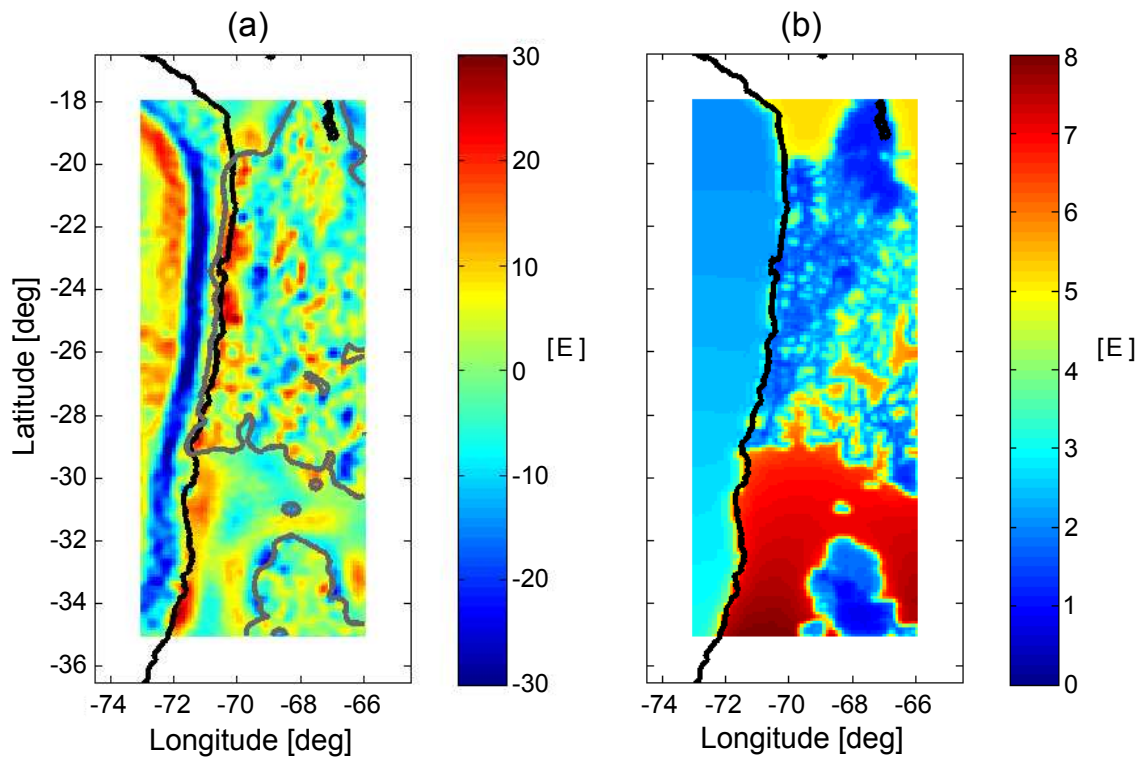


Figure 4.7: Output field of the Least Squares Collocation (before restoring the removed components) in terms of V_{zz} -Gradients at 8 km ellipsoidal height (a) and their error standard deviation (b).

4.1.5.3 The IMOSAGA01C regional gravity field model and its validation

Having prepared all its constituents, we performed a LSC according to Eq. 4.5 to generate the IMOSAGA01C regional gravity field model. Fig. 4.6c shows the output of the LSC in terms of gravity at a regular $0.1^\circ \times 0.1^\circ$ grid at 8 km ellipsoidal height before any previously removed gravity field components are restored. Fig 4.6d shows the related error standard deviation obtained by Eq. 4.6. Areas exclusively covered by satellite gravimetry are distinguishable from areas with terrestrial or ocean altimetry data by a higher error level in Fig. 4.6d (8 to 11 mGal versus 1.5 to 3.5 mGal) and by a relative smoothness of the estimated gravity patterns. Analogously to Fig. 4.6 c and d, Fig. 4.7 shows the result in terms of the V_{zz} -gradients at 8 km ellipsoidal height their formal uncertainties.

To obtain the full gravity field we restored the gravity field components removed prior to the LSC. They were now evaluated at the positions and heights of the output model grid, and no filtering was applied to the topo/iso effect. By removing the normal gravity field (evaluated at the same grid) we obtained free-air anomalies, and by additionally removing the topographic effect from TC3D we obtained Bouguer anomalies. These two fields, relevant for geophysical interpretation, are shown in Fig. 4.8a and c.

To validate our results, we first compared the LSC output to the LSC input data. For this purpose we predicted, based on the same input data, gravity anomalies at the positions

of the terrestrial input data. The residuals were found to be well within the error bounds of the input data, with a standard deviation of 6.1 mGal for the terrestrial data. Second, we compared our model to EGM2008. Fig. 4.8 shows this comparison on the level of free air anomalies and Bouguer anomalies. In the ocean area and the areas of terrestrial data coverage, differences between the two models (subplot e) are relatively small. This likely reflects the fact that both models are based on similar terrestrial and altimetric data sources. Still, the differences exceed the formal errors of IMOSAGA01C by about a factor of 2.5, on average (analysis not shown here). Errors of EGM2008 may contribute to this difference, but deficiencies in our modelling might also cause our formal errors to be too optimistic. The IMOSAGA01C – EGM2008 differences are largest in, or near, the areas with satellite-only coverage. In these areas, IMOSAGA01C is mainly determined from GOCE data, which was not available for EGM2008. Therefore we interpret these differences to mainly reflect improvements of IMOSAGA01C upon EGM2008, enabled by the GOCE data, even though EGM2008 might have utilized additional data sources unavailable to us. The largest feature in the IMOSAGA01C – EGM2008 difference is a pair of peaks about -70.5° longitude and -30° latitude. These peaks reflect respective structures in the EGM2008 anomaly maps (subplots b and d). We see no geophysical reason for them to exist (cf. also Section 4.1.6), which supports the argument that IMOSAGA01C is superior to EGM2008 in this area.

4.1.6 Application: density modelling

For comparison and evaluation purposes, we forward calculated the Bouguer anomaly field at an altitude of 8 km above Northern Chile from the well constrained density model by (Prezzi *et al.*, 2009). The original model was built without using satellite gravity data. The calculated Bouguer anomaly (black dashed line in Fig. 4.9 and Fig. 4.10) served as a reference to compare the new combined gravity field to the EGM2008 model. The same TC3D topographic correction was applied to EGM2008 and IMOSAGA01C. It was not applied to the reference anomaly because topography is not included in the forward modelling.

Fig. 4.9 shows a trench-perpendicular vertical cross section of the density model through the city of Iquique (20.2°S). This part of the study area is relatively well constrained by terrestrial gravity data. The latter are also expected to be included in EGM2008. Therefore, the new combined model and EGM2008 almost perfectly match reference gravity as expected. GOCO03S is in a generally very good agreement with the compared fields but exhibits moderate undulations in the forearc and trench region of the profile.

In contrast to the gravity data available here, Fig. 4.10 provides the same set of vertical cross profile but with significantly less terrestrial constraining data in this region at 30.3°S . The anomalies therefore coincide only in a first order trend. Viewed in more detail, the

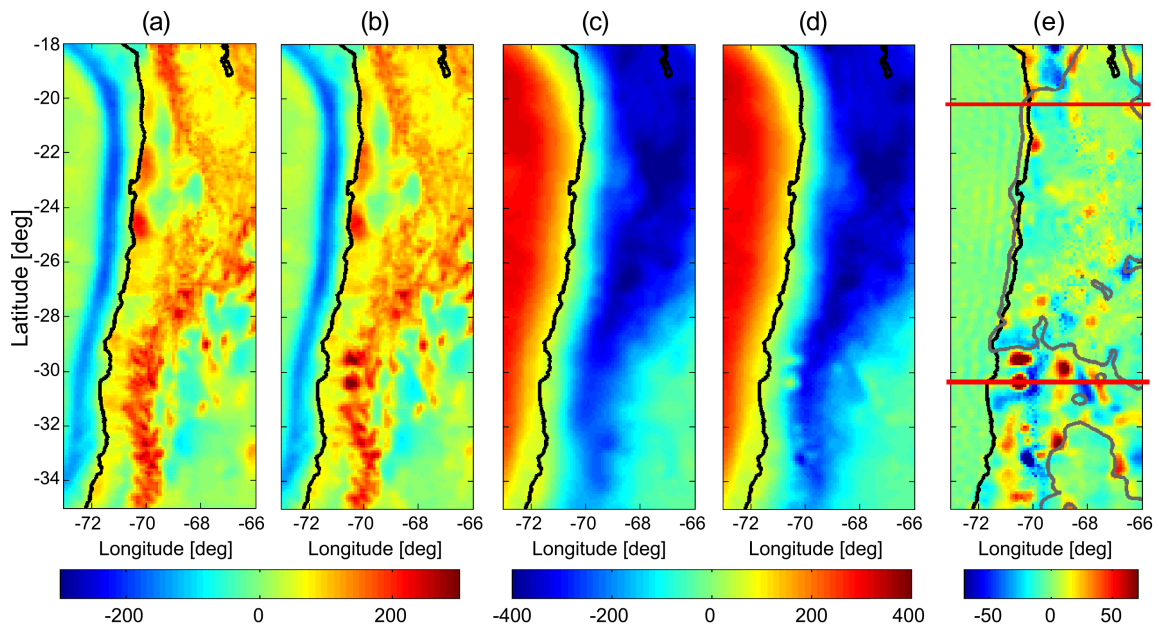


Figure 4.8: Comparison of the IMOSAGA01C regional gravity model generated in this study with the EGM2008 global model. (a) and (b) free-air gravity anomalies in 8 km ellipsoidal height according to IMOSAGA01C and EGM2008, respectively. (c) and (d) Bouguer anomalies (i.e., free air anomalies reduced by the topographic effect) according to IMOSAGA01C and EGM2008. (e) difference between IMOSAGA01C and EGM2008, which is identical for both types of anomalies. Units are mGal. Anomalies are defined as the difference between gravity and normal gravity evaluated at the same height, which corresponds to gravity disturbances in the geodetic terminology. Thin lines in (e) delineate the areas with terrestrial data coverage. The red lines in (e) show the locations of the profiles described in chapter 4.1.6.

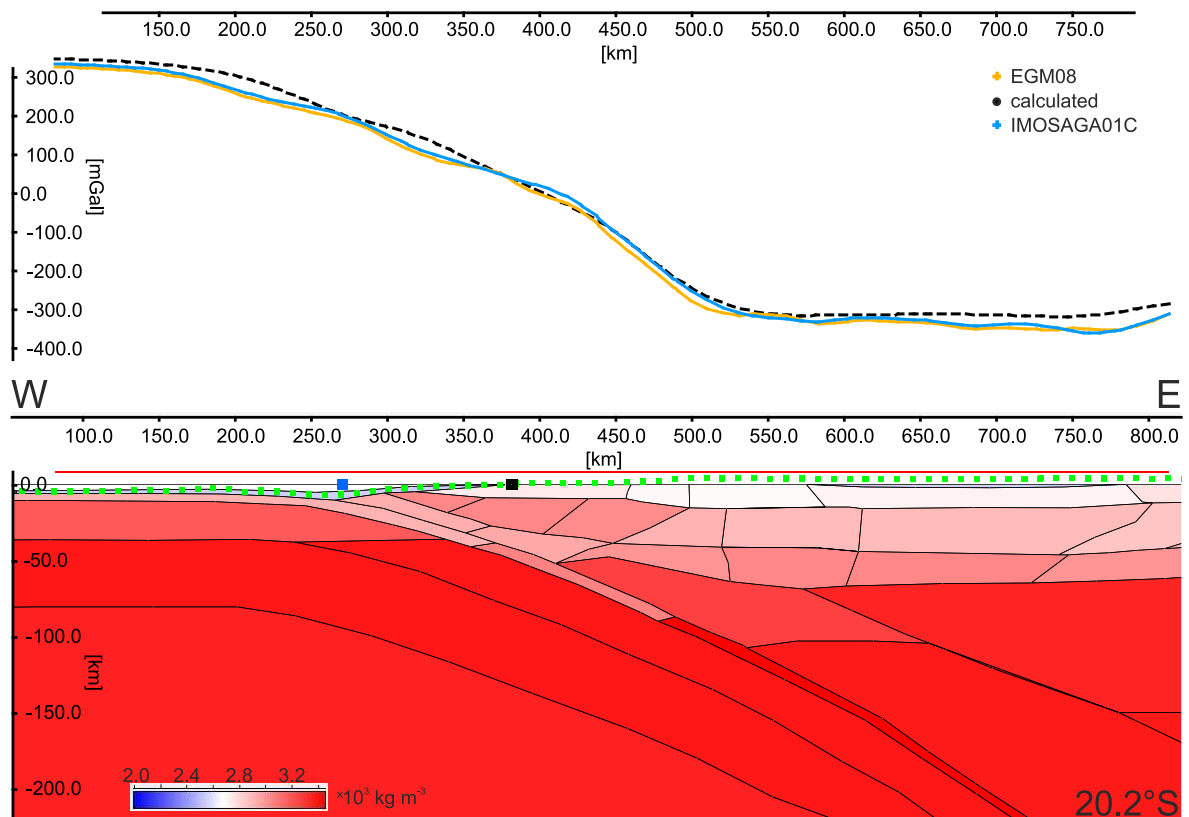


Figure 4.9: East–West striking cross section through $\sim 20.2^\circ\text{S}$ (Iquique). The black dashed curve represents the Bouguer anomaly field calculated from the underlying density model (Prezzi *et al.*, 2009) that was built using terrestrial gravity data onshore and altimetric gravity data offshore. Blue and black squares represent trench and coastline, respectively. Dotted green curve: bathymetry and topography. All fields calculated at 8 km altitude (red line). No vertical exaggeration.

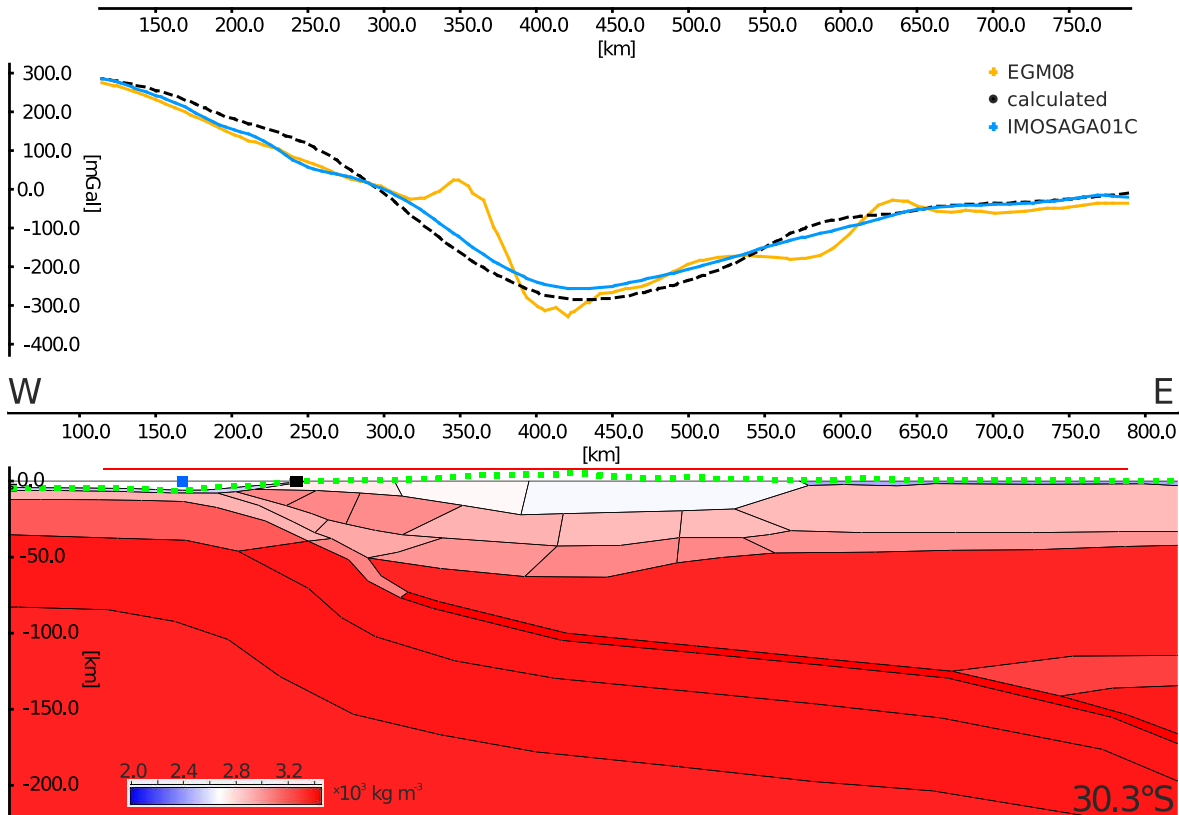


Figure 4.10: East–West striking cross section through $\sim 30.3^\circ\text{S}$. The black dashed curve represents the Bouguer anomaly field calculated from the underlying density model (Prezzi *et al.*, 2009). The density model is less well constrained at this location than in the Northern sections. Blue and black squares represent trench and coastline, respectively. Dotted green curve: bathymetry and topography. All fields calculated at 8 km altitude (red line). No vertical exaggeration.

EGM2008, whose exact terrestrial data source at this location is unknown, exhibits large deviations of up to 150 mGal. The combined solution at the same place, however, displays anomalies in agreement with expectations. This may be directly attributed to the impact of the use of GOCE–data in the combined field since it comprises the only measured gravity data in the region of the southern section. The large discrepancy of the EGM2008 at 30.3°S cannot reasonably be explained by geologic features: A gravity peak of 150 mGal and a half width ~ 40 km would be supported by an excess mass of $\sim 3 \times 10^{15}$ kg. This excess mass could be provided by a local spherical density anomaly of 20 km in size consisting of mantle–type rock composition (3200 kg m^{-3}) close to the surface. We do not see any geological evidence that the required density distribution exists at this location.

We performed a test run with adjusted geometry and density distribution along the cross section from Fig. 4.10 in order to possibly fit the EGM2008 anomaly with forward calculated gravity. The result is a rather localized block, located directly below the surface (Fig. 4.11). The density of 3200 kg m^{-3} is similar to mantle type material and is unrealistically high for this shallow proximity. The isolated peaks in the EGM2008 data thus might be unrealistic. We therefore conclude that the new combined gravity field IMOSAGA01C seems

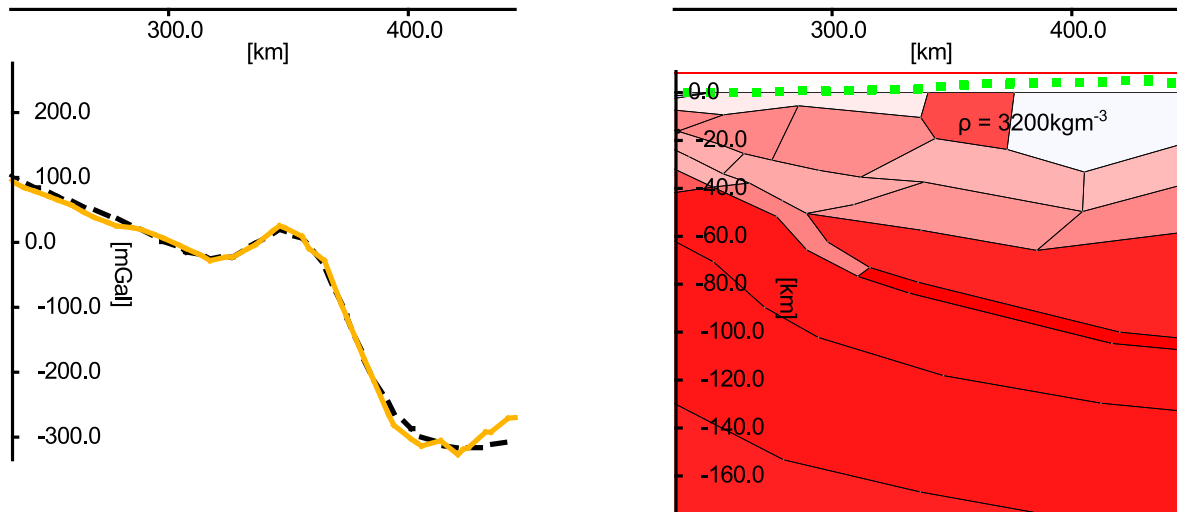


Figure 4.11: Part of the cross section in Fig. 4.10 with adjusted near surface block to fit the local peak of the EGM2008 anomaly (orange). In order to match the given magnitude of the EGM2008, the block (dark red, centred below surface) must have an unrealistically high density.

to be superior in the study area where no or only sparse terrestrial data coverage is available.

In the following we compare the agreement of the Prezzi density model (*Prezzi et al.*, 2009) and new adapted density model with gravity field information. Compared to the former core area with terrestrial data, the combined field IMOSAGA01C stretches ~150 km further to the South and North, respectively. Here, it covers regions of the Central Andes that were already part of Prezzi et al.'s density model but so far have not been forward-modelled, also due to the lack of available data.

The standard deviation between forward calculated gravity on the surface and terrestrial data originally used by *Prezzi et al.* (2009) is 16.7 mGal. When applied to the existing density model with the unconstrained patches, IMOSAGA01C and the calculated field at R + 8 km have a higher standard deviation of 20.1 mGal. This is expected since the calculated field now contains results from areas where no constraining with gravity data had been applied before.

After interactively adjusting the geometric density distribution in the additional areas in IGMAS+, the standard deviation of the total field decreased to 13.7 mGal. The most effective changes made include:

- Decreasing the crustal root depth between 29.9°S and 31.7°S by 5000m,
- Forearc and wedge adjustments between 29.9°S and 31.7°S, and between 18°S and 19.5°S, respectively.

In the wedge region, mass excess up to a few tens of mGal from the model had to be corrected; and in the forearc, minor mass deficits at the Coastal Cordillera and Batholiths section have been balanced.

The geometry of the pre-existing central part of the model remained unaffected. Expanding the adjustments also to this region as well as additional inversion of the density parameter would further enhance the field deviation towards the 10 mGal mark. The latter two tasks will be tackled in future analyses.

4.1.7 Conclusions

In this paper we present the processing and application of the combined regional gravity field model IMOSAGA01C covering the study area of the Andean convergent subduction zone in South America. It was possible for the very first time to compute a high-resolution regional gravity model for the study region, as a combination of terrestrial and satellite data. This new model has then be used as a constraint for lithospheric modelling.

In the frame of terrestrial data pre-processing, satellite gravity field information was used, together with a consistent digital terrain model derived from ACE2, to perform an independent validation and quality analysis of the terrestrial gravity databases. In the course of this process, observations affected by gross errors in gravity and position/height could be identified, and empirical error measures for all stations could be derived, resulting in a cleaned terrestrial gravity database for the Andean region as a by-product of this study.

The combination of this cleaned terrestrial gravity database with GOCE and GRACE information, which was performed by applying Least Squares Collocation including a remove-compute-restore method and taking stochastic information of both the commission and the omission errors into account, resulted in the regional gravity field model IMOSAGA01C. This model was validated by comparison with the global gravity model EGM2008, which contains to a large extent the same terrestrial gravity data information (processed in a different and completely independent way, though), but no GOCE data. This validation shows that our regional solution is very consistent with EGM2008 in regions where terrestrial gravity data is available, but shows systematic differences in areas with terrestrial data gaps. In a case study it was found out, that along a profile of $\sim 30.3^\circ\text{S}$ deviations of EGM2008 from IMOSAGA01C up to 150 mGal occur. This large deviations could only be explained geophysically by a local near-surface density anomaly with a mantle-type rock composition of 3200 kg m^{-3} , for which there is no geological evidence. Therefore, it can safely be concluded that in this region an artifact in the gravity field of EGM2008 could be identified, and that the new model shows significant improvements, clearly demonstrating the impact of GOCE data.

Concerning lithospheric modelling, compared to the former core area, now regions of the Central Andes, which lack of terrestrial data, can be forward modelled with unprecedented accuracy due to the inclusion of GOCE data. Finally, the lithospheric density models have been adapted to reduce the misfit to the newly available gravity field information of

IMOSAGA01C, and consistency between the gravity computed from the adapted density model and IMOSAGA01C down to an rms of 13.7 mGal could be achieved.

In summary, with this study we could evaluate, identify and demonstrate the impact of GOCE for lithospheric density modelling and combined interpretation of complex lithospheric structures. On the one hand, satellite gravity information was used for the validation and cleaning of inhomogeneous gravity databases, making benefit of very homogeneous error characteristics and accuracy of global satellite gravity data. On the other hand, a consistent combination of terrestrial and satellite gravity information results in a considerably improved regional gravity field model with main impact and benefit in areas with terrestrial data gaps, but also concerning the consistency in the long to medium wavelengths, down to 80–100 km.

In the future, by continuing and intensifying the collaboration of geodesy and geophysics the impact of this new gravity field model IMOSAGA01C for constraining lithospheric models will be further evaluated in much more detail. Further studies on the specific stress environment and larger scale investigations of, e. g., the gravitational potential energy (*Gutknecht et al.*, 2014) will shed light on stresses in the lithosphere and dynamic state of the margin, and will contribute to an improved knowledge of processes of the Andean continental plate margin.

4.2 Structure and state of stress of the Chilean subduction zone from terrestrial and satellite–derived gravity and gravity gradient data

- Publisher: Springer Netherlands
- Journal: *Surveys in Geophysics*, Vol. 35 (2014), pp. 1417–1440, DOI: 10.1007/s10712-014-9296-9
- Authors: ^aBenjamin D. Gutknecht, ^aH.J. Götze, ^bT. Jahr, ^bG. Jentzsch, ^{a,c}R. Mahatsente, ^bSt. Zeumann
 - a) Institute of Geosciences, Kiel University, Otto–Hahn–Platz 1, 24118 Kiel, Germany
 - b) Institute of Geosciences Friedrich–Schiller–University of Jena, Burgweg 11, 07749 Jena, Germany
 - c) Department of Geological Sciences, The University of Alabama, Tuscaloosa, AL 35487, USA
- Author’s contribution: B.D. Gutknecht was responsible for the entire publication as corresponding and composing author. Besides the general layout and discussion, all sections but about the geodynamic modelling are entirely or partly attributed to B.D. Gutknecht and he additionally contributed to the dynamic modelling sections with regards to content. Concerning the specific sections, H.-J. Götze mainly contributed to the tectonic setting– and conclusions sections; T. Jahr, G. Jentzsch and S. Zeumann are primarily responsible for the dynamic modelling sections; and R. Mahatsente’s main contribution was with Gravitational Potential Energy and general support in writing the manuscript.

Abstract It is well known that quality of gravity modelling of the Earth’s lithosphere is heavily dependent on the limited number of available terrestrial gravity data. More recently, however, interest has grown within the geoscientific community to utilize the homogeneously measured satellite gravity and gravity gradient data as well as combined models for lithospheric scale modelling. Here, we present an interdisciplinary approach to determine the state of stress and rate of deformation in the Central Andean subduction system. We employed gravity data from terrestrial, satellite–based and combined sources, using multiple methods to constrain stress, strain and Gravitational Potential Energy (GPE). Well–constrained 3D density models, which were partly optimized using the combined regional gravity model IMOSAGA01C (*Hosse et al.*, 2014), were used as bases for the computation of stress anomalies on the top of the subducting oceanic Nazca plate and GPE relative to the base of the lithosphere. The geometries and physical parameters of the 3D density models were used for the computation of stresses and uplift rates in the dynamic modelling. The

stress distributions, as derived from the static and dynamic modelling, reveal distinct positive anomalies of up to 80 MPa along the coastal Jurassic batholith belt. The anomalies correlate well with major seismicity in the shallow parts of the subduction system. Moreover, the pattern of stress distributions in the Andean convergent zone varies both along the North–South and West–East directions, suggesting that the continental fore–arc is highly segmented. Estimates of GPE show that the high Central Andes might be in a state of horizontal deviatoric tension. Models of gravity gradients from the GOCE satellite mission were used to compute Bouguer–like gradient anomalies at 8 km above sea level. The analysis suggests that data from GOCE add significant value to the interpretation of lithospheric structures, given that appropriate topographic correction is applied.

Keywords Density Modelling —Finite Element Method —GOCE —Gravity Gradients —Gravitational Potential Energy —State of Stress —Subduction

4.2.1 Introduction and motivation

A number of large earthquakes ($M_W > 7$) have occurred in the North–Chilean subduction zone within the past 25 years (Figure 1). On 1st April 2014 a magnitude 8.2 event started at $\sim 19.6^\circ\text{S}$ about 60 km offshore Pisagua. This was followed by a magnitude 7.7 aftershock on 3rd April 2014 at $\sim 20.6^\circ\text{S}$ about 50 km southwest of Iquique. Prior to that, no major hazardous seismicity at the shallower parts of the slab (0–60 km depth) had been observed along the >500 km long seismic gap between 19°S and 24°S since a $M > 8.5$ rupture in 1877 (e.g., *Schurr et al.*, 2012). Amongst others, *Metois et al.* (2013) gave a consolidated summary of the tectonic situation in the North Chile segment and identified along–strike variations in the average interseismic coupling on the slab interface from GPS velocity inversion. They found that a future rupture towards Iquique from the south could account for a $\sim M_W = 8.2$ earthquake, and a much larger event would be possible if the whole segment towards the north broke. It seems that the recent event did not relieve all stress that had built up in the region (*Witze*, 2014).

Plenty of hypotheses exist as to what could be the mechanism of asperity generation. *Tichelaar and Ruff* (1991) gave an overview of possible mechanisms that partly control coupling along the trench, i.e. oceanic plate temperature due to plate convergence rate and age; geothermal gradient; thickness of the continental crust; sediment fill in trench; depth of mineral phase change within oceanic plate. *Lamb and Davis* (2003) even argued that the high topography of the Andes is partly supported by high shear–stresses along the subducting Nazca plate that are focused by climate–induced control of erosion rates along the trench (absence of notable sediment fill leads to higher shear stresses). Some authors (*Song and Simons*, 2003; *Wells et al.*, 2003) found a positive relation between negative trench–parallel gravity anomalies and largest coseismic slip (or moment release) for large earthquakes. They

suggested that offshore basins, with gravity lows due to interseismic subsidence by basal erosion, could act as a proxy for the long-term state of stress on the plate interface.

Recent studies by *Sobiesiak et al. (2007)* and *Tassara (2010)* drew the attention to the composition of the overlaying crust: By correlating seismic moment release and isostatic residual anomalies, *Sobiesiak et al. (2007)* suggest that pressure exerted by batholithic structures and buoyancy forces acting on the Nazca plate could significantly influence asperity generation. Moreover, by calculating vertical stress anomalies from 3D density models, *Tassara (2010)* found that the density structure of the heterogeneous fore-arc crust possibly exerts control on magnitude and distribution of shear strength along the trench thrust fault.

In this paper, the state of stress in the upper plate of the subduction zone is investigated and its relation to magnitude of earthquake distributions assessed. One general idea behind the approach applied in this work is to use gravity data during density forward modelling and develop 3D density models with well-constrained geometry and density distribution. We present how such density models can be used to gain insight into the stress regime of the Central Andean subduction system in multiple ways. As will be shown, the calculation of lithostatic stresses on top of the subducting Nazca plate along the active Chilean margin is feasible and leads to evidence that seismic intensity correlates with stress anomalies along the trench. Similar to the work of *Tassara (2010)*, we found that the static stress anomalies are caused by high-density lithospheric bodies above the subducting Nazca plate.

While this static method gives insight into a possible correlation of hazardous seismicity along the Peru–Chile trench with an anomalous density distribution in the fore-arc region, the dynamic models presented in this study provide additional value in terms of uplift and strain rates. It was one of the main goals of the IMOSAGA project, to use the static 3D model geometry and parameter configuration of a gravity forward model as input to the dynamic modelling of a subduction zone using Finite Element Method (FEM) (orange box in Figure 4.12a). Thus, by adding the time domain, we obtained dynamic derivatives of the stress tensor from the same initial gravity-based model that was used for static analysis of the subsurface.

4.2.2 Tectonic setting

The study area encompasses the Peru–Chile trench and the Central Andes between 15–38°S and 65–77°W (Figure 4.12). The region is an active continental margin where the oceanic Nazca plate subducts beneath the South American continental plate by $\sim 5\text{--}6\text{ cm a}^{-1}$ (*Silver et al., 1998; Somoza, 1998; Metois et al., 2013*). The main focus of this study is the northern part of the margin (16–25°S) near the cities of Iquique and Antofagasta (Figure 4.12). Here, the Central Andes can be roughly separated into five approximately N–S–striking morpho-structural units: The Coastal Cordillera (CC), which is oriented parallel to the trench, builds

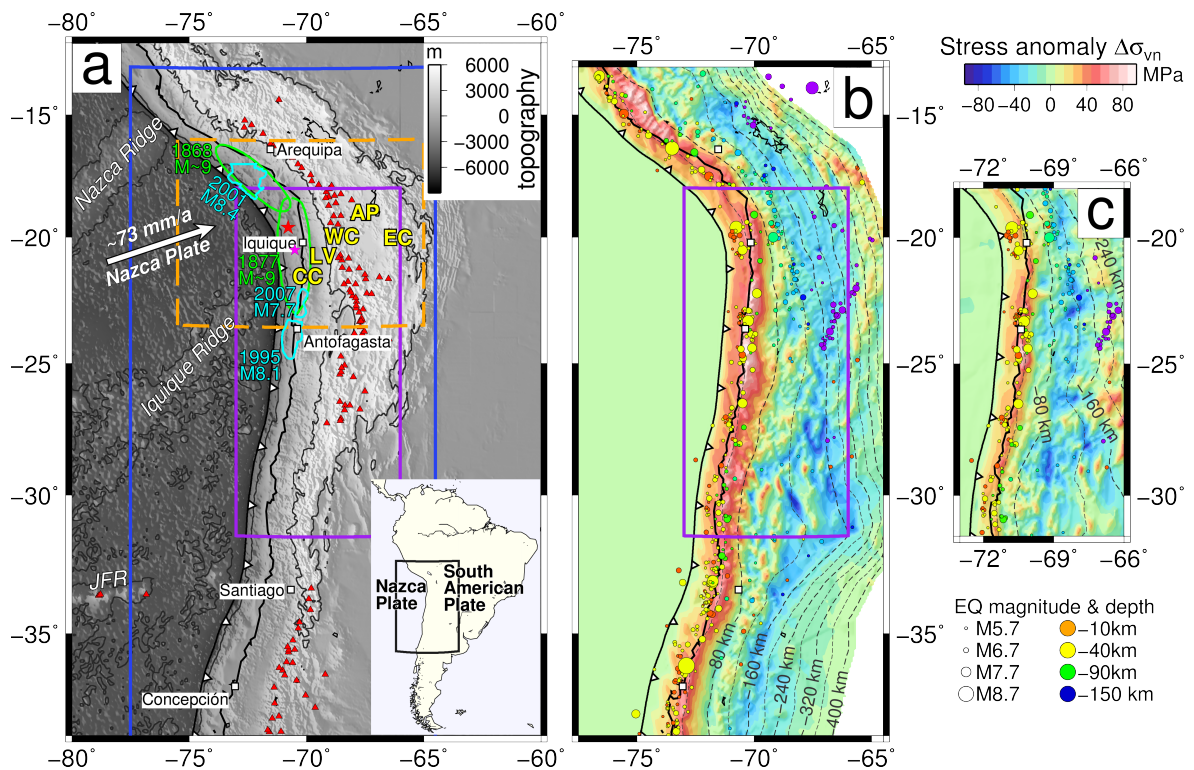


Figure 4.12: Tectonic setting and stress anomalies of the Central Andes. **a** Tectonic overview; the dark blue box denotes the study area for static stress estimates and GPE derived from the density model of Tassara et al. (2006); the purple box represents the study area from the optimized model based on Prezzi et al. (2009) and the IMOSAGA01C combined gravity model (Hosse et al., 2014); the dashed orange box approximates the area of the dynamic finite element modelling. Morpho-structural units: JFR —Juan Fernández Ridge; CC —Coastal Cordillera; LV —Longitudinal Valley; WC —Western Cordillera; AP —Altiplano; EC —Eastern Cordillera. Jagged black line represents the trench location; -4000 m and +3000 m contour lines in dark grey emphasize the offshore ridges and high topography of the Central Andes. Green ellipses approximate slip extend of historical earthquakes and light blue coloured polylines represent slip extend of recent larger earthquakes in North Chile (Pritchard et al., 2007; Schurr et al., 2012); a proposed seismic gap existed between the 2001 and 2007 patches, stretching from $\sim 19^\circ\text{S}$ towards Mejillones peninsula just north of Antofagasta; red triangles: volcanoes. Hypocentres of the M8.2 and M7.7 shocks from 1st–3rd April 2014 are marked by a red and pink star, respectively. **b** Normal component of the vertical stress anomaly on top of the subducting slab of the Nazca plate, derived from the model presented by Tassara et al. (2006). **c** Normal component of the vertical stress anomaly on top of the subducting Nazca plate, derived from the optimized model based on Prezzi et al. (2009). Epicentre locations from the NEIC/PDE catalogue ($M \geq 5.7$ since 1978) are given as colour coded circles in b and c; contour lines show the slab depth from the density models, respectively.

the westernmost range of the Central Andes. The extinct volcanic arcs of the Jurassic are major features of the CC and the fore-arc region (*Pichowiak, 1994*). Due to the positive residual gravity field here, it is assumed that the batholiths of the CC are composed of high rock densities (e.g. *Haschke et al., 2002*). They considered the evolution of La/Yb ratio in granitoid rocks through time, which is a good proxy for the density of the complementary residuum: the higher the La/Yb in the granitoid, the more dense the residuum that is stored in the lower crust. These high masses presumably partly control the locking mechanism of the subduction interface (*Husen, 1999; Sobiesiak et al., 2007*). To the East, the Longitudinal Valley (LV) separates the CC from the Western Cordillera (WC). The WC is characterized by recent volcanism and high topography. Farther to the east is the Altiplano plateau (AP) with an average elevation of more than 3600 m and the Eastern Cordillera (EC), respectively. The high topography of the Andes is partially compensated by crustal roots. This is evidenced by a pronounced negative Bouguer anomaly of several hundred mGal ($1 \text{ mGal} = 10^{-5} \text{ m s}^{-2}$) along the Central Andes (e.g., *Götze et al., 1994*).

4.2.3 Database and constraints

Availability and homogeneity of terrestrial gravity data is variable along the Peruvian and Chilean margin. The quality of high-resolution gravity models such as the EGM2008 (*Pavlis et al., 2012*) suffers significantly from varying quality and irregular distribution of terrestrial data (*Köther et al., 2012*). A general lack of accurate and evenly distributed gravity information from the offshore and close to the coast adds demand for applicable data to study composition and dynamics of the margin. The European Space Agency's gravity field mission GOCE (Gravity Field and Steady-State Ocean Circulation Explorer; *Drinkwater et al., 2003*), in contrast, provides near-globally and uniformly distributed gravity gradient data from an altitude of about 250 km above the geoid. It adds improvement of gravity field information in the medium wavelength range between ~75 and 200 km spatial resolution and has its largest contribution over regions where only sparse or low-quality terrestrial and airborne gravity data are available (*Novák and Tenzer, 2013*). The first regional high-resolution combined gravity model for the Central Andes based on GOCE and terrestrial gravity data, IMOSAGA01C, has recently been published by *Hosse et al. (2014)*. Here, it served as a new gravity database in order to optimize the 3D density model of *Prezzi et al. (2009)*.

The vertical gravity gradients, discussed in sections 4.2.5.2 and 4.2.6.3, are from the GOCO03s model (*Mayer-Gürr et al., 2012*). The model includes data from the GOCE, GRACE, SLR and CHAMP missions at various degree and time span (GOCE gradiometry: November 2009 to April 2011). The Rock-Water-Ice (RWI) model (*Grombein et al., 2011, 2014a,b*) has been used for topographic correction of vertical gravity gradients. Figure 4.13 gives an overview of the relevant gravity models and data paths of this study.

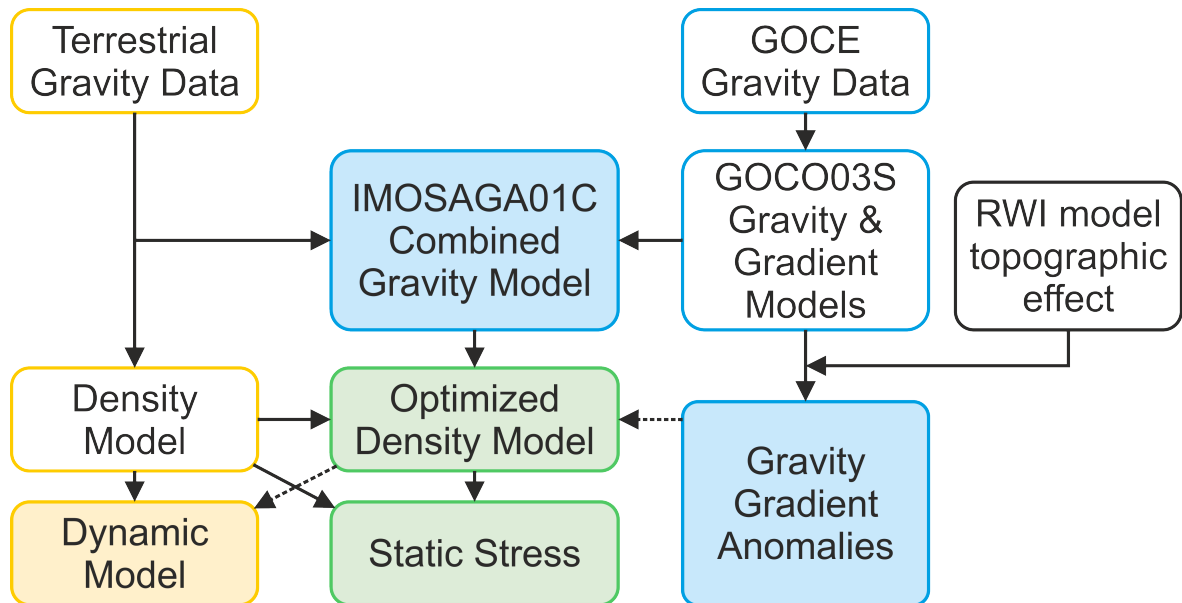


Figure 4.13: Data flow chart describing types of gravity data and models used within this study. Dashed arrows represent optional paths that can be approached in further studies. Yellow colours stand for models that are based on terrestrial gravity data, blue colours represent the integration of gravity data from the GOCE mission and green colours emphasize models and results that incorporate data from terrestrial and GOCE satellite data. Filled boxes represent work that has been accomplished during the IMOSAGA project. The combined gravity model IMOSAGA01C is described in detail in *Hosse et al. (2014)*.

The stress analysis presented here is based on well-constrained 3D density models and includes topographic load. The topographic data are from ETOPO1 global relief model and have a 0.1 degree spatial resolution (*Amante and Eakins, 2009*). The stresses have been analysed in conjunction with seismicity, using data of the PDE/NEIC earthquake catalogue from the USGS (<http://earthquake.usgs.gov/earthquakes/search/>) stretching from September 1978 to May 2014. Seismic events from the recent magnitude 8.2 shock offshore Pisagua and Iquique are included in this database but are no constraint in the density modelling. We used hypocentres from earthquakes of at least magnitude 5.7 for graphical correlation with static stress anomalies.

4.2.4 Density models

The 3D density model of *Tassara et al. (2006)* forms the base for the static stress analysis and dynamic modelling (blue and orange boxes in Figure 4.12a, respectively). The model covers the South American continental margin between $\sim 10\text{--}40^\circ\text{S}$ and $60\text{--}85^\circ\text{W}$ and consists of 43 parallel vertical sections of roughly 1 degree apart. The density model is based on gravity data from satellite altimetry (KMS01; *Andersen and Knudsen, 1998*) for the offshore and terrestrial data compiled under the German Collaborative Research Centre SFB267 (*Götze et al., 1990; Götze and Kirchner, 1997*) for the onshore. The internal geometries of this model are rather simple and provide a first-order approximation of variations at the scale of

the entire Andean margin.

The second density model that was used for the computation of static stresses originates from a model presented by *Prezzi et al.* (2009). Their model is based on the same gravity data as in *Tassara et al.* (2006). In contrast, however, the density model from 2009 has been modelled in great geological detail with more constraining data (*Prezzi et al.*, 2009). This has the advantage that distinct stress anomalies can be explained by specific density distributions and geological units or can be traced back to artefacts inherent in the model itself. The original model roughly extends from 20–29°S and 61–74°W and is made of 31 parallel vertical sections striking the East–West direction. For the static stress analysis, we applied the new combined regional gravity model IMOSAGA01C (*Hosse et al.*, 2014) to the density model and concentrated on a region between 18–31.5°S and 66–73°W (purple box in Figure 4.12a and b). The new study area has less longitudinal extent because of the limited dimension of the combined gravity field, but stretches further south and north into parts of the continental margin that previously showed a major lack of available data. After minor adjustments to the depth of interfaces in the model and after additional density inversions in the order of the tolerable variation given by *Prezzi et al.* (2009), the standard deviation of the residual anomalies could be reduced from $16 \times 10^{-5} \text{ m/s}^2$ to $6.3 \times 10^{-5} \text{ m/s}^2$. The geometry and density information of the optimized density model then served as input for the second static stress field (Figure 4.12c). Figure 4.13 summarizes the approach.

4.2.5 Methodology

We used two independent approaches to derive different components of the stress tensor at the subduction interface. The static stress components (vertical and normal to the slab) were calculated using geometry and density distributions from the gravity forward model of *Tassara et al.* (2006) and from an optimized density model that is based on the work of *Prezzi et al.* (2009). The geometry and density information of Tassara’s model has further been used as input for the dynamic modelling and GPE estimation. To test satellite gravity gradients for their use in lithospheric studies, gravity models of satellite data and topography were used and Bouguer–like gravity gradient anomalies were derived.

4.2.5.1 Static Stress and GPE

The lithostatic load on the subducting Nazca plate interface was calculated using the gravity and magnetic modelling software package IGMAS+ (*Schmidt et al.*, 2010). The software utilizes the 3D density information from forward models to compute lithostatic load at constant depth or on top of interfaces of synthetic representations of morphostructural units. The method is partly based on ideas presented by *Tassara* (2010). It accounts for the direct vertical load of an overlaying rock column and excludes any flexural compensation.

In contrast to the previous work of *Tassara* (2010), the present stress computation includes the effect of topographic masses. In addition, we estimated the static stress normal to an interface, since the angle of subduction is one of the controlling parameters on shear stress at the subduction interface (*Dahlen*, 1984; *Tichelaar and Ruff*, 1991).

The lithostatic pressure, or vertical stress, σ_v due to the weight of an overlying rock column at depth z is given by

$$\sigma_v = \int_h^z \gamma \rho(z) dz \quad (4.9)$$

where h is surface elevation, γ is normal gravitational acceleration and $\rho(z)$ is bulk density at depth z taken from the 3D density models. The latitude-dependent normal gravitational acceleration was considered as a constant mean value of 9.79 ms^{-2} . This assumption causes less than $\pm 1\%$ bias to the absolute load at the northern- and southernmost bounds of the models.

The stress anomalies at the interfaces were calculated using a homogeneously layered density distribution of a lithospheric column as a reference for computation. Each horizontal reference layer has a constant density and different vertical extent, representing the average continental crust and upper mantle. The reference layers used here are identical to the reference densities applied by *Tassara et al.* (2006) and *Prezzi et al.* (2009) for their density modelling, respectively (Figure 4.14). The normal component of the vertical stress anomaly was calculated from the density contrast between the model and reference densities at the same location as follows:

$$\Delta\sigma_{vn} = \gamma \cdot \cos^2 \alpha \cdot (\rho_{topo} h_{topo} + (\rho_1 h_1 + \rho_2 h_2 + \dots) - (\rho_{r1} h_{r1} + \rho_{r2} h_{r2} + \dots)) \quad (4.10)$$

where ρ_{topo} and h_{topo} are density and elevation of topographic masses above the geoid, respectively. $\rho_{1,2,\dots}$ and $h_{1,2,\dots}$ are density and vertical extent of the model units (also called bodies) and $\rho_{r1,2,\dots}$ and $h_{r1,2,\dots}$ are density and thickness of the reference layers, respectively. The vertical vector is rotated by α to the subduction interface normal. Figure 4.14 gives a schematic overview of the component vectors involved. The resulting anomalies may be interpreted as the amount of vertical loading from the overlying rock column by which normal stresses at the plate interface are different from stresses caused by a rock column with reference density distribution.

The state of stress within a plate depends on the balance of the intra-plate and far field forces. In the presence of high topography, gravitational stress fields generated by lateral variations in lithospheric structure and thickness could be as significant as those associated with far field forces (*Coblentz et al.*, 1994; *Jones et al.*, 1996; *Ghosh et al.*, 2006; *Pascal*

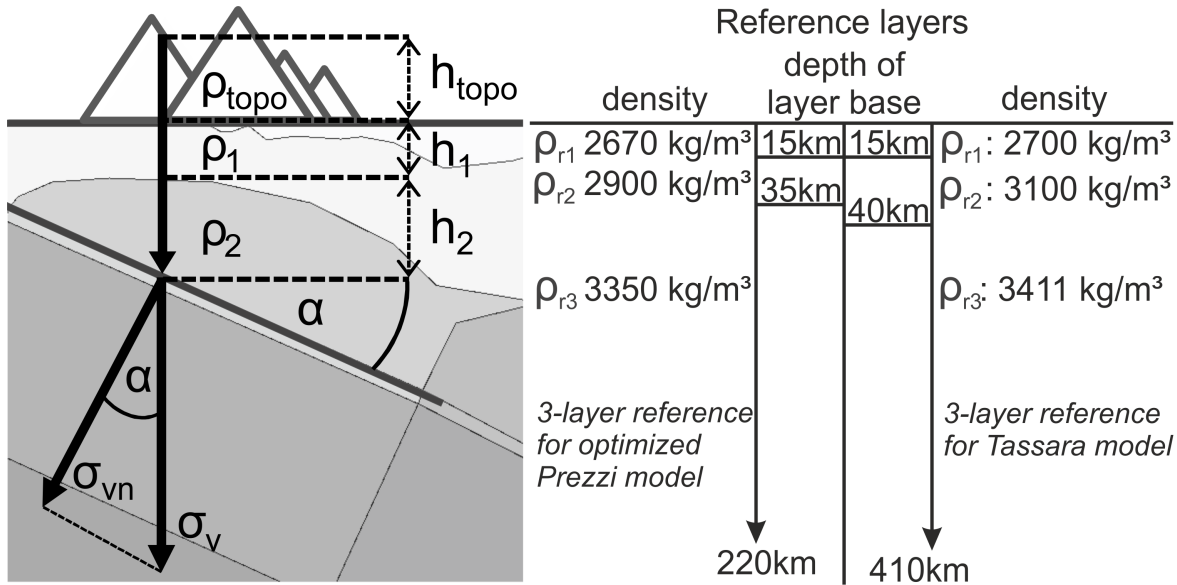


Figure 4.14: Schematic representation of the computation of stress components on a subduction interface. The normal component σ_{vn} of the lithostatic load σ_v is derived from the density distribution of a 3D gravity forward model (grey shaded polygons), rotated to the normal of the subduction interface. When calculated against a layered standard background density distribution (the two reference layers on the right, respectively), the resulting stresses $\Delta\sigma_{vn}$ represent stress anomalies on the subducting plate due to density distribution and geometry of the overlying rock column. In this study, no horizontal stress is superposed.

and Cloetingh, 2009). We used the 3D gravity model of Tassara *et al.* (2006) to estimate the distributions of Gravitational Potential Energy (GPE) in the central Andes between 14°S and 38°S. The GPE per unit area of a column of material above a given depth L is given by

$$GPE = \int_{-h}^L \rho(z)\gamma L dz - \int_{-h}^L \rho(z)\gamma z dz \quad (4.11)$$

where $\rho(z)$ is depth-dependent bulk density taken from the 3D density models; γ is normal gravitational acceleration; L is the depth of compensation and h is elevation (Jones *et al.*, 1996).

The GPE estimates have been made using the base of the mantle lithosphere (125 km) as a reference level for the computation. The method of GPE estimation assumes that the lithosphere is in isostatic balance. However, the Andean crust, as inferred from gravity study, is not fully compensated (Götze *et al.*, 1991). If partially compensated, the contribution of the high-density mantle to the overall magnitude of GPE could increase slightly, but the overall pattern of the GPE related stresses remain the same (Flesch and Kreemer, 2010).

The absolute GPE alone cannot be used to assess the state of stress in the lithosphere. Thus, the state of stress (extensional, neutral or compressional) needs to be assessed either by using integrated horizontal deviatoric stresses as derived from GPE (Ghosh *et al.*, 2006; Flesch and Kreemer, 2010) or from the difference between the absolute GPE and Tectonic Reference State (TRF) of the Earth (Coblentz *et al.*, 1994). We used the mean potential en-

ergy of the lithosphere ($2.379 \times 10^{14} \text{ N m}^{-1}$) as a reference state to predict GPE variations along the Andes. The reference state is equivalent to the potential of the continental lithosphere and cooling oceanic plate at sea level and at a depth of 4.3 km, respectively (Coblentz *et al.*, 1994).

4.2.5.2 Application of satellite gravity gradients to lithospheric structures

Since the launch of the GOCE satellite mission, global gravity and gravity gradient field solutions are being provided to the public (Mayer-Gürr *et al.*, 2012; Förste *et al.*, 2012). Several authors have claimed that, despite the high altitude of the measurement systems, gravity gradients from satellite-only models could provide valuable information for geophysical interpretation of the Earth's lithosphere (Braitenberg *et al.*, 2011; Gutknecht, 2011; Köther *et al.*, 2012). We therefore evaluate the topographically corrected vertical gravity gradient of the GOCO03s model (Mayer-Gürr *et al.*, 2012) for the purpose of lithospheric studies between 10–40°S and 60–80°W.

In order to correct the gradient data for the effect of topographic masses, we subtract the vertical gravity gradient of the Rock–Water–Ice (RWI) model (Grombein *et al.*, 2011, 2014a,b) calculated at 8 km altitude from the GOCO03s vertical gravity gradient at the same altitude. We chose this specific trade-off level in order to stay above topographic masses at all stations and in order to be preferably close to the geoid at the same time. Thus, signal-related undulations in the model may be recognized that would otherwise become indistinct at greater altitude due to the inverse distance cubed performance of gravity gradients. Both gradient models in this study have a resolution of d/o 250 which corresponds to ~75 km latitudinal half-wavelength of the spherical harmonics in the study area. The full RWI model has 5' resolution.

4.2.5.3 Dynamic modelling

Complementary to the static stresses analysis, the dynamic behaviour of the subduction system is of particular interest. Therefore, 3D dynamic models for the Central Andes were constructed using the Finite Element Method (FEM; e.g. Zienkiewicz *et al.*, 2005) and the commercial software Abaqus. The models were solved with the full Newton solution technique. The dynamic processes were modelled by solving the equations of conservation of mass (Equation 4.12) and momentum (Equation 4.13) simultaneously.

$$\frac{D\rho}{Dt} + \rho \frac{\partial v_i}{\partial x_i} = 0 \quad (4.12)$$

$$\frac{Dv_i}{Dt} = \frac{\partial \sigma_{ij}}{\partial x_j} + g_i \quad (4.13)$$

where ρ is the density, t is time, v_i are the velocities, x_i are the coordinates, σ_{ij} is the stress tensor, g_i is the gravity vector and $\frac{D}{Dt}$ is the total derivative expression defined as:

$$\frac{D}{Dt} = \frac{\partial}{\partial t} + v_j \frac{\partial}{\partial x_j}. \quad (4.14)$$

The simulation time is 100,000 years. Although it is well-known that thermal and mechanical model parameters are temperature dependent, our dynamic modelling is restricted to temperature independent analysis. The shortness of the time scale does not demand to consider temperature changes in the process. It is sufficient to consider temperature explicitly in the respective physical parameters.

The model is not truly dynamic because of the short simulation time and the given velocity boundaries. Such models are sometimes referred to as instantaneous models. However, we want to reveal the difference between static density models, which show the present situation only, and finite element models, which include a time evolution. Therefore, we call this modelling dynamic in contrast to the static density models.

Existing 2D and 3D finite element models of the Central Andes have mostly generic geometries (e.g. *Liu et al.*, 2002; *Sobolev and Babeyko*, 2005; *Babeyko and Sobolev*, 2008). However, it was shown by several authors that curved trench geometry influences the stress and strain patterns in the continental crust (e.g. *Bonnardot et al.*, 2008; *Boutelier and Oncken*, 2010; *Zeumann et al.*, 2014). For the Central Andes, the consideration of ocean-ward concave trench is crucial. One of the objectives of this study was, therefore, to develop dynamic models of the Central Andes region using realistic geometries. The geometries of the 3D density model of the Central Andes (*Tassara et al.*, 2006) have been used for the dynamic modelling. For the first time we transferred the structure of a well-constrained density model into dynamic models. The static density model shows the present situation. Thus, the starting time of the dynamic models is the present time. A time period of 100,000 years is short compared to the time span of subduction and orogenesis. Therefore, the modelled results can be considered as recent and compared to recent observations.

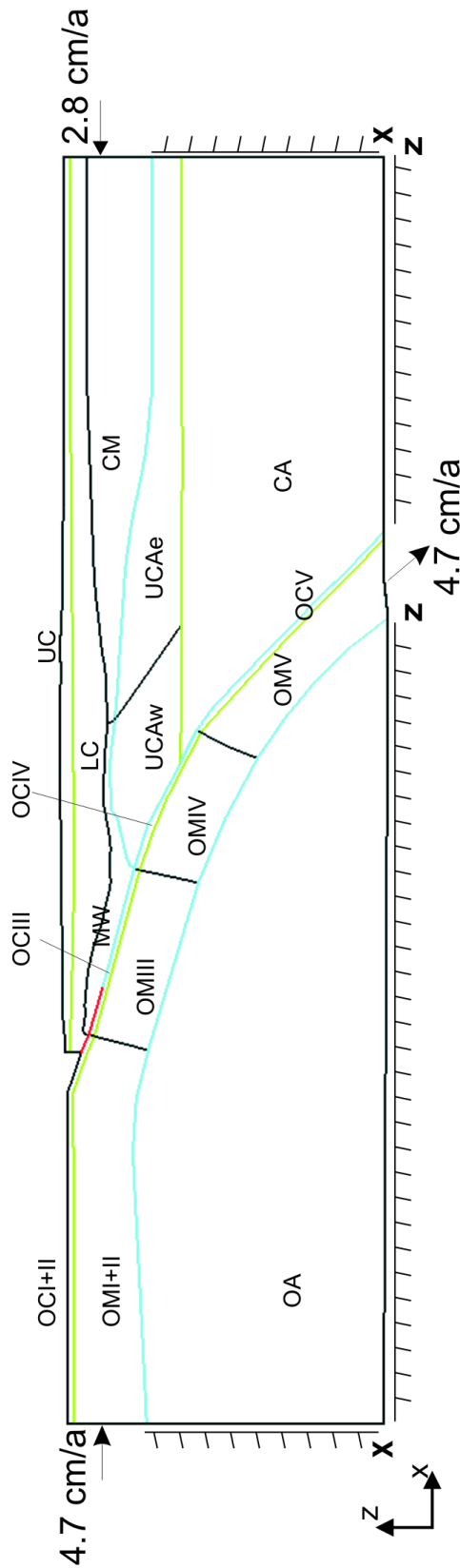


Figure 4.15: Cross section showing the different parts of the model at 22.5°S , contact interactions and applied velocity boundaries: Green lines specify tied surfaces, blue lines denote contact interactions with free sliding, and the red line highlights the frictional coupling zone with 0.3 as friction coefficient. Arrows indicate the velocity boundary conditions. At boundaries where no velocities are applied, the bottom is fixed in z -direction and the side walls are fixed in x -direction, indicated by the fences at the boundaries, respectively. Side walls not shown in the 2D section are fixed in y -direction. Black lines denote unit boundaries; see Table 1 for abbreviations and material property values.

Table 4.4: Rheological parameters for the different units of the model: Densities taken from *Tassara et al. (2006)* and Young's moduli calculated from densities and seismic velocities of the ANCORP profile. Poisson ratio for all units is 0.25.

Units of the model	density /kg m ⁻³	Young's modulus /GPa	viscosity /Pa s
Upper crust (UC)	2700	78	
Lower crust (LC)	3100	103	
Continental lithospheric mantle west (MW)	3230	110	
Continental lithospheric mantle east (CM)	3320	136	
Upper continental asthenosphere west (UCAw)	3320	164	10 ¹⁹
Upper continental asthenosphere east (UCAe)	3350	183	10 ¹⁹
Continental asthenosphere (CA)	3430	207	10 ²¹
Oceanic crust (OCI+II)	3050	98	
Oceanic crust (OCIII)	3200	113	
Oceanic crust (OCIV)	3300	116	
Oceanic crust (OCV)	3550	125	
Oceanic lithospheric mantle (OMI+II)	3350	183	
Oceanic lithospheric mantle (OMIII)	3370	184	
Oceanic lithospheric mantle (OMIV)	3400	186	
Oceanic lithospheric mantle (OMV)	3500	191	
Oceanic asthenosphere (OA)	3411	205	10 ²¹

For the dynamic modelling, the region of the Central Andes between 17–23.5°S and 60–75.5°W was chosen (orange box in Figure 4.12a). All models are 1630 km × 725 km wide and 410 km deep. As in the density model, the dynamic model is divided into 16 parts with different parameters (Figure 4.15; Table 4.4). For all units a Poisson ratio of 0.25 was used. The Young's moduli were calculated from the densities and the seismic velocities of the ANCORP profile (ANCORP Working Group, 2003; Oncken *et al.*, 2003). The ANCORP profile is a 400 km long seismic wide-angle reflection profile crossing the Central Andes at 21°S.

Frictional coupling between the two plates is important for the modelling. *Tichelaar and Ruff* (1991) estimated the down-dip from large underthrusting earthquakes and conclude that coupling extends at least as deep as 48 km. *Béjar-Pizarro et al.* (2013) investigated INSAR and GPS data and suggest a high coupling zone for the shallow part (<30 km) and a partially coupled zone (30–50 km) depth. Our dynamic model includes frictional coupling at depths between 20 and 50 km depth (red line in Figure 4.15). For this zone, a friction coefficient of 0.3 was used. Below the above mentioned zone and between lithosphere and asthenosphere free sliding was applied (blue lines in Figure 4.15).

The main driving forces for plate motion are the ridge push and the slab pull. The relative importance of these forces is still a matter of debate (e.g. *Wessel and Müller, 2007; Mahatsente et al., 2012*). Generally, the ridge-push is thought to be about one order of magnitude less than the slab-pull (e.g. *Forsyth and Uyeda, 1975; Lithgow-Bertelloni and Richards, 1998; Mahatsente et al., 2012*). The present model includes the west-ward motion of the South American plate. The trench-ward motion of the continental plate plays a key role for the development of mountain belts at convergent plate margins such as the Andes (*Hampel and Pfiffner, 2006; Babeyko and Sobolev, 2008*).

In the models, we used velocity boundary conditions (Figure 4.15). The South American plate moves west-ward with a velocity of 2.8 cm/a, which was estimated by *Silver et al.* (1998) using fracture zone orientations, sea-floor magnetic anomalies and the motion of Africa with respect to Atlantic basin hot spots. *Somoza* (1998) reconstructed relative plate motion of the Nazca plate from several existing models with respect to a fixed South America. For the models a convergence velocity of 5 cm/a has been used. In order to consider the obliquity of the convergence by 20°, the velocity of the Nazca plate (5 cm/a) has been split in an east component of 4.7 cm/a applied at the west edge of the slab and a north component of 1.7 cm/a. For the slab pull the same value as for the east component of the ridge push (4.7 cm/a) was taken. This is applied at the bottom of the slab with an angle of 30°, which is the subduction angle of the models.

The models contain over 1.3 million elements with tetrahedron shape. The mesh size is about 1 km in the crust and up to 100 km in the asthenosphere. The model time is 100,000 years. For the first 20,000 years, the models show a running in behaviour due to gravitational

force. However, the simulation time of 100,000 years over comes this running in behaviour and the model reaches steady-state.

4.2.6 Results and discussion

In this section, we consecutively present the results of the computations described in section 4.2.5. Section 4.2.6.1 deals with the estimates of static stress anomalies and GPE, while section 4.2.6.2 is about the results from the finite-element dynamic modelling. Section 4.2.6.3 gives a brief overview of the outcome of the reduction of satellite gravity gradients towards 'Bouguer-like' gravity gradient anomalies.

4.2.6.1 Static stress and GPE anomalies

The normal component of the vertical stress anomaly on the subduction interface shows a very similar general pattern for both underlying density models (Figures 4.12b and c). The most prominent feature in the fore-arc region is a chain of trench-parallel stress maxima of the order of 20–90 MPa. These are largely centred just east of the shoreline and correspond to a slab depth of ~10–45 km. They can be mainly attributed to the area of the Coastal Cordillera and former Jurassic arc. From south of Iquique, towards the Peruvian coast, the chain of positive stress anomalies follows a slightly increased westward trend towards the offshore and thus stays close to the 35 km depth contour for the advanced Prezzi model (Figure 4.12c).

This part of the active margin is of particular interest since it has not experienced any major rupture in the past ~135 years but was only sparsely covered with gravity station data for the density model built. The peaks of the stress maxima generally correlate well with seismicity east of the trench (magnitude > 5.7). *Tassara* (2010) presented a similar distribution of vertical stress anomalies and found correlation between earthquake epicentre locations and stress maxima. His estimate of stress, however, does not take into account the effects of topographic masses and slab dip angle.

The density model from *Prezzi et al.* (2009) includes more complex structures and provides a more detailed view on the anomalous stress distributions on the slab. The stress anomalies from the optimized model still show the same general pattern and they are located parallel to the coast with equivalent or slightly decreased stress magnitudes.

Figure 4.16 shows histograms of latitudinal bins of the stress anomaly shown in Figure 4.12c for slab depths between 9 and 120 km. The histograms reveal that the stress anomaly varies from North to South significantly and give evidence of segmentation of the continental fore-arc in the North–South and West–East directions. The shape of the histograms varies from a rather uni-modal distribution of slightly increased stress anomalies (19–21°S) to bi-modal (21–25°S), and then to a tri-modal distribution at 25–27°S that turns into a uni-modal

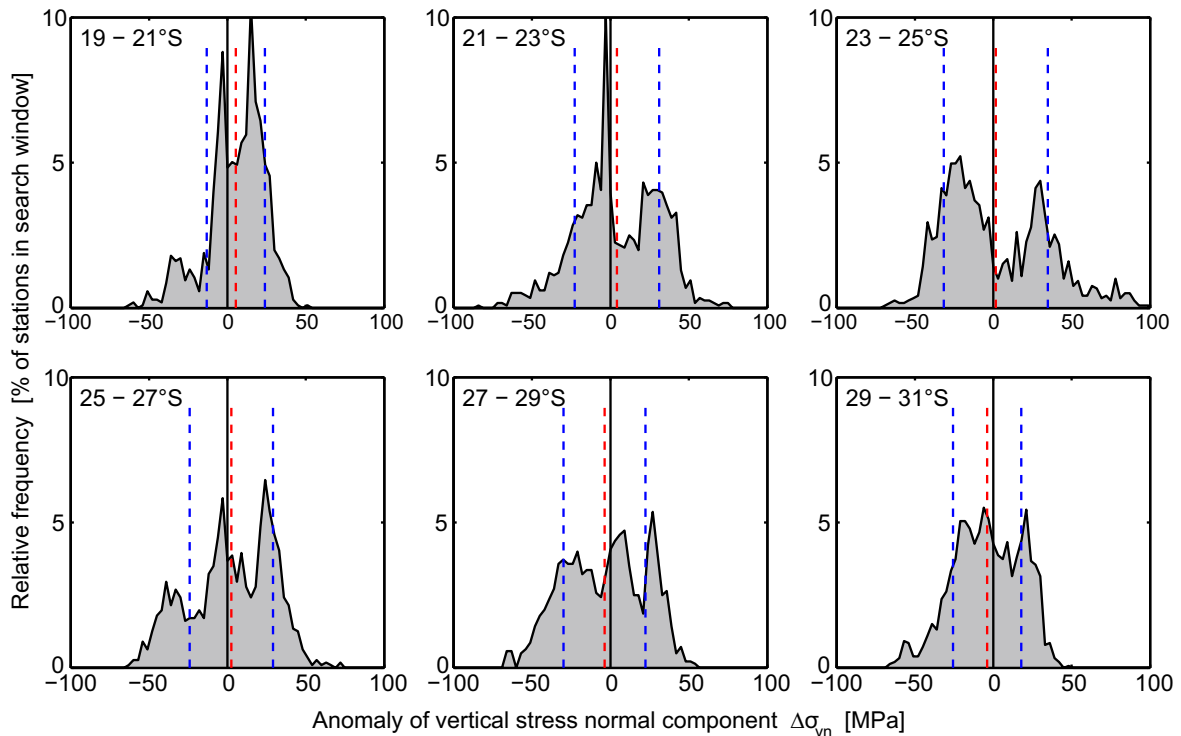


Figure 4.16: Normalized histograms of a moving–strip analysis on the stress anomaly shown in Figure 1c for slab depths between -9 and -120 km. The dashed red line is the mean value of the latitudinal sub–set and the dashed blue lines represent the standard deviation, respectively.

distribution at $\sim 30^\circ\text{S}$ again.

In the northern window between 19°S and 21°S , most of the anomalies are distributed around 0–35 MPa. Physically, this means that the subducting plate in the northern segment is exposed to slightly increased load from the overburden that does not produce much load deficit. At the Antofagasta segment ($23\text{--}25^\circ\text{S}$), however, a nearly symmetric bi–modal distribution and some additional values in the high 50–90 MPa range can be observed. The bi–modal distribution means that there might exist a prompt change of the load on the interface within a relatively short distance. Tri–modal distributions of the anomalies can be interpreted to the effect that large parts of the investigated area are in good balance but also some patches of negative and positive stress anomalies exist.

One noticeable characteristic of the anomaly between 19.5°S and 20.5°S near Iquique is that there are two distinct maxima parallel to the coast with their maxima approximately 50–80 km apart. Here, the E–W extent of the positive anomaly is considerably larger than at the profiles to the south but the amplitude is considerably smaller. It is open to discussion whether this difference could mean an increased risk for the generation of asperities due to a larger area of increased coupling or mean lower risk because of the smaller anomaly amplitudes that could support more frequent, but only medium–sized seismicity.

Figure 4.17 shows the stress anomalies plotted on top of vertical sections of the mean slab geometry and topography at six strips of adjoining latitudes between 19°S and 31°S . A

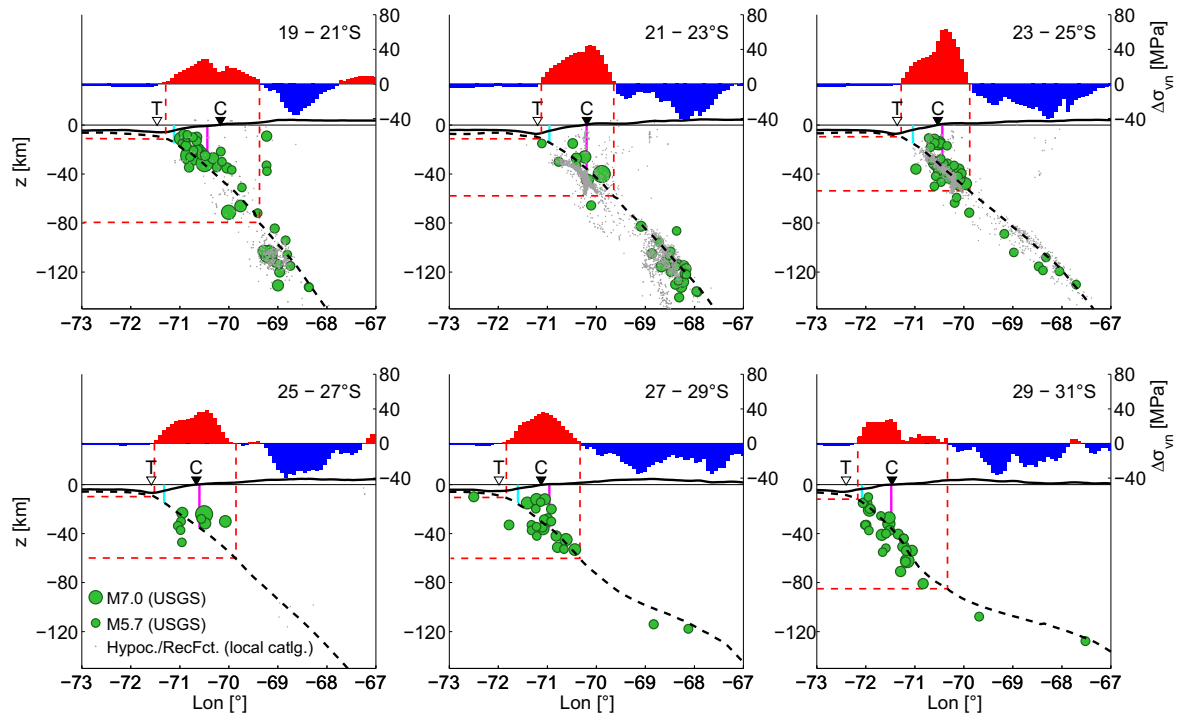


Figure 4.17: Vertical cross sections of stress anomalies, slab geometry and major seismicity. The red/blue 'wiggly' diagram on the top axis shows mean values of the normal component of the vertical stress anomaly on the subducted Nazca plate from the optimized density model based on *Prezzi et al.* (2009) and the IMOSAGA01C combined gravity model. Dashed and solid black curves depict the mean geometry of the subducted slab and bathymetry/topography, respectively. Triangles marked *T* and *C* depict the mean trench and coastline locations at the given latitudinal window, respectively. Light blue and magenta coloured vertical lines indicate the projection of depths where the top of the subducted slab crosses the density contrast of the reference density background at -15 and -35 km. Red dashed lines mark the width– and depth projection of the positive anomaly. Green circles represent major seismicity ($M > 5.7$ from USGS, Sep 1978 – May 2014); grey dots depict constraining data from local seismological studies (Eggert, pers. comm.; *Husen et al.*, 1999; *Schurr et al.*, 2006, 2012; *Sobiesiak*, 2000).

pronounced positive peak of the anomalies on the subducted Nazca–Plate is visible between the trench and a depth of ~60 km. Its projected width (in E–W) at sea–level is 150 to 200 km. The stress drop at 50–60 km depth coincides with the down–dip end of the seismogenic zone. This depth is in agreement with the seismogenic zone, as obtained from local seismology (*Comte et al.*, 1994; *Sobiesiak et al.*, 2007; *Schurr et al.*, 2012) and teleseismic data (*Tichelaar and Ruff*, 1991) for most parts of the study area. Major seismicity of magnitude 5.7 or greater correlates remarkably well with zones of increased stress anomalies on the subducted plate. Furthermore, projections of the depths where the top of the slab intersects the density contrasts of the reference background show no systematic relation with anomalies. Hence it may be concluded that the existence of stress anomalies is not an artefact of the chosen background model but can be explained by the actual mass distribution above the subducted plate. The anomaly at the cross section between 29°S and 30°S reveals a similar 'wider' pattern as observed for the northern Iquique section (Figure 4.17).

The GPE variation along the Andean chain and surroundings, relative to the reference state, is shown in Figure 4.18a (here we refer as ΔGPE). Generally, high GPE values have been obtained over elevated regions and low in the oceanic and overriding plates. Areas of elevated and thickened crust of the Andean chain, encompassing the regions of Coastal Cordillera, Western Cordillera, Altiplano and the sub Andean ranges, exhibit high positive ΔGPE values. Positive ΔGPE values (relative to the tectonic reference state) imply that the high Central Andes, the coastal regions and the overriding plate may be in a state of horizontal deviatoric tension. This result is in good agreement with estimate of tensional deviatoric stresses for the high Andes and the overriding plate between 5°N and 28°S using ETOPO5 data set (*Flesch and Kreemer, 2010*). South of 28°S, however, the positive ΔGPE values are limited to elevated regions. The overriding plate in this part of the convergence zone may be in compression.

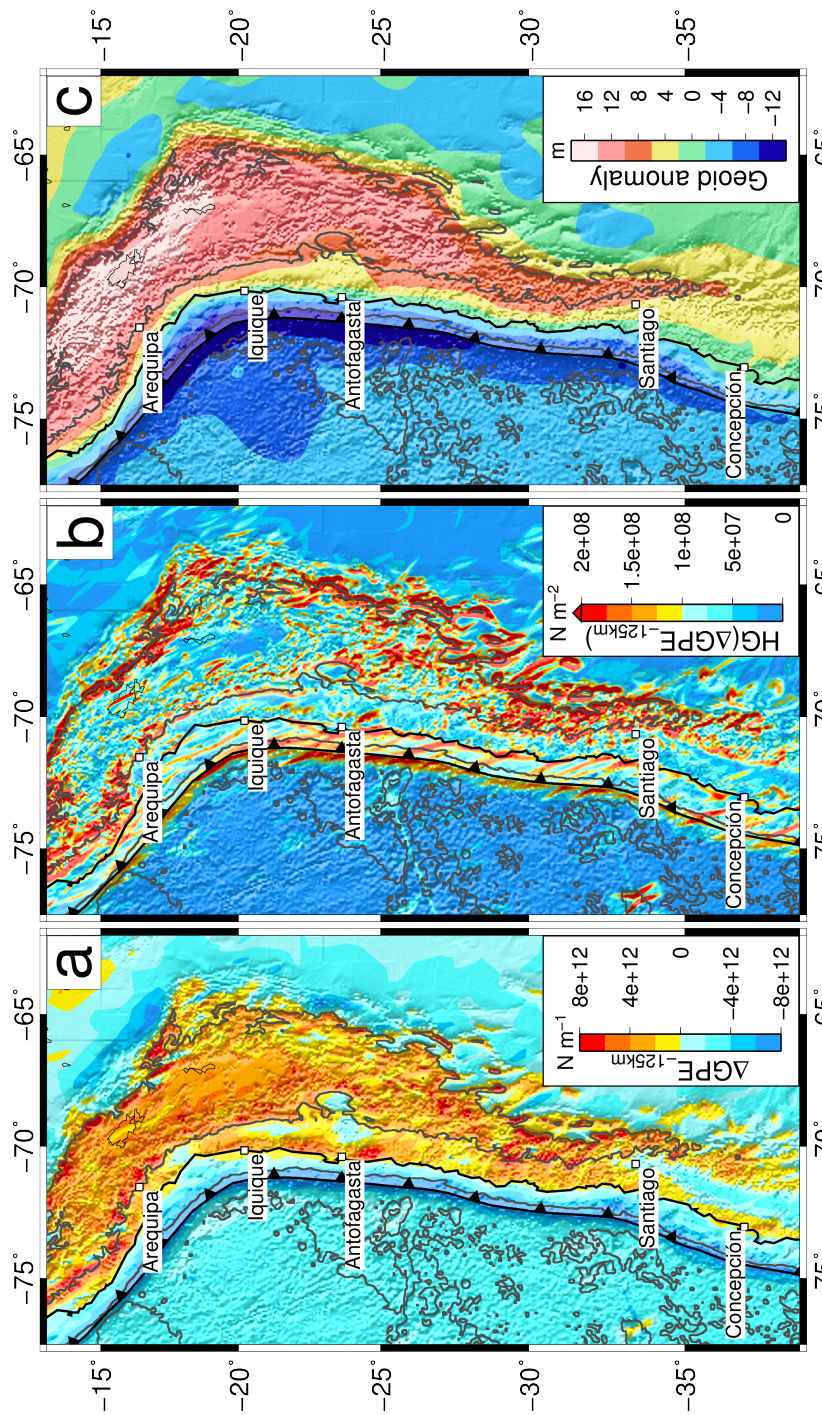


Figure 4.18: Gravitational Potential Energy of the Central Andean surroundings. **a** GPE relative to the reference state of a homogeneous lithospheric column at -125 km, **b** Absolute Horizontal Gradient of ΔGPE and **c** Residual geoid from GO_CONS_GCF_2_TIM_R3 truncated at degree and order 13 to focus the signal associated with the lithosphere. Grey contour lines in a-c depict the -4000 and +3000 m isolines.

The oceanic lithosphere is characterized by negative ΔGPE values indicating that the ocean basin and the trench are in compression. In addition, this result is consistent with previous predictions of the state of stress in the Nazca plate using different data sets and a different approach based on the solution of equation of equilibrium (*Heidbach et al.*, 2008; *Flesch and Kreemer*, 2010).

To enhance the short wavelength components in the GPE anomalies, we computed the total horizontal gradient of ΔGPE (Figure 4.18b). The gradient is related to high elevation and gives insight into the horizontal stress field. The gradient components were derived from the presented ΔGPE field within the original model frame and then combined into the total horizontal gradient

$$HG(\Delta GPE) = \sqrt{\left(\frac{d(\Delta GPE)}{dx}\right)^2 + \left(\frac{d(\Delta GPE)}{dy}\right)^2} \quad (4.15)$$

High values of $HG(\Delta GPE)$ are associated with highly elevated regions in the Andes (Figure 4.18b). Furthermore, the gradient map shows segmentation along the E–W direction. This might be associated with the locations of Coastal Cordillera, Western Cordillera, Altiplano and Eastern Cordillera (cf. Figure 4.12a).

We point out that the state of stress within a plate depends on the balance of stress fields resulting from basal shear traction, boundary forces and GPE. The effects of the former two processes have not been considered in the present study. Moreover, lack of independent constraint in the 3D gravity model could introduce uncertainty in the overall estimates of GPE. As in all model predictions, GPE estimates need validation. The geoid height is linearly related to ΔGPE and can be used to validate gravitational potential energy (*Jones et al.*, 1996). Figure 4.18c shows geoid height of the Andes and surrounding regions from GO_CONS_GCF_2_TIM_R3 model (d/o 250; *Pail et al.*, 2011). To minimize the effects of the lower mantle heterogeneities, the geoid height has been truncated at d/o 13 of the spherical harmonics expansion. The pattern of the truncated geoid height and ΔGPE coincides well in most of the regions. The positive ΔGPE values over the high Andes correlate well with the positive high in the geoid height. The negative geoid height in the Nazca plate is consistent with the negative ΔGPE .

4.2.6.2 Dynamic stress and deformation in the Andes

The main focus of the dynamic models is on the deformation in the upper Nazca plate. All results from it are shown in Figure 4.19 as a top view. The uplift after 100,000 years running time is shown in Figure 4.19a. For a better interpretation, the morphotectonic units from *Tassara* (2005) are plotted. Most parts of the continental crust show subsidence (negative values in blue). The fore–arc in the offshore area and the eastern edge are uplifted (positive

values in red). For comparison with uplift rates estimated from geological observations, the modelled uplift results are expressed as uplift rates (Figure 4.19b). Due to the running in behaviour, the displacement rates were calculated from the last 5,000 years of modelling time only. The results in the fore-arc show distinct differences between the southern and northern parts (Figure 4.19b). Due to the curved nature of the trench, the obliquity of convergence velocity of the Nazca plate varies within the model. In the southern part, where the trench is straight, the convergence obliquity is $\sim 20^\circ$. Whereas in the curved trench area of the northern part of the model, the convergence velocity is nearly perpendicular to the trench (obliquity angle=0). In the southern part, the onshore fore-arc and Coastal Cordillera (CC) show an uplift rate of 2 to 4 mm/a, which is one order of magnitude higher than the uplift rates of about 0.15 mm/a estimated from investigation of preserved marine terraces in the coastal area (Ortlieb *et al.*, 1996; Kukowski and Oncken, 2006). In contrast, the northern part of the model shows subsidence rates with values of -5 to -9 mm/a. The fore-arc subsidence at the ocean-ward concave margin (northern part) and the uplift at the straight margin (southern part) are in good agreement with the modelling results of Bonnardot *et al.* (2008) concluding that an ocean-ward concave margin induces subsidence and a convex shape margin induces uplift approximately 80 km away from the trench. It seems that the trench geometry influences the vertical deformation in the fore-arc only, because east of the Western Cordillera (WC) a distinction between north and south cannot be made. The Altiplano Plateau (AP) shows a subsidence rate of -3 to -4 mm/a. In contrast to this result, Gregory-Wodzicki (2000) estimated an uplift rate of 0.2 to 0.3 mm/a for the Eastern Cordillera (EC) and Altiplano Plateau during the last 10 million years from paleo-elevation data.

The horizontal displacement rates (velocities) can be compared with observed GPS velocities. Figure 4.19c shows the eastern component of the horizontal velocity compared to the GPS observations from Kendrick *et al.* (2001) (Figure 4.19d). An eastward decrease in velocity is seen in the modelled as well as in the GPS results. 200 km away from the trench, the modelled velocities in east direction show values between 18 and 21 mm/a. This fits fairly well the GPS observation of ~ 20 mm/a.

Another possibility to investigate deformation is to consider the strain after 100,000 years (Figure 4.19e). The east-west strain reveals that most of the model has a compressional regime and the largest compressional strain occurs in the Precordillera (PC), Western Cordillera (WC), and Atacama Basin (Ab) with values in the range of -0.004 to -0.006. Note that compression is defined as negative values in this work. The compressional strain in the arc region (PC, WC) is higher in the south than in the northern part, which means that the compressional strain increases with an increasing obliquity of angle. This was also shown by Zeumann *et al.* (2014). In the centre of the model, the fore-arc region shows an area of extensional strain (positive values) along the coast. This might be an effect of the trench geometry. Bonnardot *et al.* (2008) found that a concave shaped margin induces an extensional

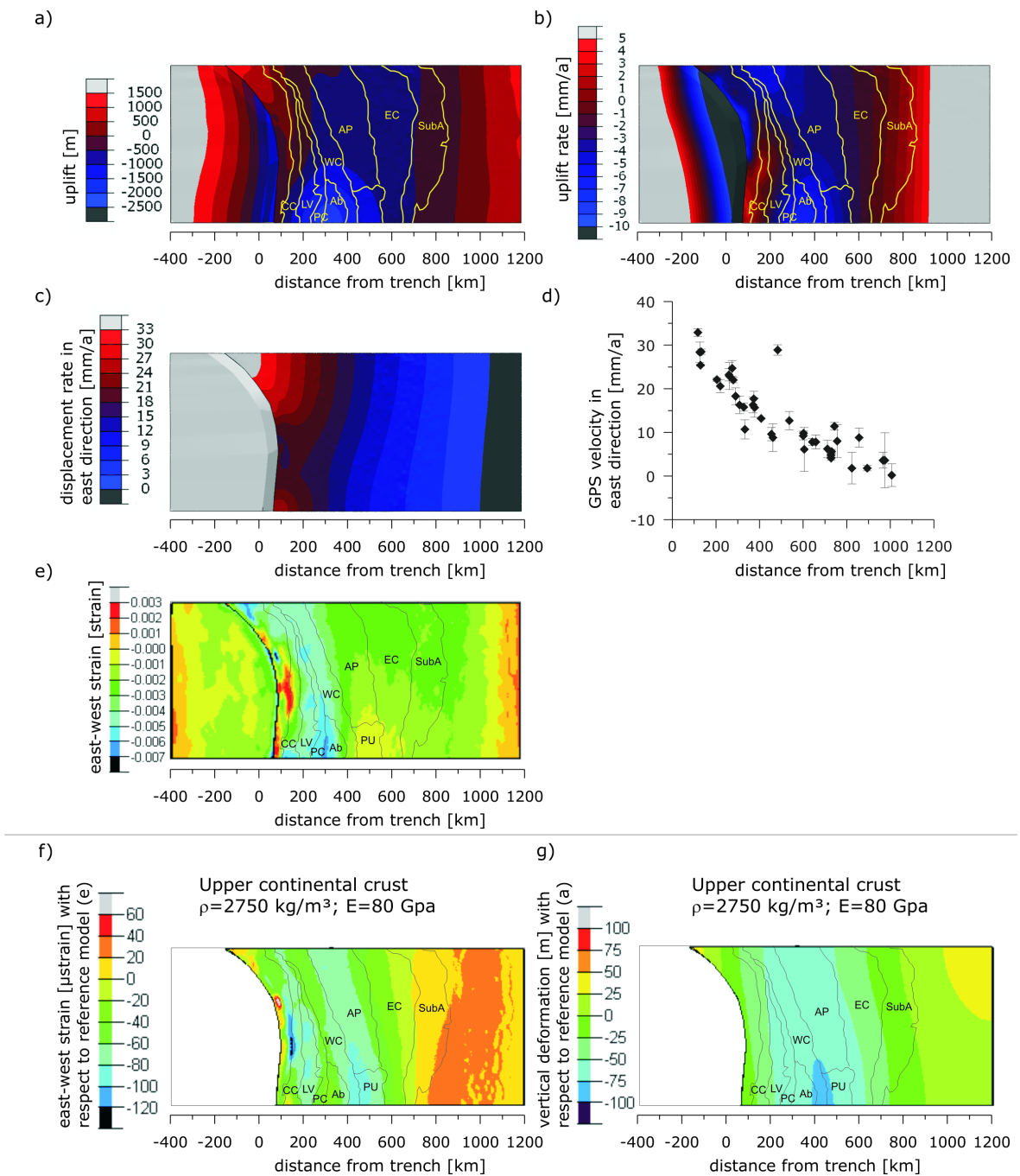


Figure 4.19: Results from the FE-modelling (top views) for the subset between 17–23.5°S and 60–75.5°W (orange box in Figure 4.12a). **a** Vertical deformation after 100,000 years. **b** Deformation rate calculated from the last 5,000 years of modelling time. **c** Displacement rate (velocity) in east direction calculated from the last 5,000 years **d** GPS observations from Kendrick et al. (2001). **e** East-west strain after 100,000 years: Compression is defined negative and extension is positive. **a–e** show the results of the reference model with parameters given in Table 4.4. **f–g** show the results for a model with increased upper crust density. **f** East-west strain with respect to the reference model. **g** Uplift with respect to the reference model. Yellow and black lines mark the morphotectonic units in the Central Andes from Tassara (2005): CC —Coastal Cordillera, LV —Longitudinal Valley, PC —Precordillera, Ab —Atacama Basin, WC —Western Cordillera, AP —Altiplano, PU —Puna, EC —Eastern Cordillera, SubA —Subandean. Higher density in the upper crust reduces the extensional strain, increases the compressional strain in LV, WC, AP, decreases the compressional strain in the Subandean region and results in lower uplift.

regime in the upper plate. But, the area of extension in Figure 4.19e is not in the zone of maximum trench curvature but a little further south.

The hypocentres of moderate subduction earthquakes are located within the descending oceanic crust and are indicators of the slab surface. Therefore, the modelled stress pattern on the Nazca plate interface can be compared to the earthquake distribution in the investigation area (Figure 4.20). Shown are only earthquakes with magnitudes >5 taken from the USGS catalogue. The modelled von Mises stress reveals a pattern of alternating higher and lower stresses. In this domain, modelled stress accumulation matches the earthquake distribution. These areas are marked by black ellipses and letters A through D. The high stress in the area of the Coastal Cordillera (A, B and C) is concentrated between the depth of 15 km and 50 km (seismogenic zone, e.g. *Comte et al.*, 1994; *Sobiesiak et al.*, 2007; *Schurr et al.*, 2012) where high friction was applied. *Husen et al.* (1999) determined the seismogenic zone between 20 km and 46 km depth, based on aftershock locations of the Antofagasta 1995 earthquake. *Tichelaar and Ruff* (1991) estimated the down-dip limit in the northern Chile region from large underthrusting earthquakes and concluded that coupling extends at least as deep as 45–47 km.

The depths of the earthquakes hypocentres fit well with the depth distributions of stress. The band denoted by 'D' at a depth of about 100 km shows an increase of stress between latitudes 20–24°S. This feature correlates well with the hypocentres in a depth between 70 and 150 km. Also, more of these hypocentres are located in the southern part.

The modelling shows that bands of high stress occur in areas where two or more model units with different parameters verge on each other. This contrast in parameters causes domains of stress accumulation at the plate interface. Furthermore, there is evidence for earthquakes that occur where slab parameters are characterized by steep gradients. The stress accumulation near the bottom of the model is not significant and probably expresses an edge effect caused by the nearby bottom of the model. In the future, a finer mesh of the descending slab is necessary to investigate the correlation between stress and earthquake hypocentres. However, the stress accumulation at the plate interface matches regions of high earthquake concentration.

Well-constrained density models derived from gravity measurements are helpful to define the geometry and density parameters for the different parts of the dynamic models. To test the effect of density on the results discussed above, the density of the upper continental crust (UC) was increased by 50 kg/m^3 . Since density and Young's modulus are related parameters, changes in density result in changes in Young's modulus, too. The newly assigned density for the UC is 2750 kg/m^3 and the corresponding Young's modulus is 80 GPa. The results of this model are shown in Figure 4.19f–g and are relative to the reference model results (parameters given in Table 4.4). A positive sign means that values are higher than in the reference model. It can be summarized that a high density UC reduces the extensional strain

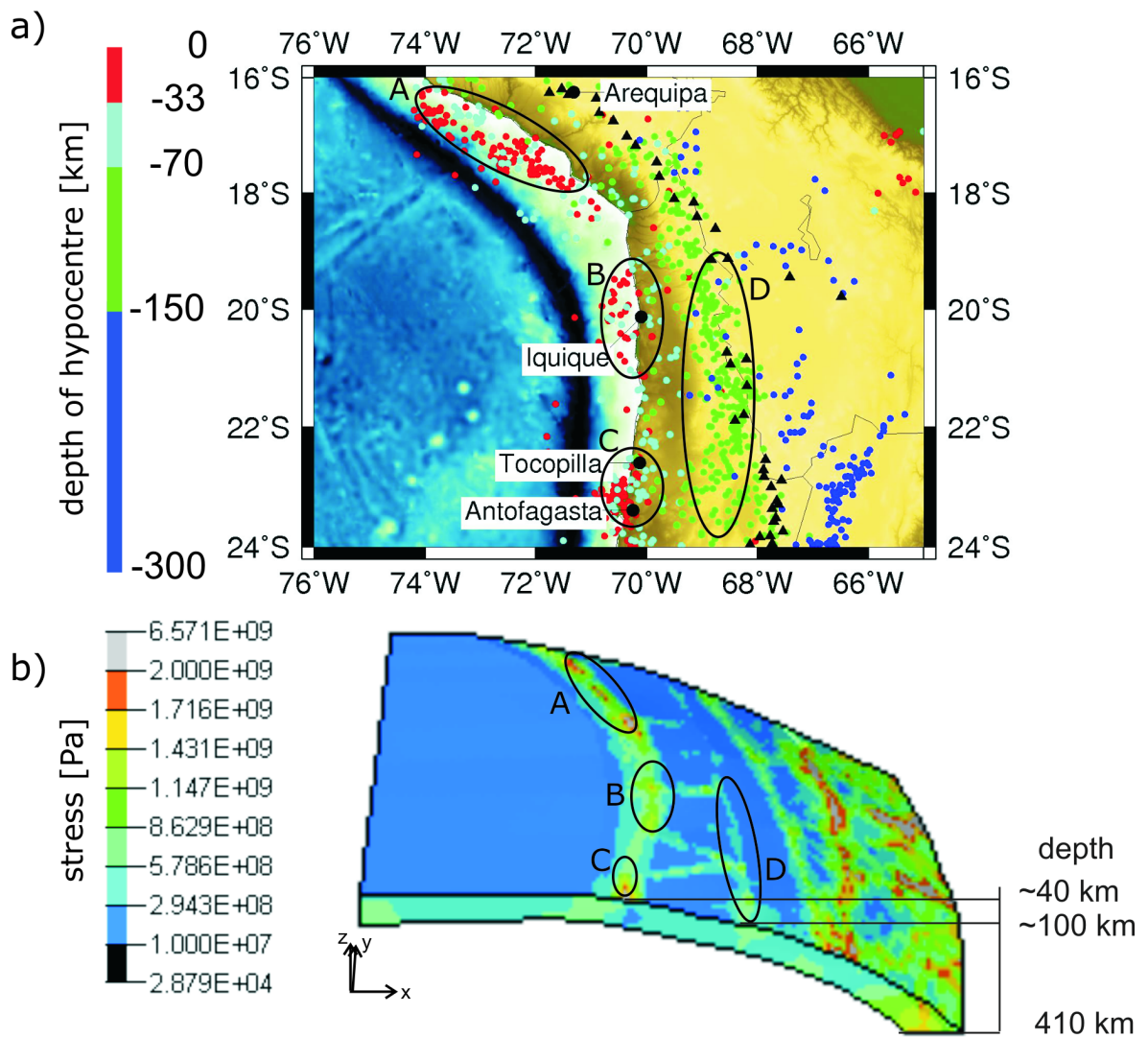


Figure 4.20: a) Earthquake distribution in the study area (NEIC/PDE M > 5), b) von Mises stress on the surface of the descending Nazca plate.

in the fore-arc of the centre of the model, increases the compressional strain in the LV, WC and AP, decreases the compressional strain in the Subandean region, and results in larger subsidence.

Increasing the density of the UC by 50 kg/m^3 leads to lower east–west strain in the Coastal Cordillera (CC) with values up to $-120 \mu\text{strain}$ (Figure 4.19f). This is the region where the reference model shows extensional east–west strain with values up to 0.003 (Figure 4.19e). Therefore, increased density in the UC reduces the extensional strain in the centre of the model. Lower east–west strain occurs in the Longitudinal Valley (LV), the Western Cordillera (WC), and the Altiplano–Puna region (AP, PU), too. These regions show compressional regime (negative values) in the reference model (Figure 4.19e). This leads to the conclusion that compressional strain in these regions increases with increasing density. The differences to the reference model in the Western Cordillera and Plateau region are large in the southern part of the model. This might be an effect of the trench geometry. In the Subandean region and further east, the resulting strain values are positive, which means that they are higher than in the reference model. The results of the same analysis for the vertical displacements or uplift (Figure 4.19g) reveal that an increased density for the UC results in lower uplift (larger subsidence) with values of $\sim 70 \text{ m}$ (blue belt).

4.2.6.3 Resolution and evaluation of GOCE gravity gradients

The vertical gravity gradient in 'free-air' at 8 km altitude calculated from the GOCO03s coefficients is shown in Figure 4.21a. It is dominated by bathymetry/topography of the trench and the Western and Eastern Cordillera. The modelled effect of the topography on the vertical gradient at the same altitude from the RWI topographic model is displayed in Figure 4.21b, excluding the isostatic effect of the Andes. The difference of these two fields (Figure 4.21c) may be referred to as vertical Bouguer gravity gradient anomaly. The spatial resolution of the models (d/o 250) at latitude of 25°S does not allow shorter half-wavelength than 72 km. Nevertheless, a narrow strip of positive gravity gradient anomalies in the order of up to $+15 \text{ Eötvös}$ ($1 \text{ Eötvös} = 10^{-9} \text{ s}^{-2}$) may be carefully recognized paralleling the coast near the locations where higher-density rocks units are expected to cause positive gravity (and stress) anomalies. The isostatically compensated Western and Eastern Cordillera may be related to negative gradient anomalies in the order of less than -20 Eötvös . However, it must be noted that the application of the RWI model at a low altitude of 8 km can only count as a first order approach since the model with its relatively coarse resolution of 5' was originally intended to approximate the topographic gravity/gradient effect at satellite orbit.

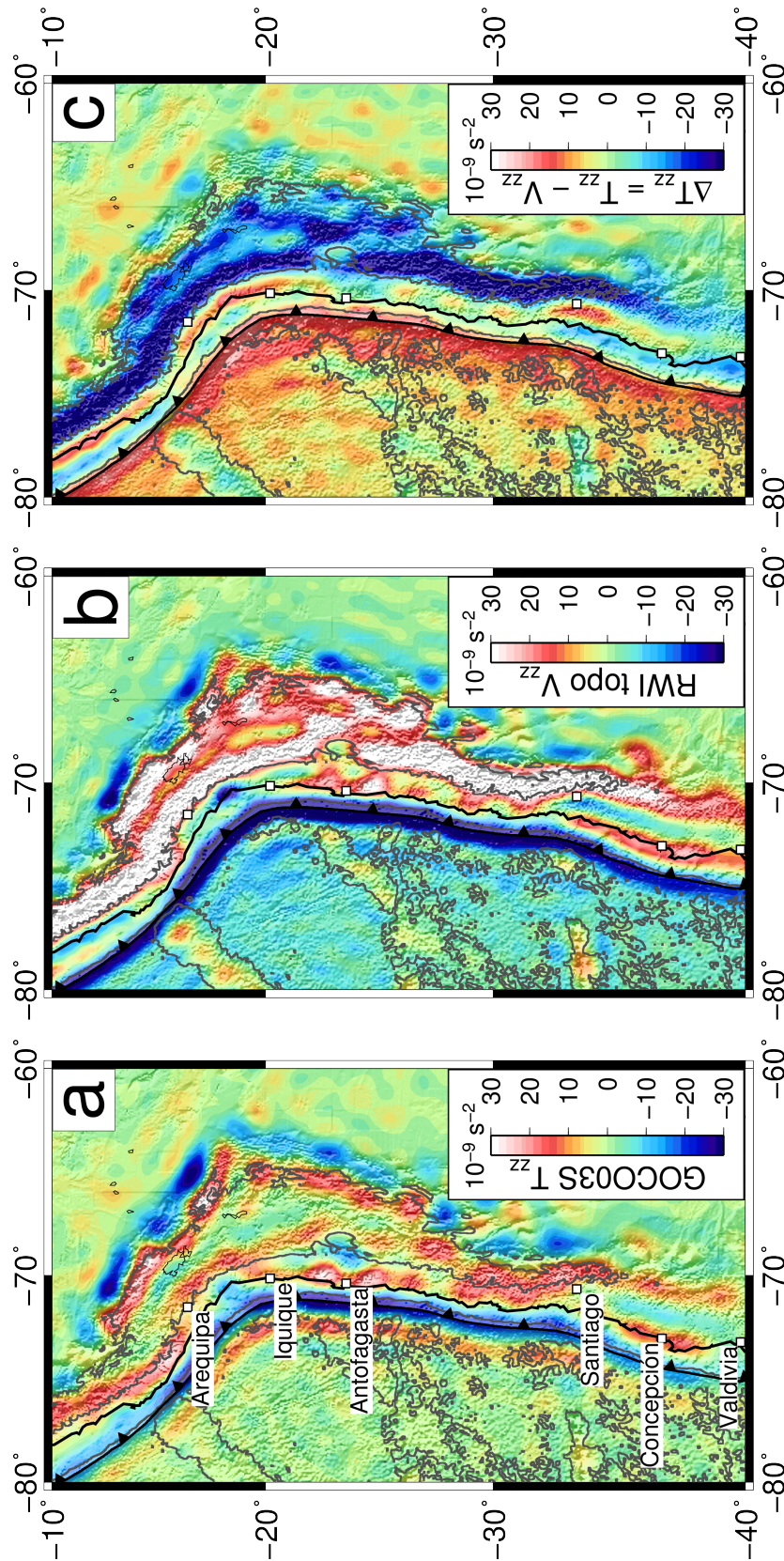


Figure 4.21: Vertical gravity gradient anomalies at 8 km altitude: **a** Vertical gravity gradient calculated from the coefficients of the GOCO03s model in 'free-air'; **b** topographic effect on the vertical gravity gradient (without isostatic effect) from RWI model; **c** topographically corrected vertical gravity gradient. Isodepth and topography contour lines at -4000 m and +3000 m in dark grey emphasize offshore ridges and high topography of the Andes. White squares in **b** and **c** denote city locations as indicated in subfigure **a**.

4.2.7 Conclusions

Using static and dynamic forward modelling techniques, we demonstrated that a well-constrained density model provides valuable information on the behaviour of stress on an interface between the South American continental lithosphere and the subducting Nazca plate. For the first time, it was shown that taking a well-constrained static density model as a basis for dynamic modelling is a practical approach. 3D density models can deliver geometries and densities for dynamic models.

In a recent paper by *Béjar-Pizarro et al.* (2013), it is stated that a segmented subduction interface plays a certain role on the occurrence of large mega thrust earthquakes due to differences in frictional parameters. The structures in the overriding and subducted lithosphere are important indicators. From Figures 4.16, 4.17 and 4.20, we conclude that combined modelling and interpretation using static and dynamic approaches adds value to a sole interpretation. It can be seen that the Chilean fore-arc is segmented between latitudes 19 and 31°S. The von Mises stresses from the dynamic modelling (refer to section 4.2.6.2) show variations in magnitude both in the E–W and N–S directions. This corresponds well with the findings of the static normal stress modelling based on 3D density models. Concerning the proposed seismic gap near the Iquique region in North Chile, we have found the normal component of the vertical stress anomaly to be different from the distribution south of ~21°S, namely lower amplitudes but wider extent into the subduction. At this point, we can only speculate that either the amplitude or the spatial extent is the dominant factor on asperity generation. A comparison with the recent rupture of magnitude 8.2 in this region indicates that the stress-anomaly distribution may explain the asperity pattern by segmentation. From this perspective, two segments to the South of the April sequence, each more than 100 km wide, are still at risk to break.

The results of the dynamic models fit GPS observations quite well. This could mean that the dynamic model is a good simulation of the Central Andean subduction zone. The investigation shows that considering the ocean-ward concave geometry of the trench is crucial for the Central Andes, because it influences the deformation patterns (strain, uplift) in the South American plate. The stress accumulation on the descending Nazca plate can be correlated with the earthquake distribution in the investigation area. However, further investigations with a finer and smoother mesh of the slab are necessary. An improvement of density models by including more data (terrestrial and satellite data) will improve the dynamic models. Including more and better constraints from seismic profiles, boreholes, geophysical measurements, petrology, and geology (among others) will improve the density models as well as the dynamic models.

Satellite-derived gravity data can improve density models in multiple ways: Data from satellite missions fill gaps in regions where no terrestrial gravity measurements exist and

are suitable to constrain the medium to long wavelength structures of the models. The new satellite mission GOCE significantly improved the coverage and availability of gravity data. Satellite only models have lower spatial resolution than the terrestrial data, but combined models from terrestrial and satellite-derived gravity data improve the density models and thus, indirectly, the dynamic models. Furthermore, the forward modelling process can be based on a more homogeneous gravity database and outliers from the terrestrial measurements or deficient gravity prediction become less effective when combined regional models are used.

A study of topographically corrected gravity gradients of the satellite-only model GOCO03s at 8 km altitude revealed that gravitational models that approximate gravity gradients from orbit can provide effective value to density modelling and interpretation of lithospheric structure. Nevertheless, adequate topographic correction of gravity gradient data is essential. Spatial resolution needs to be higher for specific studies of the Earth's crust and its state of stress. For large-scale studies such as GPE analysis and general geological and geophysical interpretation, the resolution of satellite-only models is clearly sufficient. For detailed crustal studies, however, combined gravity field solutions like IMOSAGA01C, as presented by *Hosse et al.* (2014), are appropriate. The high spatial resolution of terrestrial gravity combined with the homogeneous lower-orbit satellite data leads to more detailed and better constrained lithospheric density models, and hence improves our knowledge about the state of stress in the lithosphere.

As a next step, the direct incorporation of gradients from satellite- and combined gravity models into the forward modelling process will help to enhance the correctness of the general structure and composition of the modelled lithosphere. Furthermore, this will involve finer latitudinal resolution of the model geometry and multi-parameter inversions of density and geometry that account for the full gravity gradient tensor and its invariants. The improved lithospheric 3D density models will then serve as an advanced input to dynamic, or instantaneous, modelling. The purpose of these enhancements is to obtain a better-constrained model of the density distribution and, hence, to decrease possible ill-conditioning of the FE-modelling. A more detailed study on *b*-values from local seismicity could help to better understand the prevailing mechanism controlling asperity generation in this context. The methods presented in this paper can be utilized for studies at other tectonic belts and should lead to a better understanding of structure and the state of stress in the lithosphere.

4.3 Application summary and supplement

Hosse et al. (2014) compiled the IMOSAGA01C combined regional gravity model from terrestrial gravity data and the GOCO03s gravity model (*Mayer-Gürr et al.*, 2012) that bases on data of the GOCE satellite mission. Within the scope of the present dissertation, the new combined model was found to be superior to previously available data: Numerous outliers in the surface gravity data were removed or smoothed through weighting against the homogeneously measured GOCE-based data and recent altimetry data. And the fill-in of areas lacking in surface gravity data with GOCE-based data was proven superior to the previous fill-in approach of the EGM2008 gravity model.

Therefore, IMOSAGA01C was used to revise an existing 3D density model of *Prezzi et al.* (2009). The development of the distribution of gravity residuals during this process is given in Figure 4.22. Figure 4.23 shows a snapshot of the remaining residual of the forward calculated Bouguer anomaly after the northern and southern extension to the still original centre part have been forward-modelled to fit the IMOSAGA01C combined gravity model. Zones with values of more than $\pm 20 \cdot 10^{-5} \text{ m s}^{-2}$ can be found along the trench (at ~200–250 km Easting in the map). Those and other residuals were later corrected according to the combined gravity model (cf. figure 4.22).

The extended and optimised model was used to derive different kinds of anomalies of the lithostatically induced vertical stress which could be spatially correlated with the hypocentres of major seismicity for the interface-normal component on the subducting Nazca Plate. Figure 4.24 shows an enlarged version of the corresponding righter panel of figure 4.12.

The method was also used to derive Gravitational Potential Energy and its derivatives of the Central Andes. The stress distribution revealed distinct segmentations of the entire study area and of the forearc in particular. The results were interpreted to that effect that anomalous excess masses in the continental crust and lithosphere may partly exert control on the locking of the subduction interface.

This could furthermore be supported by comparing a seismological solution for the slip distribution of the 01 April 2014 Pisagua/Iquique main shock (*Ruiz et al.*, 2014) with local stress anomalies (see figure 4.25): The 1–2 m slip isoline range is in agreement with a more than 100 km long patch of stress anomalies of the order of 20–25 MPa that is situated 10–40 km offshore from the Pisagua/Iquique region and is clearly distinguished from neighbouring patches further to the south-east. The overlay of both parameters in figure 4.25 helps to accept the idea that excess masses in the forearc may possibly have caused a stress barrier that was finally overcome during the megathrust event.

A method to derive Bouguer-like anomaly maps of satellite gravity gradients was presented. The vertical component of the gravity gradient tensor of the GOCO03s model, which

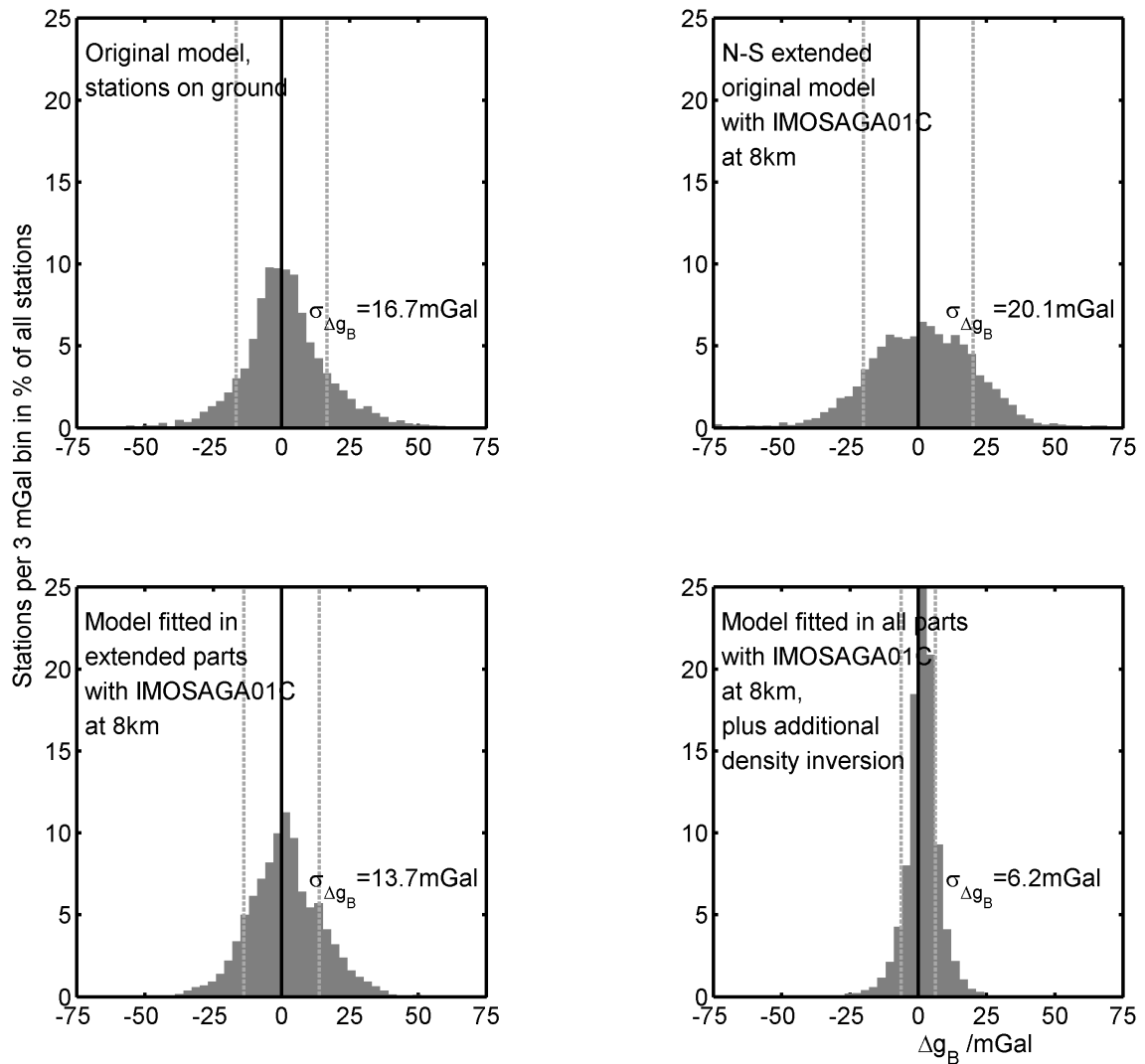


Figure 4.22: Distribution of gravity residuals. Upper left: Original residual of modelled and measured surface gravity (without northern and southern extension); upper right: the same original model (with extensions) but against the combined gravity model; lower left: as upper right but with extended area fitted to gravity; lower right: entire model adjusted to fit IMOSAGA01C (including minor density inversion within the scope of tolerable variation given by *Prezzi et al. (2009)*).

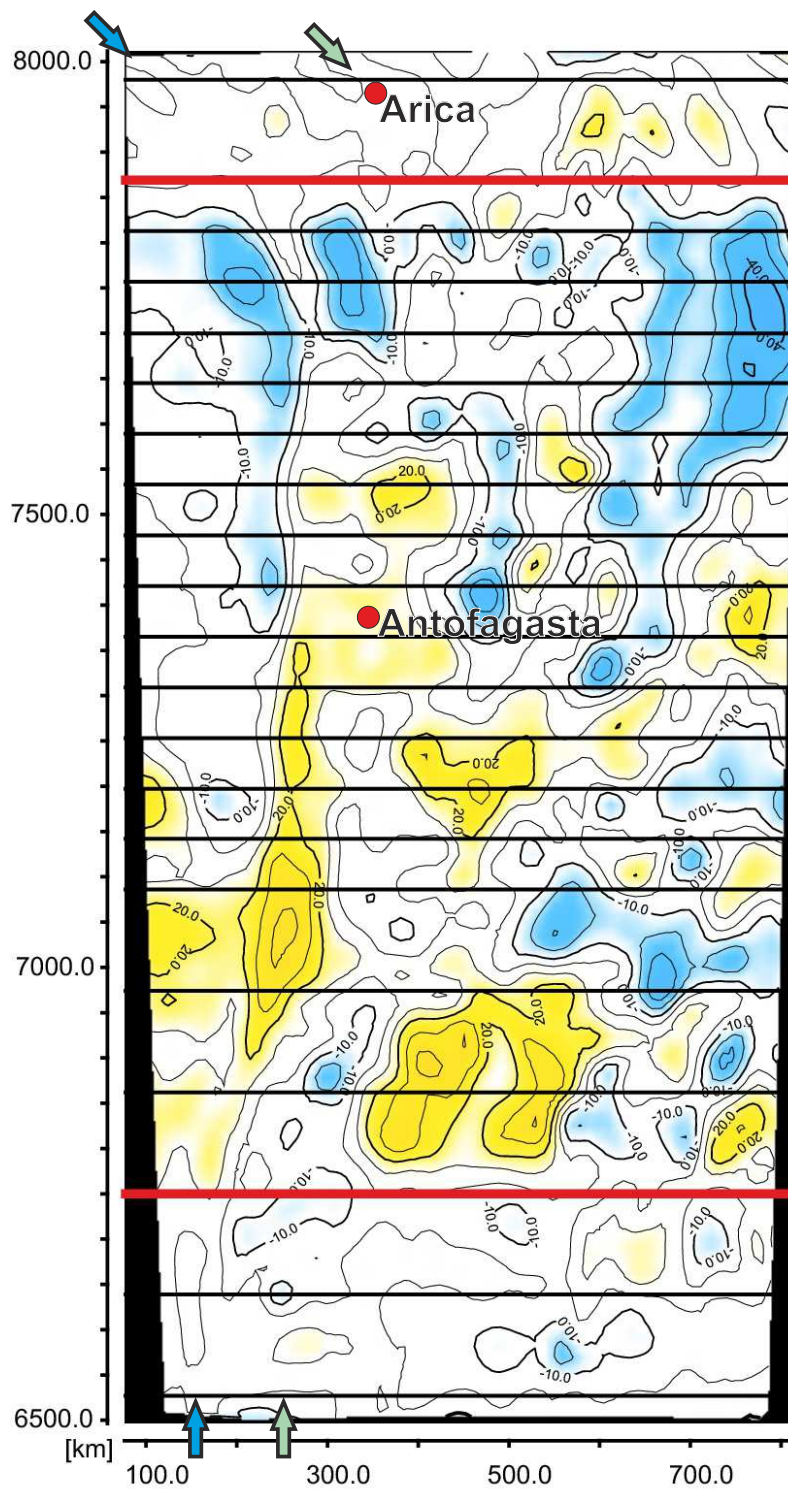


Figure 4.23: Residual gravity (snapshot) of the original density model with northern and southern extension as compared to IMOSAGA01C. The extended areas in this map are already fitted to the IMOSAGA01C combined gravity model; the centre part is still the original one. The bold red lines depict the northern and southern boundary of the original modelling. Black horizontal lines represent sections of the IGMAS density model. Contour lines are in units of 10^{-5} m s^{-2} . Confer to lower left subfigure of figure 4.22 for corresponding histogram. Coordinates are given with respect to UTM zone 19, i.e. the reference meridian at 69°W . For easier orientation, approximate locations of the trench and coastline are indicated by blue and light green arrows, respectively.

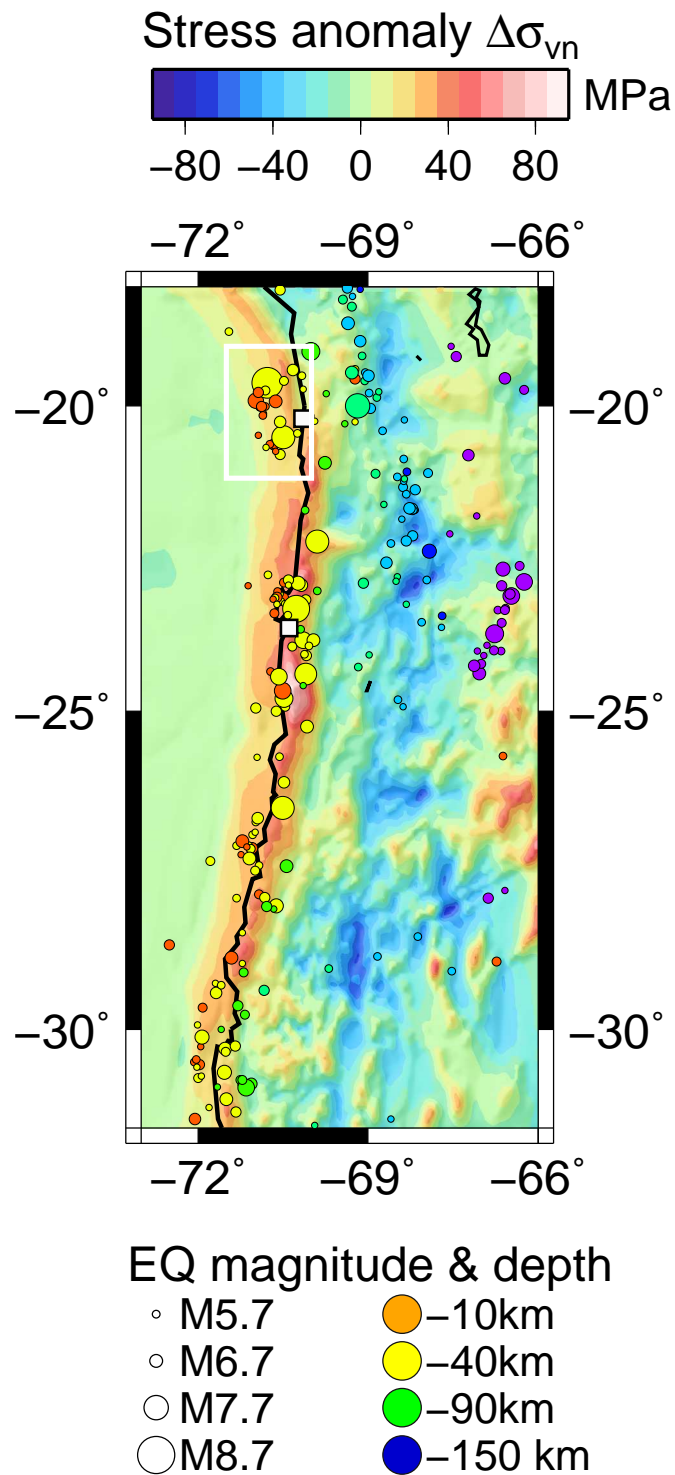


Figure 4.24: Normal component of the vertical stress anomaly on top of the subducting Nazca plate. This figure is an enlarged representation of the righter panel of figure 4.12. The white box indicates the area of figure 4.25 including the location of the 01 April 2014 Iquique earthquake.

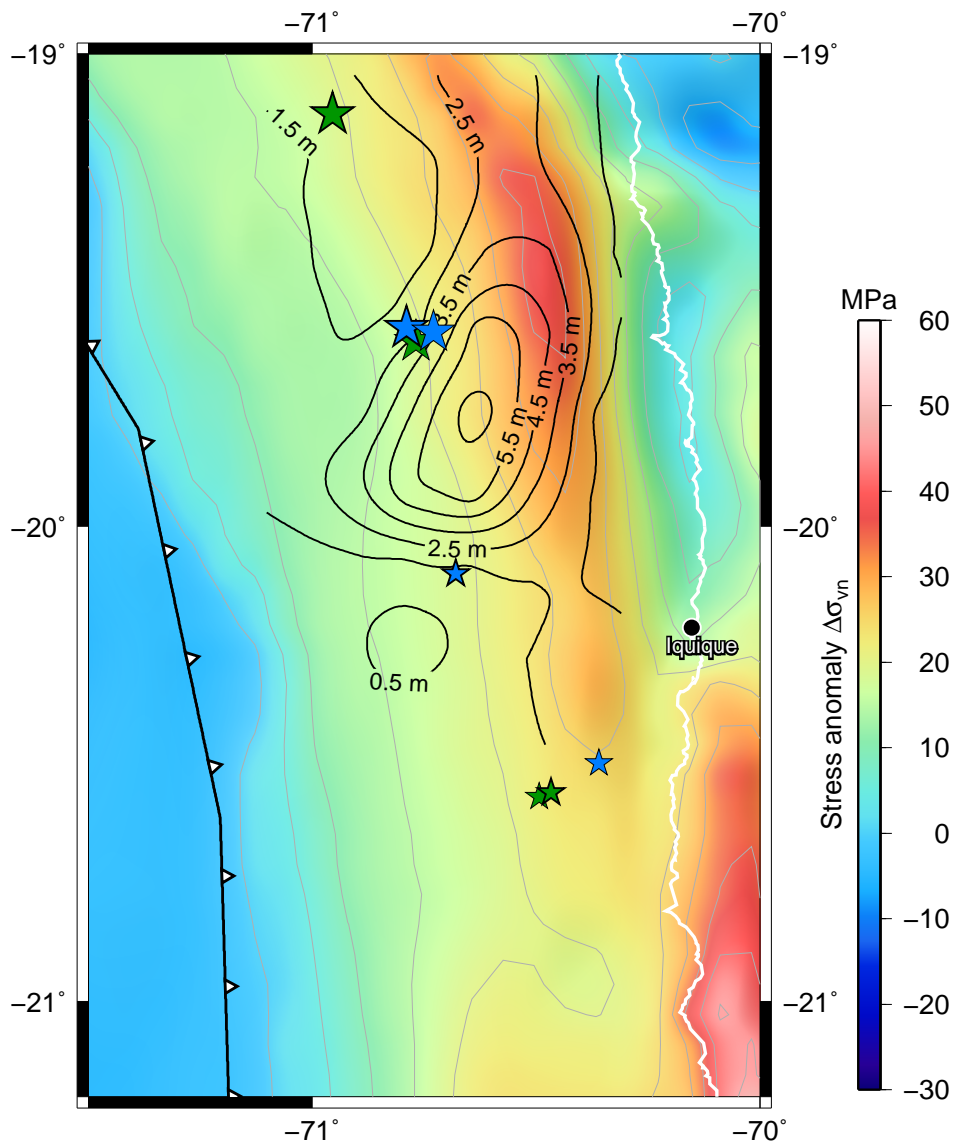


Figure 4.25: Slip distribution after *Ruiz et al.* (2014) of the 01 Apr 2014 Pisagua/Iquique main shock plotted on top of the normal component of the vertical stress anomaly. Green stars depict USGS hypocenters and centroid locations (bold edge) of the main event (big stars) and of the largest after-shock (small stars). In blue the same for GFZ solution but with moment tensor location (bold) instead of centroid. See white box in figure 4.24 for exact location.

represents the measured data of the GOCE mission, was computed from the model coefficient at an altitude of 8 km. The low altitude was chosen in order to get a display of the field preferably close above the source masses for possible geophysical interpretation. It was then corrected for topographic masses using the RWI model in order to derive the vertical gradient of the Bouguer anomaly. Several features could be identified such as the radial bulging of the Nazca Plate just west of the trench, strong negative gradients within the 3000 m contour line of the Andean topography, and rather balanced amplitudes to the East of the Central Andes. A little pronounced elongated band of positive gradient patches could be recovered between the trench and the main chain of the Andes. It had, however, to be questioned if the data resolution and topographic model were fit to effectively link this narrow band to the suspect excess masses at that location.

Some additional detailed matter that was not provided in the published content of chapters 4.1 and 4.2 follows hereafter.

Topo-Isostatic corrected satellite-only gradients In addition to the mass-correction of the vertical gradient model shown in figure 4.21 of section 4.2.6.3, the vertical isostatic gradient effect of the Andes has been considered based on the Rock-Water-Ice (RWI) model as well. The result is displayed in Figure 4.26 in accordance with the approach given in sections 4.2.5.2 and 4.2.6.3 of the previous chapter. Due to the exact approach for the isostatic component in the RWI model was not clear at the time, it was not included in the submission of the text given in chapter 4.2.

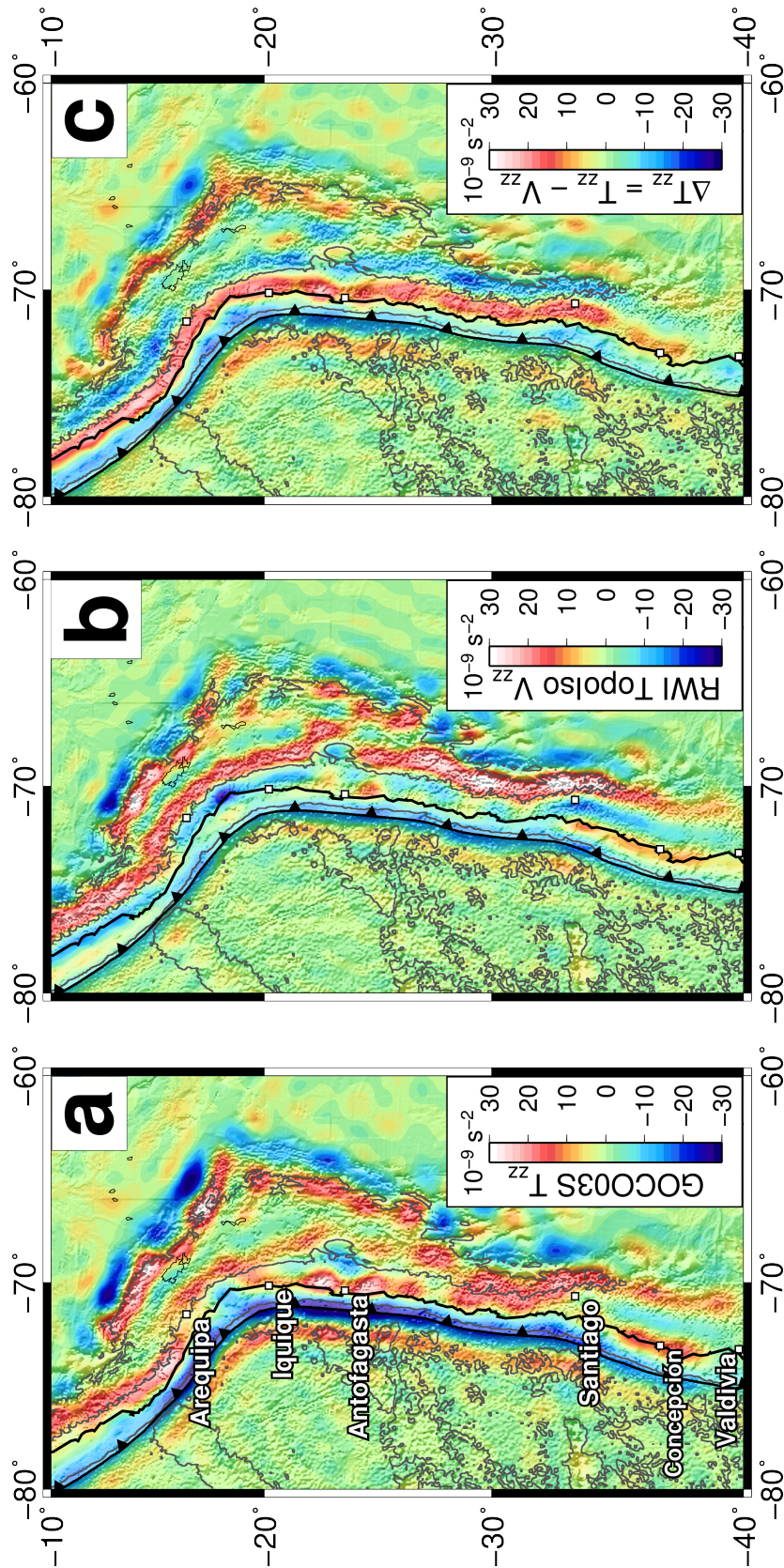


Figure 4.26: Vertical isostatic gradient anomalies at 8 km altitude: **a** Vertical gravity gradient calculated from the coefficients of the GOCC03s model in 'free-air'; **b** topographic effect on the vertical gravity gradient (including isostatic effect) from RWI model; **c** topographically corrected vertical gravity gradient (isostatic gradient anomaly). Isodepth and topography contour lines at -4000 m and +3000 m in dark grey emphasize offshore ridges and high topography of the Andes. White squares in **b** and **c** denote city locations as indicated in subfigure **a**.

The isostatic anomaly at 8 km altitude is dominated by an elongated positive band of up to $25 \times 10^{-9} \text{ s}^{-2}$ all along the Pacific-Southamerican margin, closely East of the coastline. The spatial correlation with the margin is so strong that it might seem advisable to review the isostatic parametrisation or resolution of the underlying crustal model and to check for the effective omission error of the downward computed model. However, a strong positive isostatic (gravity) anomaly of more than $50 \times 10^{-5} \text{ m s}^{-2}$ at the surface can be found both in the Vening-Meinesz based map of *Schmidt and Götze* (2006) and in the Airy-Heiskanen based World Gravity Map 2012 (*Bonvalot et al.*, 2012) at identical locations. The effect thus occurs both for regional and local corrections of isostasy. This eliminates the option of the band being a regional response to isostasy. If the observation can be attributed to physical sources, then one interpretation would be the existence of undetermined excess masses that are supported by a strong crust or lithosphere — which is indeed not an unlikely scenario here.

Most of the elongated band of high isostatic anomaly correlates with the Coastal Cordillera. Thus it is on the one hand possible that the Cordillera does not have deep roots and is instead compensated by strong material below; meaning that the isostatic correction adds more signal than a crustal root – if it exists – actually takes away at depth. On the other hand, the band sits systematically to the East and North-East of the coastline – a fact that raises a suspicion that the isostatically problematic ocean-continent transition produces this as an artefact. The Coastal Cordillera is rather narrow when compared to the entire Andes. The possibility of omission errors in the high frequency content should not be excluded, even though the vertical gradient before mass corrections provides some positive signal content that can be attributed to the Cordillera (cf. figure 4.26a). Yet it would be rather remarkable to summarize that a gravity gradient model derived from satellite-only data alone was capable of resolving suchlike crustal structure. One has to be careful in not over-interpreting features which could easily be brought in by overexciting signal power in the corrections. The truncation of coefficients of spherical defined topographic mass models is a closely related issue: omitting proper content of the integral model can lead to significant errors as the complete model is always to be understood as a superposition of all composing coefficients.

One conclusion of the approach described here is that inadequate utilisation and variations in topographic and isostatic mass correction heavily affect the interpretation and must be very carefully executed. Other approaches to correct for topographic masses and isostasy as from *Holzrichter* (2013) and Szwillus (Kiel University, pers. comm.) to substitute the RWI method used in this work are expected to give more precise results at the near-surface altitudes as the RWI model was originally built to work for corrections at orbit heights. Hence, further analysis is mandatory to this end.

The present work nevertheless demonstrates the applicability of GOCE data to lithospheric interpretation. The emphasis herein should not so much be seen in the shortest provided

wavelengths of the new models but rather in the unprecedented homogeneity and quality of the data. As welcome as the availability of some of the previous combined gravity models (e.g. EGM2008) may have been — it cannot be neglected that those contain also very false data in e.g., areas with rough topography and few reliable surface data to be included in the combined solutions (cf. section 4.1.6). The great impact of GOCE data on the 'Solid' Earth domain should therefore not primarily be seen in the direct interpretation of small-scale crustal structure but in the overall robustness and homogeneity it may yield if applied and weighted wisely.

The role of reference gravity during calculation of stress anomalies The calculation of lithostatic stresses requires the input of gravitational acceleration at the station locations, respectively. This may be easily achieved by inserting absolute reference gravity, e.g. based on the WGS84 ellipsoid. However, as gravity changes with latitude, a noticeable error may be introduced to the calculation if a constant value is used. Any hypothetical assumption that the latitudinal effect cancels out when stress *anomalies* instead of absolute stresses are considered, is incorrect: As can be easily seen from Equation 4.9 and 4.10, the gravity factor always counts linearly before any subtraction of densities and must be considered irrespective of absolute or differential lithostatic stresses. Figure 4.27 shows the progression of the deviation of absolute gravity made if a constant reference gravity (in this study: 9.79 m s^{-2}) is assumed over all latitudes of the study area. The calculation was based on the coefficients of the WGS84 reference ellipsoid and performed using self-written MATLAB functions named `gabs.m` and `gref.m`.

In fact, the value of 9.79 m s^{-2} is valid at 25.64°S in the centre of the greater study area. A deviation of $\pm 0.007 \text{ m s}^{-2}$ at 15°S and 35°S can be expected. This corresponds to a stress anomaly error in the order of $\pm 10.5 \text{ kPa}$ and $\pm 252 \text{ kPa}$ at 5 and 120 km depth even if an unusually high density anomaly of 300 kg m^{-3} is assumed, respectively. Since this is significantly smaller than the actual stress anomaly signal (up to 100 MPa), it is acceptable to neglect the latitudinal effect during stress computation. It is nevertheless recommended that a reference value from the centre of the study area should be used.

A different issue is the approach of applying local gravity instead of reference gravity during stress calculation. This has neither been concerned in the present work nor in the IGMAS+ software package but it is suggested to be tested in future studies.

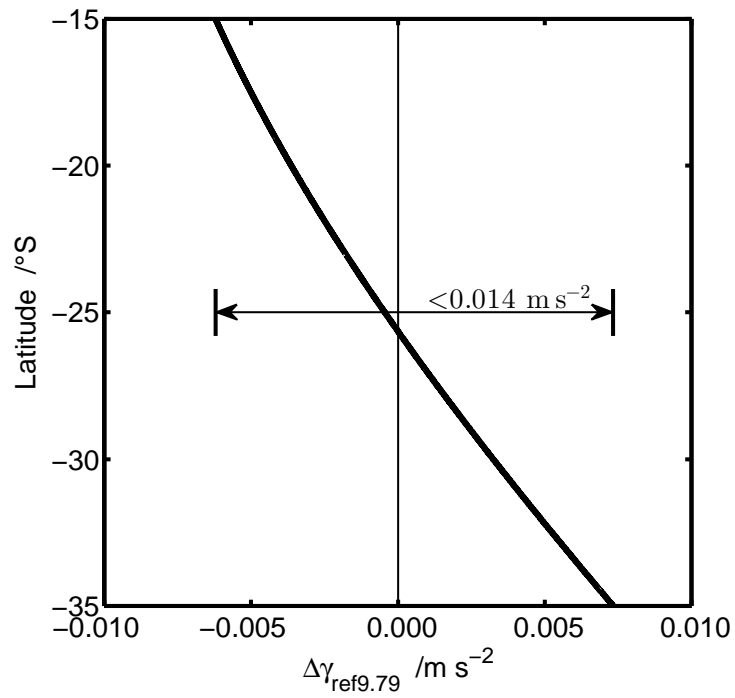


Figure 4.27: Deviation from reference gravity (WGS84) due to the use of constant absolute reference gravity $\gamma_{ref9.79}$ during the calculation of stress anomalies

5 Further implications to the seismic cycle from the combined analysis of static stress anomalies and plate coupling from GNSS observations

In addition to the analysis of static stress anomalies in conjunction with seismological findings, further implications to the nature of asperities can be found when other metrologically independent geo-data is considered. One fundamental method to the verification and observation of today's plate tectonics comes from the use of Global Navigation Satellite Systems (GNSS). Several systems like the US-American *NAVSTAR GPS*, Russian *Globalnaya navigatsionnaya sputnikovaya sistema (GLONASS)* and European *Galileo* have been in place since the mid 1990s or are currently in the set-up phase.

By the determination of positions of fixed GNSS-stations on the ground, it is possible to derive the magnitude of relative crustal motion between the station locations. At active continental margins, this method may be used in order to identify 3D-movements of the crust associated with the seismic cycle (e.g. *Chlieh et al., 2004*). In general, parts of the forearc that show 'bending' towards the stable continent over time, may be a sign of coupled patches of the subduction interface. Forearc stations that horizontally and vertically reside relative to the stable continent may indicate less- or uncoupled regions.

A combined analysis of a larger set of GNSS stations can thus deliver coupling-maps of the region of interest. However, the offshore part of the forearc is missing in such an analysis. To overcome this disadvantage, plate models of the active margin may be set up that simulate crustal displacements at the respective GNSS station locations. A realistic model is supposed to be found when the modelled displacement is in best possible agreement with the observations.

Metois et al. (2013) derived plate-coupling coefficients between the subducting Nazca Plate and its continental counterpart by inverse-modelling GPS recordings in northern Chile.

Provided that a systematic relation between lithostatic stress anomalies and locking of the plate interface exists on time scales of the order of the seismic cycle, it is suggested to carry out a joint analysis of both parameters.

Figure 5.1 shows a combined plot of stress anomalies, major seismicity and plate coupling coefficients after *Metois et al.* (2013) as vertical sections of constant latitude for the North Chile segment between 18.75° and 21.75°S. The M_w 8.2 megathrust event from April 2014 occurred within this region. As seen in the work of *Metois et al.* (2013), plate coupling appears to be increased in two distinct, trench-parallel zones: Highest values are located at the western tip of the wedge, where also the stress anomaly starts to become positive towards the East. Coupling gradually decreases landwards down to a plate depth of 80 km, which had been pre-defined to be the cut-off depth for coupling within the model. The gradual decrease is superimposed by one or several local maxima that could presumably be associated with maxima in the stress anomalies. This correlation fits best for the area at 19.25–19.75°S (including the Pisagua earthquake epicentre) and appears to be not valid for the part directly to South of the rupture-area at 21.25–21.75°S.

Figure 5.2 shows a plot of the coupling coefficient over the normal component of the static stress anomaly for the same region. The depth- and stress-anomaly information was extracted from the stress results after the enhanced density model in section 4.2 and then correlated with the horizontal position of the GPS-coupling model using a moving-window algorithm of 0.08° longitudinal width and latitudinal steps of 0.5°. A fractional inconsistency may arise here because the geometric assumption made for the subducting plate in the GPS model is less accurate than in the 3D density model.

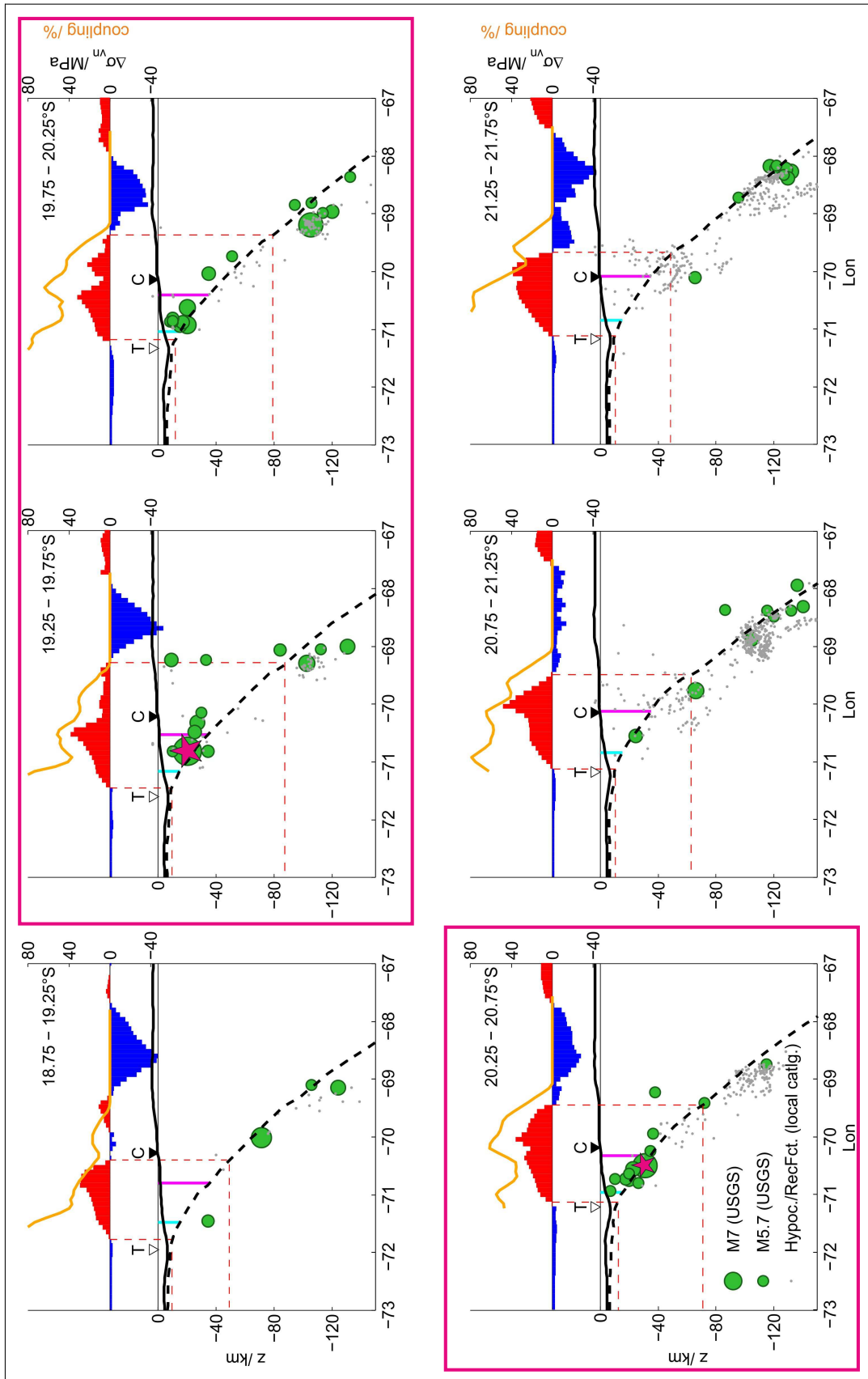


Figure 5.1: Combined plot of stress anomalies, seismicity and plate coupling. See next page for full caption

Figure 5.1: (prev. page) Combined plot of stress anomalies, slab geometry, major seismicity and plate coupling coefficients at the western Andean margin between 18.75°S and 21.75°S. Solid orange lines on the top axis represent coupling coefficients in per cent from GPS modelling as derived by *Metois et al. (2013)* before the Pisagua/Iquique event. The red/blue 'wiggle' diagram on the same axis shows mean values of the normal component of the vertical stress anomaly on the subducted Nazca plate derived from the optimized density model based on *Prezzi et al. (2009)* and the IMOSAGA01C combined gravity model. Please note that coupling in per cent and stresses in units of MPa share the same positive vertical axis. Dashed and solid black curves depict the mean geometry of the subducted slab and bathymetry/topography, respectively. Triangles marked *T* and *C* depict the mean trench and coastline locations at the given latitudinal window, respectively. Light blue and magenta coloured vertical lines indicate the projection of depths where the top of the subducted slab crosses the density contrast of the reference density background at -15 and -35 km. Red dashed lines mark the width- and depth projection of the positive anomaly. Green circles represent major seismicity ($M > 5.7$ from USGS, Sep 1978 –16 April 2014); grey dots depict constraining data from local seismological studies (Eggert, pers. comm.; *Husen et al., 1999*; *Schurr et al., 2006, 2012*; *Sobiesiak, 2000*). Subfigures representing areas affected by the 01 April 2014 Iquique event are outlined in magenta. The big and small magenta stars depict projected hypocentres of the main shock and of the largest aftershock, respectively.

A direct linear correlation of coupling coefficient and stress anomaly can *not* be observed. However, the majority of non-zero coupling data points clusters in a quadrant where positive coupling coincides with positive stress anomalies. Therein, two trends can be seen: Firstly, non-zero positive coupling (shallower than 80 km) does not significantly coincide with negative stress anomalies. Secondly, a linear trend in the positive stress sector seems to act as a threshold for a minimum interseismic plate coupling coefficient for a given positive stress anomaly. For the test region, such an empirical trend may be described as

$$c_t \geq 0.8 \frac{1}{MPa} \cdot \Delta\sigma_{vn}|_{\geq 0} \quad (5.1)$$

where c_t is the minimum coupling coefficient in per-cent for a given positive normal component of the vertical stress anomaly $\Delta\sigma_{vn}|_{\geq 0}$ in megapascal.

Figure 5.3 gives a more detailed view on the relationship between coupling and stress anomalies at the North-Chile segment. While figure 5.2 illustrates the 'bigger picture' of all data points at the segment, figure 5.3 displays the coupling-stress relation for specific latitudinal sub-segments between 18.75°S and 21.75°S.

It can be seen that for each sub-segment the data follows a specific path in the parameter space. A distinctive feature of the paths between 19.25°S and 20.75°S is that they compose a loop-like formation, respectively. For simplicity's sake, these paths may be named *streplings* (or '*Streps*') as derived from *stress* and *coupling*. Although the latitudinal spatial resolution of this analysis is rather broad at $\sim 0.5^\circ$ per search window, it should be noted that the distribution of the April 2014 megathrust sequence offshore Pisagua (including aftershocks) corresponds to the sub-segments where streplings form such loop-like patterns. When it is considered that the coupling coefficient in these graphs is a time-variable parameter over the seismic cycle, it may be argued that segments where looped streplings occur, exhibit an

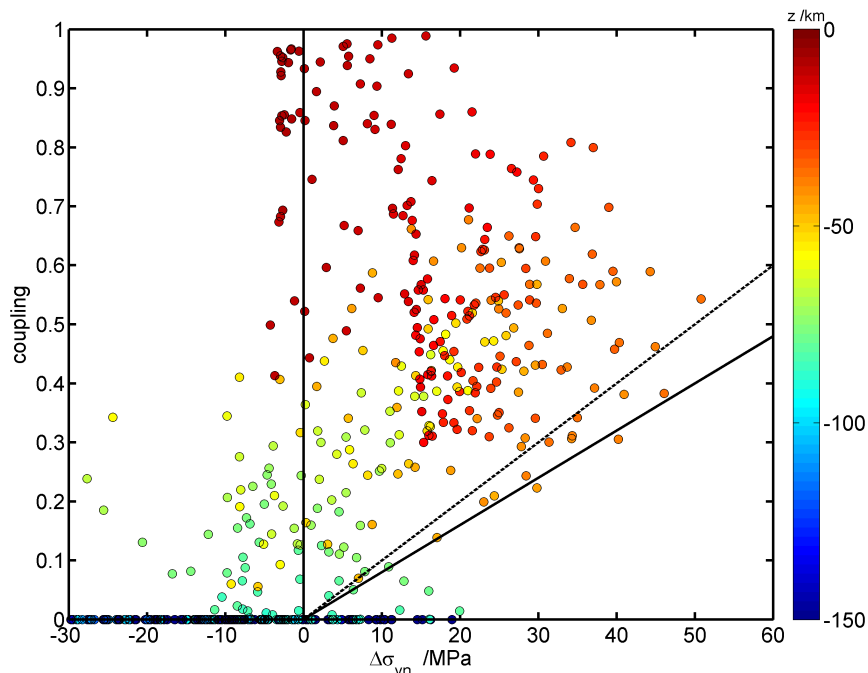


Figure 5.2: Plate coupling coefficient from a GPS model after *Metois et al.* (2013) over the normal component of the static stress anomaly from the optimized density model (section 4.2) at 18.75–21.75°S. The depth is colour-coded for each data point in kilometres. Angled black lines represent the suggested rule-of-thumb 0.8 1/MPa (solid) and 1.0 1/MPa (dashed) threshold for plate coupling (cf. text and equations 5.1 and 5.2). Coupling ranges from 0 (no coupling) to 1 (fully coupled).

increased potential to fail with high stress drop. However, at this time, the observation is rather speculative and misses a sound physical explanation yet.

It can be seen that coupling decreases continuously with depth (cf. to colour bars in the figures), i.e. with increasing distance to the trench. But at some latitudes, coupling increases locally again at depths between 25–50 km and significantly correlates with positive stress anomalies at the same place. One interpretation would be that this is evidence for excess masses in the continental lithosphere inducing anomalous normal stresses on the subduction and thereby forcing patches of the plates to be coupled at the corresponding depths. Figure 5.4 summarizes this idea schematically.

Prezzi et al. (2009) specified 34 body densities for their model that indicate a tolerable mean average variation of 40 g m^{-3} . For the purpose of a simple error estimation, a homogeneous rock column of this variation in density be considered residing above a 20 degrees inclined subduction interface. At typical seismogenic depths between 5 and 80 km, an average density of 0.040 kg m^{-3} corresponds to an error of the stress estimates in the order of 2–28 MPa, respectively. Based on this number, equation 5.1 may also be considered to be changed into a rule of thumb stating that the normal component of the vertical stress anomaly in units of megapascal approximately equals the minimum potential plate coupling in

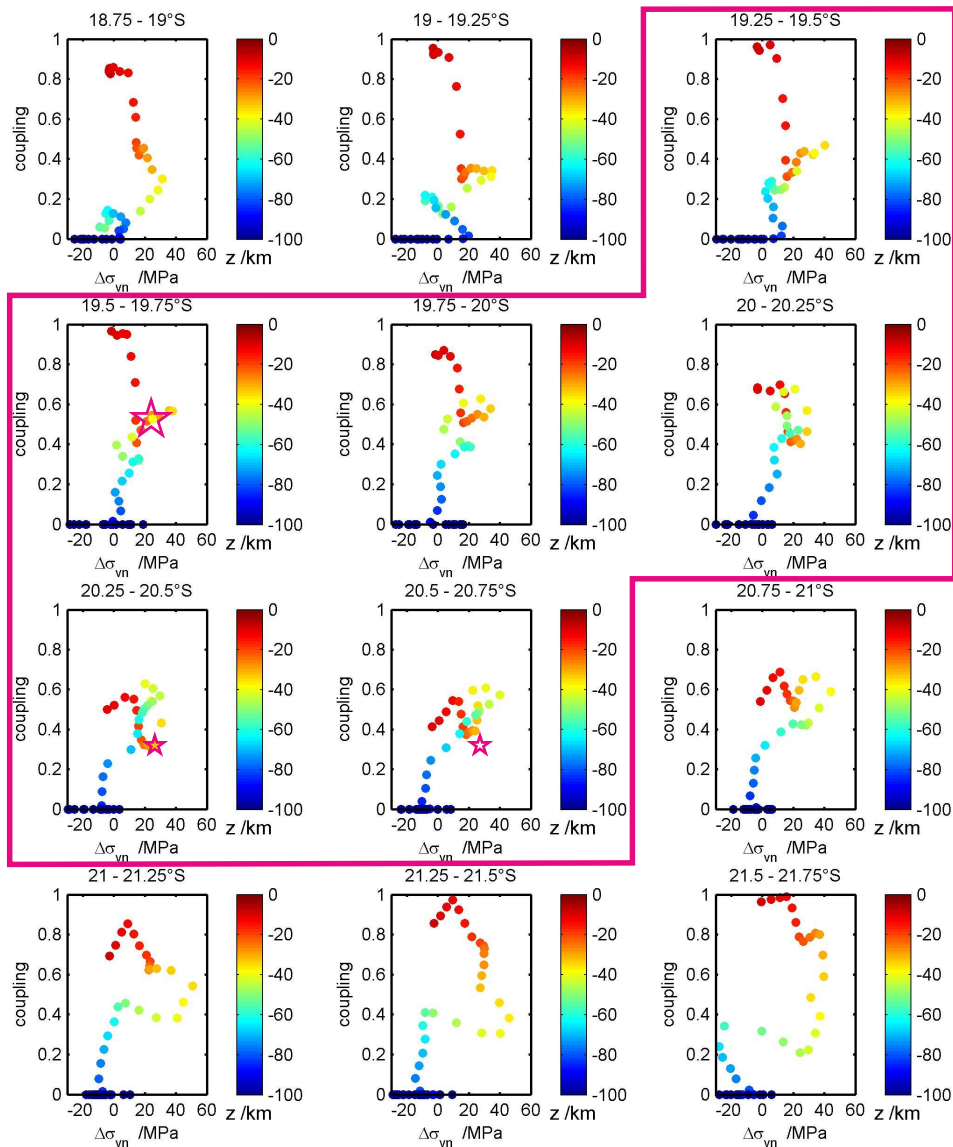


Figure 5.3: Stress anomaly and coupling from GPS modelling after *Metois et al.* (2013) at latitudinal sections between 18.75°S and 21.75°S. The 1st April 2014 megathrust earthquake offshore Pisagua and its aftershocks occurred in an area between 19.25°S and ~20.85°S (outlined in magenta). Data points are colour-coded with depth in kilometres. The big and small magenta stars depict projected hypocentres of the main shock and of the largest aftershock, respectively. For an interpretation of different shapes or patterns see figure caption 5.4.

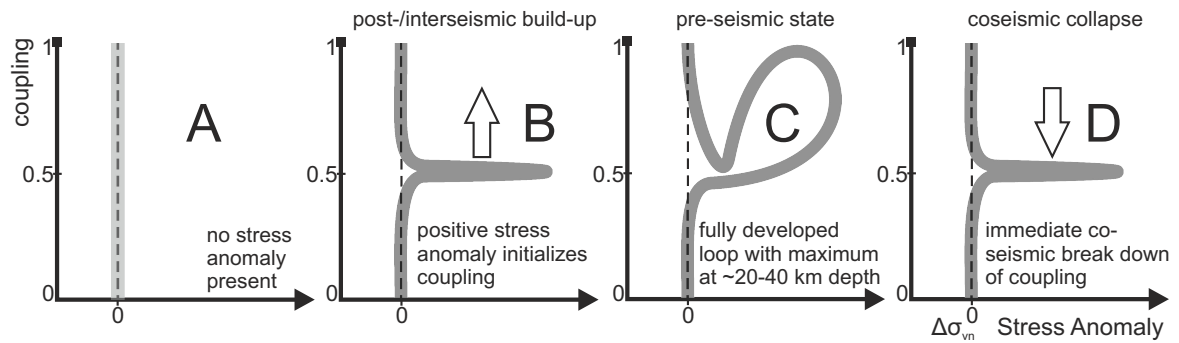


Figure 5.4: Schema describing the effect of stress anomalies on plate coupling. Note that on time scales of the seismic cycle, stress anomalies are to be considered constant whereas coupling is a time-variant parameter. In case A, no stress anomaly is present and all coupling data lie along the grey line from 1 (fully coupled) to 0 (stable sliding, no coupling). Considering the results shown in figure 5.3, the northernmost area between 18.75°S and 19.25°S shows a similar pattern and seems to be less affected by density anomalies. In case B (e.g. going southward from 19.25°S), excess masses lead to positive stress anomalies on the subduction interface, start to prevent stable sliding and increase coupling. At other places, i.e. 19.75°S–20.75°S, coupling may have risen so much that closed (overlapping) loops in the parameter space developed (case C). Areas of this type are most prone to events of high stress release since they have been gradually 'loaded' to a greater extent than other segments. By analogy with *Lay and Kanamori (1981)*'s description of asperities, it could be possible that an earthquake nucleates within a patch of type B and eventually propagates into an area of type C, where the major moment release takes place. Case D represents the immediate coseismic stress release. This state soon turns into the post- or inter-seismic state B again.

per-cent (cf. equation 5.2):

$$c_t \gtrsim \{\Delta\sigma_{vn} |_{\geq 0}\} \quad (5.2)$$

A much clearer picture of this possible relation will be achieved when future modelling of GPS signals is performed in order to obtain plate coupling coefficients also of the *post*-seismic phase during the seismic cycle. An observation of effective 'untying' of looped streplings could help to verify those as valid indicators of seismologically high-risk segments in a subduction zone. In addition, a more consistent geometry in the GPS-modelling procedure could help to strengthen the observations made in this approach as well as a density model with higher latitudinal resolution, i.e. more vertical sections in the IGMAS+-model with less latitudinal distance along the trench. Furthermore, other coupling models should be considered, as the available model used here did not allow for possible plate coupling below 80 km (*Metois et al., 2013*) as it may be argued from the abundant seismological activity at those depths in the eastern North Chile segment. Application of the combined analysis at other active margins like the Nicoya peninsula of Costa Rica or at the Japan-Pacific subduction zone could help to test the method, accordingly.

When the loops in the strepling diagrams are assumed to be a valid indicator of locked patches of increased risk to fail, then the above results imply that the coastal region south of ~24.7°S could be in increased danger to experience a major energy release through a

megathrust–earthquake (cf. figures 5.5 and 5.6). This area is located at the southern end of the 1995 M8.1 Antofagasta rupture and stretches further to the South into a ~250 km wide gap that has experienced 4 earthquakes in the magnitude 7 range over the past 150 years — but was not the centre of a significantly large one (in terms of this study). Towards the South, the last major hit in the Centennial catalogue is an M8.7 earthquake from 11 November 1922 that is listed at 28.5°S/70.8°W in the Southern Atacama province. According to studies of *Willis* (1929), this earthquake produced significant damage along more than 500 km of the coast. *Beck et al.* (1998) found that this segment of the subduction zone may have the capability to break in large multi–asperity events like in 1922, as well as clustered in smaller single events, as the historic record suggested.

However, if a projection can be made from the joint analysis of stress anomalies and coupling coefficients, the following is suggested:

1. Continued GNSS–observation of the Iquique segment is fundamental in order to get a post–seismic picture of the coupling for comparison with static stress anomalies as shown above.
2. In–depth studies of the post–seismic development of plate coupling south of the 2014 Pisagua earthquake towards the Mejillones peninsula should be considered for further studies. This refers to possible closure of strepling–loops (see above) and the theory that partly broken segments may 'load' or activate adjacent asperities.
3. The segment(s) south of the 1995 Antofagasta earthquake should be concerned in the medium term.
4. Time–sensitive monitoring of the onshore part of the study area with InSAR can assist GNSS–observations in order to identify coupled patches along the margin.

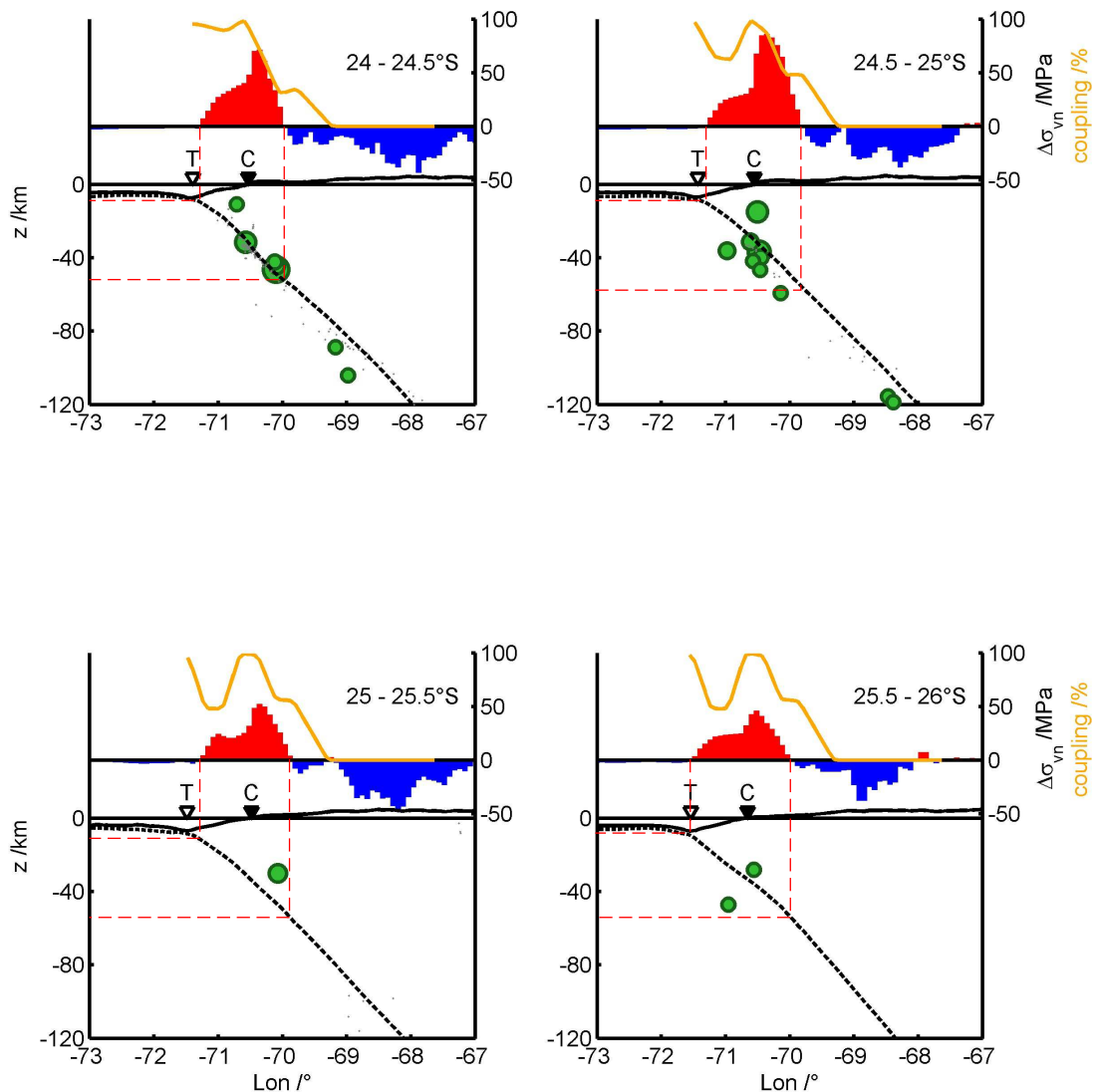


Figure 5.5: Vertical sections of average plate coupling and normal component of the vertical stress anomaly south of Antofagasta at 24–26°S by analogy with figure 5.1. Please note that coupling in per cent and stresses in units of MPa share the same positive vertical axis. The mean depth of the plate interface at the given latitude range was taken from the enhanced 3D density model and is shown as dashed black curve. Triangles entitled T and C mark the location of the trench and the coastline, respectively. It should be noted that coupling south of 24°S is less well constrained than towards the North.

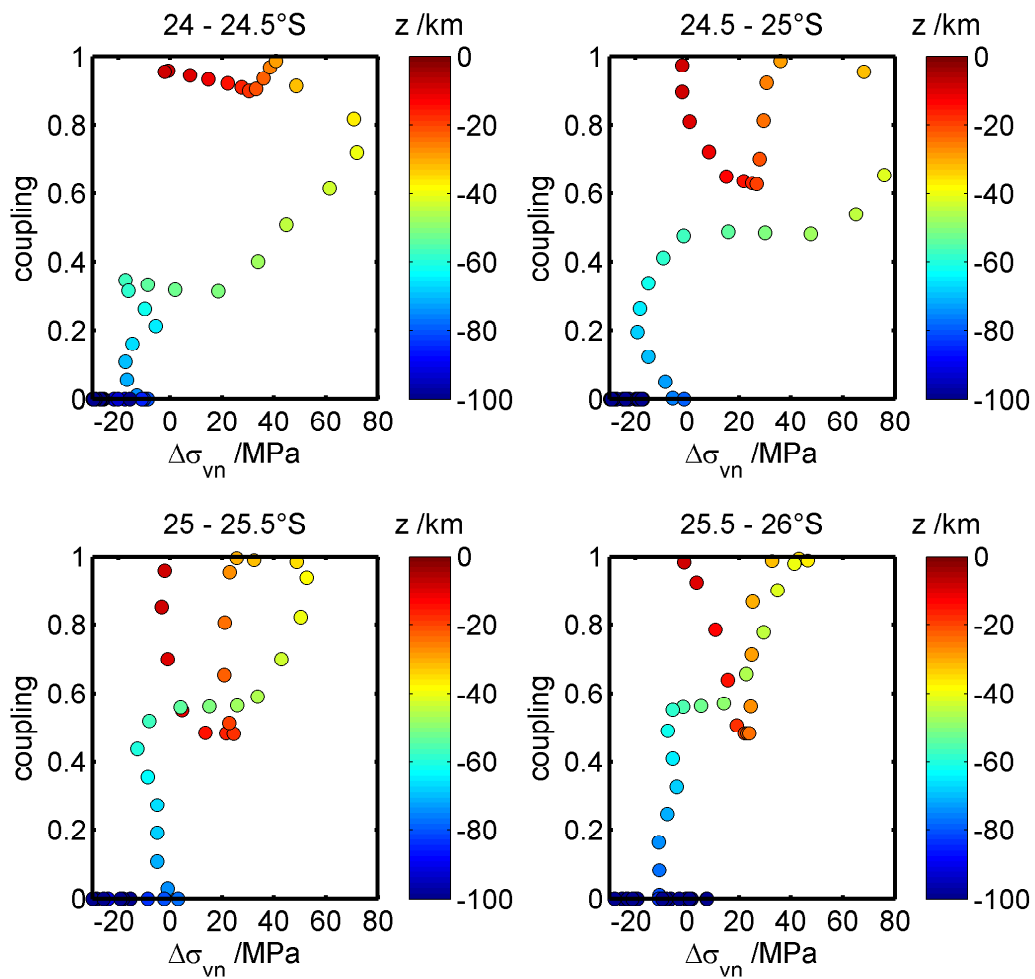


Figure 5.6: Plate coupling and stress anomaly loops south of Antofagasta at 24–26°S by analogy with figure 5.3. The parameter constellation at ~25°S is a fine example that corresponds to the 'fully developed loop' as shown in figure 5.4c: a regionally increased stress anomaly at depths of ~25–35 km correlates with high plate coupling. It should be noted that coupling south of 24°S is less well constrained than towards the North.

6 Concluding remarks and outlook

The geophysical nature of asperities in subduction zones has now been studied for several centuries. It seems to be understood that the forces behind plate tectonics are causatively related to the accumulation of strain energy. This is partially finally released through megathrust earthquakes and also hardly noticeable slow-slip events (*Hirose et al.*, 1999; *Dragert et al.*, 2001; *Schwartz and Rokosky*, 2007). It has become generally understood that portions of the interface between subducting- and overriding plates are periodically coupled and released during a seismic cycle on time scales of many decades to centuries. Highly coupled patches that extend up to hundreds of kilometres along the trench of a subduction zone may cause tsunami-generating earthquakes when asperities and the plate-composing material itself can no longer resist the accumulated strain energy of the plates. However, it has not been clearly identified to what extent the respective factors in question control plate coupling, i.e. are plate-roughness, interface properties, buoyancy effects or lithostatic stresses from the overriding plate the dominant factor.

In this work, the effect of excess masses within the overriding South-American continental plate on coupling with the incoming oceanic Nazca plate in North Chile (18–35°S) has been studied. A belt of high-density batholiths of an ancient Jurassic volcanic arc is supposed to reside here along and below the coast line. As lithostatic stress is a direct result of overlying masses, the density distribution of the South-American plate has been utilised by employing 3D density models from gravity forward-modelling of the study area. Pre-existing density models had been build based on gravity data from terrestrial measurements, what makes them — on a crustal scale — be high-resolution models at places where data exist. But the data have also been found to be extremely heterogeneously distributed in the Central Andes study area. Moreover, limited accuracy of former height measurements introduced errors into the calculation of free-air and Bouguer anomalies.

Having been part of the DFG priority program (SPP) 1257 *Mass Transport & Mass Distribution*, one goal of this work was therefore to analyse the applicability of gravity data from the GOCE satellite mission to the study of the lithosphere. Within the SPP's project NOGAPSGRAV, a theoretic analysis of the expected sensitivity and resolution was conducted. Based on projected values for GOCE-derived gravity and gradiometric tensor field models, it could be shown that the gradiometer system of the satellite could be just sensitive enough to resolve signals in the order of the supposed positive gravity gradient anomalies at

the continental margin. For gravity data, in contrast, it was demonstrated that anomalies at an orbit height of 250 km would not even be resolved in the case of an ideal parametrisation of density contrast and spatial extent of the causative masses. Furthermore, the significance of homogeneously distributed and recorded data was emphasised.

In this work, satellite-derived gravity- and gravity gradient data were at their limits when applied to resolve specific crustal structures within the lithosphere. But despite the disadvantageous spatial resolution, the GOCE gradiometer was sensitive enough in order to receive signal content that might be visible in the inverted gravity models. The combined application of gravity data from surface- and satellite measurements to studies of the Earth's crust and lithosphere, represented by the IMOSAGA01C regional combined gravity model (cf. chapter 4), yields clear benefits over the single use of one of the data types.

From today's perspective, GOCE represented the physically lowest satellite gravity mission possible (final orbit height of 235 km). Even if the error level would be decreased in future missions, a comparable measurement system can not get significantly closer to the source masses of the Earth. The derived gravity models will still be prone to the omission error at short wavelengths, which occurs when satellite data is represented at near surface levels (cf. e.g. *Ebbing et al.*, 2014).

One might speculate whether more advanced combinations of processing techniques and the utilization of other platforms, e.g. unmanned stratospheric vehicles or drones can one day overcome the unsolved challenges in this field. Such action between conventional airspace and satellite orbits would certainly give rise to complexities of political nature (claim to upper airspace and overflight rights, military interests and counter-intelligence etc.). Therefore, long-range sub-orbit concepts might need to be globally approved, led or accompanied by institutions and organisations like UNESCO, IUGG or Group on Earth Observations (GEO). National defence forces and air-space control would most likely have to be engaged and make the idea at least difficult to approach. On the European side there would be the need to discuss whether national air- and space agencies are capable of supporting such missions or the European Space Agency would expand its operational scope down below the thermosphere. Besides organisational challenges it would also have to be addressed to which extent e.g. turbulences at the respective altitudes could curtail the expectations of future gravity missions in-between the established altitudes. As long as a platform of this kind is not available, it appears fair to state that supra-aero gravity/gradient data alone are barely suitable to high-resolution crustal studies (well below 100 km resolution) but serve well as essential bases to high-quality combined gravity models.

Within the SPP's IMOSAGA project, GOCE satellite data were consequently used in form of the GOCO03S gravity field model in order to compute the IMOSAGA01C regional combined gravity field model at a constant level of 8 km above the GRS80 geocentric major radius (cf. chapter 4.1 and *Hosse et al.*, 2014). IMOSAGA01C brings together the use-

ful aspects of both types of measure: the high resolution of terrestrial gravity data and the unprecedented homogeneity of satellite data. In direct comparison to the high-resolution combined gravity field model EGM2008, IMOSAGA01C was shown to be of superior quality. This particularly holds for areas where both models depend on satellite-, or 'fill-in' data, because no terrestrial gravity data were available to neither of the gravity models at the respective areas (e.g., 30.3°S, cf. section 4.1.6).

The IMOSAGA01C model was then used to optimise the existing 3D density model of *Prezzi et al.* (2009) by gravity forward modelling and density inversion. The standard deviation of the residual anomaly could be reduced by more than 60% to $6.3 \times 10^{-5} \text{ m s}^{-2}$. Although some general improvement due to the application of an enhanced IGMAS+ modelling software (*Götze et al.*, 2010; *Schmidt et al.*, 2010) should also be considered, the main part of the improvement can be attributed to the application of the new combined gravity model: All changes to the existing geometry and parametrisation of the density model were applied within error bounds given by *Prezzi et al.* (2009) and under consideration of original constraining data.

Since the improvement of the model should inherently provide a more appropriate parametrisation of the lithosphere, the revised 3D density information was subsequently used as an input to the computation of static stresses on top of the subducting Nazca plate. The vertical stress component was determined in the meaning of lithostatic load without consideration of flexural effects. It was found appropriate to explicitly consider stress *anomalies* instead of absolute stress: Similar to previous work of *Tassara* (2010), the stress anomalies may be understood as the residual stress when compared to the effect of a standard density distribution at the same location. It may as well be interpreted as the absolute stress effect of the overlying density anomalies. In this work, this also comprised topographic loads, so that the resulting anomalies show the effect of all masses which deviate from a reference distribution. Furthermore, the interface-normal component of the vertical stress anomaly was derived by rotating the pressure vector perpendicular to the subduction interface of the optimised 3D density model.

A clear spatial correlation between major seismicity and the positive normal component of the vertical stress anomaly at the subduction interface was found. An overlay of the slip distribution of the 01 April 2014 Pisagua/Iquique event revealed a considerable congruence with stress anomalies. Both could be interpreted as strong indicators for the validity of the thesis that overlying masses may exert control over the locking of the subduction interface. The finding that this result for the normal-component of stress does not significantly differ from the vertical-component case can be attributed to the fact that the vertical fraction — at an subduction angle of up to $\sim 20^\circ$ — is still the dominant component.

A combined analysis of plate coupling coefficients from GNSS-modelling and the normal component of the vertical stress anomaly revealed that there seems to be no clear correlation

between coupling and stress anomalies, when seen as a static 'snap shot' for the entire active margin in North Chile. However, two significant findings have been made regarding the combined analysis of both parameters on top of the subducting plate:

- Firstly, a positive stress anomaly acts as a linear threshold to the minimum coupling coefficient at the same location. This means that for a given positive stress anomaly the minimum plate coupling could be estimated. If this holds true, it would also mean that there exist patches along the subduction zone that can — because of lithostatic load — hardly reach an un-coupled state during the inter-seismic phase of the seismic cycle.
- Secondly, plate coupling and stress anomalies form loop-like curves in their common parameter space, when plotted against each other for the same location, respectively. It has been found that a *closed* loop existed in the area of the 1st April 2014 earthquake offshore Pisagua but that it was *not* fully closed south of 21°S where the rupture area also stopped towards the south. In a similar picture — but with possibly larger extent — the region south of the 1995 Antofagasta earthquake shows large closed loops in the parameter space.

A sound and detailed physical explanation and interpretation to this finding is furthermore to be made. It should include Coulomb stress theory and Mohr's circle with both brittle and ductile conditions, allowing for varying temperature conditions. In the same context the issue of slow-slip events (*Hirose et al.*, 1999; *Dragert et al.*, 2001; *Schwartz and Rokosky*, 2007) is more closely to be addressed in continuation to this work.

Further GNSS-modelling and analysis of the post-seismic phase as well as studies at different subduction systems would be of particular interest. Generally, coupling results of additional GNSS-analyses from different study groups should be cross-checked in order to verify the validity of the findings made. Within this regard, it is of great importance to check the time-wise development of the stress-coupling parameter space. Consideration of InSAR data, e.g. from the SENTINEL missions of ESA (<https://sentinel.esa.int>), should add to the characterization of the respective patches along the active continental margin.

Additional data to be further utilized may come from magnetics and petrology. An interesting aspect in order to constrain the lithosphere in the domain of magnetics might be expected from the integration of both sole and combined fields of any near surface values and data of the SWARM satellite mission (www.esa.int/SWARM). With the latter, one needs to be aware of increased challenges with similar problems as with the GOCE mission: Because of the higher orbit altitude (460–300 km and 530 km, respectively) and because of the faster decay of the magnetic field/gradients with distance from magnetic sources, the

resulting satellite-only field models for the lithosphere will presumably not reach beyond a spatial resolution of d/o 150 or 200 at maximum (*DTU Space et al.*, 2013) and hence possibly not resolve very detailed structures within the crust. It remains to be seen whether variations in an elongated feature, like a hidden volcanic arc, can be expressed with these models when downward-continued to the near-surface. Dedicated aerial or high-cutted near surface magnetic field data along the Chilean coast should add to the improvement of 3D models, especially when it comes to a finer localization of relicts of the ancient volcanic arc above the subduction interface.

With the general idea of lithostatic coupling being validated geophysically, it needs also to be debated from a more petrological standpoint. However, it should once more be emphasised that the static-stress related observations made in this work depend on the amplitude of stress *anomalies* and *not absolute* stress. In terms of geodynamics this indicates that the Earth's lithosphere adapts itself to a more physically stable state in case of a present standard density distribution and that it tends to become less stable or predictable where the density-/stress distribution differs significantly from the normal condition — a very common (and expected) behaviour as specified by the description of stress-strain analysis.

Subduction zones are highly complex systems whose physical behaviour depends on numerous factors. This work does not oppose the role of the nature of a subduction interface itself, nor the effect of the nature of the incoming oceanic plate on the locking of the plates (e.g. roughness or age). But with the aid of a combination of terrestrial and satellite gravity data, it could be approved that it is very likely that the density distribution above the subducting plate is at least *one* controlling factor on the nature of the seismic cycle in North Chile.

Whether this is also the case at other active continental margins has to be analysed in future studies of, e.g., Costa Rica with focus on the Nicoya-peninsula area or the eastern margin of Japan's main island Honshū. The main fault of the southern Himalayas is an appropriate place to test the findings for the intracontinental collision case; supported by results of *Ader et al.* (2012) who summarise that microseismicity "drops under topography greater than 3500 m of elevation, i.e. where the principal Coulomb stresses become vertical".

The Cascadia subduction zone, where the Juan de Fuca Plate subducts beneath the North American Plate, may data-wise be considered one of the most fit study areas in order to test the existence of the parameter loops presented in chapter 5. *Romanyuk et al.* (1998) already set up density models between the Vancouver area and the state of Oregon. They derived "characteristics of isostatic imbalance" by applying a method which accounts for residual stresses caused by density inhomogeneities in a similar way as the calculation of static stress anomalies applied in the present work. Although the spatial resolution of their work is hardly comparable to the recent results of this present thesis, it should be noted that the order of magnitude of residual stresses at depth of the subducting plate interface is

identical.

The old models could be revised with more recent data and stresses be calculated based on the newer approach in much higher resolution and then be correlated with plate–coupling models for joint interpretation and risk assessment. If the approach presented in this work proves reliable also for other active margins, it might be considered to be included in deterministic methods of earthquake hazard estimation for risk evaluation, investment decision or emergency response preparation.

The geological evolution of an active margin's forearc, however, must generally be taken into account to be a key factor for today's asperity build–up as it potentially caused density anomalies in host units that, today, lie above and act on the subduction interface. For the North–Chile case, suchlike history is evident.

Though, varying proportions of asperity–controlling mechanisms are perfectly thinkable under differing conditions: An accretive subduction behaves differently from an erosive type. Varying fluid pathways may have considerably different impact on the frictional behaviour of an interface. And at some margins, oceanic bathymetry, plate age and buoyancy might add significantly more to the bill than at other systems. Thus, eventually, it may indeed be recognised that there is not such thing as *the one* standard behaviour of ocean–continent subduction systems. And that there is not *one* predominant controlling property. Instead, at different study areas, respectively, all suspect factors should be jointly surveyed and carefully weighted against each other — just as dynamic as the 'solid' Earth reveals itself to be.

References

- Ader, T., J.-P. Avouac, J. Liu-Zeng, H. Lyon-Caen, L. Bollinger, J. Galetzka, J. Genrich, M. Thomas, K. Chanard, S. N. Sapkota, et al. (2012), Convergence rate across the nepal himalaya and interseismic coupling on the main himalayan thrust: Implications for seismic hazard, *Journal of Geophysical Research: Solid Earth (1978–2012)*, 117(B4), doi:10.1029/2011JB009071.
- Alasonati-Tašárová, Z. (2007), Towards understanding the lithospheric structure of the southern Chilean subduction zone (36°S-42°S) and its role in the gravity field, *Geophys. J. Int.*, 170(3), 995–1014, doi:10.1111/j.1365-246X.2007.03466.x.
- Allmendinger, R. W., T. E. Jordan, S. M. Kay, and B. L. Isacks (1997), The Evolution of the Altiplano-Puna Plateau of the Central Andes, *Annu. Rev. Earth Planet. Sci.*, 25, 139–174.
- Alvarado, P., S. Beck, and G. Zandt (2007), Crustal structure of the south-central andes cordillera and backarc region from regional waveform modelling, *Geophysical Journal International*, 170(2), 858–875, doi:10.1111/j.1365-246x.2007.03452.x.
- Alvers, M. R., L. Barrio-Alvers, C. Bodor, H.-J. Götze, B. Lahmeyer, C. Plonka, and S. Schmidt (2015), Quo vadis inversion?, *first break*, 33(4), 65–74.
- Amante, C., and B. W. Eakins (2009), ETOPO1 1 Arc Minute Global Relief Model: Procedures, Data Sources and Analysis, *NOAA Technical Memorandum NESDIS NGDC-24*, p. 19 pp.
- ANCORP Working Group (2003), Seismic imaging of a convergent continental margin and plateau in the central andes (andean continental research project 1996 (ancorp'96)), *J. Geophys. Res.*, 108(B7), 2328, doi:10.1029/2002JB001771.
- Andersen, O. (2010), The dtu10 gravity field and mean sea surface, in *Second international symposium of the gravity field of the Earth (IGFS2)*, Fairbanks, Alaska.
- Andersen, O. B., and P. Knudsen (1998), Global marine gravity field from the ERS-1 and Geosat geodetic mission altimetry, *J. Geophys. Res.*, 103(C4), 8129–8137, doi:10.1029/97JC02198.

- Andersen, O. B., and P. Knudsen (2008), The dns08 global mean sea surface and bathymetry, *EGU 2008, Vienna, Austria*.
- Andersen, O. B., and P. Knudsen (2009), Dns08 mean sea surface and mean dynamic topography models, *Journal of Geophysical Research*, *114*(C11), doi:10.1029/2008jc005179.
- Aochi, H., R. Madariaga, and E. Fukuyama (2003), Constraint of fault parameters inferred from nonplanar fault modeling, *Geochem. Geophys. Geosyst.*, *4*(2), 1020, 16 pp., doi: 10.1029/2001GC000207.
- Arroyo, I. G., S. Husen, E. R. Flueh, J. Gossler, E. Kissling, and G. E. Alvarado (2009), Three-dimensional P-wave velocity structure on the shallow part of the Central Costa Rican Pacific margin from local earthquake tomography using off- and onshore networks, *Geophysical Journal International*, *179*(2), 827–849, doi:10.1111/j.1365-246X.2009.04342.x.
- Babeyko, A., and S. Sobolev (2008), High-resolution numerical modeling of stress distribution in visco-elasto-plastic subducting slabs, *Lithos*, *103*(1), 205–216.
- Babeyko, A. Y., S. V. Sobolev, T. Vietor, O. Oncken, and R. B. Trumbull (2006), Numerical Study of Weakening Processes in the Central Andean Back-Arc., in *The Andes –active subduction orogeny.*, edited by O. Oncken, G. Chong, G. Franz, P. Giese, H.-J. Götze, V. Ramos, M. Strecker, and P. Wigger, *Frontiers in Earth Science*, pp. 495–512, Springer-Verlag, Berlin Heidelberg New York.
- Barckhausen, U., H. A. Roeser, and R. von Huene (1998), Magnetic signature of upper plate structures and subducting seamounts at the convergent margin off Costa Rica, *J. Geophys. Res.*, *103*(B4), 7079–7093, doi:10.1029/98JB00163.
- Barthelmes, F. (2009), Definition of Functionals of the Geopotential and Their Calculation from Spherical Harmonic Models: Theory and formulas used by the calculation service of the International Centre for Global Earth Models (ICGEM), <http://icgem.gfz-potsdam.de>, *Tech. rep.*, GeoForschungsZentrum-Potsdam, GERMANY.
- Beck, S., S. Barrientos, E. Kausel, and M. Reyes (1998), Source characteristics of historic earthquakes along the central Chile subduction zone, *Journal of South American Earth Sciences*, *11*(2), 115–129, doi:10.1016/S0895-9811(98)00005-4.
- Béjar-Pizarro, M., A. Socquet, R. Armijo, D. Carrizo, J. Genrich, and M. Simons (2013), Andean structural control on interseismic coupling in the north Chile subduction zone, *Nature Geoscience*, *6*, 462–467, doi:10.1038/ngeo1802.

- Berry, P. A. M., R. G. Smith, and J. Benveniste (2010), Ace2: the new global digital elevation model, in *Gravity, geoid and earth observation, International Association of Geodesy Symposia*, vol. 135, edited by S. P. Mertikas, pp. 231–237, Springer Berlin Heidelberg, doi:10.1007/978-3-642-10634-7_30.
- Bohm, M., S. Lüth, H. Echtler, G. Asch, K. Bataille, C. Bruhn, A. Rietbrock, and P. Wigger (2002), The southern andes between 36° and 40°s latitude: seismicity and average seismic velocities, *Tectonophysics*, 356(4), 275–289, doi:10.1016/S0040-1951(02)00399-2.
- Bolge, L. L., M. J. Carr, K. I. Milidakis, F. N. Lindsay, and M. D. Feigenson (2009), Correlating geochemistry, tectonics, and volcanic volume along the central american volcanic front, *Geochem. Geophys. Geosyst.*, 10(12), Q12S18, doi:10.1029/2009GC002704.
- Bonnardot, M.-A., R. Hassani, E. Tric, E. Ruellan, and M. Régnier (2008), Effect of margin curvature on plate deformation in a 3-d numerical model of subduction zones, *Geophys. J. Int.*, 173(3), 1084–1094, doi:10.1111/j.1365-246X.2008.03752.x.
- Bonvalot, S., G. Balmino, A. Briais, M. Kuhn, A. Peyrefitte, N. Vales, R. Biancale, G. Gabalda, G. Moreaux, F. Reinquin, and M. Sarrailh (2012), World gravity map, 1:50000000, *Tech. rep.*, BGI-CGMW-CNES-IRD. Paris, 2012.
- Boutelier, D., and O. Oncken (2010), Role of the plate margin curvature in the plateau buildup: Consequences for the central andes, *J. of Geophys. Res.: Solid Earth*, 115(B4), doi:10.1029/2009JB006296.
- Braitenberg, C., P. Mariani, and T. Pivetta (2011), Goce observations in exploration geophysics, in *Proceedings of the 4th International GOCE User Workshop*, vol. SP-696, edited by L. Ouwehand, ESA.
- Brasse, H., G. Kapinos, L. Mütschard, G. E. Alvarado, T. Worzewski, and M. Jegen (2009), Deep electrical resistivity structure of northwestern Costa Rica, *Geophys. Res. Lett.*, 36(2), L02,310, doi:10.1029/2008GL036397.
- Buske, S., S. Lüth, H. Meyer, R. Patzig, C. Reichert, S. Shapiro, P. Wigger, and M. Yoon (2002), Broad depth range seismic imaging of the subducted nazca slab, north chile, *Tectonophysics*, 350(4), 273–282, doi:10.1016/S0040-1951(02)00117-8.
- Byrne, D. E., D. M. Davis, and L. R. Sykes (1988), Loci and maximum size of thrust earthquakes and the mechanics of the shallow region of subduction zones, *Tectonics*, 7(4), 833–857, doi:10.1029/TC007i004p00833.
- Chlieh, M., J. B. De Chabalier, J. C. Ruegg, R. Armijo, R. Dmowska, J. Campos, and K. L. Feigl (2004), Crustal deformation and fault slip during the seismic cycle in the north chile

- subduction zone, from gps and insar observations, *Geophysical Journal International*, 158(2), 695–711.
- Cloos, M. (1992), Thrust-type subduction-zone earthquakes and seamount asperities; a physical model for seismic rupture, *Geology*, 20(7), 601–604, doi:10.1130/0091-7613(1992)020<0601:TTSZEA>2.3.CO;2.
- Coblentz, D. D., R. M. Richardson, and M. Sandiford (1994), On the gravitational potential of the earth's lithosphere, *Tectonics*, 13(4), 929–945, doi:10.1029/94tc01033.
- Comte, D., M. Pardo, L. Dorbath, C. Dorbath, H. Haessler, L. Rivera, A. Cisternas, and L. Ponce (1994), Determination of seismogenic interplate contact zone and crustal seismicity around antofagasta, northern Chile using local data, *Geophys. J. Int.*, 116(3), 553–561, doi:10.1111/j.1365-246x.1994.tb03279.x.
- Dahlen, F. A. (1984), Noncohesive critical coulomb wedges: An exact solution, *J. Geophys. Res.*, 89(B12), 10,125–10,133, doi:10.1029/jb089ib12p10125.
- DeMets, C., R. G. Gordon, D. F. Argus, and S. Stein (1994), Effect of recent revisions to the geomagnetic reversal timescale, *Geophys. Res. Lett.*, 21, 2191–2194.
- DeShon, H. R., S. Y. Schwartz, S. L. Bilek, L. M. Dorman, V. Gonzalez, J. M. Protti, E. R. Flueh, and T. H. Dixon (2003), Seismogenic zone structure of the southern Middle America Trench, Costa Rica, *J. Geophys. Res.*, 108(B10), 2491, 14 pp., doi: 10.1029/2002JB002294.
- Dragert, H., K. Wang, and T. S. James (2001), A silent slip event on the deeper cascadia subduction interface, *Science*, 292(5521), 1525–1528, doi:10.1126/science.1060152.
- Drinkwater, M., R. Floberghagen, R. Haagmans, D. Muzi, and A. Popescu (2003), Goce: Esa's first earth explorer core mission, in *Earth Gravity Field from Space —from Sensors to Earth Sciences*, *Space Sciences Series of ISSI*, vol. 17, edited by G. Beutler, M. Drinkwater, R. Rummel, and R. von Steiger, pp. 419–432, Kluwer Academic Publishers, Dordrecht, The Netherlands.
- DTU Space et al. (2013), Swarm level 2 processing system – product specification for L2 products and auxiliary products, *Tech. Rep. SW-DS-DTU-GS-0001*, DTU National Space Institute, Denmark.
- Ebbing, J., N. Holzrichter, R. Abdul Fattah, and J. Meekees (2014), Goce+ geoexplore impact assessment, *Impact Assessment 1.1, Doc-ID RP-GOCE+-DNT-08*, DGFI, NGU, TNO and CAU.

- Fecher, T., R. Pail, and T. Gruber (2013), Global gravity field modeling based on goce and complementary gravity data, *International Journal of Applied Earth Observation and Geoinformation*, doi:10.1016/j.jag.2013.10.005, in Press.
- Fedi, M., L. Ferranti, G. Florio, I. Giori, and F. Italiano (2005), Understanding the structural setting in the southern apennines (italy): insight from gravity gradient tensor, *Tectonophysics*, 397(1-2), 21 – 36, doi:10.1016/j.tecto.2004.10.012, integration of Geophysical and Geological Data and Numerical Models in Basins.
- Feng, M., S. van der Lee, and M. Assumpção (2007), Upper mantle structure of South America from joint inversion of waveforms and fundamental mode group velocities of Rayleigh waves, *Journal of Geophysical Research*, 112(B4), doi:10.1029/2006jb004449.
- Finn, C. (1994), Aeromagnetic evidence for a buried early cretaceous magmatic arc, north-east japan, *Journal of Geophysical Research*, 99(B11), 22,165–22,185, doi:10.1029/94JB00855.
- Flesch, L. M., and C. Kreemer (2010), Gravitational potential energy and regional stress and strain rate fields for continental plateaus: Examples from the central andes and colorado plateau, *Tectonophysics*, 482(1-4), 182–192, doi:10.1016/j.tecto.2009.07.014.
- Forsberg, R. (1984), A study of terrain reductions, density anomalies and geophysical inversion methods in gravity field modelling, *Tech. rep.*, DTIC Document, The Ohio State University, Columbus, Ohio.
- Förste, C., F. Flechtner, R. Schmidt, R. Stubenvoll, M. Rothacher, J. Kusche, K.-H. Neumayer, R. Biancale, J.-M. Lemoine, F. Barthelmes, S. Bruinsma, R. König, and U. Meyer (2008), Eigen-g105c —a new global combined high-resolution grace-based gravity field model of the gfz-grgs cooperation, in *Geophysical Research Abstracts*, vol. 10(2008), pp. EGU2008–A–06,944.
- Förste, C., S. L. Bruinsma, F. Flechtner, et al. (2012), A preliminary update of the Direct Approach GOCE Processing and a new release of EIGEN-6C, in *AGU 2012 Fall Meeting*, AGU, San Francisco, USA.
- Forsyth, D., and S. Uyeda (1975), On the relative importance of the driving forces of plate motion, *Geophys. J. Int.*, 43(1), 163–200, doi:10.1111/j.1365-246X.1975.tb00631.x.
- Fuller, C. W., S. D. Willett, and M. T. Brandon (2006), Formation of forearc basins and their influence on subduction zone earthquakes, *Geology*, 34(2), 65–68, doi:10.1130/G21828.1.
- Ghosh, A., W. E. Holt, L. M. Flesch, and A. J. Haines (2006), Gravitational potential energy of the tibetan plateau and the forces driving the indian plate, *Geology*, 34(5), 321–324.

- Giese, P., G. Asch, H. Brasse, H. Götze, C. Haberland, and P. Wigger (1999), Procesos geodinámicos en los andes centrales, representados mediante observaciones geofísicas, in *Geología del Noroeste Argentino, Relatorio, Tomo I*, edited by G. G. B., R. Omarini, and J. Viramonte, pp. 15–17, Salta.
- Gisinger, C. (2010), Vorwärtsmodellierung des Schwerefeldes zur Analyse von Eismassenvariationen am Beispiel Novaya Zemlya, Master's thesis, TU Graz.
- Götze, H.-J., and A. Kirchner (1997), Interpretation of gravity and geoid in the central andes between 20 and 29 s, *Journal of South American Earth Sciences*, 10(2), 179–188.
- Götze, H.-J., and S. Krause (2002), The Central Andean gravity high, a relic of an old subduction complex?, *Journal of South American Earth Sciences*, 14(8), 799–811, doi:10.1016/S0895-9811(01)00077-3.
- Götze, H.-J., and B. Lahmeyer (1988), Application of three-dimensional interactive modeling in gravity and magnetics, *Geophysics*, 53(8), 1096–1108, doi:10.1190/1.1442546.
- Götze, H.-J., B. Lahmeyer, S. Schmidt, S. Strunk, and M. Araneda (1990), Central andes gravity data base, *Eos, Trans. AGU*, 71(16), 401–407, doi:10.1029/90EO00148.
- Götze, H.-J., B. Meurers, S. Schmidt, and P. Steinhauser (1991), On the isostatic state of the eastern alps and the central andes: A statistical comparison, *GSA Special Paper*, 265, 279–290.
- Götze, H.-J., B. Lahmeyer, S. Schmidt, and S. Strunk (1994), The lithospheric structure of the central andes (20–26 s) as inferred from interpretation of regional gravity, in *Tectonics of the southern Central Andes – Structure and Evolution of an Active Continental Margin*, edited by K. Reutter, E. Scheuber, and P. Wigger, pp. 7–21, Springer.
- Götze, H.-J., S. Schmidt, C. Fichler, and C. Plonka (2010), Igmast+ a new 3d gravity, FTG and magnetic modeling software, in *Geophysical Research Abstracts (12)*, EGU2010-1306, p. 1306, EGU General Assembly 2010.
- Götze, H.-J., M. Afanasjew, M. Alvers, L. Barrio-Alvers, R.-U. Börner, C. Brandes, R. Eröss, P. Menzel, U. Meyer, M. Scheunert, B. Siemon, K. Spitzer, D. Steinmetz, J. Stoll, G. Sudha, B. Tezkan, A. Ullmann, and J. Winsemann (2014), Towards an integrative inversion and interpretation of airborne and terrestrial data, in *Tomography of the Earths Crust: From Geophysical Sounding to Real-Time Monitoring*, edited by M. Weber and U. Münch, Advanced Technologies in Earth Sciences, pp. 21–41, Springer International Publishing, doi:10.1007/978-3-319-04205-3_2.

- Gregory-Wodzicki, K. M. (2000), Uplift history of the central and northern andes: a review, *Geological Society of America Bulletin*, 112(7), 1091–1105, doi:10.1130/0016-7606(2000)112<1091:UHOTCA>2.0.CO;2.
- Grombein, T., K. Seitz, and B. Heck (2011), Modelling topographic effects in goce gravity gradients, in *Observation of the System Earth from Space*, vol. 17, edited by U. Münch and W. Dransch, pp. 84–93, GEOTECHNOLOGIEN Science Report, doi:10.2312/GFZ.gt.17.13.
- Grombein, T., K. Seitz, and B. Heck (2014a), Topographic-isostatic reduction of goce gravity gradients, in *Earth on the Edge: Science for a Sustainable Planet, International Association of Geodesy Symposia*, vol. 139, edited by C. Rizos and P. Willis, pp. 349–356, Springer Berlin Heidelberg, doi:10.1007/978-3-642-37222-3_46.
- Grombein, T., X. Luo, K. Seitz, and B. Heck (2014b), A wavelet-based assessment of topographic-isostatic reductions for goce gravity gradients, *Surveys in Geophysics*, pp. 1–24, doi:10.1007/s10712-014-9283-1.
- Gutknecht, B. D. (2008), Gradiometrische Untersuchungen anhand eines variablen Dichteanomalie-Modells in homogener und inhomogener Umgebung, *F-Praktikum-Arbeit*, Institut für Geowissenschaften, Geophysik, Christian-Albrechts-Universität zu Kiel.
- Gutknecht, B. D. (2011), Lithospheric modelling by using optimized goce gravity gradient data, in *Proceedings of the 4th International GOCE User Workshop*, vol. SP-696, edited by L. Ouwehand, ESA.
- Gutknecht, B. D., H.-J. Götze, T. Jahr, G. Jentsch, R. Mahatsente, and S. Zeumann (2014), Structure and state of stress of the chilean subduction zone from terrestrial and satellite-derived gravity and gravity gradient data, *Surveys in Geophysics*, 35(6), 1417–1440, doi:10.1007/s10712-014-9296-9.
- Gutscher, M.-A., W. Spakman, H. Bijwaard, and E. R. Engdahl (2000), "geodynamics of flat subduction: Seismicity and tomographic constraints from the andean margin", *Tectonics*, 19(5), 814–833, doi:10.1029/1999TC001152.
- Haase, C. (2008), Inversion of gravity, gravity gradient, and magnetic data with application to subsalt imaging, Diploma thesis, Christian-Albrechts-Universität zu Kiel, Mathematisch-Naturwissenschaftliche Fakultät, Institut für Geowissenschaften, Kiel, Germany.
- Haase, C. (2014), On the inversion of potential field data: physical property estimations and model geometry changes, Dissertation, Christian-Albrechts-Universität zu Kiel, Kiel, Germany.

- Hackney, R., H. Echtler, G. Franz, H.-J. Götze, F. Lucassen, D. Marchenko, D. Melnick, U. Meyer, S. Schmidt, Z. Tašárová, A. Tassara, and S. Wienecke (2006), The segmented overriding plate and coupling at the south-central Chile margin, in *The Andes – Active Subduction Orogeny*, *Frontiers in Earth Science Series*, vol. 1, edited by O. Oncken, G. Chong, G. Franz, P. Giese, H.-J. Götze, V. Ramos, M. Strecker, and P. Wigger, pp. 355–374, Springer-Verlag, Berlin Heidelberg New York.
- Hackney, R. I., and W. E. Featherstone (2003), Geodetic versus geophysical perspectives of the 'gravity anomaly', *Geophysical Journal International*, *154*(1), 35–43, doi:10.1046/j.1365-246X.2003.01941.x, 1365-246X.
- Hampel, A., and A. Pfiffner (2006), Relative importance of trenchward upper plate motion and friction along the plate interface for the topographic evolution of subduction-related mountain belts, *SPECIAL PUBLICATION-GEOLOGICAL SOCIETY OF LONDON*, *253*, 105–115.
- Haschke, M., E. Scheuber, A. Günther, and K.-J. Reutter (2002), Evolutionary cycles during the andean orogeny: repeated slab breakoff and flat subduction?, *Terra nova*, *14*(1), 49–55, doi:10.1046/j.1365-3121.2002.00387.x.
- Heidbach, O., M. Tingay, A. Barth, J. Reinecker, D. Kurfeß, and B. Müller (2008), The world stress map database release 2008, *WSM. Rel2008*, doi:10.1594/GFZ.
- Heiskanen, W. A., and H. Moritz (1967), *Physical geodesy*, WH Freeman and Company, San Francisco, San Francisco, Calif.
- Herceg, M., P. Knudsen, and C. C. Tscherning (2014), Goce data for local geoid enhancement, in *International Association of Geodesy Symposia, Geoid and Height Systems GGHS 2012, Venice, Italy*, vol. 141, Springer.
- Heuret, A., and S. Lallemand (2005), Plate motions, slab dynamics and back-arc deformation, *Physics of The Earth and Planetary Interiors*, *149*(1-2), 31 – 51, doi:10.1016/j.pepi.2004.08.022, Thermal Structure and Dynamics of Subduction Zones: Insights from Observations and Modeling.
- Hirose, H., K. Hirahara, F. Kimata, N. Fujii, and S. Miyazaki (1999), A slow thrust slip event following the two 1996 hyuganada earthquakes beneath the bungo channel, southwest japan, *Geophysical Research Letters*, *26*(21), 3237–3240, doi:10.1029/1999GL010999.
- Holstein, H., E. M. Sherratt, and A. B. Reid (2007), Gravimagnetic field tensor gradiometry formulas for uniform polyhedra, *SEG Technical Program Expanded Abstracts*, *26*(1), 750–754, doi:10.1190/1.2792522.

- Holzrichter, N. (2013), Processing and interpretation of satellite and ground based gravity data at different lithospheric scales, Dissertation, Christian-Albrechts-Universität zu Kiel.
- Hosse, M., R. Pail, M. Horwath, N. Holzrichter, and B. D. Gutknecht (2014), Combined regional gravity model of the andean convergent subduction zone and its application to crustal density modelling in active plate margins, *Surveys in Geophysics*, 35(6), 1393–1415, doi:10.1007/s10712-014-9307-x.
- Husen, S. (1999), Local Earthquake Tomography of a Convergent Margin, North Chile: A combined on- and offshore study, Ph.D. thesis, Christian-Albrechts Univ., Kiel, Germany.
- Husen, S., E. Kissling, E. Flueh, and G. Asch (1999), Accurate hypocentre determination in the seismogenic zone of the subducting nazca plate in northern Chile using a combined on-/offshore network, *Geophysical Journal International*, 138(3), 687–701, doi:10.1046/j.1365-246x.1999.00893.x.
- Husen, S., R. Quintero, E. Kissling, and B. Hacker (2003), Subduction-zone structure and magmatic processes beneath Costa Rica constrained by local earthquake tomography and petrological modelling, *Geophysical Journal International*, 155(1), 11–32, doi:10.1046/j.1365-246X.2003.01984.x.
- Jones, C. H., J. R. Unruh, and L. J. Sonder (1996), The role of gravitational potential energy in active deformation in the southwestern united states, *Nature*, 381(6577), 37–41, doi: 10.1038/381037a0.
- Jordan, T. E., J. H. Reynolds III, and J. P. Erikson (1997), Variability in age of initial shortening and uplift in the central andes, in *Tectonic uplift and climate change*, edited by W. Ruddiman, pp. 41–61, Springer, Plenum Press, New York.
- Kendrick, E., M. Bevis, R. Smalley, and B. Brooks (2001), An integrated crustal velocity field for the central andes, *Geochem. Geophys. Geosyst.*, 2(11), doi:10.1029/2001gc000191.
- Kirby, S., E. R. Engdahl, and R. Denlinger (1996), Intermediate-depth intraslab earthquakes and arc volcanism as physical expressions of crustal and uppermost mantle metamorphism in subducting slabs, in *Subduction: Top to Bottom*, vol. Geophysical Monograph 96, edited by G. E. Bebout, D. W. Scholl, S. H. Kirby, and J. P. Platt, pp. 195–214, American Geophysical Union.
- Kirchner, A., H. J. Götze, and M. Schmitz (1996), 3d-density modelling with seismic constraints in the central andes, *Physics and Chemistry of The Earth*, 21(4), 289 – 293, doi: 10.1016/S0079-1946(97)00050-5.

- Klotz, J., G. Khazaradze, D. Angermann, C. Reigber, R. Perdomo, and O. Cifuentes (2001), Earthquake cycle dominates contemporary crustal deformation in central and southern andes, *Earth and Planetary Science Letters*, 193(3-4), 437–446, doi:10.1016/S0012-821X(01)00532-5.
- Klotz, J., A. Abolghasem, G. Khazaradze, B. Heinze, T. Vietor, R. Hackney, K. Bataille, R. Maturana, J. Viramonte, and R. Perdomo (2006), Long-Term Signals in the Present-Day Deformation Field of the Central and Southern Andes and Constraints on the Viscosity of the Earth's Upper Mantle, in *The Andes – active subduction orogeny*, *Frontiers in Earth Science Series*, vol. 1, edited by O. Oncken, G. Chong, G. Franz, P. Giese, H.-J. Götze, V. Ramos, M. Strecker, and P. Wigger, pp. 65–69, Springer-Verlag, Berlin Heidelberg New York.
- Köther, N., H.-J. Götze, B. Gutknecht, T. Jahr, G. Jentzsch, O. Lücke, R. Mahatsente, R. Sharma, and S. Zeumann (2012), The seismically active andean and central American margins: Can satellite gravity map lithospheric structures?, *Journal of Geodynamics*, 59-60, 207–218, doi:10.1016/j.jog.2011.11.004.
- Krarpup, T. (1969), A contribution to the mathematical foundation of physical geodesy., *Geod. Inst. Copenhagen, Medd., No. 44, 80 p., 44.*
- Kukowski, N., and O. Oncken (2006), Subduction Erosion – the "Normal" Mode of Fore-Arc Material Transfer along the Chilean Margin?, in *The Andes – Active Subduction Orogeny*, edited by O. Oncken, G. Chong, G. Franz, P. Giese, H. J. Götze, V. A. Ramos, M. Strecker, and P. Wigger, *Frontiers in Earth Science Series*, pp. 217–236, Springer-Verlag, Berlin Heidelberg New York, doi:10.1007/978-3-540-48684-8_10.
- Kusche, J., V. Klemann, and W. Bosch (2012), Mass distribution and mass transport in the earth system, *Journal of Geodynamics*, 59, 1–8, doi:http://dx.doi.org/10.1016/j.jog.2012.03.003.
- Kusche, J., V. Klemann, and N. Sneeuw (2014), Mass distribution and mass transport in the earth system: Recent scientific progress due to interdisciplinary research, *Surveys in Geophysics*, 35(6), 1243–1249, doi:10.1007/s10712-014-9308-9.
- Lamb, S., and P. Davis (2003), Cenozoic climate change as a possible cause for the rise of the Andes, *Nature*, 425(6960), 792–797, doi:10.1038/nature02049.
- Lay, T., and H. Kanamori (1981), An Asperity Model of Large Earthquake Sequences, in *Earthquake Prediction: An International Review*, edited by D. W. Simpson and P. G. Richards, pp. 579–592, AGU.

- Lessel, K. (1997), Die Krustenstruktur der zentralen Anden in Nordchile (21 - 24°S), abgeleitet aus 3D-Modellierungen refraktionsseismischer Daten, Ph.D. thesis, Freie Universität Berlin, Berlin, berliner Geowissenschaftliche Abhandlungen Reihe B, Geophysik, 31, 185pp.
- Li, X., and H.-J. Götze (2001), Ellipsoid, geoid, gravity, geodesy, and geophysics, *Geophysics*, 66(6), 1660–1668, doi:10.1190/1.1487109.
- Lithgow-Bertelloni, C., and M. A. Richards (1998), The dynamics of cenozoic and mesozoic plate motions, *Reviews of Geophysics*, 36(1), 27–78, doi:10.1029/97rg02282.
- Liu, M., Y. Yang, S. Stein, and E. Klosko (2002), Crustal shortening and extension in the central andes: Insights from a viscoelastic model, in *Plate Boundary Zones, Geodynamics Series*, vol. 30, edited by S. Stein and J. T. Freymueller, pp. 325–339, American Geophysical Union, Washington, D.C., doi:10.1029/GD030p0325.
- Lonsdale, P. (2005), Creation of the cocos and nazca plates by fission of the farallon plate, *Tectonophysics*, 404(3-4), 237 – 264, doi:10.1016/j.tecto.2005.05.011.
- Lücke, O. H., H.-J. Götze, and G. E. Alvarado (2010), A Constrained 3D Density Model of the Upper Crust from Gravity Data Interpretation for Central Costa Rica, *International Journal of Geophysics*, 2010, 9 pp., doi:10.1155/2010/860902, article ID 860902.
- Lüth, S., P. Wigger, M. Araneda, G. Asch, K. Bataille, M. Bohm, C. Bruhn, P. Giese, S. Lüth, J. Quezada, and A. Rietbrock (2003), A crustal model along 39°s from a seismic refraction profile—issa 2000, *Revista Geológica de Chile*, 30(1), 83–101, doi: 10.4067/S0716-02082003000100006.
- Madariaga, R., and A. Cochard (1996), Dynamic friction and the origin of the complexity of earthquake sources, *Proceedings of the National Academy of Sciences of the United States of America*, 93(9), 3819–24.
- Mader, K. (1951), Das newtonsche raumpotential prismatischer körper und seine ableitungen bis zur dritten ordnung, *Sonderheft 11 der Österreichischen Zeitschrift für Vermessungswesen*.
- Mahatsente, R., G. Ranalli, D. Bolte, and H.-J. Götze (2012), On the relation between lithospheric strength and ridge push transmission in the nazca plate, *Journal of Geodynamics*, 53, 18–26, doi:10.1016/j.jog.2011.08.002.
- Marsan, D. (2006), Can coseismic stress variability suppress seismicity shadows? insights from a rate-and-state friction model, *J. Geophys. Res.*, 111(B6), B06,305, doi:10.1029/2005JB004060.

- Mayer-Guerr, T. (2007), ITG-Grace03s: The latest GRACE gravity field solution computed in Bonn, in *GSTM+SPP conference*.
- Mayer-Gürr, T., D. Rieser, E. Höck, J. Brockmann, W. Schuh, I. Krasbutter, J. Kusche, A. Maier, S. Krauss, W. Hausleitner, O. Baur, A. Jäggi, U. Meyer, L. Prange, R. Pail, T. Fechner, and T. Gruber (2012), The new combined satellite only model goco03s, in *International Symposium on Gravity, Geoid and Height Systems GGHS2012*, S2-183, Venice, Italy.
- Menzel, P. (2015), CIDRe – a parameter constrained irregular resampling method for scattered point data, *Computers & Geosciences*, *submitted*.
- Meschede, M., U. Barckhausen, and H.-U. Worm (1998), Extinct spreading on the cocos ridge, *Terra Nova*, *10*(4), 211–216, doi:10.1046/j.1365-3121.1998.00195.x.
- Metois, M., A. Socquet, C. Vigny, D. Carrizo, S. Peyrat, A. Delorme, E. Maureira, M.-C. Valderas-Bermejo, and I. Ortega (2013), Revisiting the north Chile seismic gap segmentation using GPS-derived interseismic coupling, *Geophysical Journal International*, *194*(3), 1283–1294, doi:10.1093/gji/ggt183.
- Migliaccio, F., M. Reguzzoni, and F. Sansò (2004), Space-wise approach to satellite gravity field determination in the presence of coloured noise, *Journal of Geodesy*, *78*(4-5), 304–313, doi:10.1007/s00190-004-0396-z.
- Moritz, H. (1972), *Advanced least-squares methods*, vol. 175, Department of Geodetic Science, Ohio State University Columbus.
- Moritz, H. (1978), Least-squares collocation, *Reviews of geophysics*, *16*(3), 421–430.
- Norabuena, E. O., T. H. Dixon, S. Stein, and C. G. A. Harrison (1999), Decelerating nazca–south america and nazca–pacific plate motions, *Geophys. Res. Lett.*, *26*(22), 3405–3408, doi:10.1029/1999GL005394.
- Novák, P., and R. Tenzer (2013), Gravitational gradients at satellite altitudes in global geophysical studies, *Surveys in Geophysics*, *34*(5), 653–673, doi:10.1007/s10712-013-9243-1.
- Oncken, O., G. Asch, C. Haberland, J. Metchie, S. Sobolev, M. Stiller, X. Yuan, H. Brasse, S. Buske, P. Giese, and et al. (2003), Seismic imaging of a convergent continental margin and plateau in the central andes (andean continental research project 1996 (ancorp'96)), *J. Geophys. Res. Solid Earth*, *108*(B7), 2328, doi:10.1029/2002jb001771.

- Oncken, O., G. Chong, G. Franz, P. Giese, H.-J. Götze, V. Ramos, M. Strecker, and P. Wigger (2006), *The Andes –Active Subduction Orogeny*, *Frontiers in Earth Science Series*, vol. 1, 567pp. pp., Springer-Verlag, Berlin Heidelberg New York.
- Ortlieb, L., C. Zazo, J. Goy, C. Hillaire-Marcel, B. Ghaleb, and L. Cournoyer (1996), Coastal deformation and sea-level changes in the northern Chile subduction area (23°s) during the last 330 ky, *Quaternary Science Reviews*, 15(8-9), 819–831, doi:10.1016/s0277-3791(96)00066-2.
- Pail, R., N. Kühtreiber, B. Wiesenhofer, B. Hofmann-Wellenhof, G. Of, O. Steinbach, N. Höggerl, E. Imrek, D. Ruess, and C. Ullrich (2008), The austrian geoid 2007, *vgi –Österreichische Zeitschrift für Vermessung und Geoinformation*, 1, 3–14.
- Pail, R., H. Goiginger, W.-D. Schuh, E. Höck, J. M. Brockmann, T. Fecher, T. Gruber, T. Mayer-Gürr, J. Kusche, A. Jäggi, and D. Rieser (2010), Combined satellite gravity field model goco01S derived from goce and grace, *Geophys. Res. Lett.*, 37(20), L20,314, doi:10.1029/2010gl044906.
- Pail, R., S. Bruinsma, F. Migliaccio, C. Förste, H. Goiginger, W.-D. Schuh, E. Höck, M. Reguzzoni, J. M. Brockmann, O. Abrikosov, T. Fecher, R. Mayrhofer, I. Krasbutter, F. Sansó, and C. C. Tscherning (2011), First goce gravity field models derived by three different approaches, *Journal of Geodesy*, 85(11), 819–843, doi:10.1007/s00190-011-0467-x.
- Pascal, C., and S. A. Cloetingh (2009), Gravitational potential stresses and stress field of passive continental margins: Insights from the south-norway shelf, *Earth and Planetary Science Letters*, 277(3), 464–473.
- Pavlis, N. K., J. Factor, and S. Holmes (2007), Terrain-related gravimetric quantities computed for the next EGM, in *Proceedings of the 1st International Symposium of the International Gravity Field Service (IGFS), Istanbul 2006, Harita Dergisi, Special Issue*, 18, pp. 318–323, Istanbul, Turkey.
- Pavlis, N. K., S. A. Holmes, S. C. Kenyon, and J. K. Factor (2008), An Earth Gravitational Model to Degree 2160: EGM 2008, in *Geophysical Research Abstracts*, EGU General Assembly, Vienna, Austria.
- Pavlis, N. K., S. A. Holmes, S. C. Kenyon, and J. K. Factor (2012), The development and evaluation of the earth gravitational model 2008 (egm2008), *Journal of Geophysical Research*, 117(B4), doi:10.1029/2011jb008916.

- Pedersen, L. B., and T. M. Rasmussen (1990), The gradient tensor of potential field anomalies: Some implications on data collection and data processing of maps, *Geophysics*, *55*, 1558–1566, doi:10.1190/1.1442807.
- Pichowiak, S. (1994), Early jurassic to early cretaceous magmatism in the coastal cordillera and the central depression of north chile, in *Tectonics of the Southern Central Andes – Structure and Evolution of an Active Continental Margin*, edited by E. Scheuber and P. J. Wigger, pp. 203–217, Springer, doi:10.1007/978-3-642-77353-2_14.
- Prezzi, C. B., H.-J. Götze, and S. Schmidt (2009), 3d density model of the central andes, *Physics of the Earth and Planetary Interiors*, *177*(3-4), 217 – 234, doi:10.1016/j.pepi.2009.09.004.
- Pritchard, M. E., E. O. Norabuena, C. Ji, R. Boroschek, D. Comte, M. Simons, T. H. Dixon, and P. A. Rosen (2007), Geodetic, teleseismic, and strong motion constraints on slip from recent southern peru subduction zone earthquakes, *Journal of Geophysical Research: Solid Earth (1978–2012)*, *112*(B03307).
- Ramos, V., and A. Aleman (2000), Tectonic evolution of the Andes, in *Tectonic Evolution of South America*, edited by U. Cordani, E. Milani, A. Thomaz Filho, and D. Campos, pp. 635–685, 31st. International Geological Congress, Río de Janeiro.
- Ranero, C. R., and R. von Huene (2000), Subduction erosion along the middle america convergent margin, *Nature*, *404*(6779), 748–752, doi:10.1038/35008046.
- Ranero, C. R., J. Phipps Morgan, K. McIntosh, and C. Reichert (2003), Bending-related faulting and mantle serpentinization at the Middle America trench, *Nature*, *425*(6956), 367–373, doi:10.1038/nature01961.
- Reichert, C., and B. Schreckenberger (2002), Cruise report SO-161 leg 2 & 3, SPOC (Subduction Processes Off Chile), *Tech. rep.*, BGR Hannover, 142pp.
- Reigber, C., R. Schmidt, F. Flechtner, R. König, U. Meyer, K.-H. Neumayer, P. Schwintzer, and S. Y. Zhu (2005), An earth gravity field model complete to degree and order 150 from grace: Eigen-grace02s, *Journal of Geodynamics*, *39*(1), 1 – 10, doi:10.1016/j.jog.2004.07.001.
- Reutter, K., and H.-J. Götze (1994), Comments on the geological and geophysical maps., in *Tectonics of the Southern Central Andes*, edited by Reutter, Scheuber, and Wigger, pp. 329–333, Springer, Heidelberg.

- Romanyuk, T. V., R. Blakely, and W. D. Mooney (1998), The cascadia subduction zone: Two contrasting models of lithospheric structure, *Physics and Chemistry of the Earth*, 23(3), 297–301, doi:10.1016/S0079-1946(98)00028-7.
- Ruiz, S., M. Metois, A. Fuenzalida, J. Ruiz, F. Leyton, R. Grandin, C. Vigny, R. Madariaga, and J. Campos (2014), Intense foreshocks and a slow slip event preceded the 2014 iquique mw 8.1 earthquake, *Science*, 345(6201), 1165–1169, doi:10.1126/science.1256074.
- Sallarès, V., J. J. Dañobeitia, and E. R. Flueh (2001), Lithospheric structure of the Costa Rican Isthmus: Effects of subduction zone magmatism on an oceanic plateau, *J. Geophys. Res.*, 106(B1), 621–643, doi:10.1029/2000JB900245.
- Sallarès, V., P. Charvis, E. R. Flueh, and J. Bialas (2003), Seismic structure of Cocos and Malpelo Volcanic Ridges and implications for hot spot-ridge interaction, *J. Geophys. Res.*, 108(B12), 2564, doi:10.1029/2003JB002431.
- Schaller, T. (2013), Gravity-inferred 3d density model of the southern central andes, Diplomarbeit, Institut für Geowissenschaften, Christian-Albrechts-Universität zu Kiel.
- Scheuber, E., T. Bogdanic, A. Jensen, and K. Reutter (1994), Tectonic development of the north Chilean Andes in relation to plate convergence and magmatism since the Jurassic, in *Tectonics of the southern central Andes*, edited by K. Reutter, E. Scheuber, and P. Wigger, pp. 7–22, Springer, Berlin Heidelberg New York.
- Schmidt, S., and H.-J. Götze (2006), Bouguer and isostatic maps of the Central Andes, in *The Andes – active subduction orogeny*, *Frontiers in Earth Science Series*, vol. 1, edited by O. Oncken, G. Chong, G. Franz, P. Giese, H.-J. Götze, V. Ramos, M. Strecker, and P. Wigger, pp. 559–565, Springer-Verlag, Berlin Heidelberg New York.
- Schmidt, S., H.-J. Götze, C. Fichler, and M. Alvers (2010), IGMAS+ – a new 3D Gravity, FTG and Magnetic Modeling Software, in *GEO- INFORMATIK 2010 "Die Welt im Netz"*, edited by A. Zipf, K. Behncke, F. Hillen, and J. Schefermeyer, pp. 57–63, Akademische Verlagsgesellschaft AKA GmbH.
- Schmidt, S., C. Plonka, H.-J. Götze, and B. Lahmeyer (2011), Hybrid modelling of gravity, gravity gradients and magnetic fields, *Geophysical prospecting*, 59(6), 1046–1051, doi: 10.1111/j.1365-2478.2011.00999.x.
- Schmitz, M., K. Lessel, P. Giese, P. Wigger, M. Araneda, J. Bribach, F. Graeber, S. Grunewald, C. Haberland, S. Lüth, P. Röwer, T. Ryberg, and A. Schulze (1999), The crustal structure beneath the central andean forearc and magmatic arc as derived from seismic studies – the pisco 94 experiment in northern chile (21°–23°s), *Journal of South American Earth Sciences*, 12(3), 237 – 260, doi:10.1016/S0895-9811(99)00017-6.

- Schurr, B., A. Rietbrock, G. Asch, R. Kind, and O. Oncken (2006), Evidence for lithospheric detachment in the central andes from local earthquake tomography, *Tectonophysics*, 415(1), 203–223.
- Schurr, B., G. Asch, M. Rosenau, R. Wang, O. Oncken, S. Barrientos, P. Salazar, and J. P. Vilotte (2012), The 2007 m7.7 tocopilla northern chile earthquake sequence: Implications for along-strike and downdip rupture segmentation and megathrust frictional behavior, *Journal of Geophysical Research: Solid Earth (1978–2012)*, 117(B5).
- Schwartz, S. Y., and J. M. Rokosky (2007), Slow slip events and seismic tremor at circum-pacific subduction zones, *Reviews of Geophysics*, 45(3), doi:10.1029/2006RG000208.
- Sick, C. (2006), Structural investigations off Chile: Kirchhoff Prestack Depth Migration versus Fresnel Volume Migration, Ph.D. thesis, Department of Earth Sciences, Freie Universität Berlin.
- Silver, P. G., R. M. Russo, and C. Lithgow-Bertelloni (1998), Coupling of South American and African plate motion and plate deformation, *Science*, 279(5347), 60–63, doi:10.1126/science.279.5347.60.
- Sobiesiak, M., U. Meyer, S. Schmidt, H.-J. Götze, and C. M. Krawczyk (2007), Asperity generating upper crustal sources revealed by b value and isostatic residual anomaly grids in the area of Antofagasta, Chile, *J. Geophys. Res.*, 112, B12308, doi:10.1029/2006JB004796.
- Sobiesiak, M. M. (2000), Fault plane structure of the antofagasta, chile earthquake of 1995, *Geophysical Research Letters*, 27(4), 577–580, doi:10.1029/1999GL010498.
- Sobolev, S. V., and A. Y. Babeyko (2005), What drives orogeny in the andes?, *Geology*, 33(8), 617–620, doi:10.1130/G21557AR.1.
- Sobolev, S. V., A. Y. Babeyko, I. Koulakov, and O. Oncken (2006), Mechanism of the Andean Orogeny: Insight from numerical modeling, in *The Andes –active subduction orogeny.*, *Frontiers in Earth Science*, vol. 1, edited by O. Oncken, G. Chong, G. Franz, P. Giese, H.-J. Götze, V. Ramos, M. Strecker, and P. Wigger, pp. 513–535, Springer-Verlag, Berlin Heidelberg New York.
- Somoza, R. (1998), Updated nazca (farallon) - south america relative motions during the last 40 my: implications for mountain building in the central andean region, *Journal of South American Earth Sciences*, 11(3), 211–215.
- Song, T.-R. A., and M. Simons (2003), "large trench-parallel gravity variations predict seismogenic behavior in subduction zones", *Science*, 301(5633), 630–633, doi:10.1126/science.1085557.

- Tapley, B. D., S. Bettadpur, M. Watkins, and C. Reigber (2004), The gravity recovery and climate experiment: Mission overview and early results, *Geophys. Res. Lett.*, *31*(9), doi: 10.1029/2004gl019920.
- Tassara, A. (2005), Interaction between the nazca and south american plates and formation of the altiplano–puna plateau: Review of a flexural analysis along the andean margin (15–34 s), *Tectonophysics*, *399*(1), 39–57.
- Tassara, A. (2010), Control of forearc density structure on megathrust shear strength along the Chilean subduction zone, *Tectonophysics*, *495*(1-2), 34–47, doi:10.1016/j.tecto.2010.06.004.
- Tassara, A., H.-J. Götze, S. Schmidt, and R. Hackney (2006), Three-dimensional density model of the nazca plate and the andean continental margin, *J. Geophys. Res.*, *111*(B09404), 26 pp., doi:10.1029/2005JB003976.
- Tichelaar, B. W., and L. J. Ruff (1991), Seismic coupling along the Chilean subduction zone, *Journal of Geophysical Research*, *96*(B7), 11,997–12,022, doi:10.1029/91jb00200.
- Tscherning, C. C. (1993), Computation of covariances of derivatives of the anomalous gravity potential in a rotated reference frame, *Manuscripta geodaetica*, *18*(3), 115–123.
- Tsoulis, D. (1999), *Analytical and numerical methods in gravity field modelling of ideal and real masses*, *DGK Reihe C*, vol. 510, Beck, München.
- Turcotte, D. L., and G. Schubert (1982), *Geodynamics: Applications of continuum physics to geological problems*, 450 pp pp., John Wiley, New York.
- Wdowinski, S., I. Tsukanov, S. Hong, and F. Amelung (2010), Triggering of the 2010 haiti earthquake by hurricanes and possibly deforestation, in *AGU Fall Meeting Abstracts*, vol. 1, p. 08.
- Wells, R. E., R. J. Blakely, Y. Sugiyama, D. W. Scholl, and P. A. Dinterman (2003), Basin-centered asperities in great subduction zone earthquakes: A link between slip, subsidence, and subduction erosion?, *J. Geophys. Res.*, *108*(2507), 30 pp., doi:10.1029/2002JB002072.
- Wessel, P., and R. Müller (2007), Plate tectonics, in *Treatise on Geophysics*, edited by G. Schubert, pp. 49–98, Elsevier, Amsterdam, doi:10.1016/b978-044452748-6.00101-2.
- Willis, B. (1929), *Studies in Comparative Seismology: Earthquake Conditions in Chile*, 382, Carnegie Institution of Washington.

Witze, A. (2014), Chile quake defies expectations, *Nature*, 508, 440–441, doi:10.1038/508440a.

Zeumann, S. (2013), 3d finite element modelling of the central andean subduction zone with realistic geometry, Dissertation, Friedrich–Schiller–Universität Jena, Jena, Germany.

Zeumann, S., R. Sharma, R. Gassmöller, T. Jahr, and G. Jentzsch (2014), New finite-element modelling of subduction processes in the andes using realistic geometries, in *Earth on the Edge: Science for a Sustainable Planet, International Association of Geodesy Symposia*, vol. 139, edited by C. Rizos and P. Willis, pp. 105–111, Springer Berlin Heidelberg, doi: 10.1007/978-3-642-37222-3_13.

Zienkiewicz, O. C., R. L. Taylor, J. Z. Zhu, and P. Nithiarasu (2005), *The Finite Element Method*, Butterworth-Heinemann.

Appendix

Table A1: Density table for the Igmas model of Prezzi et al. (2009) and of the optimised model using IMOSAGA01C for geometry modifications and density inversion.

	Density Prezzi /10 ³ kg m ⁻³	Tolerable variation /%	Tolerable variation /10 ³ kg m ⁻³	Density optimised /10 ³ kg m ⁻³
<i>Oceanic domain</i>				
Oceanic plate				
Ocean water	2.67	2.43	0.065	2.67
Crustal sedimentary layer	2.55	5.22	0.133	2.55
Crustal basaltic/gabbroic layer	2.9	2	0.058	2.9
Lithosphere	3.29	0.24	0.008	∅3.281
Subducted slab				
Metamorphosed crust	3.05	3.84	0.117	3.05
Eclogitized crust	3.45	2.9	0.1	3.45
Lithosphere	3.38	0.27	0.009	3.386
Asthenosphere	3.35	0.15	0.005	3.35
<i>Continental domain</i>				
Upper crust				
Coastal Cordillera	2.73	1.54	0.042	2.73
Precordillera	2.69	1.19	0.032	2.69
Central Chile	2.65	1.06	0.028	2.65
Western Cordillera	2.68	1.08	0.029	2.68
Altiplano-Puna sediments	2.55	3.65	0.093	2.55
Altiplano-Puna	2.71	1.22	0.033	2.71
Eastern Cordillera	2.76	1.34	0.037	2.76
Subandean Ranges	2.74	2.04	0.056	2.74
Chaco sediments	2.45	2.53	0.062	2.45
Middle crust				
Coastal Cordillera	3.02–3.04	1.09–1.82	0.033–0.055	3.019–3.038
Precordillera	2.9	0.76	0.022	2.9
Western Cordillera	2.88	0.83	0.024	2.88
Altiplano-Puna	2.88	0.87	0.025	2.88
Eastern Cordillera	2.85	0.77	0.022	2.85
Subandean Ranges	2.86	1.12	0.032	2.86
Brazilian shield	2.88	0.59	0.017	2.88
Lower crust				
Coastal Cordill., serp. mantle	2.92–2.93	1.71–2.09	0.05–0.061	2.92–2.93
Precordillera	3	1.77	0.053	3
Western Cordillera	3.04	1.35	0.041	3.04
Altiplano-Puna	3.04	1.35	0.041	3.04
Brazilian shield	3	1.07	0.032	3
Atacama block	2.74–3.09	0.49–0.55	0.015	2.72
Lithosphere	3.34	0.15	0.005	3.343
Asthenosphere	3.37	0.3	0.01	3.378–3.382
Asthenospheric wedge	3.25	0.58	0.019	3.26

Selected Matlab scripts and functions:

MATLAB script *Ds_stats.m* (2014–10–10) for geo-referenced data extraction and combined plotting of slab geometry, seismicity, stress anomalies and plate coupling:

```

%% Import Stress data into SImport; write each value
% that is not NaN into S and clear the rest
SImport = importdata('F:\MODELS\I+Mods\P9Imo\
    DSvn_ST_ref267_Vre1200200225_topo267_dx8dy8_org_DEG.csv',',');
S = zeros(size(SImport,1)-length(find(isnan(SImport(:,5)))) , size(SImport,2));
c = 0; %line counter
for i = 1:length(SImport)
    if (isnan(SImport(i,5)) == 0)
        c = c+1;
        S(c,:) = SImport(i,:);
    end
end
clear SImport c i

%% Import seismo data (here: e.g. USGS):
EqUS = importdata('F:\DATA\EQ-data\SA-40--10_-80--60_USGSreviewed\19780909-201405091400
    _Lon_Lat_Z_M.csv',',',0);

% sort data by descending magnitude in column 4, large being plotted 1st later on):
EqUS = sortrows(EqUS,-4);

%% Importing topo, trench and coast line data
T = importdata('F:\DATA\Topo\0_015deg\egm2008-141625_-80--60_-45--5_0.015deg.gdf.xyz.csv',
    ',',0);
TR = importdata('F:\DATA\coastlines\PeruChileTrench.csv',',',0);
TR3 = mylola(TR,3); %resampling trench data
CL = importdata('F:\DATA\coastlines\outputs\10408060_coastfull_shore.xyz',',',0);
CL = CL(:,1:2);

%% Import plate coupling data (Metoi)
CC = importdata('F:\DATA\GPS\phi_bestmodel3P.txt.csv',',',0); %Lon Lat z coupling

%% Analysis over Lat loop ('strips') %%%%%%%%%%%%%%%%%%%%%%%%%%%%%%%%%%%%%%%%%%%%%%%%%%%%%%%%%%%%%%%%%%%%%%%%%%
% All LONs are used in this cell; strip moves by 'dl' southw.
z0 = -5e3; %start and stop depths, e.g. -5 - -80km
zend = -80e3; %
ms = 4; %re-define MarkerSize
fs = 12; %fontsize
MS1 = figure('name','Moving_Strip_Analysis_(\Delta\sigma_{vn}_histograms)');
MS2 = figure('name','Moving_Strip_Analysis_(\Delta\sigma_{vn}_vs_depth)');
dl = -0.5; %Shift width of strip, e.g. -2
dlfac = .5; %Strip width factor (lat)
l0 = -17; %Start and stop Lat
lend = -26; %
nolats = floor((lend-l0)/(dl)+1); %number of latitudes in loop

%Preallocations:
MShax = zeros(length(10:dl:lend),1);
MS2hax = zeros(size(MShax));
DSvnMean = zeros(length(10:dl:lend),2);
DSvnStd = zeros(size(DSvnMean));
DSvnMax = zeros(size(DSvnMean));
DSvnMin = zeros(size(DSvnMean));
EqStripMeanUS = zeros(length(10:dl:lend),3);
TopoMean = zeros(length(10:dl:lend),2);

%Subplot preparation:
sp = 0; %sub plot counter
spspan = nolats; clear nolats %number of subplots
spm = [floor(sqrt(spspan)),ceil(sqrt(spspan))]; %est. plot grid mxn
while spspan>spm(1)*spm(2)
    spmn(1) = spmn(1)+1;
end

for l = 10:dl:lend %lat loop

```

```

sp = sp+1;      %subplot counter
disp(['Lat', num2str(Lat), ' of ', num2str(sp), ' of ', num2str(spspan), ''])
LStrip.DSvn = find( (S(:,2) <=(1-dlfac*d1)) & (S(:,2) >(1+dlfac*d1)) & (S(:,3) <=z0) & (S
(:,3) >zend)); %find rows of this strip in S
LStrip.EqUS = find( (EqUS(:,2) <=(1-dlfac*d1)) & (EqUS(:,2) >(1+dlfac*d1)) & (EqUS(:,3) <=
z0) & (EqUS(:,3) >zend) & (EqUS(:,4) >5));
LStrip.Topo = find( (T(:,2) <=(1-dlfac*d1)) & (T(:,2) >(1+dlfac*d1)) & (T(:,1) >-73) & (T
(:,1) <-69.5) & (T(:,3) >=-8e3)); %find topo rows

DSvnMean(sp, 1:2) = [1, mean(S(LStrip.DSvn,5))]; %Mean of strip
DSvnStd(sp, 1:2) = [1, std(S(LStrip.DSvn,5))]; %Std of strip
DSvnMax(sp, 1:2) = [1, max(S(LStrip.DSvn,5))]; %Max of strip
DSvnMin(sp, 1:2) = [1, min(S(LStrip.DSvn,5))]; %Min of strip
EqStripMeanUS(sp, 1:3) = [1, mean(EqUS(LStrip.EqUS,3)), mean(Mw2M0(EqUS(LStrip.EqUS,4))
/1)]; %LatZMag
%EqStripSumUS(sp, 1:3) = [1, mean(EqUS(LStrip.EqUS,3)), sum(Mw2M0(EqUS(LStrip.EqUS,4))
/1)]; %LatZMag %alternative: sum instead of mean
TopoMean(sp, 1:2) = [1, mean(T(LStrip.Topo,3))];

%%% Histogram plot
MShax(sp) = subplot(spmn(1), spmn(2), sp, 'Parent', MS1);
histonum = -124:4:124; %histogram stress bins
MSHist = hist(S(LStrip.DSvn,5), histonum);
area(MShax(sp), histonum, MSHist/length(LStrip.DSvn)*100, 'EdgeColor', 'k', 'LineStyle', '-',
'LineWidth', 2, 'FaceColor', [.67 .67 .67], 'Parent', MShax(sp)) %stairs()
hold(MShax(sp), 'all')
line([0 0], [0 10], 'Color', 'k', 'LineWidth', 1, 'LineStyle', '-', 'Parent', MShax(sp))
line([DSvnMean(sp,2) DSvnMean(sp,2)], [0 9], 'Color', 'r', 'LineWidth', 1, 'LineStyle', '-',
'Parent', MShax(sp))
line([DSvnMean(sp,2)-DSvnStd(sp,2) DSvnMean(sp,2)-DSvnStd(sp,2)], [0 9], 'Color', 'b',
'LineWidth', 1, 'LineStyle', '-', 'Parent', MShax(sp))
line([DSvnMean(sp,2)+DSvnStd(sp,2) DSvnMean(sp,2)+DSvnStd(sp,2)], [0 9], 'Color', 'b',
'LineWidth', 1, 'LineStyle', '-', 'Parent', MShax(sp))
title(['Lat', num2str(Lat), ' of ', num2str(sp), ' of ', num2str(spspan), ''])
S', 'FontSize', 12, 'Parent', MShax(sp))
%text(-90, 9, [num2str(-1+dlfac*d1), ' - ', num2str(-1-dlfac*d1)], '
S', 'FontSize', fs, 'Parent', MShax(sp))
%text(-90, 7, [num2str(z0/1e3), ' - ', num2str(zend/1e3)], ' km', 'FontSize', fs, 'Parent',
MShax(sp))
xlabel('\Delta\sigma_{vn}/MPa', 'FontSize', fs, 'Parent', MShax(sp))
ylabel('%of stations', 'FontSize', fs, 'Parent', MShax(sp))
text(-90, 9, ...
['\mu(\Delta\sigma_{vn}):', num2str(mean(S(LStrip.DSvn,5)), 2), 'MPa'], ...
'Color', 'r', 'FontSize', 10, 'HorizontalAlignment', 'Left', 'Parent', MShax(sp))
text(-90, 8, ...
['std(\Delta\sigma_{vn}):', num2str(DSvnStd(sp,2), 2), 'MPa'], ...
'Color', 'b', 'FontSize', 10, 'HorizontalAlignment', 'Left', 'Parent', MShax(sp))
set(MShax(sp), 'XLim', [-100 100], 'YLim', [0 10], 'XTick', -100:50:100, 'YTick', 0:5:10,
'FontSize', fs);

%%% depth vs. Delta Sigma plot plus EQs %%%
MS2hax(sp) = subplot(spmn(1), spmn(2), sp, 'Parent', MS2);
scatter(MS2hax(sp), zeros(length(LStrip.EqUS), 1), EqUS(LStrip.EqUS,3) ./ 1e3, 3.^EqUS(LStrip
.EqUS,4), 'g')
hold(MS2hax(sp), 'all')
line([0 0], [zend/1e3 -10], 'Color', 'k', 'LineWidth', 1, 'LineStyle', '-', 'Parent', MS2hax(sp)
)
plot(MS2hax(sp), S(LStrip.DSvn,5), S(LStrip.DSvn,3) ./ 1e3, 'k', 'MarkerSize', ms)
title(['Lat', num2str(Lat), ' of ', num2str(sp), ' of ', num2str(spspan), ''])
S', 'FontSize', 10, 'Parent', MS2hax(sp))
xlabel('\Delta\sigma_{vn}/MPa', 'FontSize', 10, 'Parent', MS2hax(sp))
ylabel('Depth/km', 'FontSize', 10, 'Parent', MS2hax(sp))
set(MS2hax(sp), 'XLim', [-50 100], 'YLim', [zend/1e3-10 0], 'XTick', -50:50:100, 'YTick', zend
/1e3:20:0, 'FontSize', 10);

drawnow
end

% Fence plot along latitudes:
MS3=figure('name', 'MovingStripAnalysis(\Delta\sigma_{vn} vs LAT');
MS3hax(1)=axes('XColor', 'k', 'YColor', 'k', 'Color', 'None', 'YAxisLocation', 'left');
hold(MS3hax(1), 'all')
area(MS3hax(1), -DSvnMax(:,1), DSvnMax(:,2), 'LineStyle', 'none', 'FaceColor', [1 .85 .85]);

```



```

SLength = zeros(spspan,1);
SDepth = zeros(spspan,1);

for lati = maxLat:dlat:minLat %loop over latitude strips
    c = 0; %counter
    sp = sp+1; %subplot number
    disp(['... Lat', num2str(lati), ' of ', num2str(sp), ' of ', num2str(spspan), ''])
    SL = zeros(length(minLon:dlon:maxLon),5);

    for i = minLon:dlon:maxLon %mean stress anomaly, depth, TopoBathy AND Coupling loop
        c = c+1;
        SL(c,1:5) = [i,...
            mean(S(find(S(:,1)>=(i-whw) & S(:,1)<=(i+whw) & S(:,2)>=lati-whw & S(:,2)<=lati+whw),5)),...
            (1e-3)*mean(S(find(S(:,1)>=(i-whw) & S(:,1)<=(i+whw) & S(:,2)>=lati-whw & S(:,2)<=lati+whw),3)),...
            mean(T(find(T(:,1)>=(i-whw) & T(:,1)<=(i+whw) & T(:,2)>=lati-whw & T(:,2)<=lati+whw),3)),...
            mean(CC(find(CC(:,1)>=(i-whw) & CC(:,1)<=(i+whw) & CC(:,2)>=lati-whw & CC(:,2)<=lati+whw),4))];
    end

    TR3MeanLon = mean(TR3(find(TR3(:,2)>=lati-whw & TR3(:,2)<=lati+whw),1)); %find mean Lon of trench within LatRange
    CLMeanLon = median(CL(find(CL(:,2)>=lati-whw & CL(:,2)<=lati+whw),1)); %find mean Lon of Coast

    ALhax(sp) = subplot(spmn(1),spmn(2),sp,'Parent',AL);
    line([minLon maxLon],[0 0],'Color','k','Parent',ALhax(sp)) %zero line
    axis(ALhax(sp),'square')
    hold(ALhax(sp),'on')

    %initiate 2nd axis:
    fs = 14;%fontsize
    ALhax2(sp) = axes('Position',get(ALhax(sp),'Position'),...
        'XAxisLocation','bottom','YAxisLocation','right',...
        'Color','none','XColor','k','YColor','k',...
        'XLim',[floor(minLon),ceil(maxLon)],'YLim',[-250 comymax],...
        'XTick',minLon:1:maxLon,'YTick',-50:50:100,'FontSize',fs,'Parent',AL);
    axis(ALhax2(sp),'square')
    uistack(ALhax2,'bottom')
    hold(ALhax(sp),'all')
    hold(ALhax2(sp),'all')

    %red-blue wiggle plot of DeltaSigma:
    for i = 1:length(SL)
        if SL(i,2)>0
            bar(ALhax2(sp),SL(i,1),SL(i,2),dlon,'r','EdgeColor','none')
        else
            bar(ALhax2(sp),SL(i,1),SL(i,2),dlon,'b','EdgeColor','none')
        end
    end

    %
    % optional plot: reference depths:
    % refcolor = [0 1 1;1 0 1];
    %% line([minLon maxLon],[-15 -15],'Color',refcolor(1,:))
    %% line([minLon maxLon],[-35 -35],'Color',refcolor(2,:))
    % %find projection of reference contrast: (bei Prezzi: 15 und 35 km) and zerocrossing:
    % proj15 = median(SL(find(-17<SL(:,3) & SL(:,3)<-13),1));
    % line([proj15 proj15],[-15 0],'Color',refcolor(1,:), 'LineStyle','-', 'LineWidth',2, 'Parent',ALhax(sp))
    % proj35 = median(SL(find(-37<SL(:,3) & SL(:,3)<-33),1));
    % line([proj35 proj35],[-35 0],'Color',refcolor(2,:), 'LineStyle','-', 'LineWidth',2, 'Parent',ALhax(sp))
    % %s0Lon(1)=mean(SL(find(SL(:,1)>-72.5 & SL(:,1)<-71 & SL(:,2)>-3 & SL(:,2)<3),1))
    % ;%zerocrossingLon
    % s0Lon(sp)=mean(SL(find(SL(:,1)>-71 & SL(:,1)<-69 & SL(:,2)>-1 & SL(:,2)<4),1));%
    % zerocrossingLon
    % s0Z(1)=mean(SL(find(SL(:,1)>TR3MeanLon-0.5 & SL(:,1)<TR3MeanLon+0.5),3));
    % s0Z(2)=mean(SL(find(SL(:,1)>s0Lon(sp)-0.5 & SL(:,1)<s0Lon(sp)+0.5),3));
    % line([TR3MeanLon+0.15 TR3MeanLon+0.15 -73],[40 s0Z(1) s0Z(1)], 'Color',[1 0 0],

```

```

LineStyle','--','LineWidth',1,'Parent',ALhax(sp))
%   line([s0Lon(sp) s0Lon(sp) -73],[40 s0Z(2) s0Z(2)],'Color',[1 0 0],'LineStyle
','--','LineWidth',1,'Parent',ALhax(sp))
%   SLength(sp)=s0Lon(sp)-TR3MeanLon;
%   SDepth(sp)=s0Z(2);
%   clear proj15 proj35 s0Lon s0Z

%%EQ plot:
sf = 2.0; %[2.1]ScaleFactor, use for circle plot size
cs = 2.5; %circle size if constant size is to be used
mlw = 1; %lineWidth of scatter markers
msl = 4; %markerSize for local EQs in 'plot' mode
mcl = [.5 .5 .5];
%USGS data:
tmp = find(EqUS(:,4)>=EqTHold & EqUS(:,1)>=minLon & EqUS(:,1)<=maxLon & EqUS(:,2)>=lati
-whh & EqUS(:,2)<=lati+whh & EqUS(:,3)~=0);
scatter(ALhax(sp),EqUS(tmp,1),EqUS(tmp,3).*1e-3,sf.^(EqUS(tmp,4)), [.2 .75 .2], 'filled',
'MarkerEdgeColor',[.1 .375 .1],'LineWidth',mlw)

%plot SLAB (from stress data file):
plot(ALhax(sp),SL(:,1),SL(:,3),'-k','LineWidth',2)

%%Alternative plot mode: stress relative to slab-line:
%   plot(ALhax(sp),SL(isfinite(SL(:,2)),1),SL(isfinite(SL(:,2)),3)+1*SL(isfinite(SL(:,2))
,2),'-',...
%   'LineWidth',1,...
%   'Color',SL(isfinite(SL(:,2)),4:6)) %plot stress anomaly relative to slab
depth(!)
%   plot(ALhax(sp),SL(:,1),SL(:,3)+1*SL(:,2),'-r','LineWidth',2)
%   p=patch(SL(:,1),SL(:,2),SL(:,2),'Marker','none','FaceColor','interp');
%   plot(ALhax(sp),SL(:,1),SL(:,2),'-r','LineWidth',2) %plot stress anomaly line
%   plot(ALhax(sp),SL(:,1),SL(:,3)+3*gradient(SL(:,2)),'Color',[0 .9
.9],'LineWidth',1) %plot stress gradient

%%COUPLING plots ('strops'):
plot(ALhax2(sp),SL(:,1),100*SL(:,5),'-', 'Color',[1 .66 0],'LineWidth',2)%COUPLING FROM
GPS
plot(ALhax(sp),SL(:,1),SL(:,4).*1e-3,'-k','LineWidth',2)%plot mean TopoBathy
plot(ALhax(sp),TR3MeanLon,4,'v','MarkerEdgeColor','k','MarkerFaceColor','w','MarkerSize
,7)%plot mean trench location
text(TR3MeanLon,14,'T','HorizontalAlignment','center','FontSize',fs,'Parent',ALhax(sp))
plot(ALhax(sp),CLMeanLon,4,'v','MarkerEdgeColor','k','MarkerFaceColor','k','MarkerSize
,7)%plot mean coast location
text(CLMeanLon,14,'C','HorizontalAlignment','center','FontSize',fs,'Parent',ALhax(sp))

%set ax1:
set(ALhax(sp),'XLim',[floor(minLon),ceil(maxLon)],'YLim',[minZ,comymax],'FontSize',fs,
'Color','none','XTick',minLon:1:maxLon,'YTick',-120:40:10)
xlabel(ALhax(sp),'Lon_/°','FontSize',fs)
ylabel(ALhax(sp),'z_/km','FontSize',fs)

%set ax2:
set(ALhax2(sp),'XLim',[floor(minLon),ceil(maxLon)],'YLim',[-260 100], ...
'XTick',minLon:1:maxLon,'YTick',-50:50:100,'FontSize',fs);
ylabel(ALhax2(sp),{'\Delta sigma_{vn}/MPa';'coupling_/%'},'Position',[-66.2 20 1.001])

%range labeling:
text(-69,60,[num2str(abs(lati+whh)), '_-_', num2str(abs(lati-whh))], '°
S'],'FontSize',fs,'Parent',ALhax2(sp))

%%Scatter plot of DeltaSigma & Coupling %%%%%%%%%%%
AL2hax(sp)=subplot(spmn(1),spm(2),sp,'Parent',AL2,'FontSize',fs);
scatter(AL2hax(sp),SL(:,2),SL(:,5),50,SL(:,3),'fill','MarkerEdgeColor',[0 0 0])
title([num2str(abs(lati+whh)), '_-_', num2str(abs(lati-whh))], '°
S'],'FontSize',fs,'Parent',AL2hax(sp))
ylabel(AL2hax(sp),'coupling','FontSize',fs)
xlabel(AL2hax(sp),'\Delta sigma_{vn}/MPa','FontSize',fs)
set(AL2hax(sp),'XLim',[-30,80],'YLim',[0,1],'LineWidth',2)
AL2CB=colorbar('peer',AL2hax(sp),'FontSize',fs,'ytick',[-100:25:0],'location','
EastOutside');
caxis([-100 0])

```



```

    title (AL2CB, 'z⊥/km', 'FontSize', fs)
    drawnow

    %%Collect stress and coupling results:
    SLall=[SLall;SL(:,2:3)];
    CCall=[CCall;SL(:,5)];
end
clear lati whh

for i=1:sp %run this loop manually if needed (align axes)
    set(ALhax2(i), 'Position', get(ALhax(i), 'Position'))
    set(AL2hax(i), 'XLim', [-30 80], 'YLim', [0 1])
    set(AL2hax(i), 'PlotBoxAspectRatio', [1 1.2 1])
    box(AL2hax(i), 'on')
end

%% COUPLING over DeltaSigma plot (data of all subplots) %%%
StrepScatFig = figure('name', 'coupling⊥over⊥\Delta\sigma');
StrepScatAx = axes('Parent', StrepScatFig);
scatter(StrepScatAx, SLall(:,1), CCall, 50, SLall(:,2), 'fill'); %20(size)
set(StrepScatAx, 'XLim', [-30,60], 'YLim', [0,1], 'LineWidth', 2)
StrepScatCB = colorbar;
caxis([-80 0])
xlabel(StrepScatCB, 'z⊥/km')
line([0 85],[0 .85], 'LineStyle', '—', 'Color', 'k', 'LineWidth', 2)
line([0 85],[0 .8*85/100], 'LineStyle', '-', 'Color', 'k', 'LineWidth', 2)
line([0 0],[0 1], 'LineStyle', '-', 'Color', 'k', 'LineWidth', 2)
xlabel(StrepScatAx, '\Delta\sigma_{vn}_{⊥}/MPa')
ylabel(StrepScatAx, 'coupling')

```

Tool function *mylolati.m* (2014–10–10) for simple inverse distance weighted resampling of 2D line data:

```

function [I]=mylolati(L,r)

% MYLOLATI resamples consecutive LON-LAT information as Trench location or coastlines.
%
% I=MYLOLATI(L,r)
%
% 'L' is a two column (Lon,Lat) list of data points.
% 'r' is the resampling factor by which the original data is to
% be resampled. E.g., r=1 generates one additional data point in the center
% of two existing data points, r=2 adds two and so on. A simple linear /r
% distance weighting scheme is applied to each column, respectively.
% 'I' is of size ((length(L)-1)*(r+1)+1 , 2).
%
% (c)2014 B.D. Gutknecht, Kiel University

%% ALLOCATION
l = length(L); %length of input list
l_new = (l-1)*(r+1)+1; %length of output list
I = zeros(l_new,2); %allocation
lc = 1; %line counter

%% COMPUTING
for i = 1:(l-1)
    I(lc,1:2) = L(i,:);
    %the following line is not fit for r n.e. 1 !!
    %lLonLat(lc+1,1:2) = mean(LonLat(i:(i+1),1:2));
    for j=1:r %loop over lin.-interpol.
        I(lc+j,1:2) = (r-j+1)/(r+1)*(L(i,1:2)) ...
            + j/(r+1)*(L(i+1,1:2));
    end
    lc = lc+1+r; %increase line counter
end
clear l lc r i j
% last row:
I(l_new,1:2) = L(end,:);
clear l_new LonLat

```

Tool function *gref.m* (2015–01) for calculation of reference gravity as a function of latitude:

```

function [gref]=gref(lat,s)

% gref(lat,s) gives the reference gravitational acceleration in meters
% per second squared at latitude lat (in decimal degrees), calculated from
% ... WGS84 Ellipsoidal Gravity Formula for s='wgs84'
% ... IAG67 reference formula (parameters from Fowler 2005, The Solid Earth) for s='iag67'
%
% Example: Calculate reference gravity g_ref at 25 degrees South with
% reference to WGS84 ellipsoid:
% g_ref = gref(-25,'wgs84')
%
% ToDo(not implemented yet; wgs80?):
% gamma = gamma_e * (1 + 0.005 279 0414 sin2 PHI
%           + 0.000 023 2718 sin4 PHI
%           + 0.000 000 1262 sin6 PHI
%           + 0.000 000 0007 sin8 PHI);
%           rel.error 10^-10 ~ 10^-3µm s^-2 = 10^-4 mgal.
%
% The conventional series
%           gamma = gamma_e (1 + f* sin2 PHI - f4 sin2 2 PHI)
%           = 9.780 327 (1 + 0.005 3024 sin2 PHI
%           - 0.000 0058 sin2 2 PHI) m s^-2
% has only an accuracy of 1 µm s^-2 = 0.1 mgal.
%
% U0      = 6 263 686.0850 x 10 m2 s^-2 normal potential at ellipsoid
% J4      = -0.000 002 370 912 22
% J6      = 0.000 000 006 083 47 spherical-harmonic
% J8      = -0.000 000 000 014 27 coefficients
% m       = 0.003 449 786 003 08 m = omega^2 a^2 b/GM
% gamma_e = 9.780 326 7715 ms^-2 normal gravity at equator
% gamma_p = 9.832 186 3685 ms^-2 normal gravity at pole
% f*      = 0.005 302 440 112
% k       = 0.001 931 851 353
%
% (c)2015 B.D. Gutknecht, CAU Kiel, benjamin@geophysik.uni-kiel.de

% WGS84 factors:
gstd= 9.7803267714;
f1 = 0.00193185138639;
f2 = 0.00669437999013;

% IAG67 factors:
ge = 9.7803185;
alpha=5.278895e-3;
beta =2.3462e-5;

if strcmp(s,'wgs84') %CASE: compute using WGS84
    gref = gstd.*(1+f1.*(sind(lat)).^2)./sqrt((1-f2.*(sind(lat)).^2));
elseif strcmp(s,'iag67') %CASE: compute using IAG67
    gref = ge.*(1+alpha.*sind(lat).^2+beta.*sind(lat).^4);
else error('gref:arginCheck',... %CASE: method string not found
    ['Couldn't find a valid method string @ 2nd input parameter \n',...
    'Choose a valid method string at second input parameter, e.g. 'wgs84' or 'iag67'
    '\n',...
    'Info: Delimiter between input paramters must be comma.\n',...
    'Example: gref(-25,'wgs84') gives reference gravity after the WGS84 system at 25
    degrees South.'])
end

```

List of Figures

2.1	Anomaly of a gravity potential and its first three vertical derivatives	18
2.2	Anomaly of the gravity potential of a buried cuboid and its first and second horizontal derivative	19
2.3	Full symmetric gravity gradient tensor of a simple synthetic salt pillow . . .	21
2.4	Invariants I0, I1 and I2 over a simple synthetic salt pillow	22
3.1	Bouguer gravity anomaly map of the Japan–Pacific continental margin (EGM 2008)	33
3.2	Residual Bouguer anomaly map of the Japan–Pacific continental margin . .	34
3.3	Spherical density residual model below the geoid	35
3.4	Density contrast versus minimum diameter of a density anomaly	37
3.5	Synthetic 3D density model of a Chilean–type subduction zone	38
3.6	Bouguer anomaly of the vertical gravity component above the Andean–type density model	39
3.7	Vertical gravity gradient anomaly above the Andean–type density model . .	40
3.8	Invariants of the full gravity gradient tensor at orbit height	40
3.9	Geologic setting of Central and South America	46
3.10	Gravity anomaly and gravity disturbance	49
3.11	Comparison of the EGM2008 with surface gravity data from Costa Rica and Chile	53
3.12	Deviation of geodetic and geophysical Bouguer anomaly from terrestrial data	54
3.13	Vertical cross-section of a 3D density model from Central America	55
3.14	Vertical cross-section of a 3D density model from Central Chile at 37.4°S .	56
3.15	Gravity and gradient signal at orbit height caused by density an anomalous mass with density contrast	57
3.16	3D-Modelling of synthetic gravity, gradient tensor and invariants (‘shoe-box’ model)	59
3.17	Viscous-elastic model	60
4.1	Architectural design and the product flow of regional gravity field processing system	70

4.2	Topographic corrections calculated with different algorithms for validation .	72
4.3	Comparison of heights	74
4.4	Comparison of gravity	75
4.5	Elements of the data preparation (remove step) for the Least Squares Collocation	77
4.6	Input and output of the Least Squares Collocation	81
4.7	Output field of the Least Squares Collocation	82
4.8	Comparison of the IMOSAGA01C regional gravity model with the EGM2008 global model	84
4.9	East–West striking cross section through ~20.2°S (Iquique)	85
4.10	East–West striking cross section through ~30.3°S.	86
4.11	Part of the cross section in Fig. 4.10 with adjusted near surface block	87
4.12	Tectonic setting and stress anomalies of the Central Andes.	93
4.13	Data flow chart describing types of gravity data and models	95
4.14	Schematic representation of the computation of stress components on a subduction interface	98
4.15	Cross section of the dynamic model at 22.5°S	101
4.16	Normalized histograms of moving–strip analysis on the stress anomaly	105
4.17	Vertical cross sections of stress anomalies, slab geometry and major seismicity	106
4.18	Gravitational Potential Energy of the Central Andean surroundings	108
4.19	Results from the FE–modelling (top views)	111
4.20	Earthquake distribution and von Mises stress	113
4.21	Vertical gravity gradient anomalies at 8 km altitude	115
4.22	Distribution of gravity residuals	119
4.23	Residual gravity with N- and S-extension	120
4.24	Enlarged version of the stress anomaly as shown in figure 4.12	121
4.25	Slip isolines overlay of the Pisagua main shock over normal component of stress anomalies on subduction interface	122
4.26	Vertical isostatic gradient anomalies at 8 km altitude	124
4.27	Deviation from reference gravity	127
5.1	Combined plot of stress anomalies, seismicity and plate coupling	131
5.2	Plate coupling and stress anomaly at 18.75–21.75°S	133
5.3	Stress anomaly and coupling at latitudinal windows in northern Chile	134
5.4	Schema describing the effect of stress anomalies on plate coupling	135
5.5	Vertical sections of average coupling, stress anomaly and lithospheric geometry at 24–26°S	137
5.6	Plate coupling and stress anomaly loops at 24–26°S	138

List of Tables

2.1	Calculation of the Eötvös tensors	20
2.2	Calculation of invariants I_0 , I_1 and I_2	22
3.1	Correlation of the EGM2008 with terrestrial data.	51
4.1	Statistical parameters for the differences of terrestrial data to global gravity fields.	75
4.2	Key statistical parameters of gravity anomalies before and after the reduction process.	76
4.3	Input datasets used for the combined regional gravity model.	79
4.4	Rheological parameters for units of the dynamic model	102
A1	Density table Prezzi (2009) and IMOSAGA01C optimised	163

Acronyms

d/o	degree and order
ACE	Altimeter Corrected Elevations
CHAMP	CHALLENGING Minisatellite Payload
DFG	German Research Foundation
DTM	Digital Terrain Model
FEM	Finite Element Method
GEO	Group on Earth Observations
GLONASS	Globalnaya navigatsionnaya sputnikovaya sistema
GNSS	Global Navigation Satellite Systems
GOCE	Gravity Field and Steady-State Ocean Circulation Explorer
GPS	Global Positioning System
GRACE	Gravity Recovery and Climate Experiment
GPE	Gravitational Potential Energy
IMOSAGA	"Integrated MOdelling of Satellite- and Airborne Gravity data of Active plate margins"
InSAR	Interferometric Synthetic Aperture Radar
IPOC	"Integrated Plate boundary Observatory Chile"
LSC	Least Squares Collocation
NOGAPSGRAV	"NOvel Geophysical And Petrological applications of new-generation Satellite-derived GRAVity data with a focus on hazardous and frontier regions"

RCR	Remove-Compute-Restore
RWI	Rock-Water-Ice
SPP	Schwerpunktprogramm (Priority Programme)
SRTM	Shuttle Radar Topography Mission

Acknowledgements

I thankfully acknowledge financial support of the German Research Foundation (DFG) for the NOGAPSGRAV and IMOSAGA projects within the Special Priority Programme SPP 1257 'Mass Transport and Mass Distribution in the Earth System'.

Special thanks go to Prof. Dr. 'Hajo' Götze, supervisor and former leader of the Geophysics and Geoinformation Research Group at the Institute of Geosciences at Kiel University. I am much obliged to him for providing me guidance with my research activities throughout my studies and for giving me plenty of room to develop ideas, also in creative ways.

Also special thanks to Dr. Rezene Mahatsente, now at the University of Alabama, for never-ending discussions and correction-sessions to journal manuscripts. I am grateful for all valuable input and discussions I had with Dr. Monika Sobiesiak; be it about the formerly 'unbroken' Iquique segment or about all the other more or less important things in this prodigious world.

Thanks to Oscar Lücke and Nils Holzrichter for our collaboration during the time of the NOGAPSGRAV and IMOSAGA projects. The same accounts for our colleagues from Friedrich-Schiller University in Jena (Gerhard Jentzsch, Thomas Jahr, Stefanie Zeumann and Rekha Sharma) and at the Technical University of Munich (Roland Pail, Michael Hosse, Martin Horwath).

Thanks to Dr. Sabine Schmidt at Kiel University and the team of Transinsight GmbH in Dresden for their assistance with the IGMAS+ modelling software.

Thanks to Jörg Ebbing, Dietrich Lange, Christine Fichler, Carla Braitenberg, Ron Hackney, Andres Tassara and Roman Pasteka for inspiring discussions on several occasions.

Thank you Master Kang, Shin-Gyu, for teaching me some very effective attitudes. Thank you Ralf, for all the cycling efforts and for being a constant pole during my entire time in Kiel.

And last – but never the least – I would like to thank Susann and all my family and friends for the multitude of support and abundance of patience during the past years. It meant much more to me than I have been able to say. Thank you all. Never quit rocking.

Copyright acknowledgement

Chapter 3.1 was published in Ouwehand, L. (Ed.): Proceedings of the 4th International GOCE User Workshop, 2011, ESA Special Publication SP-696, ISBN 978-92-9092-260-5; Author: B.D. Gutknecht

Chapter 3.2 was published in Journal of Geodynamics, Volumes 59–60; Authors: N. Köther, H.-J. Götze, B.D. Gutknecht, T. Jahr, G. Jentzsch, O.H. Lücke, R. Mahatsente, R. Sharma, S. Zeumann; Title: "The seismically active Andean and Central American margins: Can satellite gravity map lithospheric structures?"; Pages 207–218; Copyright Elsevier 2012. The original article can be assessed at:

<http://dx.doi.org/10.1016/j.jog.2011.11.004>

<http://www.sciencedirect.com/science/article/pii/S0264370711001256>

Chapter 4.1 was published in Surveys in Geophysics, Volume 35, Issue 6, pp. 1393–1415, November 2014, 'online first' on 21 Oct 2014; Authors: M. Hosse, R. Pail, M. Horwath, N. Holzrichter, B.D. Gutknecht; Title: "Combined Regional Gravity Model of the Andean Convergent Subduction Zone and Its Application to Crustal Density Modelling in Active Plate Margins"; Copyright Springer 2014.

The original article can be assessed at:

<http://dx.doi.org/10.1007/s10712-014-9307-x>

<http://link.springer.com/article/10.1007/s10712-014-9307-x>

Chapter 4.2 was published in Surveys in Geophysics, Volume 35, Issue 6, pp. 1417–1440, November 2014, 'online first' on 31 July 2014; Authors: B.D. Gutknecht, H.-J. Götze, T. Jahr, G. Jentzsch, R. Mahatsente, S. Zeumann; Title: "Structure and State of Stress of the Chilean Subduction Zone from Terrestrial and Satellite-Derived Gravity and Gravity Gradient Data"; Copyright Springer 2014.

The original article can be assessed at:

<http://dx.doi.org/10.1007/s10712-014-9296-9>

<http://link.springer.com/article/10.1007/s10712-014-9296-9>

Declaration

I hereby certify that this thesis is my own composition, all sources have been acknowledged and my contribution to the thesis is clearly identified. The thesis has not previously been submitted or accepted for a degree at this or another institution. I certify that the work has been undertaken in compliance with the German Research Foundation's (DFG) rules of good academic practice.

Deutsche Fassung der Erklärung (German version):

Hiermit versichere ich, dass die vorliegende Arbeit von mir unter Anleitung meiner Betreuer und nur mit den angegebenen Hilfsmitteln verfasst worden ist. Diese Arbeit hat als solche weder in gleicher noch in ähnlicher Form einer Prüfungsstelle vorgelegen. Ich versichere, dass die Arbeit unter Einhaltung der Regeln guter wissenschaftlicher Praxis der Deutschen Forschungsgemeinschaft entstanden ist und dass jene Stellen der Arbeit, die anderen Werken wörtlich oder inhaltlich entnommen sind, durch entsprechende Angaben der Quellen kenntlich gemacht sind.

Ort, Datum

Benjamin D. Gutknecht

Curriculum Vitae

Personal Data

Name: Benjamin D. Gutknecht
Nationality: German
Date of Birth: 13. Oct 1981
Place of Birth: Lübeck, Germany

Higher Education & scientific career

09/2010-07/2015: PhD studies (geophysics)
Institute of Geosciences, CAU Kiel
04/2014-08/2014: Graduate Research Assistant
Institute of Geosciences, CAU Kiel (Prof. Ebbing)
04/2010-12/2013: Research Assistant
Institute of Geosciences, CAU Kiel (Prof. Götze)
2006-03/2010: Diplom (M.Sc.) in geophysics, physical oceanography
and extraterrestrial physics
Institute of Geosciences, CAU Kiel (Prof. Götze)
07/2007-09/2007: Student Research Assistant, Statoil Research Centre,
Trondheim, Norway (invited)
07/2006-09/2006: Student Research Assistant, Statoil Research Centre,
Trondheim, Norway
10/2003-2006: Vordiplom (~B.Sc.) in geophysics,
Institute of Geosciences, CAU Kiel

School Education

1988-2001: Primary and secondary school (German 'Gymnasium'),
Lübeck, Germany